Universidad del País Vasco
Centro de Física de Materiales

Plasmons in Nanoparticles: Atomistic *Ab Initio* Theory for Large Systems

---

Thesis
submitted to the University of the Basque Country
for the degree of
Doctor in Physics
by

Marc Barbry [1]

Under the supervision of Daniel Sánchez-Portal and Peter Koval

Donostia-San Sebastian, Spain

2014-2018

[1] marc.barbry@mailoo.org

Acknowledgements

For the incredible journey that has been my PhD, I have to thank many tutors and friends. The ones without whom this journey would not have been possible are my supervisors Prof. Daniel Sánchez-Portal and Dr. Peter Koval. They have both taught me all the necessary for me to succeed my PhD and even beyond. I have to acknowledge their exceptional patience towards my multiple mistakes. They greatly guided me during my work and support the ideas I got, even if most of them were far from being fruitful. I had a great time working with them for almost five years.

I would like to thank Prof. Dietrich Foerster without whom I would never have ended working in San Sebastian. He granted me the crucial support I needed when I started to work here.

In addition, I would like to thank Prof Javier Aizpurua and the members of his group, Dr. Nerea Zabala and Mattin Urbieta, with whom we had a pleasant collaboration. I would also like to thank the computing staff of CFM and DIPC, particularly Iñigo Aldazabal and Diego Lasa who have often provided me great help in the challenges I was facing and also for new ideas to experiment. I want to thank all my colleagues at CFM, DIPC and Nanogune with whom I enjoyed my time in San Sebastian. Particularly Moritz Müller and Iker Gallardo who have shared my daily life for almost five years.

I have to acknowledge the financial support from the Departamento de Educación of the Basque Government through a PhD grant, as well as from Euskampus and the DIPC at the initial stage of my work. I gratefully acknowledge the support of NVIDIA Corporation with the donation of the Tesla K40 GPU used for this research.

Finally, a special thanks to my family for their everyday support and particularly to my wife who illuminates my days.

Donostia-San Sebastian, May 2018

Marc Barbry

Resumen (Summary in Spanish)

La capacidad de entender la materia y su interacción con el medio determinan en gran parte el desarrollo de las nuevas tecnologías. Hoy en día, las nanotecnologías son un campo emergente de investigación debido al gran impacto que tienen en la sociedad. Las simulaciones computacionales de fenómenos físicos en la nanoescala han contribuido a la aceleración de su desarrollo.

En esta tesis doctoral nos hemos basado en simulaciones *ab initio* atomísticas para explicar el comportamiento de nanopartículas sometidas a estímulos externos. Con "atomístico" nos referimos a que la geometría del sistema se descibe mediante posiciones realístas de los átomos, es decir, que se tienen en cuenta las posiciones atómicas y la atracción Coulombiana generada por cada núcleo, en vez de reemplazarlas por un potencial efectivo suave que confina los electrónes en objetos de forma simple, como una esfera. "*ab initio*" significa que nos hemos basado en las leyes de la mecánica cuántica para modelar los electrones del sistema. De esta forma, en este trabajo hemos podido simular la interacción de centenas de electrones confinados dentro de nanopartículas, tanto entre ellos como con el medio. Este problema se conoce como el problema de muchos cuerpos (*many body problem* en inglés). Desafortunadamente, hay que recurrir a aproximaciones para resolver el problema de muchos cuerpos. Las aproximaciones adoptadas en esta tesis son las integradas en la teoriá del funcional de la densidad (DFT, en inglés *density functional theory*) implementadas en los paquetes de SIESTA (*Spanish Initiative for Electronic Simulations with Thousands of Atoms*)[1, 2], así como su extensión a fenómenos dependientes del tiempo (TDDFT, en inglés *time-dependent DFT*) implementadas en los paquetes de MBPT-LCAO (*Many Body Perturbation Theory - Linear Combination of Atomic Orbitals*) [3–5] y PySCF-NAO (*Python-Based Simulations of Chemistry Framework - Numerical Atomic Orbitals*) [6, 7]. Por otra parte, en esta tesis doctoral hemos conseguido implementar con éxito nuevas funcionalidades en los paquetes de MBPT-LCAO y

PySCF-NAO. Ambos paquetes han sido utilizados para calcular las propiedades de estados excitados de sistemas finitos como agregados atómicos (*clusters* en inglés) metálicos, fragmentos de nanotubos y moléculas pequeñas.

En el primer capítulo de la tesis, explicamos el porqué de nuestro estudio teórico. La motivación se basa en el interés genuino de poder entender en profundidad e intepretar las datos obtenidos con técnicas experimentales como la espectroscopía óptica, espectroscopía de pérdida de energía de electrones (EELS, en inglés *electron energy loss spectroscopy*) y espectroscopía de dispersión inelástica. Además de esto, nos gustaría poder predecir las propiedades de nanodispositivos electrónicos y ópticos, y así proporcionar una guía teórica en el desarrollo de la nanociencia y nanotecnología. La predicción de propiedades en la nanoescala con precisión razonable puede lograrse mediante la aplicación de los métodos *ab initio* basados en DFT y TDDFT.

En el segundo capítulo damos cuenta de forma detallada de los métodos DFT y TDDFT que hemos desarrollado y mejorado. Por completitud, comenzamos con una breve descripción del problema de muchos cuerpos y de las primeras aproximaciones que se deben hacer para resolverlo. La primera sección se centra en una pequeña introducción de la teoría funcional de la densidad. Para esto, empezamos con el modelo de Thomas-Fermi, para luego explicar los teoremas de Hohenberg-Kohn, y terminar con una descripción del método de Kohn-Sham que se utiliza en la práctica para obtener la densidad de electrones del estado fundamental. Todo esto precede a un resumen sobre TDDFT como método para obtener la respuesta de la densidad electrónica a una perturbación externa. La estructura general de dicha teoría junto con la ecuación de Kohn-Sham dependiente del tiempo se discute antes de la aproximación de la respuesta lineal y las características generales de respuesta plasmónica, ambas desde la perspectiva del método de Kohn-Sham dependiente del tiempo. Esto da pie a discustir el método empleado para implementar la respuesta lineal a nivel TDDFT dentro de los paquetes de cálculo MBPT-LCAO y PySCF-NAO. La descripción del tratamiento de los estados excitados dentro del marco de la combinación lineal de orbitales atómicos con orbitales atómicos numéricos precede a los cálculos de la densidad inducida en la utilizando respuesta lineal a nivel TDDFT. En esta sección se describe la aplicación secuencial de las matrices de la función repuesta no interaccionante, que es la base de la eficiencia de nuestro método iterativo para el cálculo de la respuesta autoconsistente del sistema. Durante el desarrollo de la tesis, se ha logrado implementar mejoras en el algoritmo iterativo y se ha optimizado los requerimientos de memoria del programa, lo que ha permitido la computación de grandes agregados metálicos que se presentan en los capítulos 3-7. Después de esto, se explica el método para calcular el tensor de la poralizabilidad óptica junto con el cálculo del campo eléctrico inducido en las cercanías de las nanoestructuras estudiadas, lo que se conoce como el "campo cercano".

Éste último es el primer logro obtenido en este trabajo. Por último, se menciona la migración del paquete MBPT-LCAO a la librería PySCF-NAO, esta última escrita en su mayoría en Python.

En el tercer capítulo comenzamos a presentar los resultados obtenidos de las simulaciones. Este capítulo se centra en la descripción del campo cercano a nivel *ab initio*, gracias a la implementación del campo eléctrico inducido en el paquete MBPT-LCAO. La influencia de los detalles estructurales en la escala atómica en el campo cercano, que tiene un gran impacto en la nanofotónica, motiva este trabajo. La primera parte del capítulo se centra en la respuesta óptica de un agregado de sodio compuesto por 380 átomos que forman una figura icosaédrica. Como consecuencia, el agregado tiene puntas, facetas y bordes. Demostramos que estas características geométricas tienen un impacto dramático en la distribución del campo cercano alrededor de la partícula. En particular, orientando el campo externo a lo largo del eje de una punta de la nanopartícula, hemos conseguido un efecto de pararrayos a escala atómica que solo depende debilmente de la frecuencia del campo externo. Superponiendo el aumento del campo eléctrico obtenido por el efecto de pararrayos que se obtiene debido al plasmón de superficie de la partícula, observamos una localización extrema del campo eléctrico inducido que conlleva a un aumento considerable del campo eléctrico en un volumen de tamaño.

Al aproximar dos nanopartículas se forman dímeros metálicos compuestos por 760 átomos. La respuesta óptica de los dímeros de agregados depende de la distancia d de separación entre ellos y de la orientación relativa de estos. Nosotros hemos estudiado tres orientaciones mutuas para distintas distancias d entre los agregados. El primero lo calificamos como "faceta-faceta", ya que los agregados enfrentan facetas planas en esta geometría. La segunda geometría se menciona como "punta-faceta" ya que un agregado tiene una punta orientada a la faceta del segundo. La última geometría se describe como "punta-punta" porque cada partícula muestra una punta al otro. Hemos estudiado la absorción óptica y la distribución del campo eléctrico inducido dentro de la cavidad para un campo électrico externo orientado a lo largo del eje del dímero. Hemos comparado estos resultados con los que se obtienen utilizando esferas modelizadas usando la aproximación de Jellium. Primero, hemos estudiado la absorción óptica en función de la distancia entre las dos partículas. La respuesta óptica de los dímeros esta caracterizada por tres regímenes. Cuando las partículas están muy lejos ($d > 10$ Å), los dímeros muestran una única resonancia que depende de forma muy débil de la geometría de la cavidad y se conoce como modo plasmónico enlazanta del dímero (BDP, en inglés *bonding dimer plasmon*). Cuando se reduce la distancia entre las partículas, el BDP se desplaza ligeramente hacia el rojo hasta una distancia crítica de 5 Å, a partir de la cual desaparece. A esta distancia aparecen dos resonancias: el plasmón de transferencia de carga (CTP, en inglés *charge transfer plasmon*) a bajas energías y el plasmón cuadrupolar (QP, en inglés *quadripolar*

plasmon) a altas energías y otros modos de orden superior a mayores energías. La intensidad de ambos modos depende en gran parte de la geometría de la cavidad. En el capítulo 3 también describimos la distribución de campo eléctrico inducido dentro de la cavidad en función de le distancia entre las dos partículas. Demostramos que el máximo valor del campo inducido se dá alrededor de 7 Å de separación y que su intensidad varía en función de la geometría. Debido a la localización del campo en la punta de las nanopartículas, las configuraciones "punta-punta" y "punta-faceta" generan mayores campos inducidos que la geometría "faceta-faceta". En la última sección de este capítulo comparamos los cálculos *ab initio* atomísticos con los cálculos clásicos realizados con el método de "elementos fronterizos" (BEM, del inglés boundary element method). Se ha demostrado que este método puede describir la distribución del campo inducido solo cuando las características geométricas de las partículas hayan sido suavizadas de forma que no haya ni vertices ni lados del polígono más puntiagudos que la dimensiones de un radio de sodio (caracterizado, por ejemplo, por el radio de Wigner-Seitz de este elemento).

El cuarto capítulo muestra cómo la respuesta plasmónica, incluso en el campo lejano, de nanoestructuras metálicas puede ser modificada por el moviento de un átomo o unos pocos átomos. La nanoestructura en la que nos hemos basado en este estudio es el dímero de sodio "faceta-faceta" estudiado en el capítulo anterior. A diferencia del estudio previo, en este caso permitimos que los átomos se muevan para relajar el sistema al mínimo energético local más cercano durante el proceso de interacción de las dos nanopartículas. La geometría inicial del dímero forma una cavidad de 16 Å. Al reducir la distancia entre los dos agregados se permite que los átomos se muevan. No se observa ningún cambio evidente hasta una distancia de unos 6 Å donde los dímeros se acercan hasta tocarse dando lugar a una reducción radical de la energía del sistema. Seguimos reduciendo el tamaño nominal de la brecha hasta 0 Å para luego volver a aumentar la distancia entre los agregados. Durante el proceso de retracción los dos agregados permanece unidos a través de un cuello de sección atómica que se va alargando a medida que las nanopartículas se separan. Este proceso viene acompañado de un aumento gradual de la energía total. Si se sigue aumentando la distancia, se pueden detectar saltos en la energía total correspondientes al movimiento de algún átomo dentro de la cavidad. Por último, la conexión entre las nanopartículas solo se rompre a una distancia nominal de 32 Å, es decir, a una distancia cinco veces mayor que la necesaria para hacer contacto. En general, la evolución de la energía total durante el proceso de retracción de las partículas (alargamiento del cuello que los conecta) se caracteriza por un aumento gradual de la energía, que corresponde a las etapas de deformación elástica, y saltos bruscos en la energía, que acompañan las deformaciones plásticas que ocurren de forma puntual.

Más interesante y novedoso es lo que ocurre con la respuesta óptica del sis-

tema acompañando estos cambios estructurales. Empezando por el proceso de acercamiento, analizamos la respuesta óptica del dímero en función de la distancia nominal de la cavidad plasmónica. En comparación con la situación no relajada, cerca de la distancia de contacto la respuesta óptica es modificada considerablemente. Se observa una singularidad en el punto de contacto en lugar de una transición suave entre el régimen capacitivo (en el que la respuesta está dominada por el modo BDP) y el régimen túnel (dominado por el CTP). Por otra parte, el cambio más interesante de la polarizabilidad óptica ocurre en el proceso de retracción. Mientras que a distancias cortas la única resonacia excitada es el CTP, al aumentar la distancia, pero siempre manteniendo el contacto que une los agregados, se excita una segunda resonancia a mayor energía. Además de esto, la absorción óptica muestra discontinuidades a ciertas distancias entre las nanoparticulas. Esta evolución discontinua de la respuesta óptica se debe a la combinación de varios efectos de los cuales la cuantización del transporte electrónico a través del cuello métalico que une los agregados metálicos es el más imortante. La cuantización de la conductacia en sistema nanométricos provoca que cambios de la sección del cuello de un solo átomo produzcan cambios importantes en la corriente que circula en el sistema. Esto produce cambios en la energía e intensidad de la resonancia CTP del sistema. Es interesante que estos efectos de cuantización también sean visibles en los cambios discontinuos que sufre la distribución de densidad inducida (por la excitación óptica) a medida que el cuello evoluciona durante la retracción. Por consiguiente, la evolución discontinua de la posición, anchura e intensidad del modo CTP detectadas en nuestras simulaciones son consecuencia directa de la cuantización del transporte en el cuello de conexión.

En el quinto capítulo nos basamos en la mejora del algoritmo iterativo y de la gestión de la memoria para realizar cálculos a una escala sin precedentes de agregados de plata y sodio conteniendo hasta 5000 átomos. Con estas nuevas capacidades del paquete MBPT-LCAO analizamos la dispersión del plasmón de superficie con el tamaño de las nanopartículas metálicas. Se sabe que la frecuencia plasmónica de las partículas de metales simples como el sodio, se desplaza hacia el rojo cuando el tamaño del agregado disminuye. Esta tendencia es opuesta al cambio de frecuencia observada en los metales nobles, que se desplaza hacia el azul cuando se hace más pequeña la partícula. Aunque existe algún modelo empírico que explica esta tendencia de dispersión opuesta, todavía no se ha llegado a entender desde un punto de vista microscópico, y en particular con el nivel de detalle que pueden proporcionar los cálculos *ab initio*. Hay que enfatizar que hasta ahora ningun método *ab initio* atomístico pudo alcanzar tamaños suficientemente grandes para confirmar de forma clara esta tendencia opuesta. Con el fin de obtener la dispersión del plasmón con el tamaño de los agregados de sodio y plata calculamos la polarizabilidad de una serie de agrupamientos

icosaédricos desde 55 hasta 5083 átomos. Para los dos materiales obtuvimos el cambio de frecuencia esperado cuando el tamaño de la partícula disminuye: un desplazamiento hacia el azul para las partículas de plata y un desplazamiento hacia el rojo para las de sodio. Los cambios de frecuencia obtenidos coinciden con los valores experimentales. Una vez obtenidos estos resultados y confirmado que los cálculos *ab initio* TDDFT reproducen el resultado experimental, realizamos una serie de análisis para intentar comprender el origen de la tendencia opuesta. En el primer análisis, estudiamos el impacto de la interacción electrón-electrón del cambio de frecuencia, para lo cual ajustamos artificialmente la fuerza de la interacción Coulombiana. En el caso de los agregados de sodio vemos que el cambio de frecuencia se invierte cuando las interacciones son débiles. Es decir, a medida que tamaño del agregado disminuye detectamos un desplazamiento hacia el azul de la frecuencia. Al aumentar la fuerza de la interacción, la tendencia cambia ligeramente de signo hasta alcanzar lo esperado para una fuerza de interacción normal e incluso hasta aumentar el corrimiento al rojo. El caso de las partículas de plata no es tan sencillo. Al igual que para el caso del sodio, el desplazamiento hacia el azul aumenta cuando la interacción se hace más débil. Sin embargo, al contrario que el sodio, las interacciones fuertes no revierten la tendencia del cambio de frecuencia mostrando siempre un desplazamiento al azul. En un segundo intento probamos quitando artificialmente los electrones 4d de la banda de valencia de la plata, pasando a considerarlos como parte del "core" atómico o bien como electrónes que no pueden ser excitados por el campo externo. Esta estrategia nos permite casi invertir la tendencia del cambio de frecuencia de las nanopartículas. A partir de este análisis, podemos concluir que las distintas tendencias encontradas son el resultado de la competición de dos factores: i) el corrimiento al azul con la disminución del tamaño característico de los efecto de confinamiento cuántico, y ii) el corrimiento al rojo que observamos aumenta con la fuerza de la interacción Coulombiana. En el caso de la plata, el apantallamiento de la interacción entre los electrones de conducción de la plata por la polarización de la capa 4d, hace que los efectos de confinamiento cuántico dominen. Para los metáles simples la dispersión con el tamaño viene determinada por la interacción electrón-electrón. En los modelos clásicos en la literatura, la dispersión con el tamaño del plasmón se asocia con la posición del centroide de la distribución de carga inducida en la superficie. Para contrastar con estas ideas, intentamos calcular dicho parámetro a partir de nuestros resultados *ab initio*. Los datos obtenidos utilizando nuestros métodos *ab initio* respaldan la correlación entre la dispersión del plasmón y la posición del centroide de carga unicamente en el caso del sodio. En el caso de la plata nuestros resultados no soportan por completo está relación, de hecho indican que definir el centroide de carga en el caso de la plata es de gran complejidad. El principal problema parece radicar en que la carga inducida asociada a la polarización de los electrones de

la capa 4d se extiende por todo el volumen de la partícula.

En el sexto capítulo, hemos realizado varios cálculos basándonos en el método de EELS implementado durante esta tesis. En primer lugar, comprobamos que el espectro de EELS calculado concuerda de forma razonable con los datos experimentales. Para esto, hemos relizado cálculos tanto con nanotubos de carbono y nitruro de boro, como con un nanopartícula de plata. Existe un buen acuerdo cualitativo entre nuestros cálculos y las medidas experimentales para los tres sistemas testeados. El acuerdo para la partícula icosaédrica de plata es satisfactorio solo en la incidencia fuera del conglomerado, es decir, en el que el espectros EELS y óptico guardan gran similitud. Sin embargo, cuando el haz de electrones pasa directamente a través del centro de la partícula se observa un desacuerdo entre las probabilidades de pérdida de energía medidas y calculadas. En dicha incidencia central, la medida exhibe una resonancia de correspondiente al plasmón de volumen a 3,8 eV, mientras que los espectros calculados muestran solo una resonancia de plasmón superficial ligeramente desplazada hacia energías más altas, a 3,4 eV. El origen de este desacuerdo se debe a las diferencias en la estructura interna de las nanopartículas. Las partículas caracterizadas experimentalmente están formados por un millón de átomos, mientras que nosotros solo pudimos hacer cálculos para agregados conteniendo un máximo de 923 átomos, para los que asumimos una estructura icosaédrica. La diferencia de la relación superficie-volumen entre los grupos cálculados y medidos es de un orden de magnitud, lo que hace que la disposición atómica interna de las nanopartículas más grandes pueda asumirse de forma razonable que debe ser similar a la red cristalina FCC del volumen, la cual es significativamente diferente a la estructura icosaédrica considerada en los agregados pequeños. Por suerte, se puede imponer artificialmente la disposición atómica correcta de la red de volumen. Para poder hacer esto, hemos realizado cálculos para un trozo pequeño de plata con esta disposición de red. Los espectros de EELS del cubo de plata con incidencia central concuerdan significativamente mejor con los datos experimentales mostrando la resonancia plasmónica principal a 3,8 eV. Pudimos concluir que las excitaciones de los modos dependen en gran medida de la posición de la nanopartícula en la que incide el haz de electrones, así como de la estructura interna de la misma.

Aparte de esto, realizamos un análisis más profundo de los espectros EELS de una serie de agrupamientos de plata de estructura icosaédrica de 13 a 923 átomos. En primer lugar, comparamos los espetros de EELS con los espectros ópticos y observamos que cuando el haz pasa lejos de la superficie de la partícula, ambos espectros muestran características similares. Estudiamos la influencia de la trayectoria del haz en los espectros EELS y así pudimos por una parte, excitar modos plasmónicos "silenciosos" (i.e., modos que no pueden ser excitados con luz) para una trayectoria del haz que pasa a través del centro del agregado, y por otra parte y con otras trayectorias, el modo dipolar del plasmón de superficie, el cual

también se puede observar con excitaciones ópticas. Por último llevamos a cabo cálculos para un dímero de plata compuesto por dos partículas de 309 átomos cada uno y comparamos los espectros de EELS obtenidos con los espectros ópticos para dos trayectorias de haz (pasando lejos de la superficie del dímero y pasando por el centro de la cavidad del dímero) y en función de la distancia entre los agregados. De esta forma, con la primera trayectoria se excita el modo BDP (modo plasmónico enlazante del dímero) y con la segunda, el modo plasmónico anti-enlazane. Este último se conoce como modo "silencioso" o modo "oscuro" (en inglés *dark*) ya que no puede ser excitado con luz.

En el séptimo capítulo, reportamos otro tipo más de espectroscopía: la espectroscopía de dispersión vibracional, la cual se origina en cambios de energía relativamente pequeños de la luz dispersada por una molécula causados por la excitaciones de modos vibracionales. Dos de las espectroscopía de vibración más habituales son las de infrarrojo y Raman, las cuales que se pueden utilizar como detectores altamente selectivos y espcíficos de moléculas. La combinación de ambas técnicas junto con el gran aumento de la intensidad de campo en las proximidades de superficies nanostructuradas, puntas o nanopartículas cuando se excitan los correspondientes modos plasmónicos, permite aumentar la sensibilidad de la detección hasta el nivel de una única molécula. Teóricamente, las espectroscopias vibracionales pueden ser simuladas utilizando métodos *ab initio* utilizando la aproximación armónica y métodos de diferencias finitas. En la aproximación armónica se asume que las fuerzas que actuan sobre los núcleos atómicos son lineales en los desplazamientos con respecto a las posiciones de equilibrio. De hecho, el cálculo de frecuencias vibracionales es parte de muchos paquetes DFT *ab initio*. Sin embargo y particularmente en el caso de la dispersión de Raman, la estimación de las secciones eficaces de dispersión requiere más pasos. Para estimar la probabilidad de dispersión Raman no resonante, se deben rastrear los cambios de polarizabilidad óptica cuando el sistema se desplaza a lo largo del correspondiente modo normal de vibración. Este cálculo puede ser relativamente rápido con nuestro TDDFT iterativo, lo que permite estimar las polarizabilidades de moléculas en las proximidades de agregados metálicas relativamente grandes y así, dar explicación a la espectroscopía Raman aumentada. Sin embargo, tal cálculo presenta complicaciones relacionadas con la altísima precisión númerica requerida, así que en el presente capítulo nos limitamos a demostrar solo cálculos de secciones eficaces de Raman (e infrarrojo) para moléculas pequeñas y especulamos sobre cómo la aproximación armónica podría extenderse para simular directamente las espectroscopías Raman aumentadas por la presencia de puntas o superficies (SERS o TERS).

Por último, en el octavo capítulo resumimos los puntos más importantes de la tesis y concluímos hablando del impacto que esperemos tenga este trabajo para la comunidad científica que trabaja en el campo de la nanociencia.

Contents

Chapter 1

Introduction

During the last century, the development of quantum physics together with the discovery of the elementary particles has permitted to understand and manipulate matter at an unprecedented scale. As Feynman predicted in his lecture back in 1959, "*There's plenty of room at the bottom*" [8], progress in nanosciences led to a tremendous number of new technologies and scientific breakthroughs. This progress has been accelerated by the use of computers to solve physical problems, leading to the new field of computational modeling in scientific research, half-way between experimental and theoretical science. In nanosciences, the fabrication, the manipulation and the operation of devices of very small sizes, down to a few nanometers, are the main motivations for scientists. For example, when nanoparticles are coupled to light (or other sources of excitation such as electrons), oscillations of the nanoparticle's electrons occur, creating a movement of charges called plasmon that has great applications in the field of nanophotonics. For instance, metallic nanoparticles play a key role in the development of nanophotonics. The ability of the conduction electrons to collectively oscillate produces surface charge density oscillations in nanoparticles, so-called surface plasmons, that couple very efficiently to light, producing subwavelength localization and a large enhancement of the optical fields induced in the proximity of nanoparticles [9–11]. Nanophotonics with localized surface plasmons has boosted a variety of technological applications in which the intense electromagnetic fields assist in enhancing the signal from vibrational spectroscopies [12, 13], improving the performance of solar cells [14, 15], optimizing the active control of nanodevices [16, 17] or implementing noninvasive thermotherapies in medicine [18], among others.

The theoretical study of nanoparticles greatly depends on our capacity to model the interaction of the nanoparticle's electrons between themselves as well

as with the environment. At the nanoscale, only quantum mechanics grants the correct description of the physical phenomena by depicting the particle's electrons using the formalism of probability amplitudes or wave functions. Unfortunately, the great complexity of the many-body wave function $\psi(\mathbf{x}_1, \mathbf{x}_2, ..., \mathbf{x}_N)$, depending on the coordinates of each electron $\mathbf{x}_i = (\mathbf{r}_i, \sigma_i)$ that contain the spatial and spin degrees of freedom, does not permit to solve the many-body problem exactly, neither analytically nor numerically, for systems with more than a few electrons. Hence, in order to obtain the properties of nanoparticles composed of tens, hundreds, thousands of electrons, various approximate methods have been developed since the advent of quantum mechanics. Perhaps, the most successful method is the density functional theory (DFT). According to DFT, the ground-state of a quantum system is determined by its electron density $n(\mathbf{r})$, which is always a function of three spatial degrees of freedom $\mathbf{r}$, independently on the number of electrons in the quantum system. In contrast to the static properties of the ground-state, the excited states determine the time-dependent, dynamical properties of a quantum system. For instance, such phenomena as optical absorption, electronic conductance, energy loss of external charged projectiles are determined by the properties of the excited states. The excited states properties can be estimated within the time-dependent extension of DFT (TDDFT). By applying TDDFT, we can explore and understand the complexity of the excitation spectrum of a nanoparticle, thus providing more relevant information about the system. In this work, we will use DFT and TDDFT to study the properties of finite systems such as metallic clusters, small molecules and finite nanotubes.

The electromagnetic field localization in nanoantennas is one of the leitmotivs that drives the development of plasmonics. The near-fields in these plasmonic nanoantennas are commonly addressed theoretically within classical frameworks that neglect atomic-scale features. The approach of classical electromagnetism is often appropriate since the irregularities produced at the atomic scale are typically hidden in far-field optical spectroscopies. However, a variety of physical and chemical processes rely on the fine distribution of the local fields at the atomic scale. Atomistic TDDFT methods are able to show how the atomistic details of the nanoparticles determine the presence of hot spots that are further enhanced by the action of the underlying nanometric plasmonic fields. This situation is analogue to a self-similar nanoantenna cascade effect, scaled down to atomic dimensions and it provides new insight into the limits of field enhancement and confinement, with important implications in the spatial resolution of field-enhanced spectroscopies and microscopies. Due to their simplicity, sodium cluster are ideal systems to demonstrate such properties within atomistic *ab initio* theory. In particular, we have used sodium particles with realistic geometries and explored the dependence of the local-field on the structural details of the cavity formed between two of them.

When the two particles approach each other and a metal neck is eventually formed connecting both of them, this system allows to demonstrate interesting relations between optical and transport properties. The correlation between transport properties across the subnanometric metallic gaps formed by two nanoparticles forming the dimer and the optical response of the system is a complex effect that is also determined by the atomic-scale details of the junction structure. As experimental advances are progressively accessing transport and optical characterization of smaller nanojunctions, a clear connection between the structural, electronic and optical properties in these nanocavities is needed. Using *ab initio* calculations, it is possible to study the simultaneous evolution of the structure and the optical response of a plasmonic junction as the particles forming the cavity approach and retract. Atomic reorganizations are responsible for a large hysteresis of the plasmonic response of the system, which shows a jump-to-contact instability during the approach process and the formation of an atom-sized neck across the junction during retractation. Atomistic *ab initio* calculations demonstrate that, due to the quantization of the conductance in metals nanocontacts, atomic-scale reconfigurations play a crucial role in determining the optical response of the whole system. Abrupt changes are observed in the intensities and spectral positions of the dominating plasmon resonances and a one-to-one correspondence between these jumps and those of quantized transport exist as the neck cross-section diminishes. Thus, our calculations remarkably show that atomic-scale reorganization involving one or a few atoms are observed in the far-field plasmonic response, even if the metallic systems explored in our calculations contain close to eight hundred atoms.

Changes of plasmonic resonances of single metallic clusters as function of their size and constituent material are other important phenomena arising at the nanoscale. In particular, a classical description using a dielectric function does not lead to any size dependence of the plasmonic resonances of particle. Therefore, they appear as a signature of quantum and non-local effects in the response of the material. Studying these changes using atomistic TDDFT leads to a better understanding of the physics of nanoparticles. Specifically, it is interesting to address an anomalous behavior of the plasmon frequency of simple metal clusters, a subject that has attracted intensive experimental and theoretical work over the last decades. The red shift of the plasmonic frequency as the size of the cluster diminishes is opposite to the expected size dispersion of the electronic properties, according to standard quantum mechanical considerations. In contrast to simple metal clusters, plasmonic resonances in noble metal and semi-conductor clusters show the opposite trend. The *ab initio* atomistic calculations presented in this thesis of plasmonic resonances in sodium and silver clusters containing up to 5000 atoms reproduce the opposite plasmon dispersion versus size observed between simple and noble metals.

Previous works, mostly using a jellium model description, have attempted a one-to-one correlation between the position of the centroid of the induced density at the surface and the size dispersion of the surface plasmon. However, here we find that the situation is not so clear for nanoparticles with realistic structures, particularly at optical frequencies. While for sodium particles we could define the centroid, and find that it appears shifted towards the vacuum side of the surface consistently to previous claims, for silver particles a sensible definition of the centroid of charge was not possible. However, the origin of the dispersion trends as a competition between quantum confinement effect and a material-dependent screening of the electron–electron interaction is clearly demonstrated in our study.

Besides optical perturbation, atomistic *ab initio* TDDFT can be as well used with other type of perturbations. Particularly, as electron energy loss spectroscopy (EELS) is presently a common tool in laboratories because of its multiple advantages over light spectroscopy, it becomes necessary to understand how swift electrons create low-energy valence excitations. A real space implementation of EELS capable of describing large systems within atomistic TDDFT presents numerous advantages over other kind of EELS implementations. In this work, we have implemented an approximate, semi-classical scheme to estimate EELS within the real-space atomistic ab initio TDDFT that was previously used for optical perturbations. We applied the implemented theory of EELS to several finite systems relevant in nanoscience. Calculations with carbon and boron nitride nanotubes show excellent agreement with experimental results, while a deeper analysis of silver clusters and silver cluster dimers grants a better understanding of plasmons in noble metals nanoparticles.

Finally, atomistic *ab initio* calculations were used to estimate the Raman intensity of the vibrational modes of molecules. The vibrational modes of a molecule can be easily obtained within the harmonic approximation and with the finite difference method. Computing the derivatives of the optical polarizability along the vibrational-mode coordinates, we were able to estimate the cross-sections of the non-resonant Raman scattering. We demonstrate proof-of-principle calculations of Raman (and infrared) cross sections for small molecules, and we mention the possibility to apply this method to study surface- and tip-enhanced Raman spectroscopy for molecules coupled to plasmonic nanocavities.

The simulations described above have been possible because of efficient implementations of DFT and TDDFT based on numerical atomic orbitals (NAO). Several programming suites were used to perform these simulations:

- SIESTA (Spanish Initiative for Electronic Simulations with Thousands of Atoms) [1, 2] was used to perform the ground-state DFT calculations;

- MBPT-LCAO (Many Body Perturbation Theory - Linear Combination of

Atomic Orbitals) [3–5] is the core program for this work. It was used for the TDDFT calculations;

- PySCF-NAO (Python-Based Simulations of Chemistry Framework - Numerical Atomic Orbitals) [6, 7] is the Python successor of MBPT-LCAO. It has been implemented as a module of the PySCF package;
- ASE (Atomic Simulation Environment) [19] is a Python library which has been largely used for the manipulation of the geometry of the system considered in this work. The computation of the Raman intensity of vibrational modes starting from SIESTA and MBPT-LCAO input was implemented within the ASE suite.

A number of implementations were accomplished to cope with optical, EELS and Raman spectroscopy mainly in MBPT-LCAO and PySCF-NAO packages, and in ASE. The most important ones will be the subject of further chapters, and are summarized below:

- Real-space Electron Energy Loss Spectroscopy;
- Improvement of the iterative procedure that permitted unprecedentedly large calculations;
- Spatial distribution of the induced density and electric field;
- Raman intensity of vibrational modes;
- Other technical improvements such as GPU parallelization and HDF support.

The thesis is organized as follows. In chapter 2, we briefly introduce the basics of DFT and TDDFT. This introduction is necessary for understanding both the simulation outcomes, as well as the methodological and programming improvements achieved. Chapter 3 presents the work about induced electric field inside nanocavities. In chapter 4, the impact of atomic relaxations in nanocavities is studied. Chapter 5 provides a detailed analysis of the size dispersion in sodium and silver clusters from *ab initio* methods. In chapter 6, simulations of real-space electron energy loss spectroscopy with atomistic *ab initio* theory are presented. Raman spectroscopy is covered in chapter 7, where we describe the theory and the implementation of non-resonant Raman spectroscopy combining SIESTA, ASE and PySCF-NAO to achieve the direct estimation of Raman intensities of small molecules. Finally, the accomplishments of this thesis are summarized in chapter 8.

Chapter 2

Theory

One of the challenges of modern physics is the description of the interaction between electromagnetic fields and matter. This interaction is at the origin of many phenomena around us and the ability to understand and control it has an important technological impact. During the previous century, great efforts had been done for the description of such interaction at the atomic and molecular levels using the theory of quantum mechanics. In the present work, the external fields (light, electric field created by a moving charge) are assumed small and, therefore, perturbation theory is applied. Furthermore, the perturbation is treated as a classical electrical potential while the perturbed systems obey the laws of quantum mechanics (QM). Therefore, we shall first summarize the QM of the unperturbed matter (ground-state) and then formulate the time-dependent perturbation theory to cope with excited states of matter. The ground-state is treated in this work according to density functional theory (DFT), while linear-response time-dependent DFT (TDDFT) will be used to describe the excited states. DFT and TDDFT are relatively recent theories within the more general framework of QM. Ideally, DFT and TDDFT allow to model the matter of arbitrary chemical composition with minimal empirical input. Thus, the whole theoretical framework is outlined as *ab initio*.

Within quantum mechanics, the electrons and nuclei are fully described by the so-called wave function $\psi(\mathbf{r}_1, \mathbf{r}_2, ..., \mathbf{R}_1, \mathbf{R}_2 ...; t)$ which depends on the electrons' coordinates $\mathbf{r}_i$, the coordinates of the nuclei $\mathbf{R}_I$ and time t. The wave function $\psi(\mathbf{r}_1, \mathbf{r}_2, ..., \mathbf{R}_1, \mathbf{R}_2 ...; t)$ represents a "probability amplitude"—notion absent in classical mechanics. The probability amplitude is not directly measurable, but the square of the wave function in an infinitesimally small volume in the many-body configurational space, $|\psi(\mathbf{r}_1, \mathbf{r}_2, ..., \mathbf{R}_1, \mathbf{R}_2 ...; t)|^2 d^3r_1 d^3r_2 ... d^3R_1 d^3R_2 ...$ gives the probability of finding the system at the time t in a given configuration [20]. In

the absence of a time-dependent perturbation, the probability of finding particles at given positions should not be time-dependent and so the wave function $\psi(\mathbf{r}_1, \mathbf{r}_2, ..., \mathbf{R}_1, \mathbf{R}_2 ...; t)$ can be factorized to a time-**dependent** phase and a time-**independent** probability amplitude $\psi(\mathbf{r}_1, \mathbf{r}_2, ..., \mathbf{R}_1, \mathbf{R}_2 ...)$. The time-independent term obeys an eigenvalue equation [20]

$$\hat{H}\psi \quad = \quad E\psi, \tag{2.1}$$

where the eigenvalues E will be the total energies the system can assume. The Hamiltonian operator $\hat{H}$ can be constructed after Schrödinger [21] in the non-relativistic approximation

$$\begin{aligned} \hat{H} = -\sum_i \frac{\nabla_i^2}{2m_e} - \sum_I \frac{\nabla_I^2}{2M_I} + \frac{1}{2}\sum_{i \neq j} \frac{1}{|\mathbf{r}_i - \mathbf{r}_j|} - \\ \sum_{iI} \frac{Z_I}{|\mathbf{r}_i - \mathbf{R}_I|} + \sum_{I \neq J} \frac{Z_I Z_J}{|\mathbf{R}_I - \mathbf{R}_J|}. \end{aligned} \tag{2.2}$$

Here, the small indices i, j run over electrons and the capital indices I, J run over nuclei. The Hamiltonian (2.2) contains the kinetic energy terms of nuclei and electrons, and the instantaneous Coulomb interaction between all pairs of bodies. Unfortunately, equation (2.2) does not allow for a simple separation of variables, neither for analytic solutions in almost all cases. Therefore, the diagonalization problem (2.1) must rely on a discretization of the multi-dimensional wave function $\psi(\mathbf{r}_1, \mathbf{r}_2, ..., \mathbf{R}_1, \mathbf{R}_2 ...)$. The computational complexity of the direct diagonalization grows exponentially with the number of particles. This exponential growth was named as "exponential wall" by W. Kohn [22] because the problem becomes already numerically impracticable for as few as 5-6 particles. Fortunately, it is possible to find sufficiently accurate approximate solution of equation (2.1) with the many-body Hamiltonian (2.2) using methods of quantum chemistry [23, 24], many-body perturbation theory [25, 26], or density functional theory [21, 27, 28]. The suitability of each of these approximations depends on the specific size and composition of the different systems. A first step used by these methods, is to separate the electron and nuclei variables in the multi-dimensional wave function $\psi(\mathbf{r}_1, \mathbf{r}_2, ..., \mathbf{R}_1, \mathbf{R}_2 ...)$. By noticing the difference of the electron mass m_e with that of the nuclei M_n, which is at least three orders of magnitude heavier than m_e, it is possible to separate the variables of the nuclei and electrons to a good accuracy. This is the so-called Born-Oppenheimer approximation [20]

$$\begin{aligned} \psi_{\text{total}}(\mathbf{r}_1, \mathbf{r}_2, ..., \mathbf{R}_1, \mathbf{R}_2 ...) = \psi_{\text{elec}}(\mathbf{r}_1, \mathbf{r}_2, ..., \mathbf{r}_N) \times \\ \psi_{\text{nuclei}}(\mathbf{R}_1, \mathbf{R}_2, ..., \mathbf{R}_M). \end{aligned} \tag{2.3}$$

Furthermore, due to the large masses of nuclei, in most cases they can be safely assumed to behave as classical point particles and treated according to classical

mechanics [21]. Thus, we can approximate the Hamiltonian (2.2) one step further by considering the nuclei as an external potential $V_{\text{ext}}(\mathbf{r})$ for the electrons. The N electrons interact through the Coulomb potential:

$$\hat{H} = \sum_{i=1}^{N} \left\{ \frac{\mathbf{p}_i^2}{2m} + V_{\text{ext}}(\mathbf{r}_i) + \frac{1}{2} \sum_{j \neq i}^{N} \frac{e^2}{|\mathbf{r}_i - \mathbf{r}_j|} \right\}, \tag{2.4}$$

$$\hat{H} = \hat{T} + \hat{V}_{\text{ext}} + \hat{W}_{\text{ee}}. \tag{2.5}$$

With $\hat{T}$ the kinetic-energy operator and $\hat{W}_{\text{ee}}$ the electron-electron interaction operator. Unfortunately, the exact wave function $\psi_{\text{elec}}(\mathbf{r}_1, \mathbf{r}_2, ..., \mathbf{r_N})$ belonging to this Hamiltonian cannot be so easily simplified and further approximations are necessary to treat it. DFT is one of the theories allowing to effectively separate variables in the electronic wave function. We summarize in the next section the ideas and theorems of DFT. The following description of DFT is based on the lecture notes of Julien Toulouse [29].

2.1 Density Functional Theory

As explained above, the exponential growth of the computational complexity with the number of particle N is the main barrier to obtain quantities of primary interest in the many-body problem. One of these quantities is the ground-state energy E_0, which can be obtained from the variational principle with the following minimization [20]

$$E_0 = \min_{\psi} \left\langle \psi \right| \hat{H} \left| \psi \right\rangle, \tag{2.6}$$

where the search is over all N-electron anti-symmetric wave functions $\psi(\mathbf{r}_1, \mathbf{r}_2, ..., \mathbf{r}_N)$, normalized to unity $\langle \psi | \psi \rangle = 1$. By reformulating the variational theorem in term of the electron density $n(\mathbf{r})$, defined from the wave function $\psi(\mathbf{r}_1, \mathbf{r}_2, ..., \mathbf{r}_N)$ by

$$n(\mathbf{r}) = N \int d^3r_2 \int d^3r_3 ... \int d^3r_N \psi^*(\mathbf{r}, \mathbf{r}_2, ..., \mathbf{r}_N)\psi(\mathbf{r}, \mathbf{r}_2, ..., \mathbf{r}_N), \tag{2.7}$$

DFT greatly reduces the complexity of the many-body problem. The electron density $n(\mathbf{r})$ is normalized to the number N of electrons in the system, $\int n(\mathbf{r}) d^3r = N$.

DFT has had a considerable success in many branches of physics. In this sections, we will present an introduction to DFT, for deeper reviews and applications of DFT in atomic, molecular and solid-state physics, we refer the reader to Jones and Gunnarsson [27] and Dreizler and Gross [21].

2.1.1 The Thomas-Fermi Model

The Thomas-Fermi model [30] is a precursor of modern rigorous DFT. Llewellyn Thomas and Enrico Fermi realized that statistical considerations can be used to approximate the distribution of electrons in an atom. The assumptions stated by Thomas are that: "*electrons are distributed uniformly in the six-dimensional phase space for the motion of an electron at the rate of two for each h^3 of volume*", (where h is the Planck's constant) and that there is an effective potential field that "*is itself determined by the nuclear charge and this distribution of electrons.*" From these assumptions, Thomas and Fermi derived that the ground-state electron density must satisfy the variational principle [28]

$$\delta \left\{ E_{\mathrm{TF}}\left[n\right] - \mu_{\mathrm{TF}} \left(\int n(\mathbf{r}) d^3 r - N \right) \right\} \quad = \quad 0, \tag{2.8}$$

where $E_{\mathrm{TF}}[n]$ is the energy functional of the atom in terms of electron density $n(\mathbf{r})$. The total number of electrons is given by $N = N[n(\mathbf{r})] = \int n(\mathbf{r}) d^3 r$ and μ_{TF} is given by the Euler-Lagrange equation

$$\mu_{\mathrm{TF}} \quad = \quad \frac{\delta E_{\mathrm{TF}}[n]}{\delta n(\mathbf{r})}. \tag{2.9}$$

Unfortunately, the simple approximations for the total energy density functional $E_{\mathrm{TF}}[n]$ fail when it comes to molecules and the accuracy for atoms is rather poor comparing to other approximations such as Hartree-Fock method. The poor accuracy caused the Thomas-Fermi model to be viewed as an oversimplified model of not much real importance for quantitative predictions of electronic structure. However, after the advent of Hohenberg-Kohn theorems, the Thomas-Fermi model turns to be a brilliant conjecture.

2.1.2 Hohenberg-Kohn theorem

The presentation of the Hohenberg-Kohn theorem follows closely the excellent account given by Julien Toulouse in Ref. [29].

The ground-state wave function $\psi(\mathbf{x}_1, \mathbf{x}_2, ..., \mathbf{x}_N)$, where $\mathbf{x}_i = (\mathbf{r}_i, \sigma_i)$, σ_i being the spin of the electron, of an electronic system perturbed by an arbitrary external potential $V_{\mathrm{ext}}(\mathbf{r})$ can be obtained in principle by solving the Schrödinger equation (2.1). The ground-state electronic density $n(\mathbf{r})$ is then obtained from equation (2.7). Hohenberg-Kohn (HK) demonstrated in 1964 [31], that the ground-state electron density $n(\mathbf{r})$ determines the potential $V_{\mathrm{ext}}(\mathbf{r})$ up to an arbitrary additive constant *cte*

$$n(\mathbf{r}) \longrightarrow V(\mathbf{r}) + cte. \tag{2.10}$$

The demonstration of this mapping is done by a two-step proof by contradiction [31]. In the first step, we assume two Hamiltonians $\hat{H}_1 = \hat{T} + \hat{W}_{\text{ee}} + \hat{V}_1$ and $\hat{H}_2 = \hat{T} + \hat{W}_{\text{ee}} + \hat{V}_2$ having the same ground-state wave function ψ, i.e

$$\hat{H}_1 |\psi\rangle = E_1 |\psi\rangle , \tag{2.11}$$
$$\hat{H}_2 |\psi\rangle = E_2 |\psi\rangle , \tag{2.12}$$

with E_1 and E_2 being the ground-state energies of the Hamiltonians $\hat{H}_1$ and $\hat{H}_2$ respectively. We assume that the potentials $\hat{V}_1$ and $\hat{V}_2$ differ by more than an additive constant *cte*

$$V_1(\mathbf{r}) - V_2(\mathbf{r}) \neq cte. \tag{2.13}$$

Subtracting eqn. (2.11) and eqn. (2.12), we obtain

$$(\hat{V}_1 - \hat{V}_2) |\psi\rangle = (E_1 - E_2) |\psi\rangle , \tag{2.14}$$
$$\sum_{i=1}^{N} [V_1(\mathbf{r}_i) - V_2(\mathbf{r}_i)] \, \psi(\mathbf{x}_1, ..., \mathbf{x}_N) = (E_1 - E_2) \, \psi(\mathbf{x}_1, ..., \mathbf{x}_N). \tag{2.15}$$

Assuming that the ground-state is non-degenerate and that $\psi(\mathbf{x}_1, \mathbf{x}_2, ..., \mathbf{x}_N) \neq 0$ for all spatial coordinates $(\mathbf{r}_1, \mathbf{r}_2, ..., \mathbf{r}_N)$ and at least one fixed set of spin coordinates $(\sigma_1, \sigma_2, ..., \sigma_N)$[1], then $\psi(\mathbf{x}_1, \mathbf{x}_2, ..., \mathbf{x}_N)$ can be eliminated from eqn. (2.15) and we obtain the following condition,

$$V_1(\mathbf{r}) - V_2(\mathbf{r}) = cte. \tag{2.16}$$

Equation (2.16) is in contradiction with the condition (2.13). Therefore, the same ground-state ψ can not be shared by two local potentials differing by more than an additive constant.

For the second step of the proof, we consider the two ground-state wave functions ψ_1 and ψ_2 of the Hamiltonians $\hat{H}_1$ and $\hat{H}_2$ respectively. From the last paragraph, The wave functions ψ_1 and ψ_2 are necessarily different. We assume that ψ_1 and ψ_2 share the same ground-state electronic density $n(\mathbf{r})$. We note E_1 and E_2 the ground-state energies of the Hamiltonians $\hat{H}_1$ and $\hat{H}_2$ respectively. The variational theorem leads to the following inequality

$$\begin{aligned} E_1 = \left\langle \psi_1 \right| \hat{H}_1 \left| \psi_1 \right\rangle < \left\langle \psi_2 \right| \hat{H}_1 \left| \psi_2 \right\rangle &= \left\langle \psi_2 \right| \hat{H}_2 \left| \psi_2 \right\rangle + \left\langle \psi_2 \right| \hat{H}_1 - \hat{H}_2 \left| \psi_2 \right\rangle \\ &= E_2 + \int [V_1(\mathbf{r}) - V_2(\mathbf{r})] \, n(\mathbf{r}) d^3 r, \end{aligned} \tag{2.17}$$

[1] This is in fact true "almost everywhere" for "reasonably well behaved" potentials

Symmetrically, by exchanging the role of system 1 and 2, we have the strict inequality

$$E_2 < E_1 + \int [V_2(\mathbf{r}) - V_1(\mathbf{r})]\, n(\mathbf{r}) d^3r. \tag{2.18}$$

Adding equations (2.17) and (2.18) gives the inconsistent result

$$E_1 + E_2 < E_1 + E_2, \tag{2.19}$$

which finally leads to the conclusion that there cannot exist two local potentials differing by more than a constant which have the same ground-state density.

According to the Hohenberg-Kohn theorem [31]: "*the ground-state density* $n(\mathbf{r})$ *determines the potential* $V_{\text{ext}}(\mathbf{r})$*, which in turn determines the Hamiltonian, and thus everything about the many-body problem. In other words, the potential* $V_{\text{ext}}(\mathbf{r})$ *is a unique functional of the ground-state density* $n(\mathbf{r})$". Therefore, all the ground-state properties will be functionals of the electronic density $n(\mathbf{r})$. The ground-state wave function ψ for the potential $V(\mathbf{r})$ is itself a functional of n, denoted by $\psi[n]$, which was exploited by HK to define the universal (i.e., independent from the external potential) density functional

$$F[n] = \left\langle \psi[n] \middle| \hat{T} + \hat{W}_{\text{ee}} \middle| \psi[n] \right\rangle. \tag{2.20}$$

The total electronic energy functional $E[n]$ for a specific external potential $V_{\text{ext}}(\mathbf{r})$ can be defined by using the universal functional $F[n]$

$$E[n] = F[n] + \int V_{\text{ext}}(\mathbf{r}) n(\mathbf{r}) d^3r, \tag{2.21}$$

Note that, for degenerate ground-state, $\psi[n]$ is not unique but stands for any degenerate ground-state wave function. However, all $\psi[n]$ give the same $F[n]$, which is thus a unique functional of the electron density n.

The ground-state energy E_0 of the system considered can be obtained by minimizing the total electronic energy functional $E[n]$ with respect to N-electron densities with some local potential (referred as V-representable densities). The minimum energy is reached for a ground-state density $n_0(\mathbf{r})$ corresponding to the potential $V_{\text{ext}}(\mathbf{r})$.

$$E_0 = \min_n \left\{ F[n] + \int V_{\text{ext}}(\mathbf{r}) n(\mathbf{r}) d^3r \right\}, \tag{2.22}$$

The existence of the mapping from a ground-state density $n(\mathbf{r})$ to the external potential $V_{\text{ext}}(\mathbf{r})$, the existence of the universal density functional $F[n]$, and the variational property of the ground-state energy with respect to the density $n(\mathbf{r})$ constitutes the set of *Hohenberg-Kohn theorem*.

2.1.3 Kohn-Sham Method

The following description of the Kohn-Sham method is based on the lecture notes from Julien Toulouse [29].

The variational principle of Hohenberg and Kohn allows the determination of the exact ground-state density of a specified many-particle system. In 1965, Kohn and Sham [32] demonstrated that the use of orbitals instead of the density with the variational theorem would have multiple advantages. The Kohn-Sham method has revealed to be very successful, and it became the standard in application of the density functional formalism [21].

2.1.3.1 Decomposition of the universal functional

Kohn and Sham (KS) [32] proposed to decompose the universal functional $F[n]$ using a single-determinant wave function Φ, and using a constrained search formulation for the kinetic energy

$$F[n] = \min_{\Phi \to n} \left\langle \Phi \middle| \hat{T} \middle| \Phi \right\rangle + E_{\text{Hxc}}[n], \tag{2.23}$$

with $E_{\text{Hxc}}[n]$ the Hartree-exchange-correlation functional. $\Phi \to n$ means that the minimization is done over normalized *single-determinant* wave function Φ. We note $T_s[n]$ the non-interacting kinetic energy functional, $T_s[n] = \min_{\Phi \to n} \left\langle \Phi \middle| \hat{T} \middle| \Phi \right\rangle = \left\langle \Phi[n] \middle| \hat{T} \middle| \Phi[n] \right\rangle$, $\Phi[n]$ being the minimizing single-determinant wave function for a given density (non necessarily unique) and is called the *KS wave function*. The idea of the KS method is then to use the exact expression of $T_s[n]$ by reformulating the variational property of $F[n]$ in terms of single-determinant wave function Φ

$$\begin{aligned}
E_0 &= \min_n \left\{ F[n] + \int V_{\text{ext}}(\mathbf{r}) n(\mathbf{r}) d^3r \right\} && (2.24)\\
&= \min_n \left\{ \min_{\Phi \to n} \left\langle \Phi \middle| \hat{T} \middle| \Phi \right\rangle + E_{\text{Hxc}}[n] + \int V_{\text{ext}}(\mathbf{r}) n(\mathbf{r}) d^3r \right\} && (2.25)\\
&= \min_n \min_{\Phi \to n} \left\{ \left\langle \Phi \middle| \hat{T} + \hat{V}_{\text{ext}} \middle| \Phi \right\rangle + E_{\text{Hxc}}[n_\Phi] \right\} && (2.26)\\
&= \min_\Phi \left\{ \left\langle \Phi \middle| \hat{T} + \hat{V}_{\text{ext}} \middle| \Phi \right\rangle + E_{\text{Hxc}}[n_\Phi] \right\}, && (2.27)
\end{aligned}$$

the minimizing single-determinant KS wave function giving the exact ground-state density $n_0(\mathbf{r})$. Thus, the exact ground-state energy and density can in principle be obtained by minimizing over single-determinant wave functions only. The advantage of the KS scheme is to use the single-determinant wave function Φ instead of the multi-determinant wave function ψ, which represents a tremendous

simplification. With the single-determinant wave function Φ the kinetic energy can be treated explicitly, only $E_{\mathrm{Hxc}}[n]$ remains to be determined as a functional of the density.

In practice, $E_{\mathrm{Hxc}}[n]$ is separated into the Hartree and exchange-correlation terms

$$E_{\mathrm{Hxc}}[n] = E_{\mathrm{H}}[n] + E_{\mathrm{xc}}[n]. \tag{2.28}$$

Here $E_{\mathrm{H}}[n]$ is the Hartree energy functional and $E_{\mathrm{xc}}[n]$ is the exchange-correlation energy functional. $E_{\mathrm{H}}[n]$ represent the classical electrostatic repulsion energy for the electronic density $n(\mathbf{r})$

$$E_{\mathrm{H}}[n] = \frac{1}{2} \iint \frac{n(\mathbf{r})n(\mathbf{r}')}{|\mathbf{r} - \mathbf{r}'|} d^3r d^3r', \tag{2.29}$$

The exchange-correlation energy functional $E_{\mathrm{xc}}[n]$ in eqn. (2.28) remains to be approximated. This functional is often decomposed as

$$E_{\mathrm{xc}}[n] = E_{\mathrm{x}}[n] + E_{\mathrm{c}}[n], \tag{2.30}$$

where $E_{\mathrm{x}}[n]$ is the exchange energy functional

$$E_{\mathrm{x}}[n] = \left\langle \Phi[n] \middle| \hat{W}_{ee} \middle| \Phi[n] \right\rangle - E_{\mathrm{H}}[n] \tag{2.31}$$

and $E_{\mathrm{c}}[n]$ is the correlation energy functional

$$E_{\mathrm{c}}[n] = \left\langle \psi[n] \middle| \hat{T} + \hat{W}_{ee} \middle| \psi[n] \right\rangle - \left\langle \Phi[n] \middle| \hat{T} + \hat{W}_{ee} \middle| \Phi[n] \right\rangle = T_c[n] + U_c[n], \tag{2.32}$$

which contains a kinetic contribution $T_c[n] = \left\langle \psi[n] \middle| \hat{T} \middle| \psi[n] \right\rangle - \left\langle \Phi[n] \middle| \hat{T} \middle| \Phi[n] \right\rangle$ and a potential contribution $U_c[n] = \left\langle \psi[n] \middle| \hat{W}_{ee} \middle| \psi[n] \right\rangle - \left\langle \Phi[n] \middle| \hat{W}_{ee} \middle| \Phi[n] \right\rangle$.

2.1.3.2 Kohn-Sham Equations

The minimization (2.27) over the single-determinant wave function Φ can be reformulated to a minimization of the total electronic energy $E[\{\phi_i\}]$

$$E[\{\phi_i\}] = \sum_{i=1}^{N} \int \phi_i^*(\mathbf{r}) \left(-\frac{1}{2}\nabla^2 + V_{\mathrm{ext}}(\mathbf{r}) \right) \phi_i(\mathbf{r}) d^3r + E_{\mathrm{Hxc}}[n], \tag{2.33}$$

with respect to the spatial orbitals $\phi_i(\mathbf{r})$. The spatial orbitals $\phi_i(\mathbf{r})$ form a set of N orthonormal occupied orbitals $\{\phi_i(\mathbf{r})\}_{i=1,\ldots,N}$. The density is then expressed in terms of the spatial orbitals $\phi_i(\mathbf{r})$ as

$$n(\mathbf{r}) = \sum_{i}^{N} |\phi_i(\mathbf{r})|^2. \tag{2.34}$$

The method of the Lagrange multipliers can then be used to perform the minimization with the Lagrangian

$$\mathcal{L}\left[\{\phi_i\}\right] = E\left[\{\phi_i\}\right] - \sum_{i=1}^{N} \varepsilon_i \left(\int \phi_i^*(\mathbf{r})\phi_i(\mathbf{r}) d^3r - 1 \right). \tag{2.35}$$

The Lagrange multiplier ε_i is associated to the normalization condition of $\phi_i(\mathbf{r})$. The functional derivative of the Lagrangian $\mathcal{L}$ with respect to ϕ_i^* leads to the following equation

$$\left(-\frac{1}{2}\nabla^2 + V_{\text{ext}}(\mathbf{r}) \right) \phi_i(\mathbf{r}) + \frac{\delta E_{\text{Hxc}}[n]}{\delta \phi_i^*(\mathbf{r})} = \varepsilon_i \phi_i(\mathbf{r}), \tag{2.36}$$

since the Lagrangian $\mathcal{L}$ should be stationary with respect to the variations of orbitals $\phi_i(\mathbf{r})$. The derivative of the functional Hartree-exchange-correlation energy $E_{\text{Hxc}}[n]$ with respect to $\phi_i^*(\mathbf{r})$ is given by

$$\frac{\delta E_{\text{Hxc}}[n]}{\delta \phi_i^*(\mathbf{r})} = \int \frac{\delta E_{\text{Hxc}}[n]}{\delta n(\mathbf{r}')} \frac{\delta n(\mathbf{r}')}{\delta \phi_i^*(\mathbf{r})} d^3r'. \tag{2.37}$$

One can introduce the Hartree-exchange-correlation potential $V_{\text{Hxc}}(\mathbf{r})$, which is functional of the density, as the functional derivative of $E_{\text{Hxc}}[n]$ with respect to $n(\mathbf{r})$

$$V_{\text{Hxc}}(\mathbf{r}) \quad = \quad \frac{\delta E_{\text{Hxc}}[n]}{\delta n(\mathbf{r})} \tag{2.38}$$

Using the decomposition of $E_{\text{Hxc}}[n]$ (see eqn. (2.28)), we get

$$V_{\text{Hxc}}(\mathbf{r}) \quad = \quad \frac{\delta E_{\text{H}}[n]}{\delta n(\mathbf{r})} + \frac{\delta E_{\text{xc}}[n]}{\delta n(\mathbf{r})} = V_{\text{H}}(\mathbf{r}) + \frac{\delta E_{\text{xc}}[n]}{\delta n(\mathbf{r})} \tag{2.39}$$

where the Hartree potential $V_{\text{H}}(\mathbf{r}) = \frac{\delta E_{\text{H}}[n]}{\delta n(\mathbf{r})}$ is defined as

$$V_{\text{H}}(\mathbf{r}) \quad = \quad \int \frac{n(\mathbf{r}')}{|\mathbf{r} - \mathbf{r}'|} d^3r'. \tag{2.40}$$

Furthermore, from eqn. (2.34) we can obtain the derivative of $n(\mathbf{r})$ with respect to the orbitals $\phi_i(\mathbf{r})$

$$\frac{\delta n(\mathbf{r}')}{\delta \phi_i^*(\mathbf{r})} = \phi_i(\mathbf{r}) \delta(\mathbf{r} - \mathbf{r}'). \tag{2.41}$$

Injecting eqn. (2.41) into eqn. (2.37) and using the definition of the Hartree-exchange-correlation potential $V_{\mathrm{Hxc}}(\mathbf{r})$ (2.39), we finally obtain the Kohn-Sham equations

$$\left(-\frac{1}{2}\nabla^2 + V_{\mathrm{ext}}(\mathbf{r}) + V_{\mathrm{Hxc}}[n](\mathbf{r})\right)\phi_i(\mathbf{r}) = \varepsilon_i\phi_i(\mathbf{r}), \tag{2.42}$$

$$H_{\mathrm{eff}}(\mathbf{r})\phi_i(\mathbf{r}) = \varepsilon_i\phi_i(\mathbf{r}), \tag{2.43}$$

where ε_i is the KS orbital energies and $H_{\mathrm{eff}}(\mathbf{r}) = -\frac{1}{2}\nabla^2 + V_{\mathrm{eff}}(\mathbf{r})$ the one-electron KS Hamiltonian. $V_{\mathrm{eff}}(\mathbf{r}) = V_{\mathrm{ext}}(\mathbf{r}) + V_{\mathrm{Hxc}}[n](\mathbf{r})$ is the so-called KS potential. The orbitals ϕ_i which satisfy the KS equations (2.43) are called KS orbitals. The KS equations constitute a set of coupled self-consistent equations since the potential $V_{\mathrm{Hxc}}[n](\mathbf{r})$ depends on all the occupied orbitals $\{\phi_i(\mathbf{r})\}_{i=1,\ldots,N}$ through the density $n(\mathbf{r})$. The ground-state density $n(\mathbf{r})$ of the KS system of N non-interacting electrons, defined by the effective Hamiltonian H_{eff}, is the same that the exact ground-state density $n_0(\mathbf{r})$ of the physical system of N interacting electrons. The exact ground-state energy E_0 is then easily obtained by injecting the KS orbitals into equation (2.33). The self-consistent field loop of the KS equations is shown in Figure 2.1.1.

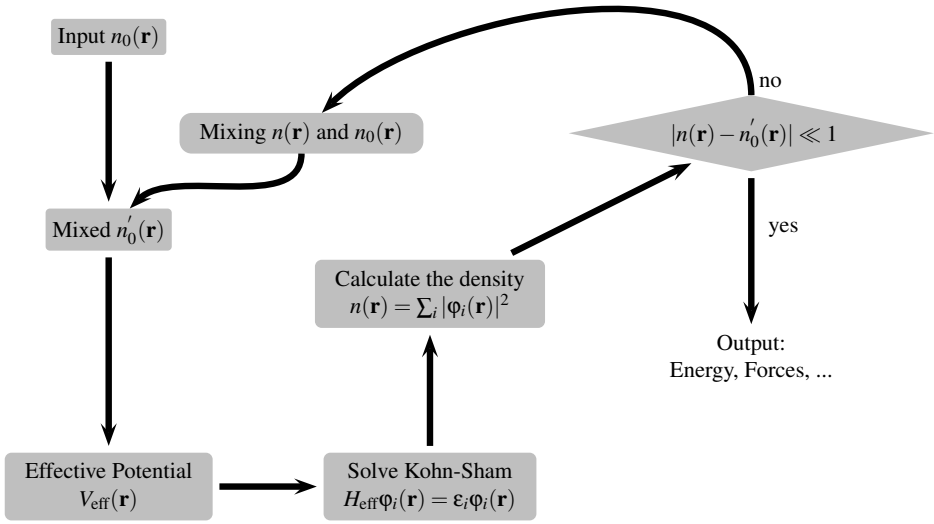

Figure 2.1.1: Schematic representation of the self-consistent field loop for solving the KS equations.

2.1.4 Local Density Approximation

Ideally, DFT is an exact theory and with the Kohn-Sham method described previously, the approach is very appealing since the solution of a self-consistent one body problem is much simpler than the original correlated many-body problem. Unfortunately, the exchange-correlation (xc) energy $E_{\rm xc}$ can not be determined exactly and must be approximated. A number of approximations exist such as the local-density approximation (LDA) [33, 34] or the generalized gradient approximation (GGA) [35, 36] which are the ones used in this work. The simplest and most used functional for $E_{\rm xc}$ is the LDA described below.

The LDA for a finite system with variable density $n(\mathbf{r})$ consist in assuming the local xc energy density $e_{\rm xc}$ to be that of the electron gas with density $n = n(\mathbf{r})$

$$E_{\rm xc}^{LDA}[n] = \int n(\mathbf{r}) e_{\rm xc}(n(\mathbf{r})) d^3r. \tag{2.44}$$

The extension to the spin-density formalism is straightforward; it is usually termed "Local-spin density" (LSD) formalism.

The exchange energy part of the LDA was derived by Dirac (1930)

$$E_{\rm xc}^{LDA}[n] = -\frac{3}{4}\left(\frac{3}{\pi}\right)^{1/3} e^2 \int [n(\mathbf{r})]^{4/3}\, d^3r, \tag{2.45}$$

and is also often referred to as the Slater approximation. The most commonly used correlation energy functionals in cluster physics are those by Wigner (1934), with

$$e_{\rm c}^{\rm W} = -\frac{0.88}{r_{\rm s}(n) + 7.8}, \tag{2.46}$$

and by Gunnarsson and Lundqvist [37], with

$$e_{\rm c}^{\rm GL} = -0.0666\left[(1+x^3)\log\left(1+\frac{1}{x}\right) + \frac{1}{2}x - x^2 - \frac{1}{3}\right], \quad x = \frac{r_{\rm s}(n)}{11.4}; \tag{2.47}$$

both are in atomic energy units (Ry) and are written in terms of the electronic Wigner-Seitz radius $r_{\rm s}(n) = (3/4\pi n)^{1/3}$.

2.2 Time-Dependent Density Functional Theory

In chapter 2.1, we presented Density Functional Theory, however, DFT can be used only to calculate physical quantities corresponding to the ground-state of the studied system. In order to calculate the response of a system under a perturbation we need to use the time-dependent version of DFT, the Time-Dependent

Density Functional Theory (TDDFT). TDDFT follows the same scheme as DFT but assumes that the time-dependent xc energy functionals $E_{\rm xc}[n](\mathbf{r})$ depend on the time-dependent density $n(\mathbf{r};t)$.

2.2.1 One-to-one correspondence

As it has been described in the introduction of this chapter, the evolution of N electrons in time is fully described by the time-dependent wave function $\psi(\mathbf{x}_1, \mathbf{x}_2,$ ..., $\mathbf{x}_N; t)$. Similarly to the previous section, the variables $\mathbf{x}_i = (\mathbf{r}_i, \sigma_i)$ contains the spatial and spin coordinates. The wave function $\psi(\mathbf{x}_1,\ \mathbf{x}_2,\ ...,\ \mathbf{x}_N; t)$ obeys the time-dependent Schrödinger equation [20]

$$\hat{H}(t)\psi(t) = i\frac{d\psi(t)}{dt}, \tag{2.48}$$

with $\hat{H}(t)$ is the time-dependent Hamiltonian operator similar to the time-independent Hamiltonian but with a time-dependent external potential $V_{\rm ext}$

$$\hat{H}(t) = \sum_{i=1}^{N}\left\{\frac{\mathbf{p}_i^2}{2m} + V_{\rm ext}(\mathbf{r}_i;t) + \frac{1}{2}\sum_{j\neq i}^{N}\frac{e^2}{|\mathbf{r}_i - \mathbf{r}_j|}\right\}. \tag{2.49}$$

The initial wave function $\psi(\mathbf{x}_1, \mathbf{x}_2, ..., \mathbf{x}_N; t = 0)$ is typically obtained from the ground-state DFT and must be specified because of the first order differential equation (2.48). Similarly to the ground-state density (2.7), the time-dependent density is defined by

$$n(\mathbf{r};t) = N\int d^3r_2 ... \int d^3r_N |\psi(\mathbf{r}, \mathbf{r}_2, ..., \mathbf{r_N}; t)|^2, \tag{2.50}$$

and has the interpretation that $n(\mathbf{r};t)d^3r$ is the probability of finding any electron in the volume d^3r around $\mathbf{r}$ at time t.

In the section 2.1.2, we briefly discussed the Hohenberg-Kohn theorem demonstrating the one-to-one mapping between the ground-state density and the external potential (2.10). E. Runge and E. K. U. Gross demonstrated that a time-dependent analogue to the HK theorem exists; the Runge-Gross theorem [38]. The Runge-Gross theorem shows a one-to-one correspondence between the time-dependent density $n(\mathbf{r};t)$ and the external potential $V_{\rm ext}(\mathbf{r};t)$ up to an arbitrary constant cte

$$n(\mathbf{r};t) \longrightarrow V(\mathbf{r};t) + cte, \tag{2.51}$$

which is the time-dependent version of eqn. (2.10).

2.2.2 Time-Dependent Kohn-Sham Equations

The Runge-Gross theorem [38] establishes that the one-body potential $V_{\text{ext}}(\mathbf{r};t)$ is a functional of the density $n(\mathbf{r};t)$ and initial state $\psi(\mathbf{x}_1,\mathbf{x}_2,...,\mathbf{x}_N;t=0)$. Following the idea of Kohn and Sham, we define a fictitious system of non-interacting electrons that satisfy the time-dependent Kohn-Sham equations

$$i\frac{\partial\phi_i(\mathbf{r};t)}{\partial t} = \left[-\frac{\nabla^2}{2} + V_{\text{eff}}[n](\mathbf{r};t)\right]\phi_i(\mathbf{r};t). \tag{2.52}$$

Here, $n(\mathbf{r};t)$ is the electron density computed from the time-dependent KS orbitals $\phi_i(\mathbf{r};t)$ similarly to eqn. (2.34) but now depending on time

$$n(\mathbf{r};t) = \sum_{i=1}^{N} |\phi_i(\mathbf{r};t)|^2. \tag{2.53}$$

The KS density $n(\mathbf{r};t)$ is defined to be precisely that of real system. By virtue of the one-to-one correspondence, the potential $V_{\text{eff}}(\mathbf{r};t)$ yielding this density is unique. We then define the xc potential

$$V_{\text{eff}}(\mathbf{r};t) = V_{\text{ext}}(\mathbf{r};t) + V_{\text{H}}(\mathbf{r};t) + V_{\text{xc}}(\mathbf{r};t), \tag{2.54}$$

where the Hartee potential reads

$$V_{\text{H}}(\mathbf{r};t) = \int d^3r' \frac{n(\mathbf{r}';t)}{|\mathbf{r}-\mathbf{r}'|}. \tag{2.55}$$

The xc potential $V_{\text{xc}}(\mathbf{r};t)$ is a functional of the entire history of the density, $n(\mathbf{r};t)$. Moreover, the xc potential depends on the initial many-electron wave function $\psi(\mathbf{x}_1,\mathbf{x}_2,...,\mathbf{x}_N;t=0)$ and on the initial Kohn-Sham wave function, $\Phi(\mathbf{x}_1,\mathbf{x}_2,...,\mathbf{x}_N;t=0)$. This time-dependent functional $V_{\text{xc}}(\mathbf{r};t)$ is more complex than the similar functional for the ground-state case. Knowledge of it implies solution of all time-dependent Coulomb interacting problems.

According to the KS theorem discussed in section 2.1.3, the ground-state of a quantum system is determined uniquely if the ground-state is non-degenerate. Therefore, if the many-electron and KS wave functions are non-degenerate, the time-dependent xc potential is a functional of the time-dependent density alone.

In ground-state DFT, the xc potential $V_{\text{xc}}(\mathbf{r};t=0)$ is the functional derivative of the xc energy functional $E_{\text{xc}}[n]$ (eqn. 2.37). It would be useful to find an xc functional $E_{\text{xc}}[n]$ whose functional derivative gives the xc potential $V_{\text{xc}}(\mathbf{r};t) = \frac{\delta E_{\text{xc}}[n](t)}{\delta n(\mathbf{r};t)}$. Such xc functional exist and is called the xc action $A_{\text{xc}}[n]$. A plausible approximation to it was proposed by E. Runge and E. K. U. Gross [38]. However, it turned out later [39] that this action leads to an unfortunate consequence.

Paradoxically, the second functional derivative of the proposed xc action over the electron density (so-called xc kernel used in linear-response TDDFT) violates the causality principle [40]. In this work, we are using adiabatic time-dependent xc functionals. In the adiabatic functionals, the xc action $A_{\mathrm{xc}}[n](\mathbf{r};t)$ depends on the instantaneous density $n(\mathbf{r};t)$, i.e., there is no memory of previous times. This is a strong but very common approximation. Besides allowing us to use any standard approximation for the ground-state (as far as the xc kernel can be computed), it solves the problem of the causality breaking, since all xc effects only depend on the instantaneous electron density. Moreover, because we focus on spectroscopical properties, we will further assume a weak time-dependent addition (perturbation) $\delta V_{\mathrm{ext}}(\mathbf{r};t)$ to the time-independent external potential $\tilde{V}_{\mathrm{ext}}(\mathbf{r})$

$$V_{\mathrm{ext}}(\mathbf{r};t) = \tilde{V}_{\mathrm{ext}}(\mathbf{r}) + \delta V_{\mathrm{ext}}(\mathbf{r};t). \tag{2.56}$$

The perturbation theory for TDDFT can be formulated via so-called linear-response functions. In the following we discuss the linear-response theory for TDDFT.

2.2.3 Linear-Response Theory

A straightforward way of extracting spectroscopical information about optical excitations within the time-dependent KS formalism would be using the time-dependent KS equations (2.52) with a simple adiabatic functional for the time-dependent xc potential $V_{\mathrm{xc}}[n](\mathbf{r};t)$. Before the perturbation is applied at $t = 0$, the system is usually assumed to be in its ground-state. Thus the KS ground-state (occupied KS orbitals) can be used as an initial condition. Adding a weak kick-like dipole perturbation $\delta V_{\mathrm{ext}} = \mathbf{E}_{\mathrm{ext}}\mathbf{r}\delta(t)$ at the time $t = 0$ and solving the KS equations (2.52), we can compute the time-dependent induced dipole moment $D_i(t) = \int \mathbf{r}_i \delta n(\mathbf{r};t) d^3r$. The Fourier transform of the dipole moment will give the spectrum of the dipole polarizability $\alpha(\omega)$ which is simply connected to the optical absorption cross section. In fact, this procedure is found in many implementations of TDDFT [41, 42]. However, the real-time TDDFT generally provides much more information on the excitations (non-linear processes) and is capable to model many scenarios (charging/discharging) beyond what is needed in spectroscopy. The versatility of the real-time TDDFT contributes to its high computational cost despite its favorable computational complexity scaling with number of atoms. One of the main drawbacks of real-time TDDFT for spectroscopic calculations is the fact that the frequency resolution of the computed spectrum is linked to the total propagation time, i.e., in order to increase the energy resolution of the response properties longer simulations are needed. Besides the associated increase of the computational cost, this requires sufficiently stable algorithms for the time propagation, which are not completely trivial. In contrast,

linear-response TDDFT is less general, being restricted to small perturbations. As we will describe in detail below, it can be formulated in an efficient way that allows to study very large systems. Moreover, the linear-response TDDFT is formulated directly in frequency domain, simplifying the interpretation of the results. In this work, we continued to develop and apply the linear-response TDDFT. Below, we summarize the linear-response TDDFT for the sake of the self-contained presentation.

In the framework of linear-response TDDFT, the induced density $\delta n(\mathbf{r};t)$ is given by the convolution product in time of the external potential $\delta V_{\text{ext}}(\mathbf{r};t)$ with the so-called response function $\chi(\mathbf{r},\mathbf{r}';t)$

$$\delta n(\mathbf{r};t) = \int dt' \int d^3r' \chi(\mathbf{r},\mathbf{r}';t-t')\delta V_{\text{ext}}(\mathbf{r}';t'), \tag{2.57}$$

i.e., if you make a small change in the external potential at point $\mathbf{r}'$ and time t', χ tells you how the density will change at point $\mathbf{r}$ and later time t. An important property of χ is that it does not depend of the time t_0 at which the perturbation is switched on. This is why χ is function only of $t-t'$ and not of (t,t'). Since the present framework is in real-space, we can drop the spatial variables temporarily for the sake of clarity

$$\delta n(t) = \int dt' \chi(t-t')\delta V_{\text{ext}}(t'). \tag{2.58}$$

Now, the Fourier transform of expression (2.58) is simply

$$\delta n(\omega) \quad = \quad \chi(\omega)\delta V_{\text{ext}}(\omega), \tag{2.59}$$

or

$$\delta n(\omega) \quad = \quad \chi_0(\omega)\delta V_{\text{eff}}(\omega), \tag{2.60}$$

where $\delta V_{\text{eff}} = \delta V_{\text{ext}} + V_{\text{Hxc}}$ is the KS potential which includes the small perturbation δV_{ext}. $\chi_0(\omega)$ is the non-selfconsistent response defined by eqn. (2.60). $\chi_0(\omega)$ tells you how the non-interacting KS electrons would respond to the changes in the effective potential $\delta V_{\text{eff}}(\omega)$. Thus, χ and χ_0 are generally very different, but both must yield the same density response $\delta n(\omega)$. The advantage of equation (2.60) over equation (2.59) is that $\chi_0(\omega)$ has a close expression in terms of KS orbitals and energies, which is not the case of $\chi(\omega)$

$$\chi_0(\mathbf{r},\mathbf{r}';\omega) = \lim_{\varepsilon\to 0}\sum_{n,m}(f_n - f_m)\frac{\phi_n^*(\mathbf{r})\phi_m(\mathbf{r})\phi_m^*(\mathbf{r}')\phi_n(\mathbf{r}')}{\omega - (E_m - E_n) + \mathrm{i}\varepsilon}, \tag{2.61}$$

where (n,m) are indices over the KS orbitals. f_n are occupation terms, if n and m are both occupied or unoccupied states then $f_n - f_m = 0$, otherwise, $f_n - f_m \neq 0$.

E_n are the eigenenergy of the corresponding KS states ϕ_n. Thus, χ_0 is obtained from the occupied and virtual KS orbitals ϕ_n obtained in the ground-state KS DFT. If the Hartree-exchange-correlation potential V_{Hxc} is not allowed to change in response to the external perturbation $\delta V_{\text{ext}}(\omega)$, then $\chi = \chi_0$. In such case the excitations of the system can be exactly described as one-electron excitation in the KS potential obtained from the ground-state density. From equations (2.59) and (2.60) we obtain

$$\begin{cases} \chi(\omega) = \dfrac{\delta n(\omega)}{\delta V_{\text{ext}}(\omega)}, \\ \chi_0(\omega) = \dfrac{\delta n(\omega)}{\delta V_{\text{eff}}(\omega)}. \end{cases} \tag{2.62}$$

Since $\delta V_{\text{eff}}(\omega) = \delta V_{\text{ext}}(\omega) + \delta V_{\text{Hxc}}(\omega)$ and taking the variational derivative with respect to $\delta n(\omega)$, we get

$$\frac{\delta V_{\text{eff}}(\omega)}{\delta n(\omega)} = \frac{\delta V_{\text{ext}}(\omega)}{\delta n(\omega)} + \frac{\delta V_{\text{Hxc}}(\omega)}{\delta n(\omega)}. \tag{2.63}$$

Taking into account that $\delta V_{\text{eff}}/\delta n = \chi_0^{-1}$ and $\delta V_{\text{ext}}/\delta n = \chi^{-1}$, and defining $\frac{\delta V_{\text{Hxc}}(\omega)}{\delta n(\omega)} = K_{\text{Hxc}}(\omega)$, usually called xc kernel, we obtain

$$\chi_0^{-1}(\omega) = K_{\text{Hxc}}(\omega) + \chi^{-1}(\omega), \tag{2.64}$$

or

$$\chi(\omega) = \left[\chi_0^{-1}(\omega) - K_{\text{Hxc}}(\omega)\right]^{-1}. \tag{2.65}$$

Then,

$$\left[\chi_0^{-1}(\omega) - K_{\text{Hxc}}(\omega)\right]^{-1} = \left\{\chi_0^{-1}(\omega)\left[1 - \chi_0(\omega)K_{\text{Hxc}}(\omega)\right]\right\}^{-1}, \tag{2.66}$$

$$\chi(\omega) = \left[1 - \chi_0(\omega)K_{\text{Hxc}}(\omega)\right]^{-1}\chi_0(\omega), \tag{2.67}$$

$$1 = \chi_0^{-1}(\omega)\chi(\omega) - K_{\text{Hxc}}(\omega)\chi(\omega), \tag{2.68}$$

$$\chi(\omega) = \chi_0(\omega) + \chi_0(\omega)K_{\text{Hxc}}(\omega)\chi(\omega). \tag{2.69}$$

Equation (2.69) is the well known Petersilka-Gossman-Gross equation [43]. We can continue to simplify the Petersilka-Gossman-Gross equation further using relations (2.62)

$$\chi(\omega) = \frac{\delta n(\omega)}{\delta V_{\text{ext}}(\omega)} = \chi_0(\omega) + \chi_0(\omega)K_{\text{Hxc}}(\omega)\frac{\delta n(\omega)}{\delta V_{\text{ext}}(\omega)}, \tag{2.70}$$

$$\delta n(\omega) = \chi_0(\omega)\delta V_{\text{ext}}(\omega) + \chi_0(\omega)K_{\text{Hxc}}(\omega)\delta n(\omega), \tag{2.71}$$

$$\left[1 - \chi_0(\omega)K_{\text{Hxc}}(\omega)\right]\delta n(\omega) = \chi_0(\omega)\delta V_{\text{ext}}(\omega). \tag{2.72}$$

Furthermore, inserting equation (2.60) into equation (2.72), we get the system of integral equations

$$[1 - \chi_0(\omega)K_{\mathrm{Hxc}}(\omega)]\,\chi_0(\omega)\delta V_{\mathrm{eff}}(\omega) \quad = \quad \chi_0(\omega)\delta V_{\mathrm{ext}}(\omega), \tag{2.73}$$

Acting from the left in the last equation with the inverse of the non-interacting response function $\chi_0^{-1}(\omega)$, we get

$$\boxed{[1 - K_{\mathrm{Hxc}}(\omega)\chi_0(\omega)]\,\delta V_{\mathrm{eff}}(\omega) = \delta V_{\mathrm{ext}}(\omega).} \tag{2.74}$$

Setting up and solving this equation is the main part of the iterative TDDFT algorithm that we use along this thesis [44]. Eqn. (2.74) is slightly more preferable than eqn. (2.72) because after determination of the effective potential $\delta V_{\mathrm{eff}}(\mathbf{r};\omega)$ we can easily organize several types of analysis of the induced density $\delta n(\mathbf{r};\omega)$ [44] which are difficult to achieve otherwise. The algorithm to discretize and solve the linear equations (2.74) or (2.72) will be further detailed in section 2.3

2.2.4 Plasmons within TDDFT

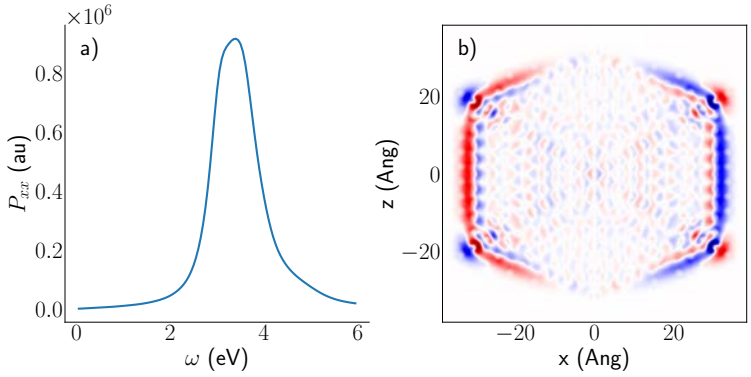

Figure 2.2.1: Panel (a) shows the imaginary part of the polarizability of a sodium cluster containing 3871 atoms. The broad resonance is caused by the surface plasmon at 3.40 eV. The corresponding distribution of the imaginary part of the density change δn for a cut through the center of the cluster is shown on panel (b). The clear dipolar character of the surface plasmon of this system can be appreciated.

A number of unprecedented technologies for applications in optics, chemical and biological sensing, and medicine have been developed based on the intense extinction spectra associated with localized surface plasmon excitation [45, 46]. A plasma consists of a gas of charged particles in dynamic equilibrium. When

an external electric field perturbs the system, the distribution of charges is not anymore in equilibrium and regions with excess of charges of a given sign are created. Once the perturbation is switched off, a restoring force appears between the regions of opposite charge, which leads to the oscillation of the charges in the system. This oscillatory motion is called *plasma oscillations*. When such oscillations are localized at the interface between a plasma and a dielectric material, it produces quantized electromagnetic surface waves localized at the interface, called *surface plasmons*. Finally, when the particle has a finite size, comparable or smaller to the wavelength of the excitation then the charges are confined to this small volume, they can not therefore freely propagate, creating a *localized surface plasmon* [47]. These localized surface plasmons (LSP) are the main objects of study in this thesis.

Commonly, LSPs are described using classical electrodynamics of continuous media with some approximate model dielectric functions describing the frequency-dependent attenuation of the electric field in media [48, 49]. However, for nano-sized systems on which we focus here, the classical theory hits serious limitations. One of these limitations is the poor definition of the dielectric function for the nanoparticles with a diameter below ten nanometers. In contrast to the classical electrodynamics, quantum mechanics backed up with *ab initio* methods can provide a much more credible description for such systems. For instance, *ab initio* TDDFT predicts material-dependent and size-dependent surface plasmon energies ω_{sp} of the LSP using only basic information on the chemical composition and shape of the clusters. However, the finite lifetime of the electronic excitations, the finite resolution of the spectrometers, and the temperature effects exhibit larger broadening constants than the energy separation between the individual electronic excitations that build up the LSP. Therefore, LSP resonances appear as strong, broad peaks in the optical polarizability of the clusters. An example of the polarizability is shown in Figure 2.2.1 panel (a). In this example, we computed the polarizability of a Na_{3871} cluster using the linear-response theory discussed in the previous section. In panel (b), we show the induced density $\delta n(\mathbf{r};\omega)$. The atomically-resolved oscillations of the induced density $\delta n(\mathbf{r};\omega)$ are indeed localized predominantly at the surface of the cluster, justifying the name of the resonance.

The linear-response theory is less computationally demanding than the real-time TDDFT when realized with suitable methods and optimized from programming point of view. In the next section, we will present the methods allowing the linear-response theory to be competitive in the next section.

2.3 Method

In this section, we describe the methodology behind our implementation of the linear-response TDDFT. The methodology is realized in the software package MBPT-LCAO which is an acronym for Many Body Perturbation Theory with Linear Combination of Atomic Orbitals. The package is a tool to determine and analyze the electronic excitations in condensed matter systems. The ground-state of the studied system must be provided to MBPT-LCAO. Currently, we use the DFT package SIESTA [1, 2] for the determination of the ground-state properties. The usage of atomic orbitals allows to study quantum systems of general chemical composition with moderate computational cost. The methods implemented in the MBPT-LCAO package for finite systems, like molecules and clusters, are:

- Linear-response TDDFT [4, 7, 44];
- Hartree-Fock SCF-calculations;
- Hedin's GW approximation for quasi-particle levels [5, 50];
- Bethe-Salpeter equation [51].

In this work, the efforts were concentrated in the TDDFT part of the code.

The spatial dependencies of the KS orbitals and response functions are represented by means of atomic orbitals and their products, correspondingly. The atomic orbitals are localized functions allowing to represent the studied electronic system efficiently in term of resources. The short-sightedness of the atomic orbitals is especially pronounced when using the so-called numerical atomic orbitals (NAO) [52, 53]. NAOs possess both a desirable flexibility of their shape and a strictly-defined spatial extend. The DFT package SIESTA and our methods for excited-states employ NAO throughout all the steps. In the following, we provide details, starting with the description of the spatial degrees of freedom.

2.3.1 Response Function within LCAO with Numerical Atomic Orbitals

The linear combination of atomic orbitals (LCAO) method was developed in the early days of quantum mechanics to expand molecular orbitals. Using LCAO method we expand the KS states $\phi_n(\mathbf{r})$ in equations (2.42) and (2.61) as

$$\phi_n(\mathbf{r}) = X_a^n f^a(\mathbf{r} - \mathbf{R}_a). \tag{2.75}$$

Here, the expansion coefficients X_a^n are determined by self-consistently solving equation (2.34) and (2.42), while $f^a(\boldsymbol{r})$ is a set of atomic orbitals, i.e., a set of

known functions centered at the atomic nuclei R_a. Here and later in this thesis we use the Einstein's summation convention over repeated indices. The atomic orbitals $f^a(\mathbf{r})$ possess a radial-angular decomposition

$$f^a(\mathbf{r}) = f^a(r)Y_{l_a,m_a}(\mathbf{r}), \tag{2.76}$$

where $f^a(r)$ is a radial function depending on the distance to the origin r, and $Y_{l,m}(\mathbf{r})$ are the spherical harmonics which will be chosen as real spherical harmonics. In order to assert in the notation the independence of the radial orbitals $f^a(\mathbf{r})$ on the magnetic quantum number m_a we use also a multiplet index μ

$$f^{a_{\mu,m}}(\mathbf{r}) = f^{\mu,m}(\mathbf{r}) = f^{\mu}(r)Y_{l_\mu,m}(\mathbf{r}). \tag{2.77}$$

In this notation, the multiplet index μ and magnetic quantum number m determine the orbital index $a = a_{\mu,m}$.

When inserting the LCAO ansatz (2.75) into eqn. (2.61) to describe the density response, one encounters products of localized functions $f^a(\mathbf{r})f^b(\mathbf{r})$—a set of quantities that are known to be linearly dependent. There is extensive literature [54–56] on the linear dependence of products of atomic orbitals. For example, Baerends *et al.* use an auxiliary basis of localized functions to represent the electronic density [56, 57], a procedure that is quite popular in the quantum chemistry community. Their procedure of fitting densities by auxiliary functions is essential both for solving Casida's equations [58] and in van Gisbergen's iterative approach [59].

In the alternative approach of Beebe and Linderberg [54], one forms the overlaps of products $\langle ab|\ a'b'\rangle$ to disentangle the linear dependence of the products $f^a(\mathbf{r})f^b(\mathbf{r})$. The difficulty with this approach is its lack of locality and the $O(N^4)$ cost of the construction of the overlaps [60].

Our approach, initially devised by D. Foerster [61], of constructing the basis for the products of orbitals $f^a(\mathbf{r})f^b(\mathbf{r})$ relies on the diagonalization of a Coulomb metric in the basis of original orbital products $\langle ab|\ cd\rangle$. The diagonalization is done for each atomic pair individually in order to maintain the locality of the constructed product basis (PB). Moreover, in the process of constructing, we use the spatial symmetry of the orbitals' products in order to further reduce the dimension of the diagonalized metric [7, 61]. The resulting basis set of *dominant products* is of controlled quality and is locally-optimal by construction. However, the dominant functions belonging to different atom pairs could still overlap strongly and, thus, the problem of linear dependence is not fully solved. Therefore, the basis of dominant products was augmented by a re-expression procedure allowing to use only atom-centered product functions. Both product basis sets: the dominant product's as well as the atom-centered PB set allow

to expand the atomic orbital's products $f^a(\mathbf{r})f^b(\mathbf{r})$ within the so-called product vertex ansatz [62]

$$f^a(\mathbf{r})f^b(\mathbf{r}) = V_\mu^{ab} F^\mu(\mathbf{r}), \tag{2.78}$$

where V_μ^{ab} are the product vertex coefficients. Inserting the product vertex ansatz (2.78) into the response function (2.61), we obtain

$$\chi_0(\mathbf{r},\mathbf{r}';\omega) = \sum_{\mu,\nu} F^\mu(\mathbf{r})\chi^0_{\mu\nu}(\omega)F^\nu(\mathbf{r}'), \tag{2.79}$$

$$\tag{2.80}$$

where the matrix $\chi^0_{\mu\nu}(\omega)$ reads

$$\chi^0_{\mu\nu}(\omega) = (f_n - f_m)\frac{(X_a^n V_\mu^{ab} X_b^m)(X_c^m V_\nu^{cd} X_d^n)}{\omega - (E_m - E_n) + \mathrm{i}\varepsilon}. \tag{2.81}$$

Furthermore, inserting the expansion (2.79) into the Petersilka-Grossman-Gross equation for the interacting response (2.69), we obtain the matrix equation

$$\chi_{\mu\nu}(\omega) = \chi^0_{\mu\nu}(\omega) + \chi^0_{\mu\mu'}(\omega)K_{\mathrm{Hxc}}^{\mu'\nu'}\chi_{\nu'\nu}(\omega), \tag{2.82}$$

for the interacting response matrix $\chi_{\mu\nu}(\omega)$. Inserting the PB in equation (2.74), we get the linear equation for the induced effective potential $\delta V^\nu_{\mathrm{eff}}(\omega)$

$$\boxed{\left[\delta_{\mu\nu} - K_{\mathrm{Hxc}}^{\mu\mu'}\chi^0_{\mu'\nu}(\omega)\right]\delta V^\nu_{\mathrm{eff}}(\omega) = \delta V^\mu_{\mathrm{ext}}(\omega).} \tag{2.83}$$

Equation (2.83) is the equation that will be solved iteratively using the solver described in section 2.3.2. The interaction kernel $K_{\mathrm{Hxc}}^{\mu\nu}$ is defined by

$$K_{\mathrm{Hxc}}^{\mu\nu} = \int d^3r d^3r' F^\mu(\mathbf{r})K_{\mathrm{Hxc}}(\mathbf{r},\mathbf{r}')F^\nu(\mathbf{r}'), \tag{2.84}$$

while the external $\delta V^\mu_{\mathrm{ext}}(\omega)$ and effective $\delta V^\mu_{\mathrm{eff}}(\omega)$ potentials are defined by

$$\delta V^\mu_{\mathrm{ext}}(\omega) = \int d^3r F^\mu(\mathbf{r})\delta V_{\mathrm{ext}}(\mathbf{r};\omega), \tag{2.85}$$

$$\delta V^\mu_{\mathrm{eff}}(\omega) = \int d^3r F^\mu(\mathbf{r})\delta V_{\mathrm{eff}}(\mathbf{r};\omega). \tag{2.86}$$

In the following, we describe the iterative method of solution of equation (2.83) which relies on the locality of the product basis vertex V_μ^{ab} in the matrix representation of the non-interacting response function (2.81).

2.3.2 Iterative Method to Calculate the Induced Density

Linear-response TDDFT describes how the external perturbation $\delta V_{\text{ext}}(\mathbf{r};\omega)$ induces the density change $\delta n(\mathbf{r};\omega)$ in the KS system. Namely, the induced density change $\delta n(\mathbf{r};\omega)$ is linearly connected to the external perturbation $\delta V_{\text{ext}}(\mathbf{r};\omega)$ by means of the interacting response function $\chi(\mathbf{r},\mathbf{r}';\omega)$. However, for the sake of computational efficiency one should avoid the computation of the whole operator $\chi(\mathbf{r},\mathbf{r}';\omega)$ and seek for an algorithm allowing to compute the action of the operator on a given perturbation. In this section we will formulate such algorithm. The algorithm uses the Krylov subspace technique to compute the action of the interacting response function $\chi(\mathbf{r},\mathbf{r}';\omega)$ on a given external perturbation $V_{\text{ext}}(\mathbf{r};\omega)$ without explicit storage of neither the interacting response function nor the non-interacting response functions. The method has been described in detail in Refs. [4, 7, 44]. In this thesis the iterative TDDFT was applied to two types of external perturbations: a dipolar field $V_{\text{ext}}(\mathbf{r};\omega) = (\mathbf{E}_0\mathbf{r})$ and the Coulomb field of an electric charge moving uniformly and rectilinearly $V_{\text{ext}}(\mathbf{r};t) = |\mathbf{r}-\mathbf{r}_e(t)|^{-1}$, $\mathbf{r}_e(t)$ being the position of a probe-electron at time t. The former model has been used to address optical excitations (see section 2.3.4), while the latter has been used to address electron energy loss spectra (see section 2.3.6). Several enhancements of the iterative TDDFT were implemented during this thesis. For instance, the action of the non-interacting response function to a vector was improved allowing to treat larger systems with less computational resources. Moreover, the electron energy loss spectroscopy (EELS) within the iterative TDDFT was first realized in this work.

2.3.2.1 Krylov Subspace Method

The system of linear equations (2.83) will be solved separately for each frequency ω. In order to solve this system of linear equations, we apply the generalized minimal residual method (GMRES) [63, 64]. GMRES belongs to the Krylov-type methods [64, 65] that represent a large matrix $\mathbf{A}$ in an iteratively built up Krylov-type basis $|0\rangle, |1\rangle \dots |i\rangle$. The first vector $|0\rangle$ in the basis is chosen to be equal to $|b\rangle$, while further vectors are computed recursively via $|i\rangle = \mathbf{A}\,|i-1\rangle$. As the vectors $|i\rangle = A^i\,|0\rangle$ are not mutually orthogonal, one may enforce their orthogonality by using the Gram-Schmidt method

$$|i\rangle = \mathbf{A}\,|i-1\rangle - \sum_{j=0}^{i-1} |j\rangle\,\langle j|\,\mathbf{A}\,|i-1\rangle\,. \tag{2.87}$$

The orthonormal basis built in this way is used in the GMRES method to approximately solve the linear system of equations $\mathbf{A}\,|\mathbf{X}\rangle = |b\rangle$ by minimizing the residual $|r\rangle = \mathbf{A}\,|\mathbf{X}\rangle - |b\rangle$ within the Krylov-type subspace eqn. (2.87). The minimization of the residual occurs when the equation $\sum_j \langle i|\,\mathbf{A}\,|j\rangle\,\langle j|\,x\rangle = \langle i|\,b\rangle$ is

satisfied and this set of equations is of much smaller size than the original problem. Once the solution in the Krylov subspace $\langle i|\ x\rangle$ is found, then an approximate solution in the original space can be computed from $|\mathbf{X}\rangle = \sum_i |i\rangle\langle i|\ x\rangle$.

A suitable stopping criterion is essential for our method, and several criteria were tested when the program was initially written [4] in order to keep the number of iterations small and achieve a reliable result at the same time. The conventionally used criterion that $\varepsilon_r = |r|/|b|$ should be small is unreliable when the tolerance threshold is comparatively large ($\varepsilon_r \sim 1\%$). Therefore, it was suggested an alternative combined criterion.

A natural stopping criterion for an iterative solver of the linear system of equations $\mathbf{A}\,|\mathbf{X}\rangle = |b\rangle$ is a condition on the relative error of the solution $\varepsilon_X = |\Delta\mathbf{X}|/|\mathbf{X}|$. In the case of optical absorption and EELS, the convergence condition using either the relative error ε_X or absolute error $|\Delta\mathbf{X}|$ lead to accurate values of the optical polarizability (see eqn. 2.91) and the energy loss probability (see eqn. 2.116). In the case of Raman spectroscopy presented in chapter 7, it is necessary to compute the derivative of the polarizability using finite difference. Therefore, the polarizability used to estimate the Raman signal need to be converged more strictly and only the absolute error provides the necessary accuracy.

A general iterative method of the Krylov type involves only matrix-vector products $\mathbf{A}\,|z\rangle$. For an explicitly given matrix $\mathbf{A}$, the operation $|z\rangle \to \mathbf{A}\,|z\rangle$ requires $O(N^2)$ operations. Therefore, the whole iterative method will scale as $O(N^2 N_{\text{iter}})$, where N_{iter} is the number of iteration until convergence. This is better than direct methods when $N_{\text{iter}} \ll N$, since a matrix-matrix multiplication takes $O(N^3)$ operations.

To avoid matrix multiplications, the application of the matrix $\mathbf{A} = 1 - K_{\text{Hxc}}\chi_0(\omega)$ to a vector $|z\rangle$ is done sequentially by computing first $|z'\rangle = K_{\text{Hxc}}\,|z\rangle$ and then $\mathbf{A}\,|z\rangle$. The kernel matrix K_{Hxc} is computed before the iterative procedure. Because it is frequency independent, it can be easily stored and reused. By contrast, the response matrix $\chi_0(\omega)$ is frequency dependent and computationally expensive, and its explicit construction should be avoided. Therefore, only the matrix-vector products $\chi_0(\omega)\,|z\rangle$ will be computed as explained below without ever calculating the full response matrix $\chi_0(\omega)$.

2.3.2.2 Application of the Non-Interacting Response Matrix

The Krylov method briefly presented above allows a fast computation of the effective potential $\delta V_{\text{eff}}(\omega)$, despite its relatively high computational complexity. As we will see below, the computational complexity of our iterative TDDFT method, $O(N^3)$, scales asymptotically with the third power of the number of atoms N. For a comparison, the real-time TDDFT possesses a much lower computational complexity scaling of $O(N)$.

The starting point of our construction of the matrix-vector product $\chi_0 |z\rangle$ is the expression in eqn. (2.81) for the KS response matrix in the basis of dominant products. To compute the matrix-vector product $\chi_0 |z\rangle$ efficiently, we decompose its calculation into a sequence of multiplications that minimizes the number of arithmetical operations by exploiting the sparsity of the vertex V_μ^{ab}. The sequence we chose is shown in equation (2.88). For clarity, the frequency-dependent denominator $(\omega - (E_n - E_m) + \mathrm{i}\varepsilon)$ is omitted. Boxes represent the operations to be performed at different steps. An algebraic representation of the computational steps is given in table 2.1.

$$\chi^0_{\mu\nu} z^\nu = V_\mu^{ab} \, X_a^n \, X_b^m \, X_c^m \, V_\nu^{cd} z^\nu \, X_d^n \tag{2.88}$$

Step	Expression	Complexity	Memory
1	$\alpha^{cd} = V_\nu^{cd} z^\nu$	1	1
2	$\beta^{cn} = \alpha^{cd} X_d^n$	2	2
3	$\gamma^{mn} = X_c^m \beta^{cn}$	3	2
4	$\gamma^{\tilde{m}n} = c\gamma^{mn}$	0	2
5	$\beta^{\tilde{b}n} = X_b^m \gamma^{\tilde{m}n}$	3	2
6	$\tilde{\alpha}^{ab} = \beta^{bn} X_a^n$	2	2
7	$\delta n_\mu = V_\mu^{ab} \tilde{\alpha}^{ab}$	1	1

Table 2.1: Sequence of operations for the calculation of $\chi^0_{\mu\nu} z^\nu$ of equation (2.88) with the respective computational complexity and memory scaling. The powers p of respective scaling demands $O(N^p)$ are stated in the table.

The procedure starts with a trace over the product index ν to obtain a sparse overlap-like matrix $\alpha^{cd} = V_\nu^{cd} z^\nu$. This operation takes asymptotically $O(N)$ operations and, as a matter of fact, it spends a minor portion of runtime. In the second step, we multiply the sparse matrix α^{cd} with the occupied-states eigenvectors $\beta^{cn} = \alpha^{cd} X_d^n$. The product takes $O(N^2)$ operations because the eigenvectors X_d^n form a dense matrix. In the third step, we multiply the (dense) matrix β^{cn} with the virtual-states eigenvectors $\gamma^{mn} = X_c^m \beta^{cn}$. This operation takes $O(N^3)$ operations, but with parsimonious NAOs, it becomes the largest time-consumer only for large systems (thousands of atoms). In the next step, the matrix γ^{mn} is updated with the frequency denominator $\tilde{\gamma}^{mn} = \gamma^{mn} \left[(f_n - f_m) \,/\, (\omega - (E_m - E_n) + \mathrm{i}\varepsilon) \right]$.

The update is not shown in equation (2.88) and takes a negligible run time. Remaining steps include a matrix-matrix multiplication $\tilde{\beta}^{bn} = X_b^m \tilde{\gamma}^{mn}$, which takes $O(N^3)$ operations and a matrix-matrix multiplication $\tilde{\alpha}^{ab} = \tilde{\beta}^{bn} X_a^n$ in which only an overlapping part of $\tilde{\alpha}^{ab}$ is computed and, therefore, it takes $O(N^2)$ operations. Finally, a trace over orbital indices a and b delivers the result $\delta n_\mu = V_\mu^{ab} \tilde{\alpha}^{ab}$.

The sequence described above was implemented in sparse algebra during this thesis for the first time. In older versions of the procedure, we were using an alternative sequence in which an auxiliary table $A_\mu^{an} = V_\mu^{ab} X_b^n$ was precomputed to diminish the number of mathematical operations. Although this table takes $O(N^2)$ storage elements of random-access memory (RAM), it becomes too big for large systems. Moreover, due to the size of the table A_μ^{an}, the machine cache gets obstructed and the computation gets slower than with the current sequence of operations we presented above. The improved operation sequence that we detailed above does not involve any approximations comparing to the old version. In fact, the new algorithm has a great impact on the performance of the iterative algorithm in all cases.

The sequence of matrix operations described above involves the operations of $O(N^3)$ computational complexity at most. Therefore, the computation of $\chi^0_{\mu\nu} z^\nu$ (eqn. 2.88) should be the most time consuming part of the program. However, the measurements of runtime show another pattern. The table 2.2 shows the total runtime (in hours) of the MBPT-LCAO program (third column) for a series of icosahedral silver clusters composed of 13 up to 2057 atoms (see the chapter 5 for more details about the clusters and appendix B for further details on the calculations). The percentage of the total runtime for the iterative procedure

Number atoms	Number electrons	Total runtime (hours)	iterative procedure: % of total runtime	$\chi^0_{\mu\nu} z^\nu$: % of total runtime
13	143	0.01	22.7	10.1
55	605	0.08	33.6	13.2
147	1617	0.36	48.0	18.7
309	3399	1.62	68.1	31.5
561	6171	5.88	74.1	43.6
923	10153	27.67	79.6	51.9
1415	15565	102.61	90.8	69.4
2057	22627	349.00	92.7	76.0

Table 2.2: Timing of the MBPT-LCAO program for a series of silver clusters. First and second columns indicate the number of atoms and the corresponding number of electrons of the clusters. Third column shows the total runtime of the program in hours. The percentage of the total runtime for the iterative procedure and the calculation of $\chi^0_{\mu\nu} z^\nu$ (eqn. 2.88) are indicated in the fourth and fifth columns respectively.

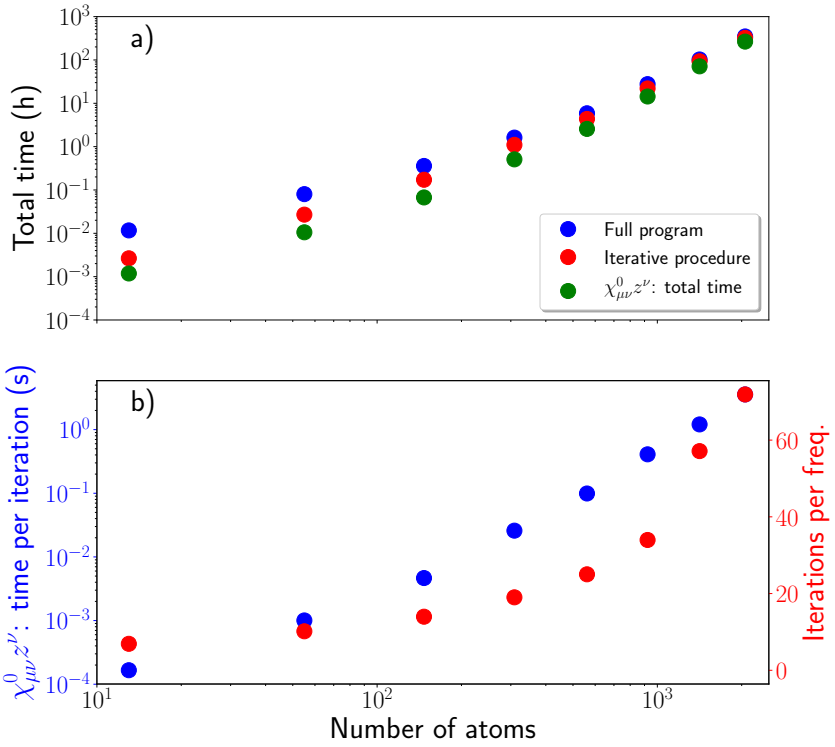

Figure 2.3.1: Panel (a) shows the time scaling of the MBPT-LCAO program for the series of icosahedral silver clusters from 13 to 2057 atoms indicated in the table 2.2. The running time of the full program (blue dots), of the iterative procedure (red dots) and of the the χ_0 algorithm (green dots) are represented. The blue dots of panel (b) show the average time by iteration to calculate $\chi^0_{\mu\nu}z^\nu$ (eqn. 2.88) on the left axis and the average number of iterations by frequency (red dots) on the right axis. For both panels, the *x*-axes and the left *y*-axes are given in logarithmic scale, while the right *y*-axis of panel (b) is using a linear scale.

and the χ_0 algorithm described in this section are indicated in the fourth and fifth columns respectively. The data of table 2.2 are represented on panel (a) of Figure 2.3.1 as function of the number of atoms. The blue dots shows the total runtime (third column of table 2.2) of the MBPT-LCAO program, the red dots indicate the runtime of the iterative procedure while the green dots the total time to perform the matrix operations (2.88) described above. The indicated times are in hours and both axes are in logarithmic scale. The blue dots of panel (b) of Figure 2.3.1 gives the average time by iterations to compute $\chi^0_{\mu\nu}z^\nu$ (left axis) in seconds (logarithmic scale). The red dots of the same panel (right axis) indicate the average number of iteration by frequency necessary to achieve convergence

(the threshold used in these calculations is $\varepsilon = 1 \times 10^{-3}$). Fitting the blue dots with a polynom, we obtain the expected cubic behavior. Nevertheless, as shown in table 2.2, the computation of $\chi^0_{\mu\nu} z^\nu$ takes the majority of the runtime only for clusters larger than one thousand atoms. In fact, we see that the iterative procedure, which the calculation of $\chi^0_{\mu\nu} z^\nu$ is part of, takes the largest part of the total runtime for small cluster as the Ag_{309}. Therefore, it seems that further optimizations of the iterative procedure are necessary to improve the performance of the program. Furthermore, as observed in panel (b) of Figure 2.3.1, we can see that the average number of iterations by frequency increases considerably for large clusters. The GMRES algorithm has thus more difficulties to converge when the size of the system increases. We will see in section 2.3.7, that this issue is not affecting the Python version of the program (PySCF-NAO) in which we used the GMRES solver provided by the SciPy library [66].

It is worth noting the relatively small absolute runtimes of the program. These calculations were done for a total of 61 frequencies and were using only 12 cores of a modern central processing unit (CPU)[2] with OpenMP parallelization to compute systems containing up to several thousands of atoms. Moreover, the sequence of operations described in this section relies on simple matrix-matrix multiplications in a manner facilitating the parallelization using graphical processing units (GPUs). As a consequence, it has been relatively easy to parallelize these matrix-matrix operations using the CUDA and CUBLAS [67] libraries. The usage of GPU allows for a faster and energy-efficient computation. More details are gathered in the appendix F.

2.3.2.3 Memory Requirements of the Algorithm

The scaling of the RAM requirement in the sequential application of the non-interacting response matrix described above in section 2.3.2.2 does not exceed $O(N^2)$ scaling with the number of atoms N. The interaction kernel (eqn. 2.90), which does not depend on frequency for the density functionals used in this work, is computed before the iterative calculation of the induced density. The interaction kernel should take as well $O(N^2)$ elements of RAM but using an optimized method (explained in section 2.3.3) the storage requirement for the interaction kernel scales as $O(N)$. Therefore, we expect an overall RAM requirements to scale with the second power of the number of atoms. In Figure 2.3.2 we show the actual memory consumption as function of the number of atoms for a series of icosahedral silver clusters. The Figure shows indeed a quadratic increase of the RAM requirement. The fitting of the RAM as function of the number of atoms

[2] Intel(R) Xeon(R) CPU E5-2683 v4 at 2.10GHz

N gives the following equation

$$\begin{aligned} \mathrm{RAM}(N) &= aN^2 + bN + c, \\ \text{with} \quad a &= 5.76 \times 10^{-3}, b = 18.76, c = 0.0. \end{aligned} \tag{2.89}$$

Since $a \ll b$, the quadratic behavior is rather weak and for small systems it evolves quasi linearly. In fact, the quadratic term will dominate only for $N > \frac{b}{a} \sim 3254$ atoms. This excellent scaling has been achieved thanks to careful optimization of the memory consumption. More details on the TDDFT calculations of these silver clusters are given in the appendix B.

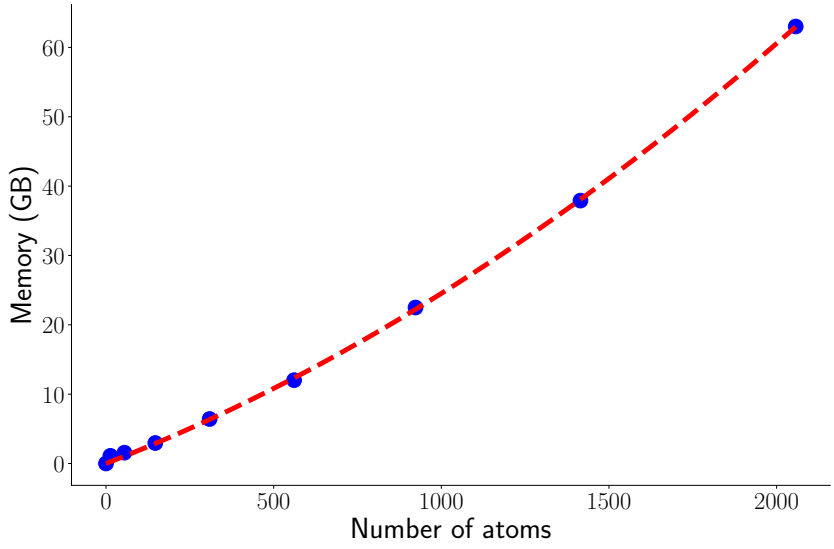

Figure 2.3.2: Memory scaling of the MBPT-LCAO program for several icosahedral silver particles from 13 to 2057 atoms (blue dots). The memory consumption has been interpolated (red dashed line) with the second order polynom (2.89).

2.3.3 Calculation of the kernels

The interaction kernel K appearing in equations (2.64) becomes a matrix in the PB set $\{F^\mu(\mathbf{r})\}$. Here we write the matrix as a sum of the Hartree and exchange-correlation kernels

$$K^{\mu\nu}_{\mathrm{Hxc}} = \int \frac{F^\mu(\mathbf{r})F^\nu(\mathbf{r}')}{|\mathbf{r}-\mathbf{r}'|} dr dr' + \int F^\mu(\mathbf{r}) K_{\mathrm{xc}}(\mathbf{r}) F^\nu(\mathbf{r}) dr. \tag{2.90}$$

In this work we use semi-local energy functionals $E[n]$ of the electron density n such as the local-density approximation (LDA) [33, 34] and the generalized gradient approximation (GGA) [35]. The exchange-correlation kernels of these functionals becomes local in spatial variables [44, 68–70]. However, the Hartree kernel $K_{\mathrm{H}}^{\mu\nu}$ is a dense matrix. Previously we suggested to view the application of the interaction kernel (2.90) to a vector as a simple matrix-vector product where the matrix $K_{\mathrm{Hxc}}^{\mu\nu}$ is stored in the dense matrix format. However, for large systems, the storage of the $O(N^2)$ matrix elements of TDDFT kernel $K^{\mu\nu}$ is prohibitive. For instance, in case of silver clusters (described in chapter 5), using the atom-centered PB set, we have to use about 60 functions per atom. Therefore, for Ag_{5083}, the storage of the (upper part of) interaction kernel in single precision will take 173 GBytes, which is prohibitive for many machines. Therefore, we realized a more sophisticated kernel operator. Namely, the non-overlapping part of Hartree kernel $K_{\mathrm{H}}^{\mu\nu}$ can be computed much faster than the overlapping part, using the multipole moments of PB functions. Therefore, in order to save RAM, we store only overlapping part, spending only $O(N)$ memory elements, while the remaining non-overlapping elements are computed on the fly just before a matrix-vector operation $K^{\mu\nu}z_\nu$ that is organized block-wise. In fact, this sophistication slows down the whole iterative loop only by a minor amount.

2.3.4 Optical Polarizability Tensor

The external electric field of the monochromatic optical stimuli is given by the plane wave $\delta\mathbf{E}_{\mathrm{ext}}(\mathbf{r};\omega) = \mathbf{E}_0 e^{i\mathbf{kr}}$. If the wavelength of the optical oscillations $\lambda = \frac{2\pi}{k} = \frac{2\pi c}{\omega} \gg R$ is much larger than the size of the excited quantum system R, then the simple dipole approximation for the external potential $\delta V_{\mathrm{ext}} = \mathbf{E}_0\mathbf{r}$ provides an accurate description of the optical perturbation. The dipole approximation gives rise to the notion of the optical polarizability tensor

$$P_{ij}(\omega) = \int d^3r d^3r' r_i \chi(\mathbf{r},\mathbf{r}';\omega) r'_j. \tag{2.91}$$

The indices i and j enumerate the Cartesian space coordinates (x, y, z). The trace of the imaginary part of the polarizability $P_{ij}(\omega)$ is proportional to the optical cross section $\sigma(\omega)$

$$\sigma(\omega) = -\frac{4\pi\omega}{3c}\Im\left[P_{xx}(\omega) + P_{yy}(\omega) + P_{zz}(\omega)\right]. \tag{2.92}$$

In order to compute the optical response $\delta V_{\mathrm{eff}}^{\mu}(\omega)$ for any direction of the external field $\boldsymbol{E}_0$, we shall compute the response for three unit vectors along Cartesian axes x, y and z

$$\left[\delta_{\mu\nu} - K_{\mathrm{Hxc}}^{\mu\mu'}\chi^0_{\mu'\nu}(\omega)\right]\delta V_{\mathrm{eff}}^{\nu}(\omega) = d_i^{\mu}, \tag{2.93}$$

where the dipole moment d_i^μ reads

$$d_i^\mu = \int d^3 r F^\mu(\mathbf{r}) r_i. \tag{2.94}$$

Once the effective KS potential $\delta V_{\text{eff}}^\nu(\omega)$ is known, we can calculate the induced density

$$\delta n_\mu^i = \chi_{\mu\nu}^0(\omega) \delta V_{\text{eff}}^\nu(\omega), \tag{2.95}$$

which can then be easily transformed back into real space

$$\delta n_i(\mathbf{r};\omega) = F^\mu(\mathbf{r}) \delta n_\mu^i. \tag{2.96}$$

The induced density in Cartesian coordinates $\delta n(\mathbf{r};\omega)$ will be analyzed in the chapters 3,4,5 and 6 for different physical systems and external stimuli. Moreover, we will see in the next section that the induced near-field can be easily obtained form the induced density $\delta n(\mathbf{r};\omega)$.

2.3.5 Calculation of the Induced Electrical Field in the Near-Field regime

The optical polarizability tensor $P_{ij}(\omega)$ characterizes the so-called far-field response of the electro-dynamic system. In this work we will also analyze the near-field response of the quantum systems. The near-field is crucial to overcome the diffraction limit of optical light which is approximately $\lambda/2$. For instance, near-field scanning optical microscopy (NSOM) overcomes the diffraction limit by using the sub-wavelength tips at the end of a fiber that brings (concentrates), collects and scatters light, pushing the spatial resolution of optical spectroscopic measurements down to tens of nanometer [71, 72]. Therefore, the near-field technique is determinant in enhanced Raman spectroscopy and other applications of plasmonics [12–17].

The induced near-field of the quantum systems will be computed out of the induced density change $\delta n(\mathbf{r};\omega)$ in frequency domain using the definitions from electrostatics

$$\delta \mathbf{E}_{\text{ind}}(\mathbf{r};\omega) = \int \frac{\mathbf{r}-\mathbf{r}'}{|\mathbf{r}-\mathbf{r}'|^3} \delta n(\mathbf{r}';\omega) d^3 r'. \tag{2.97}$$

In our approach, we use intertwined spatial grids to represent the density $\delta n(\boldsymbol{r};\omega)$ and the induced field $\delta \mathbf{E}_{\text{ind}}(\boldsymbol{r};\omega)$. The points of one grid occupy central positions in the cells created by the points of the other grid. For visualization purposes, the induced field $\delta \mathbf{E}_{\text{ind}}(\mathbf{r};\omega)$ will be computed on a 3D equidistant grid. Direct

evaluation of the integral (2.97) takes $N_E N_n$ operation where N_E is the number of points at which we evaluate the electric field and N_n is the number of point used to represent the induced density $\delta n(\mathbf{r};\omega)$ with a sufficient accuracy. Because the number of point N_E and N_n can be rather large, the direct evaluation to the Coulomb field is impractical. Instead, we will apply the convolution theorem of the Coulomb field (2.97) and use *Fast Fourier Transform* (FFT) to compute the successive Fourier transforms (FT). As it can be easily seen, the Coulomb field (2.97) is a convolution of two functions

$$\delta\mathbf{E}_{\mathrm{ind}}(\mathbf{r};\omega) = \frac{\mathbf{r}}{|\mathbf{r}|^3} \otimes \delta n(\mathbf{r};\omega). \tag{2.98}$$

The convolution theorem reads

$$\mathrm{FT}\left[\delta\mathbf{E}_{\mathrm{ind}}(\mathbf{r};\omega)\right] = \mathrm{FT}\left[\frac{\mathbf{r}}{|\mathbf{r}|^3}\right] \mathrm{FT}\left[\delta n(\mathbf{r};\omega)\right], \tag{2.99}$$

i.e., FT of a convolution is the product of the FTs of the functions. Using inverse FT we can then recover the spatial distribution of the induced electric field

$$\delta\mathbf{E}_{\mathrm{ind}}(\mathbf{r};\omega) = \mathrm{FT}^{-1}\left(\mathrm{FT}\left[\frac{\mathbf{r}}{|\mathbf{r}|^3}\right] \mathrm{FT}\left[\delta n(\mathbf{r};\omega)\right]\right). \tag{2.100}$$

Notice that here, in spite of the use of the FFT as a key ingredient, we are computing the electrostatic field associated with isolated charge distributions. In order to do this, the periodicity is taken to be at least twice the extension of the charge distribution along a given direction, i.e., a conveniently large buffer region is defined surrounding the charge distribution, and the Coulomb kernel in real-space is taken to be identical to zero for distances larger than the maximum linear dimension of the charge distribution. In this way it is possible to use FFTs to compute exactly the field associated with isolated objects.

2.3.6 Electron Energy Loss Spectroscopy

In section 2.3.4, we applied the iterative TDDFT method to compute the optical polarizability tensor in the dipole approximation. However, the iterative method of computing the induced density can be used for other types of external perturbations. During this work, we extended the iterative TDDFT method to the case of an external field produced by a moving point like charge (typically considered to be a fast electron).

The external field of a point-like charge moving uniformly and rectilinearly models the perturbation suffered by condensed-matter systems (clusters and molecules) in transmission electron microscope (TEM). TEM exhibits better spatial resolution than optical spectrometers [73]. The relevant experimental

techniques demonstrate that Electron Energy Loss Spectroscopy also shows a high energy resolution [74]. In this work, we compute and analyze the trajectory-dependent power of electron energy losses $\Gamma_{\mathrm{EELS}}(\omega)$—one of the principal observables measured in TEM. We are using our efficient *ab initio* atomistic approach to probe the response of a system under such perturbation.

2.3.6.1 Perturbation of Matter by Fast Electrons

The probe electrons in TEM possess a kinetic energy in the range from tens up to hundreds of keVs. The wavelength of such electrons is rather short (from 0.5 to 4 Å) and the interaction time of such electrons with the nanoparticles is too short to provoke significant changes in the initial velocity of the projectile. Correspondingly, we model the probe electrons as uniformly moving point charges. Moreover, the current density of the probe electrons can be kept small and the interaction of the probe electrons with the target electrons remains in the linear-response regime. Furthermore, in this work we focus on computing valence excitations. This, together with the high speed of electrons, justifies to some extent the use of a linear-response formulation.

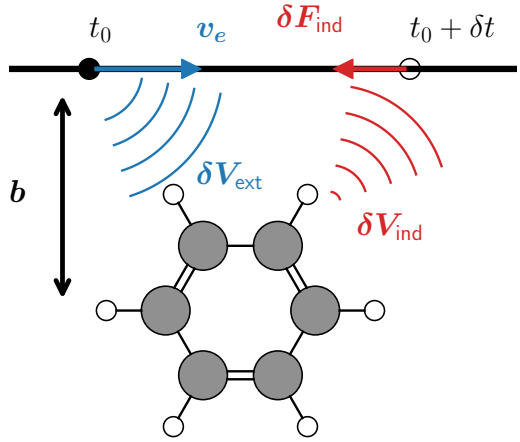

Figure 2.3.3: Representation of the interaction between an electron and a benzene molecule when the electron is passing in the vicinity of the molecule. The electron is represented at the time t_0 and $t_0+\delta t$ with a velocity v_e and with the impact parameter b. The electron's trajectory is represented by the dark line. The potential created by the probing electron $\delta V_{\mathrm{ext}}(\mathbf{r};t) = 1/|\mathbf{r_e}(t) - \mathbf{r}|$ is represented by blue arcs. While the the target's electrons creates an induced potential δV_{ind} represented by the red arcs which create an induced force δF_{ind} acting back on the electron.

The total mechanical work performed by the uniformly moving charged particle is given by [73]

$$\Delta E = \int \mathbf{v_e} \cdot \mathbf{E}_{\mathrm{ind}}(\mathbf{r_e}(t); t) dt, \tag{2.101}$$

where $\mathbf{E}_{\mathrm{ind}}(\mathbf{r_e}(t); t)$ is the electrical field induced due to the electronic excitations of the probed system, and $\mathbf{r_e}(t) = \mathbf{v_e}t + \mathbf{r_e}(t = 0)$ is the position of the projectile. The probe is assumed to have an electric charge of one atomic unit. Performing the Fourier transform of the induced electric field, we obtain the following expression of the total energy loss (see derivation below)

$$\Delta E = \int \omega \Gamma_{\mathrm{EELS}}(\omega) d\omega, \tag{2.102}$$

where $\Gamma_{\mathrm{EELS}}(\omega)$ is the energy loss probability. $\Gamma_{\mathrm{EELS}}(\omega)$ is interpreted as the probability for the probe electron to change its energy by amount of ω.

Let's perform the Fourier transform of the induced electric field and obtain an expression for the energy loss probability suitable for linear-response TDDFT. The Fourier transform of the induced electric field $\mathbf{E}_{\mathrm{ind}}(\mathbf{r_e}(t); t)$ reads

$$\mathbf{E}_{\mathrm{ind}}(\mathbf{r_e}(t); t) = \frac{1}{2\pi} \int \mathbf{E}_{\mathrm{ind}}(\mathbf{r_e}(t), \omega) e^{i\omega t} d\omega, \tag{2.103}$$

therefore, eqn. (2.102) becomes,

$$\Delta E = \frac{1}{2\pi} \int dt d\omega \mathbf{v_e} \cdot \mathbf{E}_{\mathrm{ind}}(\mathbf{r_e}(t); \omega) e^{i\omega t}. \tag{2.104}$$

Furthermore, since $\mathbf{E}_{\mathrm{ind}}(\mathbf{r_e}(t); t) \in \mathbb{R}$ we can transform the integral over all positive and negative frequencies into an integral over the positive frequencies only

$$\int_{-\infty}^{+\infty} d\omega \mathbf{E}_{\mathrm{ind}}(\mathbf{r_e}(t); \omega) e^{i\omega t} = 2\Re \int_{0}^{+\infty} d\omega \mathbf{E}_{\mathrm{ind}}(\mathbf{r_e}(t); \omega) e^{i\omega t}. \tag{2.105}$$

Thus, equation (2.104) becomes

$$\Delta E = \frac{1}{\pi} \Re \int dt \int d\omega \mathbf{v_e} \cdot \mathbf{E}_{\mathrm{ind}}(\mathbf{r_e}(t); \omega) e^{i\omega t}, \tag{2.106}$$

From the other side, the induced field $\mathbf{E}_{\mathrm{ind}}(\mathbf{r}; \omega)$ is created by the induced density $\delta n(\mathbf{r}; \omega)$. A simple Coulomb law can be used here since relativistic effects are neglected and there are no appreciable retardation effects due to the nanometer size of the particles we consider

$$\mathbf{E}_{\mathrm{ind}}(\mathbf{r}; \omega) = \int d^3 r' \frac{\mathbf{r} - \mathbf{r}'}{|\mathbf{r} - \mathbf{r}'|^3} \delta n(\mathbf{r}'; \omega). \tag{2.107}$$

By inserting equation (2.107) into equation (2.106) one gets,

$$\Delta E = \frac{1}{\pi}\Re\int d\omega\int dtd^3r'\frac{d\mathbf{r}_e(t)}{dt}\frac{\mathbf{r}_e(t)-\mathbf{r}'}{|\mathbf{r}_e(t)-\mathbf{r}'|^3}e^{i\omega t}\delta n(\mathbf{r}';\omega) \quad (2.108)$$

Calculating the derivative of the external potential $\delta V_{\text{ext}}(\mathbf{r};t) = 1/|\mathbf{r_e}(t)-\mathbf{r}|$ created by the probe,

$$\frac{d}{dt}\delta V_{\text{ext}}(\mathbf{r};t) = \frac{d}{dt}\frac{1}{|\mathbf{r_e}(t)-\mathbf{r}|} \quad (2.109)$$

$$= \frac{d\mathbf{r_e}(t)}{dt}\frac{\mathbf{r_e}(t)-\mathbf{r}}{|\mathbf{r_e}(t)-\mathbf{r}|^3} \quad (2.110)$$

which is the expression in the integral of equation (2.108)

$$\Delta E = \frac{1}{\pi}\Re\int d\omega\int dtd^3r'\frac{d}{dt}\delta V_{\text{ext}}(\mathbf{r}';t)e^{i\omega t}\delta n(\mathbf{r}';\omega). \quad (2.111)$$

Because $\delta V_{\text{ext}}(\mathbf{r}';t)$ is real, one can write

$$\int dte^{i\omega t}\frac{d}{dt}\delta V_{\text{ext}}(\mathbf{r}';t) = \left(\int dte^{-i\omega t}\frac{d}{dt}\delta V^*_{\text{ext}}(\mathbf{r}';t)\right)^* \quad (2.112)$$

$$= -i\omega\delta V^*_{\text{ext}}(\mathbf{r}';\omega). \quad (2.113)$$

Inserting equation (2.112) into equation (2.108) we get

$$\Delta E = -\tfrac{1}{\pi}\Re\int d^3r'd\omega\left(-i\omega\delta V^*_{\text{ext}}(\mathbf{r}';\omega)\delta n(\mathbf{r}';\omega)\right). \quad (2.114)$$

Finally using the relation $\Re(-iz) = \Im(z)$ with $z\in\mathbb{C}$ we simplify the last equation

$$\Delta E = -\frac{1}{\pi}\int\omega\int d^3r'\Im\left[\delta V^*_{\text{ext}}(\mathbf{r}';\omega)\delta n(\mathbf{r}';\omega)\right]d\omega. \quad (2.115)$$

Comparing the last equation with the probability ansatz (2.102), we derive the electron loss probability

$$\Gamma_{\text{EELS}}(\omega) = -\frac{1}{\pi}\Im\int d^3r\delta V^*_{\text{ext}}(\mathbf{r};\omega)\delta n(\mathbf{r};\omega), \quad (2.116)$$

$$\Gamma_{\text{EELS}}(\omega) = -\frac{1}{\pi}\Im\iint d^3rd^3r'\delta V^*_{\text{ext}}(\mathbf{r};\omega)\chi_0(\mathbf{r},\mathbf{r}';\omega)\delta V_{\text{eff}}(\mathbf{r}';\omega). \quad (2.117)$$

Using the analytical properties of the response function, e.g., using the Lehmann representation of the many-body response function, it can be easily shown that the expression in eqn. (2.117) must be non-negative for every ω. Therefore, $\Gamma_{\text{EELS}}(\omega)$ can be safely interpreted as an excitation probability. We see in eqn. (2.117) how $\Gamma_{\text{EELS}}(\omega)$ is simply related to the induced density $\delta n(\mathbf{r};\omega)$ and the external potential $\delta V_{\text{ext}}(\mathbf{r};\omega)$. The calculation of the external potential $\delta V_{\text{ext}}(\mathbf{r};\omega)$ is discussed below.

2.3.6.2 Iterative Computation of the Energy Loss

In section 2.3.6.1 we derived the electron energy loss probability $\Gamma_{\mathrm{EELS}}(\omega)$. The electron energy loss probability is determined by the induced density $\delta n(\mathbf{r};\omega)$ and the external potential created by the moving charge $\delta V_{\mathrm{ext}}(\mathbf{r};\omega)$. In this work, we use linear-response theory to compute the induced density $\delta n(\mathbf{r};\omega)$. We calculate the induced density $\delta n(\boldsymbol{r};\omega)$ expanding it in terms of product functions $\{F^{\mu}(\boldsymbol{r})\}$ (see eqn. 2.96)) and using linear equations (2.60) and (2.74) to compute the expansion coefficients $\delta n_{\mu}(\omega)$. The right-hand side of equation is a vector of the external potential moments $\delta V^{\mu}_{\mathrm{ext}}(\omega)$ in frequency domain. The moments of the external potential $\delta V^{\mu}_{\mathrm{ext}}(\omega)$ read

$$\delta V^{\mu}_{\mathrm{ext}}(\omega) = \frac{1}{2\pi}\int dt e^{i\omega t}\int \frac{F^{\mu}(\mathbf{r})}{|\mathbf{r}-\mathbf{R}^{\mu}_{\mathrm{elec}}(t)|}d^3r, \tag{2.118}$$

where $\mathbf{R}^{\mu}_{\mathrm{elec}}(t) = \mathbf{R}_0 + \mathbf{v_e}t - \mathbf{R}^{\mu}$ and $\mathbf{R}^{\mu}$ are the positions of atomic nuclei at which the product functions $\{F^{\mu}(\boldsymbol{r})\}$ are centered. Comparing with the calculation of the optical absorption, the only difference is in the definition of these moments. In contrast to the dipole (2.94) needed for optical polarizability tensor, the rectilinear moments (2.118) depend on the impact parameters (trajectory of the probe electron), on the velocity of the probe electron $\mathbf{v_e}$ and are generally frequency-dependent quantities. In order to compute the rectilinear moments (2.118), we will use the Laplace expansion of the Coulomb interaction and Fourier transform of the moments in time domain

$$\delta V^{\mu}_{\mathrm{ext}}(t) = \int \frac{F^{\mu}(\mathbf{r})}{|\mathbf{r}-\mathbf{R}^{\mu}_{\mathrm{elec}}(t)|}d^3r. \tag{2.119}$$

We use the Laplace expansion

$$\frac{1}{|\mathbf{r}-\mathbf{r}'|} = \sum_{lm}\frac{4\pi}{2l+1}\frac{r^l_<}{r^{l+1}_>}Y^*_{lm}(\hat{\mathbf{r}})Y_{lm}(\hat{\mathbf{r}'}), \tag{2.120}$$

where $r_< = \min(r,r')$ and $r_> = \max(r,r')$. Inserting eqn. (2.120) into eqn. (2.118) we get

$$\delta V^{\mu}_{\mathrm{ext}}(t) = \sum_{lm}\frac{4\pi}{2l+1}\int d^3r\frac{r^l_<}{r^{l+1}_>}Y^*_{lm}(\hat{\mathbf{r}})Y_{lm}(\hat{\mathbf{r}}^{\mu}_{\mathrm{elec}}(t))F^{\mu}(\mathbf{r}). \tag{2.121}$$

Since $F^{\mu}(\mathbf{r}) = F^{\mu}(r)Y_{l_\mu m_\mu}(\hat{\mathbf{r}})$ and $\int Y^*_{lm}(\hat{\mathbf{r}})Y_{l'm'}(\hat{\mathbf{r}})d\Omega = \delta_{ll'}\delta_{mm'}$, we can then remove the sum over l and m

$$\delta V^{\mu}_{\mathrm{ext}}(t) = \frac{4\pi}{2l_\mu+1}Y_{l_\mu m_\mu}(\hat{\mathbf{r}}^{\mu}_{\mathrm{elec}}(t))\int r^2\frac{r^l_<}{r^{l+1}_>}F^{\mu}(r)dr. \tag{2.122}$$

A final step consist in separating the radial integral into two ranges

$$\delta V^{\mu}_{\text{ext}}(t) = \frac{4\pi}{2l_\mu+1} Y_{l_\mu m_\mu}(\hat{\mathbf{r}}^{\mu}_{\text{elec}}(t)) \left[\frac{1}{\left(R^{\mu}_{\text{elec}}(t)\right)^{l_\mu+1}} \times \right.$$
$$\left. \int_0^{R^{\mu}_{\text{elec}}(t)} r^{l_\mu+2} F^{\mu}(|\mathbf{r}|) dr + \left(R^{\mu}_{\text{elec}}(t)\right)^{l_\mu} \int_{R^{\mu}_{\text{elec}}(t)}^{+\infty} \frac{F^{\mu}(|\mathbf{r}|)}{r^{l_\mu-1}} dr \right]. \tag{2.123}$$

Using the computed moments in time domain (2.123), we apply Fourier transform (FFT is used) and get the moments (2.119) in the frequency domain. In principle, following the work of Ferrel and Echenique [75] it is possible to find a close analytical expression for $\delta V^{\mu}_{\text{ext}}(\omega)$ when the trajectory passes outside the support region of a given product basis functions $F^{\mu}(\mathbf{r})$. However, for a general trajectory that overlaps with the functions $F^{\mu}(\mathbf{r})$ it is necessary to compute it numerically and, therefore, we decided to use the same numerical procedure for all the moments of the external potential. Using the product basis set, the electron energy loss probability becomes a scalar product

$$\Gamma_{\text{EELS}}(\omega) = -\frac{1}{\pi} \Im \left(\delta V^{\mu *}_{\text{ext}}(\omega) \delta n^{\mu}(\omega) \right). \tag{2.124}$$

The expansion coefficients of the induced density $\delta n^{\mu}(\omega)$ are obtained by iteratively solving the system of linear equations (2.83) using the Krylov subspace methods (see section 2.3.2.1).

2.3.7 The PySCF-NAO Program: the Pythonic Version of MBPT-LCAO

The software package MBPT-LCAO was written in Fortran language. The cumbersomeness of coding in Fortran made maintenance and extensions of the code difficult. During the last period of the PhD, we managed to port the program to a Python version which is more user-friendly, easier to maintain and to extend. The code is integrated into the Python-based Simulations of Chemistry Framework (PySCF) [6] that provides the possibility of reusing the open-source programs developed by many leading scientists. The module Numerical Atomic Orbital (NAO) corresponding to our code can be found in the development version of PySCF and loaded from Python shell with:

```
import pyscf.nao
```

Most of the functionalities of the code have been re-implemented in Python, except for heavy calculations (mainly the product basis generation and the computation of the exchange-correlation kernel). The heavy computations are done

in a Fortran library `libnao` which is interfaced with Python by means of the standard Python module `ctypes` [76]. The Fortran library `libnao` is part of the PySCF package. The flexibility of Python in the data managing made possible to interface the iterative TDDFT not only with SIESTA [1, 2], but also with other software packages such as GPAW [77] and PySCF [6]. Several other software packages such as OpenMX [78] or Fireball [79] can also be interfaced with PySCF-NAO with some more programming effort. Examples of Python scripts to run PySCF-NAO are available in the appendix C. The Python code is almost as fast as the Fortran code because of the use of the NumPy [80] and SciPy [66, 81, 82] libraries. In fact for large system such as silver cluster of 1415 atoms, the PySCF-NAO code is even faster than MBPT-LCAO because of improved GMRES solvers available in the SciPy library.

To demonstrate the capability of the code, we calculated the optical polarizability of a series of silver clusters containing 55 up to 1415 atoms. The iterative procedure is done for a set of 100 frequencies between 1.0 and 6.0 eV, with the imaginary part equal to 0.15 eV. The interacting polarizabilities are collected in panel (a) of Figure 2.3.4. Inspecting the polarizabilities, we see a pronounced low-frequency plasmonic peak. The resonance frequency of this peak is slowly changing with the cluster size, giving rise to a well-known $1/D$ scaling of the plasmonic frequency ω_{sp} with the cluster diameter D. In panel (b) of Figure 2.3.4 we show the runtime needed to compute the polarizability together with the number of applications of the response function The actual runtime scaling is closer to $T \sim N^2$ for the cluster sizes we consider. Furthermore, if we compare the number of iteration per frequency of Figure 2.3.4 to the one of the Fortran code (see Figure 2.3.1), we observe that the Python GMRES routine (from SciPy [66]) converges three times faster than the Fortran GMRES, for large systems (Ag_{923}). This improvement makes PySCF-NAO even more efficient than MBPT-LCAO for large systems.

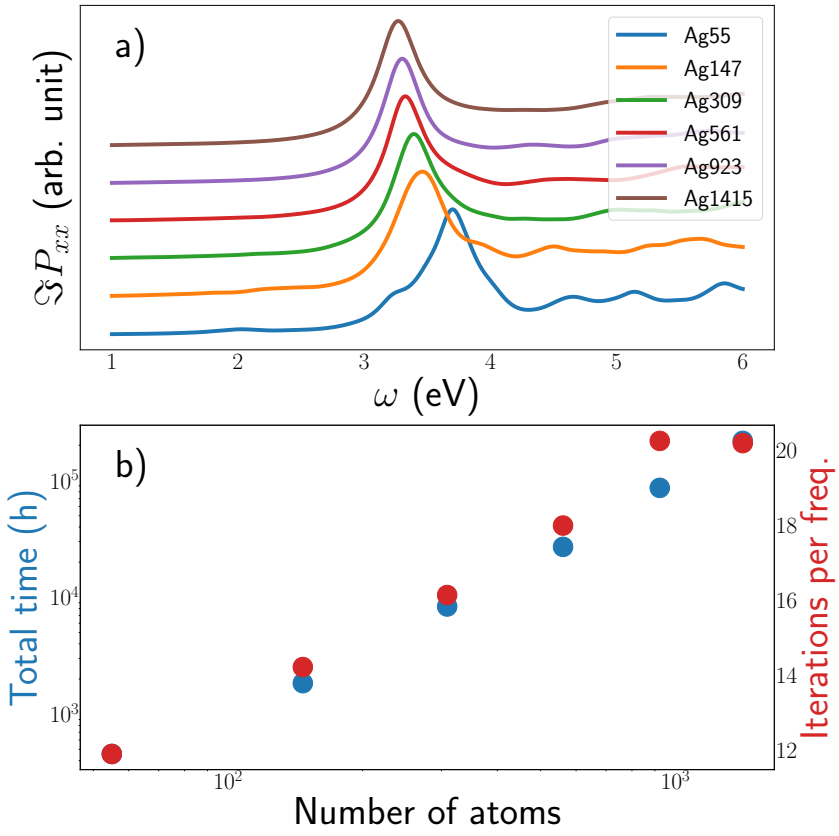

Figure 2.3.4: Polarizabilities, runtime and number of iterations for a series of icosahedral silver clusters. Panel (a) shows the interacting polarizability. In panel (b) the total runtime of the Python script spent to compute the dynamical polarizability show on panel (a) is represented on the left y-axis as function of the number of atom in logarithmic scale. The number of applications of the non-interacting response function (per frequency) is shown on the right y-axis with red dots.

Chapter 3

Atomistic Near-Field Nanoplasmonics: Reaching Atomic-Scale Resolution in Nanooptics

Electromagnetic field in nanoantennas is one of the leitmotifs that drives the development of plasmonics. The near-fields in these plasmonic nanoantennas are commonly addressed theoretically within classical frameworks that neglect atomic-scale features. This approach is often appropriate since the irregularities produced at the atomic scale are typically hidden in the far-field optical spectroscopy. However, a variety of physical and chemical processes rely on the fine distribution of the local fields at the ultraconfined scale. Using the efficient TDDFT program presented in section 2.3, we studied the optical response and the induced electric field at the vicinity of sodium clusters and dimers under the perturbation of an external electric field [83].

3.1 Motivation

Metallic nanoparticles are key in the development of nanooptics. The ability of the conduction electrons to collectively oscillate produces surface charge density oscillations in nanoparticles, so-called surface plasmons, that couple very efficiently to light, producing subwavelength localization and large enhancement of the optical fields induced at the nanoparticles [9–11]. Nanooptics with lo-

calized surface plasmons has thus boosted a variety of technological applications in which the intense electromagnetic fields can assist in enhancing the signal from vibrational spectroscopies [12, 13], improving the performance of solar cells [14, 15], optimizing the active control of nanodevices [16, 17], or implementing non-invasive thermotherapies in medicine [18], among others. In a majority of these applications, the optical response that determines the properties of plasmonic surface modes can be estimated in sufficient detail with classical electrodynamics, by solving Maxwell's equations for a particular material, shape, and environment. In this way, for instance, plasmonic modes of spherical nanoparticles [48, 49], nanoshells [84], nanorings [85], nanorods [86–89], nanostars [90, 91], dimers [11, 92, 93], or particle oligomers [94, 95] have been routinely estimated during the last years. The mode volumes typically reached in these structures are in the range of some tens of nanometers, and the actual degree of their field confinement is determined by the morphology of the nanostructure (curvature, thickness, interaction between different particles,...) [96–99]. The effective squeezing of electromagnetic energy into these nanometric dimensions has triggered out referring to plasmonic nanostructures as optical nanoantennas [100, 101].

As nanotechnology reaches a control of nanoarchitectures at scales of the order of the nanometer and even subnanometer [102, 103], nanooptics is called to face new regimes of interaction, where the atomic scale needs to be considered to correctly determine the optical response of the nanosystem. Optical processes at the atomic scale can be critical in many branches of nanoscience such as in field-enhanced photochemistry [104–107], in single molecule spectroscopy [13, 108], or in electronics at optical frequencies [109, 110].

Most of these situations require a complete theoretical framework that accounts for the quantum nature of the electrons in their interaction with light. Time-dependent Density Functional Theory (TDDFT) [38, 111] provides the adequate framework to tackle the optical response of plasmonic nanoantennas where the complex nonlocal screening [112, 113], the smooth electronic density profile at the metal interface [114], quantum size effects [115–117], and electron tunneling across metallic nanogaps [118, 119] can be properly taken into account. Furthermore, an atomistic description of the nanostructures [120] can address the effect in the optical response of atomic-scale features at the surfaces such as the presence of protruding atoms, steps, vertices, or edges at the contact of crystallographic planes. Although these atomic-scale effects might be sometimes masked in experimental far-field techniques, they are very relevant in spectroscopy techniques that directly rely on the ultrafine details of the near-field intensity and distribution.

3.2 Description of the System: the Na_{380} Cluster and Cluster Dimers

The cluster that we used for this study is a sodium cluster with an icosahedral like shape showing tips, facets and edges. The geometry is presented in Figure 3.2.1 for three orientations. A tip and a facet are highlighted in panels (b) and (c). The cluster is composed of 380 atoms; was initially determined using semi-empirical force fields [121]. We further relaxed the initial semi-empirical geometry using ab-initio DFT with LDA density functional as implemented in SIESTA code (see appendix A for further details). The geometry relaxation was done towards an energy minimum until the residual forces were smaller than 0.02 eV/Å. The *ab initio* relaxation confirms that the structure is stable, at least corresponding to a local minimum of the DFT energy landscape of Na380 .

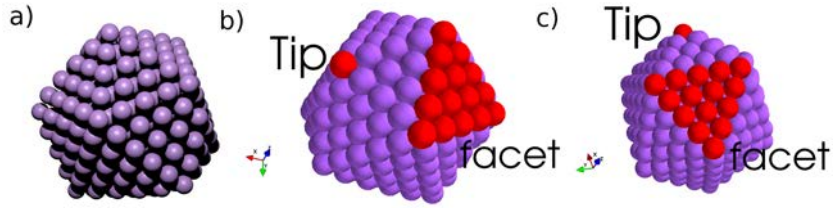

Figure 3.2.1: Atomistic structure of the Na_{380} cluster. The facet and tip atoms used to define the plasmonic gaps of different structures in our calculations are highlighted in red on panels (b) and (c) for two orientations.

To model a plamonic cavity, we brought two Na_{380} clusters in a close proximity. As shown in Figure 3.2.2, we examined three mutual orientations of the clusters forming the nanogaps. One of the nanogaps is formed by two parallel planar facets in a facet-to-facet configuration [Figure 3.2.2 panel (a)]. Another configuration, the tip-to-facet, is formed by a planar facet and a tip [Figure 3.2.2 panel (b)]. The last configuration is constituted of two tips facing each other in a tip-to-tip configuration [Figure 3.2.2 panel (c)]. In the following, we will study the response of these systems as function of the distance d_{sep} between the two clusters. The distance d_{sep} is defined as the minimal distance between atoms located in different clusters.

The ground-state calculations for the Na_{380} cluster and dimers were preformed using DFT as implemented in the SIESTA code (see app. A for methodological details). The resulting Kohn-Sham orbitals and energies were used as an input for the TDDFT calculations of the optical response using the iterative scheme described in section 2.3.

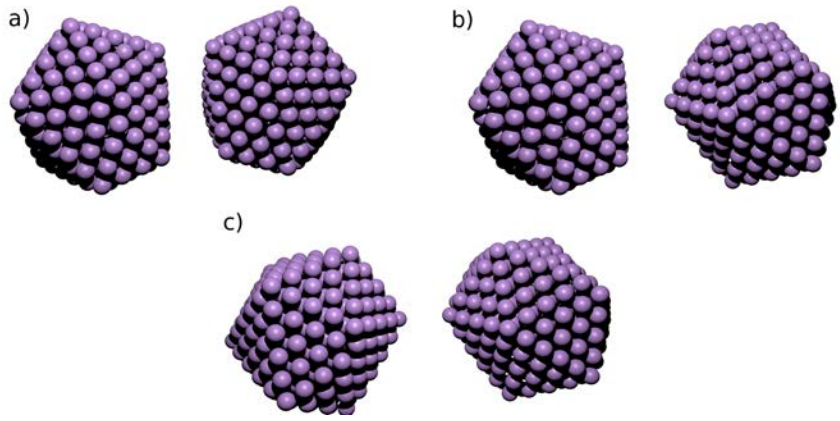

Figure 3.2.2: Structures of the three plasmonic gaps studied for a distance between the clusters of 10 Å. Panel (a) shows the facet-to-facet geometry, panel (b) the tip-to-facet and panel (c) the tip-to-tip.

We used the local density approximation [33, 34] (LDA), norm-conserving pseudo-potentials [122] to effectively describe core electrons, and a double-ζ polarized basis set of numerical atomic orbitals generated using an *energy shift* of 10 meV [52]. The fineness of the real-space grid used to compute the Hartree and exchange-correlation contributions to the energy and Hamiltonian corresponds to a plane-wave cutoff of 130 Ry [2].

3.3 Atomic-Scale Lightning Rod Effect

3.3.1 Induced Field Localization of a Single Cluster

Using the cluster geometry described in Figure 3.2.1, we calculated the response of the Na_{380} perturbed by an homogeneous (in space and time) external electric field. As explained in the chapter 2, the homogeneous external field approximates the optical perturbation and gives rise to the notion of the optical polarizability (eqn. 2.91). We computed the dipole polarizability of the single Na_{380} cluster in a range of frequencies from 0 to 8 eV to capture the LSP response of the cluster. In Figure 3.3.1 we present the diagonal components of polarizability tensor (eqn. 2.91) and the orientationally averaged polarizability $< P >= (P_{xx} + P_{yy} + P_{zz})/3$. The symmetry of the cluster is not perfect, therefore, the polarizability is slightly different along the Cartesian axes, but the differences are barely discernible on the plots. The symmetry of the dipole

polarizability will be used in chapter 5 to reduce the computational load of the iterative procedure.

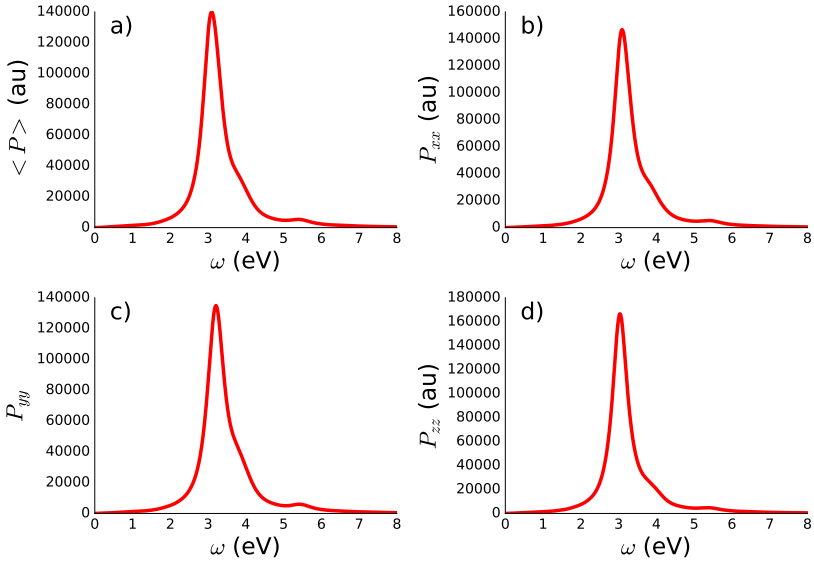

Figure 3.3.1: Polarizability of the Na_{380} cluster. Panel (a) shows the average polarizability $< P >= \frac{1}{3}(P_{xx} + P_{yy} + P_{zz})$. Panels (b), (c) and (d) show the polarizability along the respective direction xx, yy and zz. Since the symmetry of the cluster is not perfect the polarizability is slightly different along the axes.

In this chapter, we theoretically show how the atomic features at the surface of plasmonic nanoparticles do localize the electromagnetic fields down to atomic-scale dimensions, showing resonant (plasmonic) and non-resonant (lightning-rod effect) field enhancement (eqn. 2.97). With the help of our TDDFT calculations, we show near-fields maps of plasmonic nanoparticles which produces atomic hot spots superimposed to the plasmonic resonance. This is the atomic-scale analogue of the lightning-rod effect [123–125], which can be understood as the atomistic limit of the classical field divergence at an infinitely sharp metallic tip. Indeed, the sharpest possible structure is given by a tip ending with a single atom. In such small scale, the quantum mechanics determines a limit for the attainable field enhancement. When the atomic-scale enhancement is combined with the overall field enhancement given by the plasmon resonance, the very intense and localized atomic-scale hot spots is obtained. The presence of such hot spots has been proposed and even exploited experimentally in subnanometer-resolved sur-

face enhanced optical spectroscopies [126–130]. An accurate description of the physical properties of atomic-scale local near-fields has been elusive to date due to the limitations of classical and quantum description that even if capable of correctly reporting the main trends of the response, are typically based on strong approximations either on the electromagnetic boundary conditions or the atomic structure of surfaces. Our calculations provide a faithful description of the actual near-field induced in metallic interfaces considering realistic atomic structures, unambiguously resolving the near-field features at the hot spots with unprecedented resolution and detail. We can thus quantify the level of confinement of the near-fields relevant in complex photochemical processes and near-field spectroscopies. Our results indicate that, at the vertices and edges formed at the contact of different facets, it is possible to localize plasmons with subnanometric resolution. Figure 3.3.2 shows the confinement of the field at the vertices of the cluster very clearly, and depending the orientation of the external field, different tips localize the field. The extreme plasmon localization reported here already allowed the exploitation of novel probes, capable to provide ultraresolution and reach access to information on single molecules [131].

Figure 3.3.2 shows the local near-field distribution around the Na_{380} cluster for different polarizations of the incident field of amplitude E_0, both at the dipolar plasmonic resonance energy [panels (a-c)] and out of resonance [panels (d-f)]. We show the data in the (y, z) plane passing through the center of the cluster for two different incident linear polarizations [along y axis in panel (a) and along z axis in panel (b)]. As observed in the plots, when the atomistic structure is accounted for, the near-fields dramatically depend on the cluster orientation with respect to the polarization direction. Even if the general dipolar pattern of the induced fields is preserved, the underlying icosahedral geometry of the atomic arrangement can be clearly recognized. Most importantly, we can undoubtedly identify sub-nanometric 'hot-spots' characterized by strongly localized fields at the metal-vacuum interface. The enhancement at these 'hot-spots' is not dramatically larger than that of the overall background of the plasmon-enhanced near-fields, but it carries a very distinctive localization with it. The 'hot-spots' of the Na_{380} cluster in panels (a) and (b) are related to the atomic-scale vertices and edges of the icosahedron cluster structure. Obviously, a quantum (or classical) calculation that considers smooth surfaces and thus ignores the atomistic nature of the clusters cannot address these subnanometric features in the near-fields, and misses the description of atomic-scale field localization (we will see in section 3.4, how classical methods can reproduce the 'hot-spots' of atomistic structures). This is illustrated in panel (c) where the results based on the jellium model (JM) for the perfectly spherical cluster are shown for comparison. In this case, the induced fields are independent of the cluster orientation with respect to the incident field, and feature the typical smooth dipolar pattern of the plas-

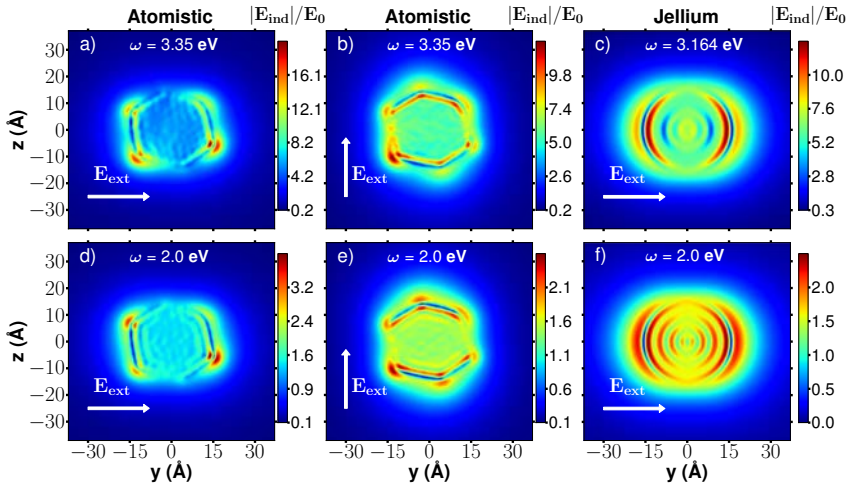

Figure 3.3.2: Induced-field enhancement, $|E_{ind}|/E_0$ with E_0 the amplitude of the incident field, in the proximity of a Na_{380} cluster and a jellium sphere ($r_s = 2.12$ Å) of radius $R = 15.57$ Å. The induced field is represented in the (y, z) plane, that passes through the center of the cluster/sphere. Top panels show the results at the dipolar plasmonic excitation (at 3.35 and 3.16 eV, for the atomistic and jellium models, respectively), (a) for a polarization of the external field along the y-axis, (b) along the z-axis, and (c) along the y-axis (although the response is isotropic in the jellium case). Panels (d-f) show the same information as (a-c) for an energy of the exciting field out of resonance (2 eV).

mon induced along the polarization direction (y-axis chosen here). While outside the cluster the TDDFT-JM description is very similar to the classical Mie [132] results for a metal sphere described with a Drude dielectric function, quantum effects are apparent inside the cluster where the screening of fields is accompanied by Friedel-like oscillations [133].

Remarkably, in the atomistic results we observe an atomic-scale lightning rod effect [123] that can be related to the macroscopic lightning rod effect [124, 134] resulting from the classical field divergence at infinitely sharp tips. The atomistic structure of the material naturally sets a quantum constraint to the notion of "infinitely sharp" since, obviously, an effective curvature radius cannot be smaller than that given by the electron density profile of the single atom. The local dipoles responsible for the subnanometric field confinement are formed by the collective response of the protruding groups of atoms screened by the rest of the cluster. Therefore, at resonance excitation conditions, the near-field structure of the cluster, as obtained from our atomistic calculations, can be understood as

a combination of two effects: (i) The overall plasmonic near-field enhancement at the dipolar mode, and (ii) the atomic scale lightning rod effect which arises because of the presence of vertices and edges between the atomic planes forming the cluster surface, allowing to further focus the energy into an extremely small area. We can thus establish an analogy with the macroscopic self-similar plasmonic nanoantennas, where larger antennas produce further enhancement on the smallest ones, like in a plasmonic lens [135–137]. Here, the sub-nanometer hot spots induced around atomically sharp features are fed in a cascade fashion by the plasmonic field of the larger and smoother nanometric plasmonic system (hosting particle or dimer).

The lightning rod effect is also present in the off-resonant response of the metal cluster. We illustrate this in Figure 3.3.2 (d-f) where we plot the near-field distribution around the Na_{380} cluster, obtained for incident plane wave irradiation off-resonance with the plasmonic dipolar mode. Except for this change of wavelength, we used the same conditions regarding polarization, geometry, and atomistic or jellium modeling of the cluster, as in panels (a-c). In the off-resonance situation, the atomic-scale hot-spots are still present for the Na_{380} cluster for both polarizations, providing a substantial local enhancement that extends a few Ångstroms from the cluster surface. In this case, the lightning rod effect is isolated from the plasmonic effect, even though overall, in the absence of the resonant dipolar plasmon mode, the induced near-fields are several times weaker, which also holds at the hot-spots.

3.3.2 Electric Field Enhancement of Sodium Dimers

In the following, we emphasize the importance of atomic-scale features in a canonical structure in plasmonics—the metallic nanogap. By placing two metallic nanoparticles together, we can create a plasmonic nanogap where the coupling of plasmonic modes generates new hybridized solutions that are red shifted with respect to the original resonances of the individual particles [11, 138]. In Figure 3.3.3 we analyze the importance of the atomistic details of the nanogap by selecting results obtained for three main configurations that present different terminations of the interfaces at the gap: (i) facet-to-facet, (ii) tip-to-facet, and (iii) tip-to-tip. For completeness, we also consider the case of a dimer formed by two jellium spheres, thus forming a nanogap bound by smooth surfaces. The spectral behavior of the nanogap resonances as a function of the interparticle separation distance, d_{sep}, is displayed in Figure 3.3.3 (a-d), where we plot the absorption cross-section, σ_{abs}, for each case: (a) facet-to-facet, (b) tip-to-facet, (c) tip-to-tip, and (d) jellium. The polarization of the incident field is set along the dimer axis.

The corresponding atomistic structure of the different nanogap models are represented on Figure 3.3.3 (e-g), along with the distribution of the induced near-

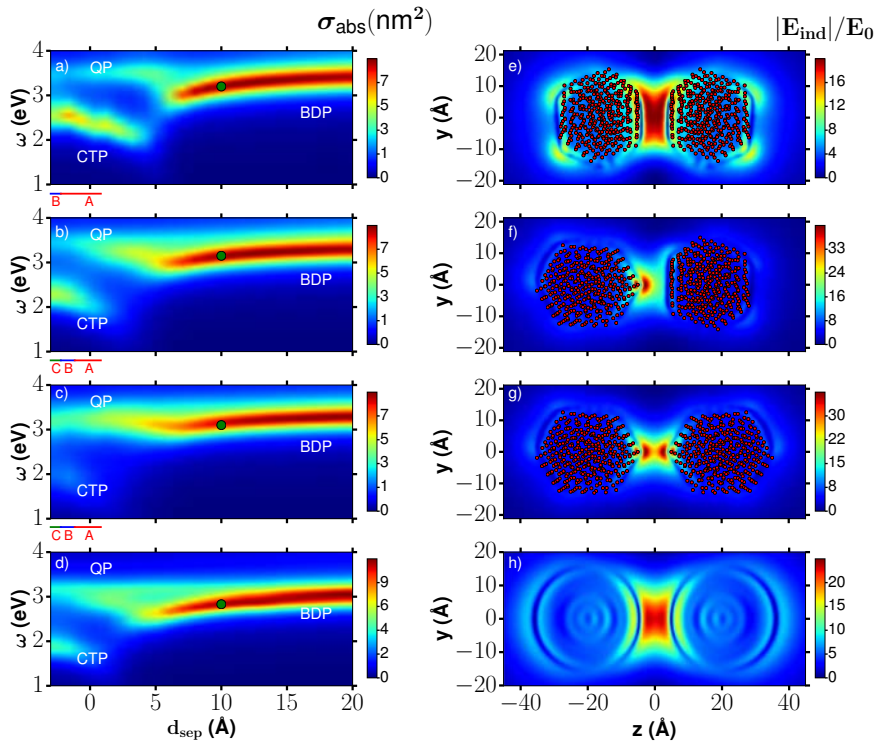

Figure 3.3.3: Panels (a-d) show the spectral evolution of the absorption cross-section of the plasmonic dimers depicted in (e-g), and a dimer of jellium spheres (h), for a polarization of the incident field along the dimer axis as a function of separation distance between the particles, d_{sep}. The hybridized bonding dipolar plasmon (BDP), the charge-transfer plasmon (CTP) mode and the quadrupolar (QP) are identified on the spectra. Separation distances lower than 1 Å, and negative distances represent overlapping clusters and have been modeled in (a-c) by modified geometries in which atomic layers of one of the clusters are subsequently removed (region A, one layer removed; region B, 2 layers; region C, 3 layers). Panels (e-h) show the distribution of the local induced-field produced in a longitudinal cross section ($x = 0$ plane) of the dimer for an energy in resonance with the BDP and for a separation distance of 10 Å: (e) the gap is formed by a facet-to-facet junction, (f) facet-to-tip, and (g) tip-to-tip configurations. In (h) the same situation for a dimer described by the jellium model is displayed.

field for an interparticle distance of 10 Å, evaluated at the resonance frequency for each type of gap. In the case of the atomistic calculations, the separation distance, d_{sep}, is measured between the closest atoms across the gap. Separation

distances smaller than 1 Å, as well as negative distances (corresponding to the case of overlapping clusters [11]), were modeled using modified structures in which atomic layers are successively removed from one of the clusters. For a consistent comparison, in the jellium case we also consider the separation distance as defined from the hypothetical surface atomic layers rather than from the jellium edges present in JM.

In Figures 3.3.3 (a-d) we recognize clearly the evolution of the hybridized Bonding Dimer Plasmon (BDP) for each gap configuration: the BDP red shifts as the separation distance between the nanoparticles decreases [11, 92, 93]. Consistent with previous descriptions, this trend holds down to separations of the order of a few Ångstroms. When the particles are even closer together, the system enters a new regime due to the emergence of the tunneling current across the gap at optical frequencies [118, 119, 139]. In the quantum tunneling regime, the BDP is progressively screened, and it disappears from the spectrum [118, 119, 139]. For increasing current across the gap, charge-transfer plasmons (CTPs) emerge [140]. The CTP corresponds to the polarization of the entire dimer with interparticle charge transfer. Despite the common general trends for the three atomistic calculations, remarkable differences arise with regard to the exact separation distance where the quantum effects occur. For the same separation distance d_{sep}, in the facet-to-facet configuration the tunneling current density is larger because of the larger contact area. Thus the BDP disappears and the CTP emerges at the largest separation distances, (6 Å and 4 Å respectively). In the configurations characterized by the presence of a tip, the tunneling current is confined mainly to the area around the tip, thus the overall tunneling current is smaller. As a consequence, smaller separation distances, d_{sep}, are required for the quenching of the BDP and appearance of the CTPs in such cases, as clearly observed in Figures 3.3.3 (b) and (c).

We now explore the influence of the different atomistic configurations of the plasmonic gap on the near-field distribution at the resonance position. In Figures 3.3.3 (e-h) the induced near-fields are shown in the (y, z) plane of the dimer passing through the centers of the nanoparticles for the facet-to-facet (e), tip-to-facet (f), tip-to-tip (g), and jellium spherical (h) configurations. The width of the gap is set in all the cases to $d_{\mathrm{sep}} = 10$ Å, with incident light in resonance with the hybridized BDP corresponding to the position marked with a green dot on the spectra to the left. The Coulomb coupling between induced charges of opposite signs across the gap leads to a strong localization and enhancement of the near-fields in the gap. This effect is widely exploited in surface-enhanced spectroscopies and microscopies. Overall, the nanometric near-field distributions obtained in the full atomistic calculations at the BDP frequency show similar gross features to those in the JM calculations. However, the exact atomistic structure of the junction determines the details of the near-field distribution,

and in particular the appearance of the extremely localized hot spots. As observed in Figure 3.3.3 (e), the gap characterized by a facet-to-facet configuration features a well-defined and rather homogeneous field enhancement that extends over the entire gap, as expected from a scaled parallel plate capacitor. The lateral localization of the hot-spot between the particles is thus determined by the corresponding nanometric facet size. Albeit much less intense, atomic-scale hot spots can be also identified at the edges and vertices of the different facets of the cluster surfaces, both near and opposite to the plasmonic gap. These are due to the atomic-scale lightning rod effect, similar to that found in Figure 3.3.2 for the single particle. Compared to the JM with a perfectly spherical geometry, atomic-scale features between the cluster facets increase the Landau damping of the BDP and thus broaden the plasmon resonance peaks.

A remarkable situation is achieved when exploiting the atomic-scale lightning rod effect in the tip-to-facet or in the tip-to-tip configurations in the gap [Figure 3.3.3 (f) and (g)]. In such situations, the tip-induced enhancement is superimposed on the already intense background field of the plasmonic resonance, producing a further increase of the value of the enhancement, and more importantly, an extreme localization of this local near-field down to an extension of a few Ångstroms. This extreme confinement of the fields is missed in the JM model that assumes a smooth density profile, as shown in Figure 3.3.3 (h). By means of our realistic atomistic calculations, we have thus shown that atomic-scale hot spots are possible, and they may be relevant to allow super-resolution in a variety of experimental near-field techniques [126, 128, 141].

To analyze the field enhancement induced at each of the plasmonic nanogaps quantitatively, we show in Figure 3.3.4 the maximum induced near-field enhancement at resonance in the middle of the gap, $|\mathbf{E}_{\rm ind}^{\rm max}|/\mathrm{E}_0$ [panel (a)], and the effective localization area of the near-field, $\mathcal{A}$ [panel (b)], as a function of the gap separation $d_{\rm sep}$. $\mathcal{A}$ is defined according to the following expression:

$$\mathcal{A} = \frac{1}{h}\int_V \frac{|\mathbf{E}_{\rm ind}(x,y,z)|^2}{|\mathbf{E}_{\rm ind}^{\rm max}|^2} dV, \tag{3.1}$$

where $|\mathbf{E}_{\rm ind}(x,y,z)|$ is the modulus of the induced field in a thin slab of volume V and thickness h=0.63 Å in the z direction, with $z = 0$ at the center of the gap. $|\mathbf{E}_{\rm ind}^{\rm max}|$ is the maximum value of the field in the integration volume. Therefore, $\mathcal{A}$ provides a measure of the effective area in which the induced field is localized within the middle of the gap.

We have chosen to plot and analyze the field distributions at those resonance energies that produce the largest maximum of the induced near-field at each configuration. Thus, for the tip-to-facet and tip-to-tip gaps we follow the BDP-QP mode around 3 eV, whereas for the facet-to-facet configuration data, for $\mathrm{d_{sep}} \leq$ 5 Å we follow the CTP mode appearing at lower energies. The local near-fields are

obtained for the same configurations and light incidence as in Figure 3.3.3. The maximum enhancement is found in all the cases for $d_{\text{sep}} \approx 7$ Å [see Figure 3.3.4 (a)].

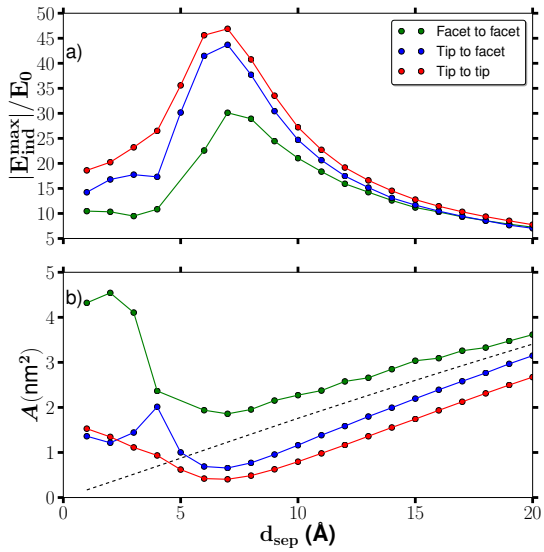

Figure 3.3.4: (a) TDDFT calculations of the maximum enhancement of the local induced-field $|\mathbf{E}_{\text{ind}}^{\text{max}}|/\text{E}_0$ at the center of a gap between two particles showing different atomistic configurations, as a function of the separation between the particles forming the gap, d_{sep}. The separation is defined as the distance between the most protruding atoms in both clusters. The green line stands for the facet-to-facet configuration in the gap, the blue line stands for the tip-to-facet configuration and the red line stands for the tip-to-tip configuration. (b) Effective localization area $\mathcal{A}$ of the local field in the midplane of the gap as defined in the text [eqn. (3.1)] for each of the three configurations. As a reference, the localization of the BDP for a pair of spherical particles given by a classical calculation is displayed as a dashed line. The plotted data correspond to the resonance energies that produce the largest maximum of the induced near-field for each configuration and distance. For the facet-to-facet case this corresponds to the CTP mode for $d_{\text{sep}} < 5$ Å. For the the tip-to-facet and tip-to-tip gaps we follow the BDP and QP modes around 3 eV. The different dependence of $\mathcal{A}$ on d_{sep} for the BDP and QP modes is clearly visible in the singular behavior of the $\mathcal{A}$ data around 4 Å for the tip-to-facet case, which is almost undetectable in the more gradual BDP-QP transition of the tip-to-tip gap.

The electron tunneling neutralizes the plasmon-induced charges at the metal surfaces across the gap, and quenches the induced fields [118, 119] when the gap size is reduced below $d_{\text{sep}} \approx 7$ Å. For larger separations, the coupling between the plasmons of the individual particles becomes smaller thus the field enhancement

progressively decreases, and the differences due to the atomic-scale features are also attenuated. When atomic-scale tip(s) is (are) present in the junction, the maximum near-field enhancement is about 1.5 times larger than that of the facet-to-facet configuration [red and blue lines vs. green line in Figure 3.3.4 (a)], emphasizing the importance of the fine details of the gap.

Together with the absolute value of the field enhancement, the confinement is an aspect of particular interest in nanophotonics. In Figure 3.3.4 (b), we plot the effective localization area, $\mathcal{A}$, of the BDP for each atomistic configuration. The results are plotted in Figure 3.3.4 (b) as a function of separation distance, for the same excitation wavelengths used in Figure 3.3.4 (a). As expected, the three different atomistic configurations show maximum localization of the BDP mode at separations of about 7 Ångstroms, corresponding to the separation of maximal enhancement described above. For smaller separation distances, when the tunneling current is established, the field is expelled out from the gap and thus becomes less localized [126]. The tip-to-tip morphology, for which the lightning rod effect is more pronounced, provides the strongest localization among all. The minimum $\mathcal{A}$ in this case is 0.4 nm^2, clearly indicating that the plasmonic fields can be localized down to lateral dimensions of a few thousandths of the incident wavelength with the help of an atomic feature. This value of $\mathcal{A}$ is up to 4 times smaller than that for the facet-to-facet configuration, for the same $d_{\text{sep}} = 7$ Å.

For reference purposes, we also plot in Figure 3.3.4 (b), as a black dashed line, the localization corresponding to a classical calculation of the BDP in a gap formed by spherical particles of the same size, and characterized by a Drude-like response that corresponds to the same electronic density as in the atomistic calculations. As observed in the figure, the localization in this case tends linearly to zero for small d_{sep}. This unphysical result is due to the lack of dynamical screening and tunneling in the classical description. It is interesting to note that all the systems show a linear dependence of the localization with separation distance, as the gap is opening. This is a reminiscence of the two effects involved: the overall plasmonic effect, plus the atomistic effect. The classical estimation in spherical particles indeed establishes a reference for the behavior of the localization at the different atomistic gaps, but when an atomic-scale tip is present in the gap, the linear dependency is pushed below this classical result (larger slope of red and blue lines). However, for the case of a facet-to-facet gap, the linear dependency shows a smaller slope, setting values of the localization area that exceed those of the classical confinement. In this case the minimal localization area of the field is approximately given by the surface of the facet, as one would expect for a flat capacitor. Therefore, our classical result for the induced-field localization establishes a good benchmark to distinguish between subplasmonic and plasmonic localization, depending on whether the linear tendencies show a more or less pronounced change, respectively, compared to the classical reference

of spherical particles.

As a further remark, it should be noted that the presence of subnanometric hot spots would only weakly affect the effective localization area $\mathcal{A}$, as defined by eqn. (3.1), in large plasmonic systems because the integral will be dominated by the overall plasmonic field structure in the gap. This is actually one of the reasons why plasmonic enhancement is a robust and reliable tool in many standard field-enhanced spectroscopies. Nonetheless, such local behavior at the atomic scale can be important to determine the precise properties of the near-field at particular positions, probed, for example, by molecular targets [127, 130] or by electron emission [142], which are extremely sensitive to these spatial inhomogeneities independently of how large the plasmonic background is.

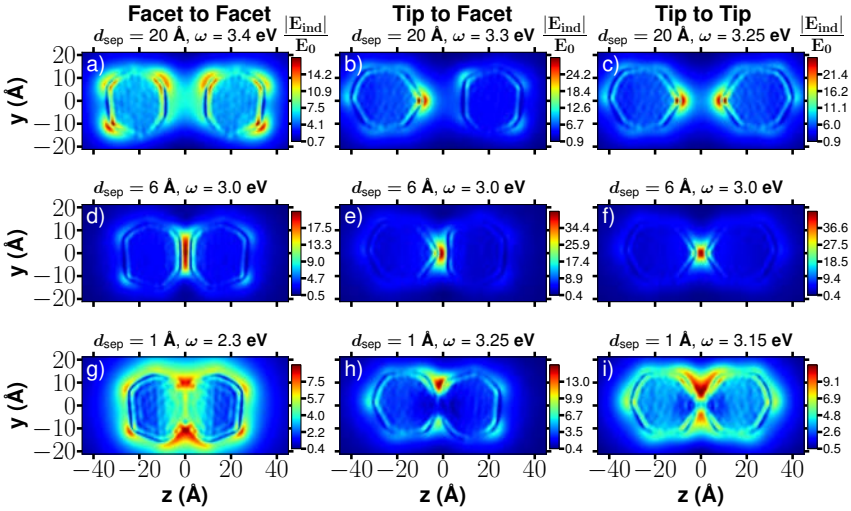

Figure 3.3.5: Local induced-field enhancement in a transversal cross section that contains the axis of a Na metallic dimer for the case of a facet-to-facet configuration at the gap (left column), tip-to-facet configuration (middle column) and tip-to-tip configuration (right column). From top to bottom, three cases of decreasing separation distance are shown for each case: d_{sep} = 20 Å (top row, a-c), d_{sep} = 6 Å (middle row, d-f) and d_{sep} = 1 Å (bottom row, g-i). The field is always plotted at the frequency of the most intense resonance in the absorption cross-section of the dimer. This corresponds to the BDP mode in most cases, except for the facet-to-facet and tip-to-face cases at the closest separation, that corresponds to the CTP mode [panels (g) and (h)].

The evolution of the near-fields response with the gap size d_{sep} is further illustrated in Figure 3.3.5 and Figure 3.3.6. In Figure 3.3.5 we plot the distribution of induced near-fields in the (y, z) plane containing the centers of the nanoparticles.

The results are shown for the facet-to-facet (left column), tip-to-facet (middle column), and tip-to-tip (right column) configurations of the nanogap. Three separations, $d_{\text{sep}} = 20$ Å (top row), $d_{\text{sep}} = 6$ Å (middle row), and $d_{\text{sep}} = 1$ Å (bottom row), are chosen here to represent respectively weak interaction, strong interaction and strong tunneling regimes. For the largest separation, $d_{\text{sep}} = 20$ Å, the coupling between nanoparticles is weak, therefore the near-fields around each nanoparticle of the dimer resemble those of the individual particles, as presented in Figure 3.3.2. Nevertheless, stronger fields at the facing surfaces across the gap can be clearly observed, indicating the onset of the hybridization of the BDP.

Atomic-scale hot-spots are visible all over the nanoparticle surface, particularly in regions associated with atomic edges at the contact of the crystalline facets. These hot-spots are apparent for the flat-facet gap (top row, left), but are even more pronounced in the presence of a tip-like geometry pointing towards the junction, and aligned with the polarization direction (middle and right). As the particles get closer, d_{sep} =6 Å (middle row), the field enhancement at the gap becomes very intense (notice the absolute value of the corresponding scales). For the facet-to-facet situation (middle row, left column) the enhancement is nearly homogeneous inside the gap as a consequence of the flat-surface capacitor geometry. In contrast, when a tip-like configuration is present in the gap, it leads to a particularly strong field enhancement and to clear subnanometer localization at the center of the gap, consistent with the results of Figure 3.3.4. For very small separation distances (bottom row), the electronic densities of the two particles strongly overlap, essentially producing a nanometric neck of continuous electron density. Therefore, the region of enhanced field is expelled to the edges of the junction [139, 140]. This is accompanied with an overall weakening of the fields in the junction region, which eventually become comparable in intensity to the hot spots at other locations of the dimer surfaces.

The evolution of the field confinement in the gap as a function of separation distance, d_{sep} and the corresponding change of the localization area $\mathcal{A}$ is illustrated in Figure 3.3.6, where the field enhancement is shown in the (x, y) mid-plane between the two particles for each configuration (facet-to-facet on the left column, tip-to-facet on the middle column, and tip-to-tip on the right column). When the particles are far away from each other ($d_{\text{sep}} = 20$ Å), a relatively broad spatial profile of the plasmonic near-field is obtained (top row). This profile is mainly determined by low-order multipoles at each nanoparticle so that the features due to the specific atomistic structures of the nanoparticle surfaces are weak. For smaller separation, $d_{\text{sep}} = 10$ Å, the profile of the near-fields reflects the atomistic structure of the nanoparticle surfaces across the gap, showing a triangular shape for the facet-to-facet configuration, a round spot for the tip-to-tip configuration, and a round spot on top of a triangular background for the tip-to-facet configuration. As expected from the results in Figure 3.3.4, the

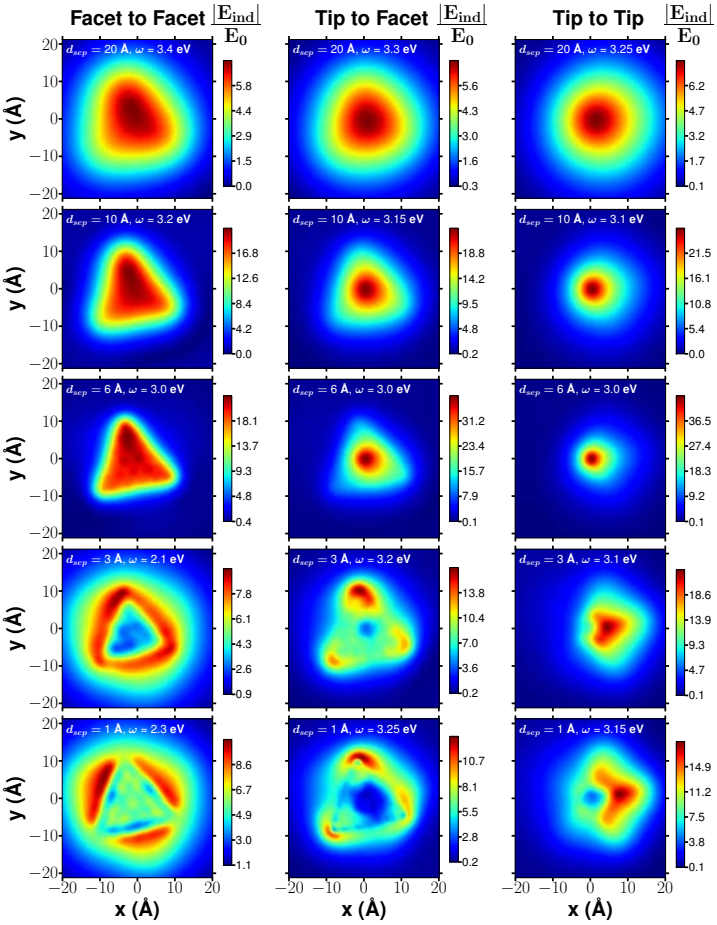

Figure 3.3.6: Local induced-field enhancement at resonance in the midplane of the gap between two Na_{380} clusters for our three configurations, facet-to-facet gap (left column), tip-to-facet (middle column) and tip-to-tip (right column). From top to bottom each case shows a decreasing separation distance for each configuration, from d_{sep} =20 Å (largely separated particles, on the top row) to d_{sep} =1 Å (interpenetrating situation on the bottom row). The influence of the atomic scale features at the nanogaps is directly noticeable.

tip-to-tip configuration corresponds to the strongest field confinement with the smallest spot size reduced to atomic dimensions, below 1 nm^2 for $d_{\mathrm{sep}} \approx 6$ Å. For the parallel capacitor facet-to-facet configuration, the spot profile and size change only slightly when d_{sep} is reduced from 10 Å to 6 Å, and the tip-to-facet configuration features the intermediate situation (see also Figure 3.3.5). We thus show here that the widely accepted picture of the overall reduction of the localization area $\mathcal{A}$ for smaller d_{sep}, as obtained from previous studies for smooth particles [118, 139, 143], has to be taken with caution, as it can be altered by the atomistic structure of the gap. For separation distances d_{sep} below 6 Å (lower rows), the tunneling current expels the fields from the middle of the gap. This effect is particularly strong for the CTP mode in the facet-to-facet configuration.

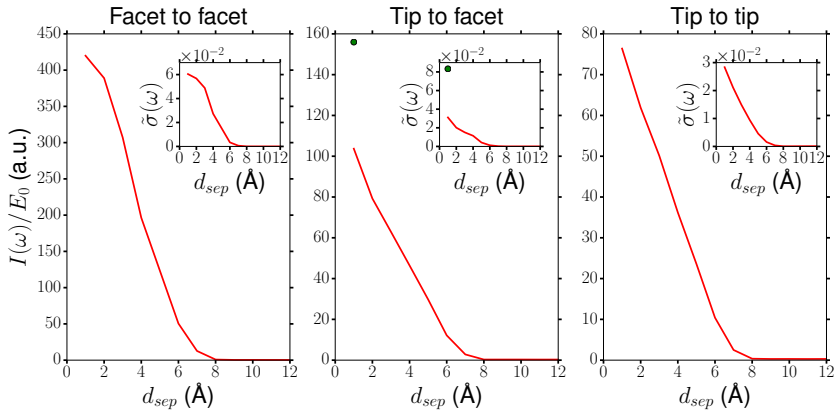

Figure 3.3.7: Amplitude of the electron current (in atomic units and normalized by the external field) flowing between the two Na_{380} clusters as a function of the interparticle distance d_{sep} for the three plasmonic gaps considered here. The continuous lines represent the data computed at the frequencies of the most intense resonances of the absorption cross-section show in Figure 3.3.3. At sufficiently large distances this corresponds to the BDP mode for three configurations. For the facet-to-facet case at $d_{\mathrm{sep}} < 5$ Å we plot the current associated to the CTP mode; while for the tip-to-facet and tip-to-tip gaps we follow the QP mode around 3 eV at small values of d_{sep}. In the tip-to-facet case we also show for comparison (green dot) the current calculated for $\omega \sim 1.9$ eV at $d_{\mathrm{sep}} = 1$ Å, i.e., at the onset of the CTP mode for this configuration. The insets of each panel show an estimation of the conductivity, $\tilde{\sigma}$, as a function of separation distance for each configuration considered. This conductivity is obtained as a ratio between the effective current density, and the local field at the gap.

The link between the appearance of the CTP mode (and the quenching of the BDP mode) and the increase of the electron current flowing through the gap can be clearly established with help of Figure 3.3.7. In this figure we present the amplitude of the electron current divided by the external field as a function of

the interparticle separation d_{sep}. The currents are computed at the frequencies of the most intense resonances of the absorption cross-section (see Figure 3.3.3) for each distance. At sufficiently large distances this frequency always corresponds to the BDP mode for the three configurations. However, for $d_{\text{sep}} < 5$ Å we plot the current associated to the CTP mode for the facet-to-facet case, while for the tip-to-facet and tip-to-tip gaps we follow the QP mode around 3 eV for those small values of d_{sep}. The currents are calculated, using the induced electron density at a given frequency, as the charge crossing a surface bisecting the gap by unit of time. As expected, in all cases the current grows steeply as d_{sep} is reduced. The strongest currents are obtained at the frequencies and distances where the well-defined CTP mode appears (left panel for the facet-to-facet configuration, and filled circle in the middle panel for the tip-to-facet configuration). For example, at small separation distance d_{sep} the current is approximately four times larger for the CTP mode in the facet-to-facet case than that computed for the QP mode in the tip-to-facet geometry. In the tip-to-facet case, we also show (filled circle) for comparison the current computed at $\omega \sim 1.9$ eV and $d_{\text{sep}} = 1$Å, i.e., at the onset of the CTP mode. It is a $\sim 50\%$ larger than the current for the QP mode at the same distance. This clearly indicates that, for the same geometry and gap separation, the current is considerably larger in the CTP mode than in the QP mode. It is also interesting to note that the current computed at the onset of the CTP mode for the tip-to-facet configuration is almost identical to the current computed at the onset of the CTP mode mode for the facet-to-facet case (although d_{sep} is in the range 4-5 Å in the latter case and 1 Å in the former). This is to be expected, since the establishment of the CTP mode depends on the possibility of charge to be transferred through the gap. Another interesting conclusion from our analysis is that an atomic contact formed by a single Na atom (like in our "tip configurations") is insufficient to sustain the current flow necessary for the appearance of a fully developed CTP mode, consistent with the results of Figure 3.3.3.

Finally, we also show in the insets of Figure 3.3.7 an estimation of the conductivity, $\tilde{\sigma}$, as a function of separation distance d_{sep} for each configuration considered. The conductivity $\tilde{\sigma}$ is obtained as a ratio between the effective current density, and the local field at the gap. The effective current density is obtained by dividing the current intensity $I(\omega)$ by the minimum localization area $\mathcal{A}$, defined in eqn. (3.1), while the local field is estimated as a product of the external field and the maximal local field enhancement. The minimal localization areas $\mathcal{A}$ and the maximal local field enhancements $\mathbf{E}/\mathbf{E}_0$ are shown in Figure 3.3.4, on panels (a) and (b), correspondingly. The currents and conductivities estimated in this way for the facet-to-facet configuration (inset of the left panel in Figure 3.3.7) are consistent with those recently reported between two large jellium spheres representing Na clusters [144].

3.4 Comparison with Classical Methods

As we have been describing in the previous section, atomistic *ab initio* methods can provide a very accurate response of a system under an external perturbation, specifically, the polarizability and the induced field enhancement distribution. However, because of their high computational cost, these methods are limited by the size of the systems they can be applied for (typically a few hundreds atoms). Light scattering of nanoparticles of arbitrary shape and size is usually well addressed within a classical electrodynamics framework, by solving Maxwell's equations for specific compositions, morphologies and environments [48, 140]. When the size or the separation distance between plasmonic nanoparticles becomes of the order of a few nanometers or even smaller, the quantum nature of the electrons emerges due, among others, to the particle-size effect in the electron confinement [115, 145], the inhomogeneous dynamical screening of the electrons response, the electron spill-out at the metal interfaces, the presence of atomistic inhomogneities, or even the activation of quantum tunneling across subnanometer interparticle gaps. All of these effects are initially not included in typical local classical electro-dynamical descriptions of the optical response, and different levels of approximation have been adopted to address their influence in the response in extended classical models [139]. Nevertheless, only an atomistic *ab initio* method is suitable to properly address the quantum physics that arises for small particle sizes that we study here. Furthermore, thanks to progress we did during this thesis, we are able to perform calculations for very large particles (containing a few thousands of atoms) using *ab initio* atomistic method (see chapter 5). In this section, we compare our *ab initio* calculations for the Na_{380} cluster and cluster dimers presented previously with classical calculations performed by our colleagues [146].

3.4.1 The Boundary Element Method

The electrodynamic calculations have been performed using the boundary element method (BEM) [147]. Within BEM, particles of arbitrary shape is treated. The particles and surrounding media are assumed to be homogeneous with given dielectric permeabilities. Moreover, the particles are assumed to have abrupt boundaries. It is worth mentioning that this model requires only the discretization of the boundary surfaces, instead of the whole volume of the dielectric regions considered. For the size of the nanoparticles considered in this study, which is below the intrinsic mean free path of conduction electrons in bulk metals, surface scattering becomes very important. In order to account for the surface scattering, we included a correction to the free-electron model of the cluster's dielectric function (Drude model) in the calculations. In the classical standard approach it is assumed that the surface scattering effects lead to a reduced effective mean

free path L_{eff}, which adds a damping factor in the Drude dielectric function of the bulk metal. When a peculiar reflection of electrons at the boundaries is assumed, as in the so-called Billard model [148, 149], the effective mean free path is given by $L_{\text{eff}} = 4V/A$, where V and A are the volume and area of the particle respectively [150]. Therefore, within the Drude model the dielectric function is given by

$$\varepsilon(\omega) = \varepsilon_\infty - \frac{\omega_p^2}{\omega^2 + i\omega(\gamma_{\text{d}+\frac{v_f}{L_{\text{eff}}}})}, \tag{3.2}$$

where v_f is the Fermi velocity, which is $v_f = 1.07\times10^6$ m/s for Na, and the intrinsic damping term $\gamma_{\text{d}} = 27.6$ meV. Electron-hole excitations and other quantum effects such as electron tunneling in close interparticle gaps are not considered in the Drude model. Nevertheless, we have preserved the main geometrical features of the sodium cluster such as the positions of apexes, edges, and facets, and their relative orientations, to keep the shape as close as possible to that of the particle used for the *ab initio* calculations. With this idea in mind, we observed that the regular icosahedron fits the requested conditions. In Figures 3.4.1 (a) and (b) we show the particles used for both atomistic and continuous calculations respectively. The simulations were carried out with the MNPBEM toolbox [151] implementation of BEM.

3.4.2 Na_{380} Cluster and Dimers with BEM

As for the *ab initio* calculations, we looked at the absorption cross section and near-field of single particle (Figure 3.4.1) and dimers using the BEM theory and compare the results to the *ab initio* one [83]. For BEM, a continuous particle with icosahedral symmetry was used for the calculations as we displayed in Figure 3.4.1 (b). The icosahedral particle is circumscribed into a sphere of radius $r = 1.85$ nm (distance between the center of the particle and a tip), which was chosen based on the approximate size of the atomistic structure shown on Figure 3.2.1. The tips and edges were further smoothed in such a way that their minimum curvature was the Wigner-Seitz radius of sodium $r_{\text{Na}} \sim 2.08$ Å.

In Figure 3.4.1 (c) the absorption cross section from TDDFT and BEM are compared. For TDDFT (blue line) we observe a single peak at 3.15 eV, corresponding to the dipolar plasmon (DP) resonance as shown on Figure 3.3.1, and a shoulder around 3.8 eV. The BEM cross section (red line) shows two peaks emerge at 3.2 eV and 3.6 eV, corresponding to the DP and quadrupolar plasmon (QP) modes, respectively. The energy difference between the DP mode of TDDFT and BEM is minimal but they are more relevant with respect to the intensity, which depends on the size of the particle. Moreover, when a smoother geometry

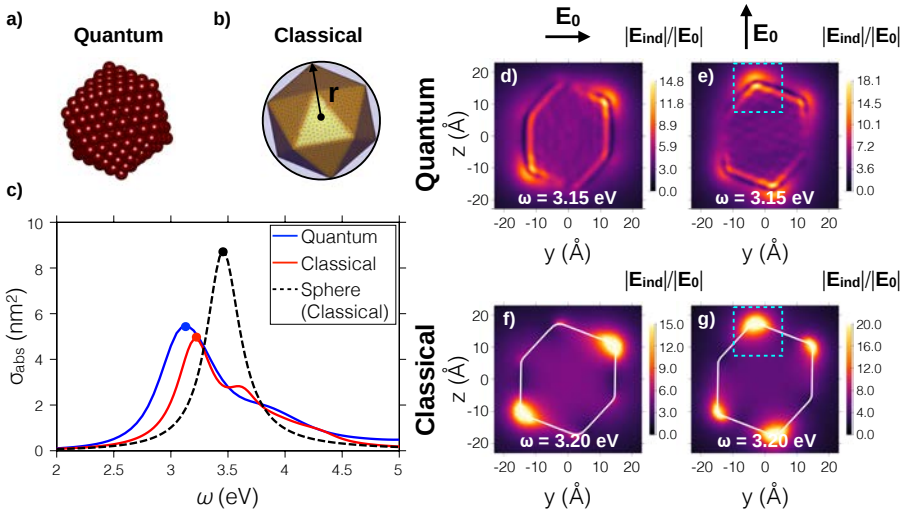

Figure 3.4.1: (a) Atomistic cluster composed by 380 atoms used in TDDFT calculations. (b) Sketch of the continuous icosahedral cluster used for BEM calculations. The sphere of radius $r = 1.85$ nm circumscribing the icosahedron has been drawn for reference. The tips and edges have been rounded to have a minimum radius of $r_{Na} = 2.08$ Å. (c) Absorption cross-section of the particle calculated using TDDFT (blue line) and BEM (red line). The energies of the dipolar plasmons obtained for the two models are highlighted with dots. The dashed black line corresponds to the absorption cross section of the sphere in (b), as calculated with BEM. A peak corresponding to the QP is observed for BEM at $\omega = 3.6$ eV, while a shoulder is appreciated for TDDFT around $\omega \sim 3.8$ eV. Induced near-field enhancement for a single icosahedral nanoparticle obtained using TDDFT (d-e) and BEM (f-g). The external field $\mathbf{E}_0$ is polarized along the y-axis (left column) and along z-axis (right column).

is considered for the BEM calculations a stronger dominance of the DP mode and a smearing of the QP mode is observed, which may explain up to a certain level the presence of the second peak, instead of the shoulder as for the TDDFT. The spectrum corresponding to a spherical particle of the same size as the icosahedral one is represented with dashed line on Figure 3.4.1 (c) for comparison.

Figure 3.4.1 (d-g) compare the near-field maps around a single Na particle with two different field orientations for the two models. The frequency of the external field correspond to the dipolar mode. Even if the BEM method does not show any atomistic features (in contrary to the atomistic *ab initio* method), it can reproduce the strong localization of the field at the tips of the particle as shown on Figure 3.4.1 (f) and (g). Therefore subnanometric localization of the field is possible even if smooth surfaces and continuous media are used instead of the realistic atomistic structure.

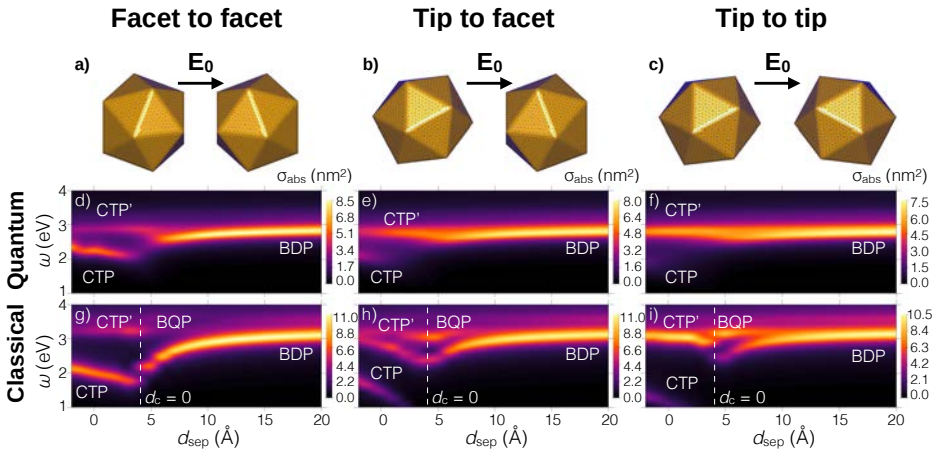

Figure 3.4.2: Sketch of the three interparticle gap geometries use with the BEM approach, (a) facet-to-facet, (b) tip-to-facet and (c) tip-to-tip, the external field $\mathbf{E}_0$ is oriented along the dimer axis. (d-f) Absorption cross-section of the icosahedral dimers obtained from the *ab initio* calculations and (g-i) the absorption cross-section obtained with BEM as function of the separation distance d_{sep}. The hybridized bonding dimer plasmon (BDP) mode, the bonding quadrupolar plasmon (BQP) mode, charge transfer plasmon (CTP) mode and higher-order charge transfer plasmon (CTP') mode are highlighted in the spectra when them identification is possible. The minimum distance ($d_c = 0.0$) for which the continuous (BEM) particles overlap is represented with white dashed lines.

As for the *ab initio* atomistic calculations shown previously, we also studied the field enhancement of nanocavities formed by two Na_{380} clusters using BEM. In this case, the separation distance has been considered as the distance between the closest points of the particles surface, which includes an additional correction term corresponding to the distance between the center of an outermost sodium atom and the surface of the particle (the Na atoms are considered as spheres of radius $r_{\text{Na}} = 2.08$ Å), $d_{\text{sep}} = d_c + 2r_{\text{Na}}$. As previously the direction of the external field is along the dimer axis, as shown in the top row of Figure 3.4.2.

The far-field behavior of the systems are studied in Figure 3.4.2 (d-i), where the absorption cross-section of the gap size, σ_{abs} color maps, calculated with TDDFT and BEM models for the three geometries. At large separation distances ($d_{\text{sep}} > 6$ Å), the single particle's DP hybridize into the bonding dimer plasmon (BDP), which has a lower energy than the DP mode of single particle. As the particles get closer, the BDP is red shifted in the both models, and for $d_{\text{sep}} = 6$ Å major differences among the models arise.

- For the TDDFT calculations (second row of Figure 3.4.2) the BDP red shifts as the inter-particle distance decreases, and below 6 Å it eventually

fades away, indicating that the quantum regime has been reached as explained in the previous section. Then the CTP at lower energy (around 2 eV) emerges due to the tunneling effect, even if the particles are not in contact ($d_{\text{sep}} \sim 5\,\text{Å}$). Notice the higher intensity of the CTP mode for the facet-to-facet geometry due to the largest particle surface area as explained previously. Furthermore, for these short distances the higher-order charge transfer plasmon(CTP')[1] mode is also excited at higher energy (about 3 eV).

- For the continuous BEM cross-section shown in the third row of Figure 3.4.2, it is observed that the BDP mode vanishes for practically overlapping particles ($d_{\text{sep}} \sim 4\,\text{Å}$, which is equivalent to $d_{\text{c}} \sim 0\,\text{Å}$, represented by the dashed white lines) in contrast to the TDDFT case. Moreover, there is a larger red shift of the BDP than what is observed in the TDDFT case, which is balanced by the stronger coupling between the single particles higher order modes such as BQP. This behavior is also observed for dimers composed by spheres [11], but it is enhanced by the geometrical features of the system, as can be clearly seen by comparing the facet-to-facet [Figure 3.4.2 (g)] with a slight excitation of the BQP and intense BDP mode, and the tip-to-tip [Figure 3.4.2 (i)] with a much stronger BQP and lower BDP. Notice that within this classical model, the CTP mode emerges only for particles with physical contact ($d_{\text{sep}} < 4\,\text{Å}$), as no effective quantum tunneling effects are introduced in this model, although they could be included by using a quantum corrected model [139]. The evolution of this mode, both in intensity and energy, shows high dependence on the geometry of the neck that links both particles, although for the three gap configurations it is red shifted compared to the TDDFT results. Furthermore, the relative intensity of CTP' is extremely dependent on the geometry and width of the neck, which stabilizes in energy as the overlapped dimer size gets smaller, thus resembling a single particle. Overall, major differences with TDDFT are observed in the $2 < d_{\text{sep}} < 6\,\text{Å}$ regime, where electron spilling effects and non-zero tunneling probability take place and are captured by TDDFT, contrary to classical electrodynamics calculations, which do not incorporate these effects related to the wave nature of electrons.

To compare quantitatively the field localization provided by the two models we represent the maximum induced near-field at the center of the gap on Figure 3.4.3 (a-c). The maximum induced field show similar trend for large separation distances ($d_{\text{sep}} > 10.0\,\text{Å}$). For smaller distances major differences between geometries and models are observed. For TDDFT, a maximum is observed at $d_{\text{sep}} = 8.0\,\text{Å}$ for the facet-to-facet and at $7.0\,\text{Å}$ for the tip-to-facet and tip-to-tip

[1] The CTP' mode was called QP in the previous section, but since a new mode appears with BEM, we preferred to rename this mode.

configurations. The presence of the tip in the cavity is reducing the tunneling effect compare to the facet-to-facet geometry, increasing the maximum value of the induce field since a stronger lightning rod effect is observed. In the other hand, for BEM, the field enhancement increases exponentially as the particles get closer, with larger values for tip-to-tip and tip-to-facet due to lightning rod effect. Quantitatively, at $d_{\text{sep}} = 5\,\text{Å}$, the values obtained using BEM are between 7.8 and 9.5 larger than the ones obtained with TDDFT.

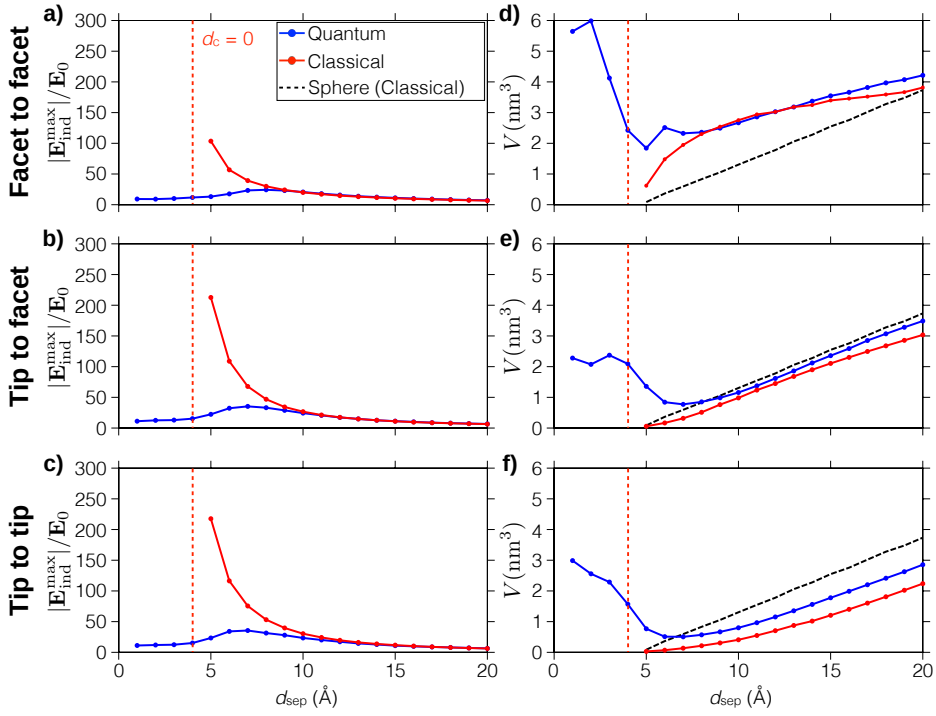

Figure 3.4.3: (a-c) Maximum local induced-field enhancement $\mathbf{E}_{\text{ind}}^{\text{max}}/\mathbf{E}_0$ at the center of the gap between the two particles for the three dimer geometries as function of the cavity size [as in Figure 3.3.4 (a) for TDDFT]. The blue lines stand for TDDFT calculations and the red lines show the BEM calculations. The vertical dashed red lines the touching distance $d_c = 0.0$. (d-f) Effective mode volume V of the local field in the mid of the gap as define in equation (3.3) for the three geometries and the two models. The plotted data correspond to the energies for which the largest maximum of the induced field for each configuration and distance are obtained. The dashed black lines represent the effective mode volume calculated classically using spheres.

Along with the maximum absolute value of the induced field, another char-

acteristic of the induced near-fields is the effective mode volume V defined by

$$V = \int_V \frac{|\mathbf{E}_{\text{ind}}(x,y,z)|^2}{|\mathbf{E}_{\text{ind}}^{\max}|^2} dV. \tag{3.3}$$

The effective mode volume V is shown in Figure 3.4.3 (d-f) as function of the inter-particle separation d_{sep} which is similar to expression (3.1). The effective mode volume V depends on the excitation frequency ω among the other parameters. We computed the effective mode volume V at the frequency of the BDP resonance (which is slightly changing with the inter-particle separation d_{sep}). In the *ab initio* calculations, for large distances ($d_{\text{sep}} > 5\,\text{Å}$), there is a smooth increase of the field confinement, i.e. a smooth decrease of V, for the three geometries. Then for small cavities ($d_{\text{sep}} < 5\,\text{Å}$), the confinement depends on the geometry:

- For the facet-to-facet [Figure 3.4.3 (d)], a transition is observed from the BDP ($d_{\text{sep}} > 5\,\text{Å}$) to the CTP ($d_{\text{sep}} < 5\,\text{Å}$), while a characteristic dip [83], corresponding to the emergence of the CTP' mode, is observed.

- At $d_{\text{sep}} = 5\,\text{Å}$, the tip-to-facet [panel (e)] and tip-to-tip [panel (f)] show a transition from BDP to CTP', which is more gradual for the latter.

Regarding the BEM calculations, the BDP mode shows slightly larger field enhancement until the particles overlap ($d_{\text{sep}} = 4\,\text{Å}$), with an increase of the localization as the particles get closer, following a similar pattern than for the TDDFT results until the inter-particle separation $d_{\text{sep}} = 8 - 9$ Å. For smaller distances, differences arise. The tip-to-tip configuration shows the strongest localization due to the intense lightning rod effect. When the tip is rounded, the effective mode volume V increases since the field is spread around.

In order to get further insight in to the similarities and differences of the induced field, we looked at the distribution of the field around the dimer for the both models on Figure 3.4.4. The Figure 3.4.4 is similar to Figure 3.3.5 but for the tip-to-facet geometry only since it gathers both tip and facet features and illustrates the outcomes due to each geometrical feature. Four separation distances has been chosen to illustrate the different interaction regimes: 20 Å on the first row, 10 Å on the second row, 6 Å on the third row and 1 Å on the last row. The TDDFT results are plotted on the left column while the BEM results on the right column.

- In the weak interaction regime ($d_{\text{sep}} = 20\,\text{Å}$), the near-fields look like the single particle one for both models. Moreover, an enhancement is observed inside the cavity, meaning that an hybridization of the dipolar mode of the particles into the BDP also emerges at this distance.

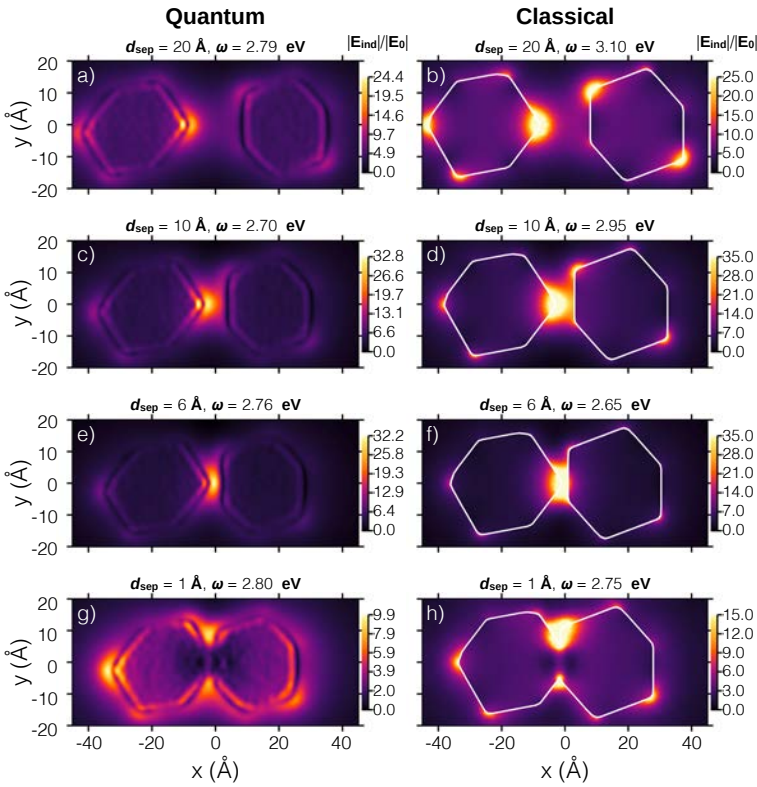

Figure 3.4.4: Induced near-field maps in the plane (y, z) for the tip-to-facet geometry calculated with TDDFT (left column) and BEM (right column). Separation distances are 1, 6, 10 and 20 Å. The frequency at which the map are plot are the frequencies of the most intense resonances.

- Medium interaction and, specially, strong interaction regimes show a major localization and enhancement of the field in the cavity for both models, with minor hot spots around the tips of the clusters.

- The near-fields map in the charge-transfer regime plotted for the CTP' mode energies in panel (g) and (h) shows the differences between the models. In the TDDFT case [panel (g)] charge is transferred through the cavity due to the overlap of the electron wave functions, so that the field is expelled outside the cavity and the induced field decreases. Similar phenomena occurs for BEM [panel (h)] where particle are overlapping, thus the field is expelled to the outside showing a similar pattern to TDDFT. Furthermore,

the field distribution around the terminal tip is also preserved.

3.5 Conclusions

In conclusion, by means of first-principles atomistic TDDFT calculations we have demonstrated that the distribution of the near-field close to plasmonic nanoparticles presents subnanometric hot spots that reflect atomic-scale features at the nanoparticle surface. In our case, these features consist of vertices and edges at the contact of the crystallographic facets of the particles. In particular, for the plasmonic dimer, we have shown that the field localization and enhancement inside the plasmonic nanogaps can be very different depending on whether the distribution of the atoms at the gap define a flat surface, or present atomic-scale tip-like protrusions. We obtain that the far-fields also depend on the atomic configuration but in a less marked fashion as expected.

Our findings provide new insights into the limits of plasmonic localization. The presence of atomic-size features, e.g., formed by edges and vertices between crystalline facets in a nanoparticle, gives rise to near-fields localized in regions with linear dimensions of a few Ångstroms, i.e., literally of atomic size. This effect is related to the classical divergence of a field due to the presence of sharp edges. Indeed, the vertex ending by a single atom, as the one considered here, would be the example of the sharpest possible tip. Furthermore, the field enhanced at the atomic-scale hot spots are intensified by the presence of the overall plasmonic background enhancement, following a cascade effect. Based on this parallelism, we can establish an atomic-scale analogy with the macroscopic plasmonic lens of self-similar antennas [135–137, 152].

We demonstrate that classical methods such as BEM can be used to predict the electro-magnetic enhancement in proximity of atomic-scale protrusions. Nevertheless, only full *ab initio* atomistic calculations are able to provide a fair description of the response of the system under external perturbation. Particularly when the two clusters approach, quantum phenomena play important role. Furthermore, classical calculations strongly depend on how the geometry of the system is defined, while in the *ab initio* calculations, the geometry is a result of an energy-minimization procedure which is itself a part of the *ab initio* framework. For instance, as we will see in the next chapter, the geometry relaxations of the sodium cluster dimer critically influence the response of the plasmonic cavity. In particular, we will show that even a motion of single atom can strongly affect the optical response of the sodium cluster dimer.

Chapter 4

Plasmonic Response of Nanojunctions Driven by Single Atom Motion: Quantum Transport Revealed in Optics

The correlation between transport properties across sub-nanometric metallic gaps and the optical response of the system is a complex effect which is determined by the fine atomic-scale details of the junction structure. As experimental advances are progressively accessing transport and optical characterization of smaller nanojunctions, a clear connection between the structural, electronic and optical properties in these nanocavities is needed.

In this chapter we continue to model the optical response of two Na_{380} clusters. We present a study of the simultaneous evolution of the structure and the optical response of a plasmonic junction as the particles forming the cavity approach and retract. Atomic reorganizations are responsible for a large hysteresis of the plasmonic response of the system, that shows a jump-to-contact instability during the approach process and the formation of an atom-sized neck across the junction during retraction. Our calculations demonstrate that, due to the quantization of the conductance in metal nanocontacts, atomic-scale reconfigurations play a crucial role in determining the optical response of the whole system. We observe abrupt changes in the intensities and spectral positions of the dominating plasmon

resonances, and find a one-to-one correspondence between these jumps and those of the quantized transport as the neck cross-section diminishes. These results point out to an unforeseen connection between transport and optics at the atomic scale, which is at the frontier of current optoelectronics and can drive new options in optical engineering of signals driven by the motion and manipulation of single atoms.

4.1 Motivation

It has recently been shown that the interaction of metal surfaces in sub-nanometric proximity drives new optoelectronic phenomena, where an interplay between the photons, single electron transitions, plasmons, vibrations and motion of atoms present in the junction, determines the complex outcome of the optical response including strong quantum effects and nonlinearities [119, 153]. On the one hand, strong non-local dynamical screening [154] and quantum tunneling [118, 139, 143] have been shown to drastically modify the optical response in a metallic sub-nanometric gap, establishing the limit of localization and enhancement of the optical fields far below the predictions from simple classical approaches [83, 118, 120, 144]. On the other hand, even if typical surface plasmon excitations localize in the nanometer scale, we have shown in the previous chapter that the fine atomistic details of the crystallographic facets and vertices of the metal particle, with the presence of single atomic protrusions and edges, introduce further non-resonant light localization [83, 155]. This is analogue to the macroscopic lightning rod effect, [134, 135] but brought down to the atomic scale.

We are here interested on how the optical response of plasmonic cavities simultaneously correlates with their structural and transport properties [156], going beyond the macroscopic description to focus on the influence of strong atomic-scale structural reconfigurations of the cavity (that has been previously ignored) [83, 157]. This is important since, when two metallic surfaces are approached and put into contact, the formation of small metal necks or nanojunctions connecting them is a very likely process [158], and indeed, we are also able to rigorously model the formation of the metal necks in our simulation. The formation of such metal nanocontacts has been theoretically predicted [158, 159] and experimentally observed [158, 160–162]. These structures are at the root of friction phenomena in metal surfaces [163, 164] and give rise to quantized transport following discontinuous changes in the contact cross-section [158, 165–167]. Thus, the key question that we want to address in this chapter is whether a slight modification of the geometry of the cavity, involving the movement of a few or even a single atom in such sub-nanometric junction, e.g., due to migration or repositioning driven by strain accumulation in a metal neck, and its correspond-

ing change in conductance are clearly reflected in the optical response. If this were the case, one could expect to observe a discontinuous change in the plasmonic response of the system accompanying each plastic deformation event. As shown below, our simulations indeed confirm that such expectations are fulfilled.

The present study is particularly relevant in the light of recent progress in fabrication and processing techniques. As the dimensions of nanoscale architectures are progressively reduced, we are facing a regime where the actual distribution of the atoms in a system matters [168]. The fact that optics might follow the atoms is of utmost importance in optical engineering and optoelectronics, targeting optical modulators or electro-active control of optical signals, where instabilities and modifications of the performance can be attributed to atomic-scale features [169].

In order to address the complex correlation of electronics and optics in subnanometric junctions where the atoms in the system are allowed to adapt to the mechanical boundary conditions, we performed atomistic quantum mechanical calculations of the electronic structure, the optical response, and the structural evolution of a plasmonic cavity. We employed our efficient implementation [170–172] of linear-response Time-Dependent Density Functional Theory (TDDFT) as described in section 2.3 in conjunction with the SIESTA Density Functional Theory (DFT) package (appendix A) [1, 2]. The plasmonic cavity used for this simulation is the facet-to-facet dimer depicted in Figure 3.2.2 (a). This is a canonical example of a metallic system whose properties can be quite straightforwardly extrapolated, with care, to other metallic systems. The use of sodium allows performing larger calculations, in terms of the number of atoms, as compared to other more technologically relevant materials like, e.g., gold. This increases the relevance of our results, since the number of atoms involved in the structural reorganizations of the neck is indeed a small percentage of those contained in the system.

The structural relaxations of the Na_{380} dimers were performed within DFT as implemented in the SIESTA code [1, 2]. We used the Perdew-Burke-Erzenhorf density functional (GGA-PBE) [35], norm-conserving pseudo-potentials [122] to effectively describe core electrons, and a double-ζ polarized (DZP) basis set of numerical atomic orbitals generated using an *energy shift* of 100 meV [52]. The other parameters are similar to those stated earlier in chapter 3 (section 3.2).

Figure 3.2.1 shows the relaxed initial structure of one of the Na_{380} clusters that form the plasmonic cavity. The cluster presents an nearly-icosahedral structure and has been obtained starting from a configuration optimized with empirical potentials [173] and available at the Cambridge Cluster Database (CCD) [121]. The relaxed structure obtained using GGA-PBE is very similar to the one provided at the CCD site, and it is characterized by the presence of planar facets, sharp edges and single-atom vertices.

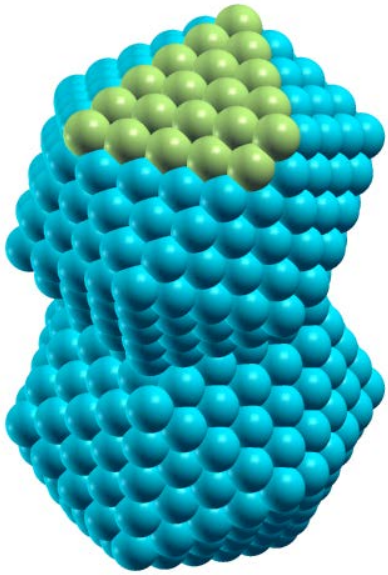

Figure 4.1.1: The atoms in the outer facets of both clusters (the atoms in one of these facets have been highlighted in yellow) are kept fixed during the relaxation process.

Figure 4.1.1 shows a snapshot of the relaxation of the plasmonic cavity when the two clusters are approached towards each other. As a mechanical constraint, and mimicking the presence of macroscopic scanning probe tips or surfaces where the clusters are attached, the atoms in the outer surfaces of both clusters (highlighted in yellow in Figure 4.1.1) remain fixed and move rigidly during the approach/retraction events. Each new configuration is generated by changing the distance between these fixed facets by 0.2 Å. The rest of the atoms, blue atoms in Figure 4.1.1, are then moved to minimize the total energy of the cluster dimer. The presence of two unrelaxed facets allows to measure the displacement applied to the system unambiguously, which in turn permits the definition of a *nominal gap size*, corresponding to the distance between the inner facets of the neighboring clusters in case the system were not allowed to relax. This is the magnitude that is used to define the inter-particle distance.

Our approach consists in tracing the energetics, the geometrical and the optical response of the two metallic clusters which gradually get closer while allowing atoms to rearrange. Remarkably, at a given separation distance, the clusters show a jump-to-contact instability [174] leading to a strong modification of the optical response, a result in striking contrast to the smooth evolutions found in the context of previous classical and quantum descriptions based on static geometries [83, 118, 120, 139]. The subsequent process of retraction of the clusters is particularly interesting. In such a situation, consistently with previous studies [175, 176], a metallic atom-sized contact is formed and the conductance across the gap gets quantized. This allows revealing the strong correlation between the transport and optical properties of the system and how, paradoxically, the motion of a few atoms or even a single atom in a nanometric gap can drive a quantized-like (abrupt, discontinuous) evolution of the optical response.

4.2 Atomic Rearrangements in the Plasmonic Junction: Nanoparticles Approach and Retraction

Our model of the plasmonic cavity is formed by two sodium clusters that are progressively approached and retracted from each other. Structural relaxations, using forces obtained from DFT calculations, are performed for each approaching and retraction step. Each cluster forming the dimer has an icosahedral shape and contains 380 sodium atoms as explained in the previous sections. The lateral dimension of each cluster is ∼25 Å. The initial configuration consists of the two clusters placed at a distance of 16 Å—distance large enough to avoid direct interaction between the nanoparticles. The cavity is initially symmetric with the two clusters opposing planar facets. Starting from that distance the two clusters are slowly brought together. We monitor the inter-particle distance using the *nominal gap size*, defined as the distance between the two cluster inner facets if the system would remain unrelaxed (as it was the case in the chapter 3). Thus, a nominal size gap of zero value would correspond to the superposition of the atoms forming the two opposing facets in the absence of relaxation. Approaching steps of 0.2 Å were chosen as a compromise between computational convenience and an approximately adiabatic evolution of the structure. As described in the previous section, in order to control the inter-particle distance and to mimic the presence of tips or surfaces the clusters are attached to [143], the atoms belonging to the outer facet of each cluster. The outer-facet atoms are kept fixed during the relaxations after each approaching or retracting step, i.e, they are not relaxed but move rigidly as shown on Figure 4.1.1. Once the distance between clusters corresponds to the typical inter-layer distance in bulk sodium, a process of retraction is started by pulling the clusters apart, again in steps of 0.2 Å, until they completely separate.

The total energy of the system during this process of approaching and retracting is shown as a function of the nominal gap size in Figure 4.2.1. The evolution of the clusters and junction geometry is shown in the panels of Figure 4.2.1 for selected separation distances. The latin letters that label each panel relate the geometry of the system to the corresponding nominal gap size and energy, as indicated in the curves of the figure. During the approach (red circles) the total energy remains constant until a nominal gap size of about 7.5 Å is reached. From this separation, the total energy starts decreasing smoothly. At a nominal gap size of ∼ 6.1 Å the two clusters suddenly jump to contact [174]. At this point the actual interface distance abruptly decreases and the energy is substantially reduced. The clusters are now connected and elongated along the intermolecular axis. The inset in Figure 4.2.1 shows the actual gap size indicating the real

distance between the inner facets of the clusters. After the jump-to-contact, the value of the actual gap size drops to a value of about 3.2 Å remaining fairly constant and close to 3.0 Å as the two clusters get closer together. The abrupt

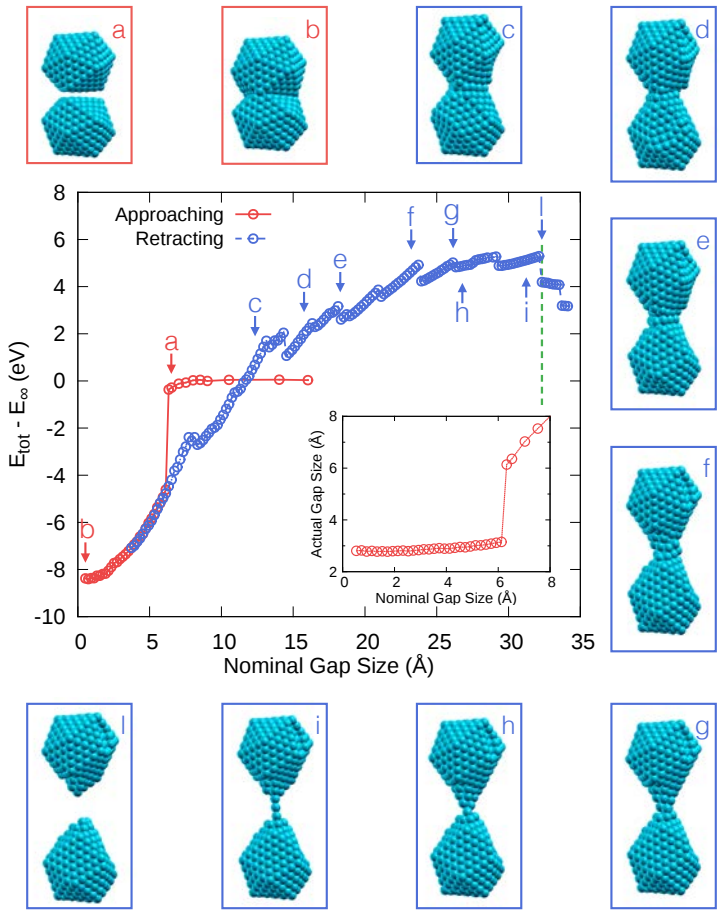

Figure 4.2.1: Total energy of a plasmonic cavity formed by two Na_{380} clusters as a function of the nominal distance between them (*nominal distance* is defined as the distance among the facets defining the cavity if the system would not be relaxed). Red circles represent the approaching process while blue circles indicate the retracting process. The inner panel shows the actual gap size as a function of the nominal value during the approach, showing the clear signature of a jump-to-contact event. Images of the geometries around the graph show the rearrangement of the atoms in the clusters and the formation of a nanojunction during retraction. Latin letters indicate the correspondence between some of the total energy points in the graph and the configurations shown in the surrounding panels.

reduction of the energy at the jump-to-contact point is mostly due to the reduction of the surface energy of both clusters (two facets disappear). However, this happens at the expense of a large elastic deformation of the clusters. By further approaching the two clusters we reduce the elastic deformation of the system and, correspondingly, the total energy decreases. Eventually the system suffers some reorganizations which are also reflected (although they are somewhat less obvious than the jump-to-contact) in the energy versus distance curve in Figure 4.2.1. For example, the stacking of the atomic layers at the interface, initially imposed by the mirror symmetry of our starting geometry, gets optimized at a nominal gap size of approximately 2.5 Å. Later, the particles start to deform reducing further their surface area by increasing the contact cross-section. The energy finally stabilizes and starts to slowly increase for nominal gap sizes below ~ 1 Å. We stop our approaching process at this point.

Once the two clusters are clumped together at a nominal distance comparable to the interlayer distance in bulk sodium, we start pulling them apart (blue circles in Figure 4.2.1). During the retraction process the structure evolves creating and thinning a neck that connects the two clusters until a mono-atomic chain is formed and, eventually, until a complete separation of the clusters is achieved (point l in Figure 4.2.1). In agreement with previous studies, the evolution of the contact structure takes place via an alternation of elastic and plastic deformation events [158, 167, 176, 177]. The contact is elongated until the accumulated elastic energy is sufficient to produce atomic rearrangements, mainly driven by the atoms in the neck area. During these plastic events the energy of the system decreases abruptly. Thus, there is a one-to-one correspondence between the discontinuities of total energy in Figure 4.2.1 and the changes in the configuration of the metal neck. It is striking to note the dramatic contrast between the distance at which the jump-to-contact takes place and the clusters "touch" for the first time during the approaching process (close to point a in Figure 4.2.1), and the distance at which they finally detach (indicated by a vertical green dashed line). A nominal gap distance of 32.3 Å is needed to separate completely the clusters.

In summary we have seen that the geometry of the system strongly departs from the idealized situation in which two clusters simply change their relative position. These structural rearrangements had been overlooked by most previous studies of plasmonics although, as we describe in the following, they play a key role in determining the optical response of the cavity.

4.3 Optical Response of a Forming Plasmonic Cavity: Relaxed vs. Unrelaxed Cases

To explore the connection between the structural evolution and the plasmonic response of the cavity, we compare the optical absorption of a plasmonic junction as the clusters approach for two situations:

- first, no relaxation of the clusters is allowed and the only parameter modified is the distance between the particles [Figure 4.3.1 (a)] as it was shown in the chapter 3 [Figure 3.3.3 (a)];

- second, the relaxation of the atoms is taken into account, meaning the atoms are free to move inside the cavity as explained in the previous section, [Figure 4.3.1 (b)] following the atomic-scale restructuring shown in Figure 4.2.1 (red symbols).

The resonant plasmonic modes of the forming cavity, as obtained from the calculated polarizability of the system, are displayed as a function of the inter-particle distance in both situations. The component of the polarizability parallel to the dimer axis is considered here, i.e., induced by an electrical field polarized along the same axis, that we take hereafter as z-axis. In both cases, and depending on the separation, we can identify three distinct resonances as it has been largely explained in the previous chapter 3 [83, 118, 120, 139, 140, 143, 144]. We will now briefly recall the main feature of the polarizability in the unrelaxed case for the sake of the comparison.

The so-called Bonding Dipolar Plasmonic (BDP) resonance around 3 eV dominates the response at large inter-cluster distances when the two clusters interact weakly. The BDP shows an induced charge distribution characterized by a capacitive coupling of charges of opposite sign at both sides of the cavity, as schematically depicted in the right drawing of the top panel in Figure 4.3.1. When both clusters are in contact, so that free charges can efficiently move across the junction, we enter a conductive coupling regime characterized by the so-called Charge Transfer Plasmon (CTP) and the associated high-energy Charge Transfer Plasmon (CTP') modes. The conducting link of the CTP through the junction of the clusters, produces a screening of the charges in the cavity, and thus redistributes the induced charge density to produce a net dipole that extends to the whole dimer structure, as depicted in the top-left scheme in Figure 4.3.1 [see also the panel (c) and (d)].

The BDP resonance is red-shifted as the inter-cluster distance is reduced and the Coulomb interactions between the clusters increase. This shift is due to the strong interaction of the parallel induced dipoles along the dimer axis, which hybridize [178] lowering the energy of the resulting optically active mode.

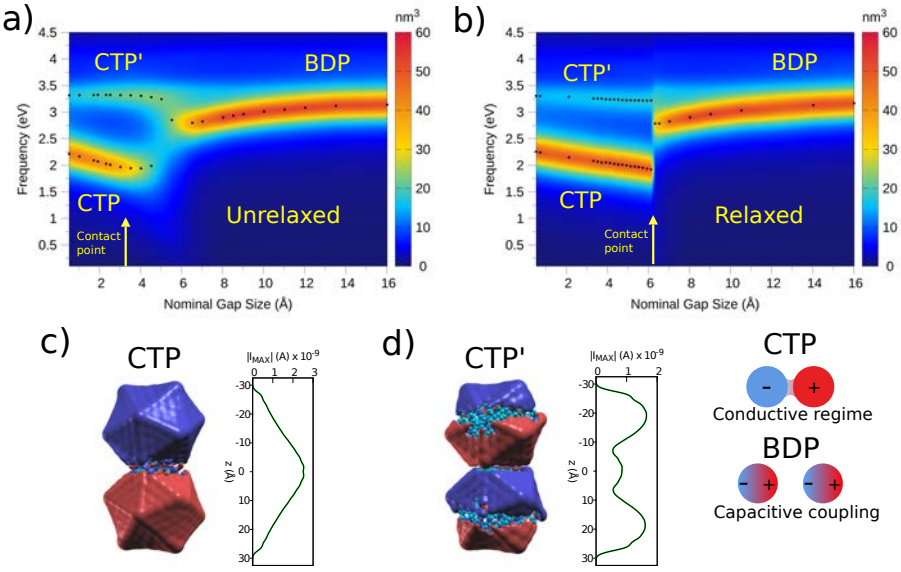

Figure 4.3.1: Evolution of the imaginary part of the polarizability of a Na_{380} dimer (external field applied along the dimer axis) as the clusters are approached, plotted as a function of the separation distance and photon energy. Both unrelaxed (a) and relaxed (b) geometries of the cluster dimer are considered. The dark dots indicate the position of the peak maximum in the polarizability for those distances for which the optical response has been computed. The arrow lines indicate the *contact point* for the two cases, i.e., the distance at which the clusters merge into one single larger object. The top panel shows the schematic representation of the induced charge in the modes that dominate the optical response before contact (bonding dipolar plasmon mode, BDP) and after contact (charge transfer plasmon mode, CTP). Panels (c) and (d) show the imaginary part of the induced density and the corresponding modulus of the electron current flowing through each cross sectional [i.e., (x, y)] plane along the dimer axis. An external electric field of magnitude of $1\text{x}10^{-9}$ atomic units is assumed here with a polarization parallel to the junction main axis. The nominal gap size is 6.1 Å, corresponding to the jump-to-contact configuration in the relaxed case.

In this capacitive (weak interaction) regime both unrelaxed and relaxed cases show the same dependence on the inter-particle distance. The BDP mode "lives until" the clusters are brought to a distance of about 6.1 Å. At this point, for the unrelaxed dimer [see Figure 4.3.1 (a)], the BDP mode is quenched and higher energy modes start gaining intensity. If the clusters are approached further we observe a smooth transition from the capacitive to the conductive coupling regime. For separation distances right below 6 Å, the electron tunneling current at relevant frequencies gradually starts flowing, giving rise to the progressive emergence of the CTP resonance (see section 3.3.2 [83, 119, 139, 144]). This transition region is frequently referred to as the quantum tunneling regime of

plasmonic cavities [143]. At a distance comparable to the sodium interlayer distance, ~ 3.0 Å, the clusters become chemically bonded and obvious mechanical contact is established. Under those conditions, a substantial current can be established and the CTP appears fully developed.

In contrast, the situation shown in Figure 4.3.1 (b) for the relaxed dimer is strikingly different. The relaxed dimer undergoes a jump-to-contact instability (see red curve in Figure 4.2.1) that dramatically modifies the evolution of the optical spectrum. The transition regime, found between 6 Å and 3 Å for the unrelaxed dimer, has almost completely disappeared in the relaxed case. There are no stable geometries for those intermediate gap sizes and, thus, the resistive tunneling (transition) regime cannot be clearly identified in the optical response. Although the details of the jump-to-contact process strongly depend on the size and shape of the facets and the effective elastic constants of the systems being brought into contact, this effect is a quite general behavior which is routinely taken into account in the interpretation of data from scanning probe microscopies [179]. Our results indicate that the effect of the jump-to-contact must be considered when exploring and interpreting the optical response of metallic particles in close proximity, particularly when large atomic-scale reconfigurations can be expected. Importantly, this phenomenon can hinder the appearance of a smooth transition between the capacitive and charge-transfer regimes in the optical response of plasmonic cavities.

In panels (c) and (d) of Figure 4.3.1 we show the real space distribution of the induced charge for the CTP and CTP' modes right after the clusters get into contact, i.e., right after the jump-to-contact instability. Here we plot the imaginary part of the induced density at the resonant frequencies. We also plot the corresponding electron current (graph to the right of each charge density plot) flowing through (x, y) planes (i.e., perpendicular to the dimer axis) as function of z, the coordinate along the dimer axis.

Since we are dealing with a finite object we can use the continuity equation and an integration region like the one shown in Figure 4.3.2 to define the current that flows across a plane perpendicular to the dimer axis and passing through the center of the junction. From our TDDFT calculation we obtain the induced electron density $\delta n(\mathbf{r};\omega)$ in response to a monochromatic field with frequency ω. We can now integrate the induced density over the volume in Figure 4.3.2

$$\delta\tilde{Q}(\omega) = \int_{\Omega} dr^3 \delta n(\mathbf{r};\omega), \tag{4.1}$$

to obtain $\delta\tilde{Q}(\omega)$ the Fourier transform of the time-dependent total induced charge contained in Ω. The continuity equation provides with the trivial relation between the total induced charge in Ω, $\delta Q(t)$, and the current flowing across the junction $I(t)$ at each instant of time t. In frequency domain this relation is expressed as

$$\tilde{I}(\omega) = -i\omega\delta\tilde{Q}(\omega). \tag{4.2}$$

Thus, we can easily obtain the modulus of the current (maximal current) flowing through the junction in response to the monochromatic electric field $\mathbf{E} = \mathbf{E}_0 \cos(\omega t)$

$$|I_{max}(\omega)| = \omega\sqrt{\left[\delta\tilde{Q}'(\omega)\right]^2 + \left[\delta\tilde{Q}''(\omega)\right]^2}, \tag{4.3}$$

with $\delta\tilde{Q}'(\omega)$ and $\delta\tilde{Q}''(\omega)$, respectively, the real and imaginary parts of $\delta\tilde{Q}(\omega)$. In our calculations we compute the current at the frequencies of the plasmonic resonances for each geometry, and $\delta\tilde{Q}(\omega)$ is calculated by integrating the density change $\delta n(\mathbf{r};\omega)$ over a given real space volume (Ω). By changing the integration volume we define the (x, y) plane through which the current is calculated. For example, the current as a function of the position of such plane is shown, for a particular configuration and two different resonance frequencies, in the panels (c) and (d) in Figure 4.3.1. It is important to stress that such maps do not refer to a given instant of time, but they rather depict the maximum current passing through (x, y) plane as function of the plane's location z. In order to compute the current flowing through the center of the junction (As shown on Figure 4.4.5) we need to integrate the induced charge over a volume similar to that depicted in Figure 4.3.2.

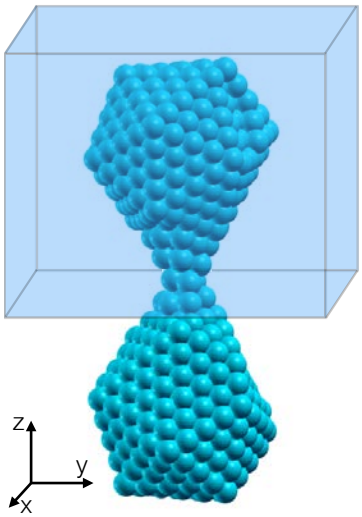

Figure 4.3.2: Representation of the integrating volume used to define the current passing through the junction with the help of the continuity equation.

The induced density associated with the CTP forms a dipolar pattern over the whole system having a single node placed at the center of the system. Thus, the charge accumulation does not take place in the cavity interfaces, but rather extends to the whole system. Correspondingly, the current associated with the CTP resonance has its maximum at the cavity center. On the other hand, the CTP' mode presents two dipolar patterns on each cluster with nodes of the induced density charge in the center of the system as well as in the middle of each cluster. The charge distribution in this case is somewhat similar to what one can expect for the BDP mode. However, the current reveals a key piece of information to rule out this interpretation. In the case of the CTP' resonance the maxima of the

current are found both in the center of the system as well as within each cluster. This indeed confirms the existence of the charge transfer among both clusters also in this high-energy mode. Thus, the observed induced density pattern is better interpreted as the second optically active mode of a single metal rod.

Finally, below 2 Å nominal gap size the conductive coupling regime of the junction is fully developed in both the unrelaxed and relaxed cases, with the CTP and the CTP' resonances converging to similar values of energy, around 2.25 eV and 3.3 eV, respectively. This underlines the fact that the details of atom rearrangements at the cluster interface might not be so important in the determination of the optical response once the two clusters are fully chemically bonded.

4.4 Optical Response of a Retracting Plasmonic Junction: Optics Driven by Individual Atoms

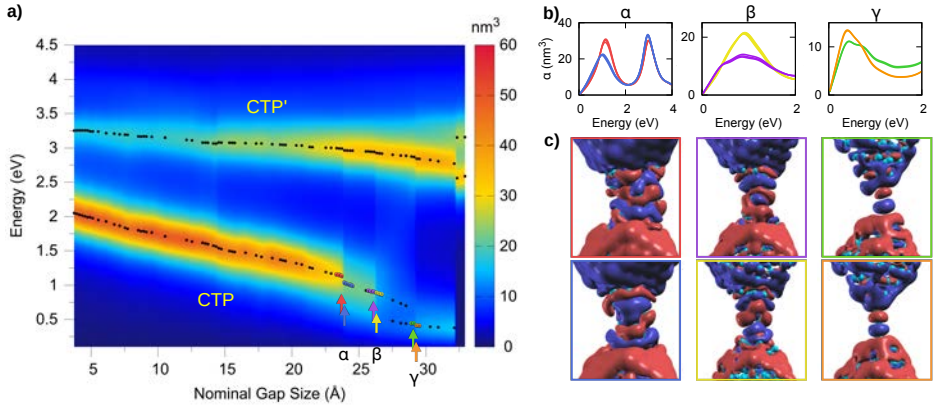

Figure 4.4.1: (a) Evolution of the resonances in the polarizability of a plasmonic junction as a function of the nominal gap size and energy, as the clusters forming the junction move apart (i.e., move towards larger nominal gap sizes). The dots indicate the positions of the peak maxima in the polarizability for the considered configurations. Panels (b) show the spectral lines of the polarizability at distances before and after each of the jumps highlighted in panel (a) by means of Greek letters and colored arrows and dots. The colors of the lines of the spectra correspond to the colors of those arrows and dots, thus indicating whether a given spectrum corresponds to a configuration before or after the jump. (c) Imaginary part of the induced charge density distribution around the junction for the three selected distances in (a) and (b), before (top) and after (bottom) the jumps.

Figure 4.4.1 shows the optical polarizability of the junction during the retraction process. Surprisingly, as the two clusters are retracted, the CTP and CTP'

modes dominate the spectrum for most separation distances, all the way to nominal inter-particle distances of several tens of Ångstroms. This is in clear contrast with the results obtained in the previous section (approaching situation), and it is a result of the structural evolution of the junction, characterized by the formation of a thin conducting neck among the clusters [as shown in the panels (c)-(i) of Figure 4.2.1]. As the clusters get separated, the neck gets longer and thinner. As a consequence, the charge-transfer modes disperse towards lower energies (due to the overall elongation of the system). Moreover, as the neck cross-section is reduced, the intensity of the CTP' mode increases at the expense of the lower-energy CTP resonance, consistent with calculations of stretched clusters [157]. As the current flowing across the neck diminishes, the CTP' mode converges towards the BDP mode while the CTP mode tends to disappear.

While the polarizability of the approaching situation in Figure 4.4.1 exhibits only one definite discontinuity associated with the jump-to-contact instability of the cavity, the retracting situation shows a dramatically different behavior as a function of the separation distance. During retraction the optical spectrum is characterized by the appearance of many discontinuities both in the spectral position and the intensity of the resonances. A careful inspection of Figure 4.4.1 reveals that these discontinuities happen at exactly the same nominal distances where jumps in the total energy are detected. The largest jumps are highlighted with arrows of different colors and marked with Greek letters in Figure 4.4.1 (a), and the corresponding polarizability is plotted in detail on the panels of Figure 4.4.1 (b), which extracts the spectral lines from the panel (a). Each panel shows spectra corresponding to distances before and after one of the jumps, identified in the panel (a) of Figure 4.4.1 with the corresponding colored dots and arrows. Consecutive curves correspond to configurations in which the inter-particle distance is changed by 0.2 Å. In each panel there are several, almost indistinguishable, spectra of the same color. This highlights that noticeable changes in the spectrum are indeed linked to the plastic deformation events in the neck, and not to the small rearrangements during elastic deformation. At each jump we observe clear changes in the intensities, widths and positions of the resonance peaks. The jumps affect primarily the low energy resonance, CTP, although they are also visible in the CTP' mode. They are owing to the atomic reorganization in the neck region and they are strongly pronounced for distances above ~ 20 Å due to the small cross-section of the neck. Remarkably, for such thin necks even single-atom movements produce visible changes in the optical response of the system, clearly associated with the quantized nature of the conductance through the junction neck. The jump at 29.3 Å indicates the formation of a well-ordered mono-atomic neck, i.e., the clusters are connected by a single row of atoms. The formation of such structures has been observed for many metals, for example in the case of Au, for which these mono-atomic wires have even been visualized by

electron microscopy [158, 175, 180–183].

The intensity of the CTP resonance suffers an abrupt decrease for a nominal gap size of around 23 Å, becoming broader between 27 and 29.3 Å. Afterwards, simultaneously to the mono-atomic neck formation, the CTP resonance gets sharper with a consequent regain in intensity. This evolution is due to a combination of several effects, the most important being the quantization of electron transport in the metal neck. Such quantization is a well-known effect due to the small cross-section of the contact, comparable to the electron wavelength [184]. As a result of the lateral confinement, the electronic energy levels in a thin metal nanowire or neck get quantized and, at a given energy, only a discrete number of bands (or "channels" using the standard terminology in quantum transport) can contribute to the electron transport. Thus, under a small, static bias, if the electron injection from the electrodes (in our case the clusters) is efficient and the neck structure is sufficiently long and ordered, we can expect each channel at the Fermi level to contribute to transport with a quantum of conductance $G_0 = 2e^2/h$ [184], with h the Planck's constant. In the presence of defects or strong scattering in the connections to the electrodes, the transmission probability of the channels gets reduced [184].

With these ideas at hand, we can easily explain the observed behaviors. The abrupt jump in the intensity of the CTP peak around 23 Å (α jump) is caused by the sudden reduction of the neck's cross-section, as can be clearly seen in Figure 4.4.1 (c) and the inset of Figure 4.4.4. As expected, the reduction of the cross-section reduces the number of conduction channels and, therefore, the electric current flowing through the junction (this is confirmed in Figure 4.4.4, discussed later in detail). The resonance peak also shifts to slightly lower energies. The origin of the intensity jump at $\sim$ 27 Å (β jump) is also similar: a cross-section reduction that translates onto a sudden decrease of the current as can be seen in Figures 4.4.1 (c) and 4.4.4. After this jump at 27 Å, the neck develops into a less ordered structure, creating a region of high scattering that hampers the electron transport between the clusters. As a consequence the CTP resonance broadens. Finally, once the relatively defect-free mono-atomic wire is formed, the transport through the neck becomes completely ballistic, i.e. all the electron that are injected to the mono-atomic wire get across the junction, and the peak in the polarizability becomes more defined again.

These quantization effects can also be observed in the shape of the distributions of induced charge density as the neck evolves during retraction. In panels (c) of Figure 4.4.1 the imaginary part of the induced density associated with the CTP mode is plotted for those configurations immediately before and after the α, β and γ jumps (indicated by the colored arrows in the polarizability plot). Although the density change has a quite complex distribution, it is possible to follow the evolution of the patterns towards simpler schemes of charge oscillation

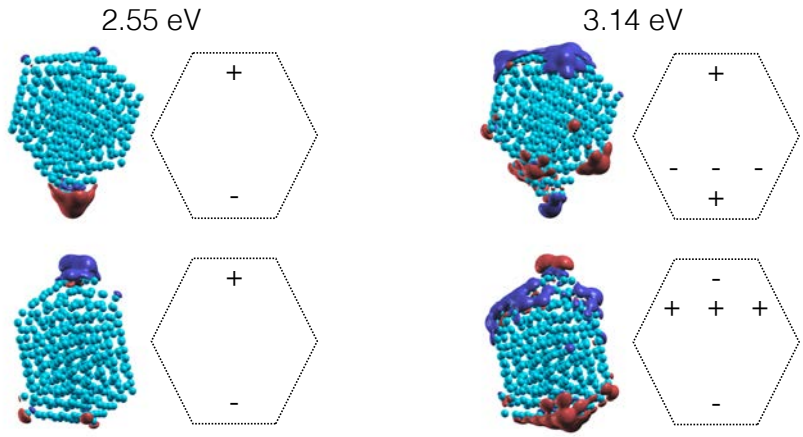

Figure 4.4.2: Imaginary part of the induced charge density distribution for the frequencies of the two plasmon resonances found after the break of the connecting neck and final separation of the clusters.

after each jump. The induced density presents a complex distribution and nodal structure, with a decreasing number of nodes as the cross-section of the neck gets thinner, a fact that reflects the larger number of open conduction channels for the wider structures. Subtle changes in the structure that have a direct translation in the optical response can also be observed in the plots of the induced density. For example, in the case of the γ jump, the three-atoms-long mono-atomic wire becomes more straight and the connections to the cluster more symmetric. This slightly increases the current flowing through the structure and produces the aforementioned changes in the plasmonic response.

Once the two clusters totally separate, breaking the neck, two split resonances arise near the CTP' resonance at about 2.6 and 3.2 eV. The initial face-to-face configuration has been substituted by an asymmetric tip-to-tip configuration (see panel l in Figure 4.2.1). The lower energy resonance recalls a BDP mode, with the largest charge accumulations around the central gap.

When the metal contact connecting the two clusters finally breaks and they separate, their final structure differs considerably from the initial one. The two clusters are not anymore identical and the mirror symmetry in the junction is

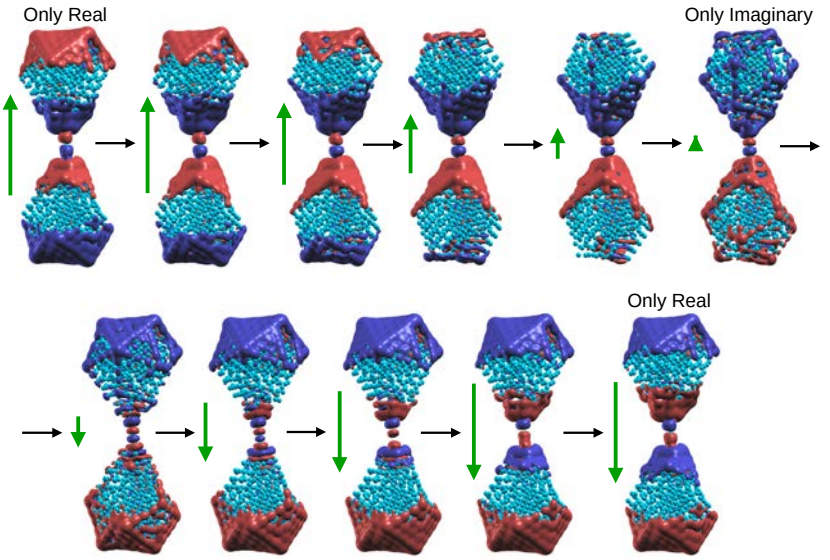

Figure 4.4.3: Real time evolution of the induced density associated with the CTP mode when the cavity is connected by a short mono-atomic wire. Black arrows indicate the time direction while green arrows indicate the direction and intensity of the external electric field in each instant. At $t = 0$ and $t = \pi/\omega_{\text{res}}$ the distribution is completely derived from the real part $\delta n'(\mathbf{r}, \omega_{\text{res}})$, at $t = \pi/2\omega_{\text{res}}$ it is given by the imaginary part $\delta n''(\mathbf{r}; \omega_{\text{res}})$.

lost. Furthermore, rather than in the initial facet-to-facet configuration, the clusters now present some sort of tip-to-tip configuration. With the rupture of the connecting neck, the CTP and CTP' modes that dominated the optical response of the system during the whole retraction process disappear and give way to two modes, rather than a single BDP resonance. The new modes are found at slightly different energies. Moreover, the corresponding induced charge density distributions in Figure 4.4.2 show different patterns. The lower energy resonance at 2.55 eV recalls a BDP mode, with the largest charge accumulations around the central gap. The higher energy resonance at 3.14 eV has a more complex charge distribution, corresponding to higher order mode, showing charge accumulations both in the tips inside the cavity and in the facets of the clusters.

The real space distributions of the induced charge density shown in Figures 4.3.2, 4.4.1 and 4.4.2 only correspond to the imaginary part. Therefore, although they can serve to characterize the resonant modes at a particular frequency, they may not give a complete picture of the time evolution of the screening charge in the system.

The imaginary part of the polarizability (induced density distribution) correspond to the optical absorption and provides information about the resonance frequencies (spatial distribution) of the different modes. For a single, sharp excitation the maximum of the peak in the imaginary part of the polarizability coincides with a zero in the real part of the polarizability. Therefore, when at resonance the external field and the induced dipole in the system are always out of phase. However, when dealing with a system having multiple resonances and especially at low frequencies, even at resonance the real part can be different from zero and have a non-negligible intensity as compared to the imaginary part. In these cases, at the resonance frequency the real time evolution of the induced charge is a combination of the contributions coming from the imaginary and real part of the density change

$$\begin{aligned}\delta n(\mathbf{r};t,\omega_{\mathrm{res}}) = \quad & \delta n'(\mathbf{r};t,\omega_{\mathrm{res}})\cos(\omega_{\mathrm{res}}t) \\ & +\delta n''(\mathbf{r};t,\omega_{\mathrm{res}})\sin(\omega_{\mathrm{res}}t),\end{aligned} \tag{4.4}$$

being induced by the external electric field $\mathbf{E} = \mathbf{E}_0\cos(\omega t)$. The real part is in phase with the external field and the imaginary part representing the out-of-phase (resonant) component of the complex-valued density change. This is the case for the CTP low energy mode seen in the polarizability once the mono-atomic neck is formed, that shows a large real part of the induced density charge even at resonance.

The sequence of imagines shown in Figure 4.4.3 describes the evolution in time of the CTP mode across the cavity when there is a mono-atomic wire connecting the clusters. At $t = \pi/2\omega_{\mathrm{res}}$, the induced density $\delta n(t)$ reflects the imaginary part of the induced density in the frequency domain $\delta n(\omega)$. As expected, the dipole pattern extents all over the whole system with the presence of a node in the center of the junction. Thus, it corresponds to the expected charge transfer among the clusters. In contrast, the real part, found at $t = 0$ and $t = \pi/\omega_{\mathrm{res}}$, presents a pattern formed by dipoles placed on each cluster that resembles a BDP mode.

From a physical point of view what we see here is quite transparent. The mono-atomic wire across the junction represents a bottleneck for electron conduction as compared to the facile movement of charges within each of the clusters. As a consequence, electrons can easily move across each of the clusters and react fast to the applied external field. However, when they reach the gap in the center of the system they accumulate there, since the movement of charge across that gap is limited by the mono-atomic chain, which provides just a single channel for electron conduction.

To fully account for the connection between high-frequency electron transport and optical response of the plasmonic junction, we have calculated the current through the junction as a function of the nominal gap size. In Figure 4.4.4 the

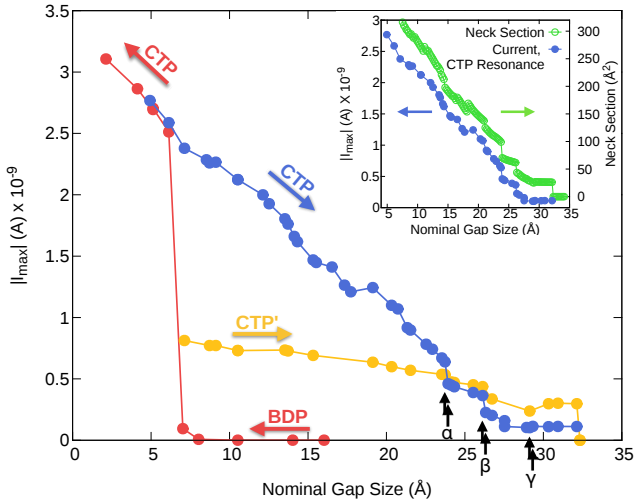

Figure 4.4.4: Modulus of the current flowing through a plasmonic junction as a function of the separation of the clusters forming the junction. The current is evaluated at a cross-sectional plane passing through the center of the cavity (and cutting the center of the neck when present). Colored arrows indicate the direction of the process (approaching or retracting). The current is computed at the resonance frequency of the different modes of the cavity, as indicated by the labels and described in the text. Black arrows indicate the position at which the spectral jumps in Figure 4.4.1 occur. The inset shows the one-to-one correspondence between the jumps in the current for the CTP mode and the cross-section of the metal neck. An external electric field of $1\text{x}10^{-9}$ atomic units is assumed with a polarization parallel to the junction main axis.

results for the modulus of the current passing through a plane cutting the center of the junction are shown. Here we present the current computed at the frequencies of the main resonances of the polarizability, described in previous sections.

The current during the approach process is shown by red solid circles, corresponding first to the BDP mode, and later to the CTP mode, once the clusters are in contact. The current for the BDP mode is negligible until the jump-to-contact event takes place. Once the clusters are connected the current can flow through the whole system and therefore its value increases dramatically. The current calculated for the CTP resonance increases almost linearly as we decrease the nominal gap size.

The values of the current across the junction at the energies of the CTP and CTP' resonances, while retracting the clusters and the neck is getting thinner, are plotted respectively in blue and yellow. The current related to the CTP resonance decreases monotonously as we elongate the system. As commented above, its evolution is characterized by abrupt jumps whenever the neck suffers a plastic deformation. The current eventually reaches a plateau associated with

the formation of a well-defined mono-atomic neck. Interestingly, once the mono-atomic neck is formed, a further neck stretching does not affect considerably the current. This can be expected since the conductance of such small necks mostly depends on the cross-section, which is fixed for the mono-atomic wire. It is interesting to mention that for the low energy CTP mode, it was possible to define the conductance of the mono-atomic neck as the ratio of the current and the voltage drop across the wire. The modulus of the optical conductance (which is a complex number now) computed in this way at the CTP frequency is ~ 0.65 G_0, close to the expected value for a mono-atomic sodium wire at low frequency, G_0. In this case it was possible to define the conductance without ambiguity since the potential drop is confined to the gap region, with the electrostatic potential flat inside the clusters. For larger cross-sections of the necks and/or higher energies of the mode, this condition is not fulfilled and the definition of the conductance is hampered by the ambiguity of determination of the potential difference. The current associated with the CTP' mode follows the same trends than that of the CTP, although it shows a less pronounced dependence on the overall elongation of the system. Obviously, once the clusters separate the current becomes negligible.

The arrows in Figure 4.4.4 indicate the position of the jumps shown in Figure 4.4.1 (a). Except for the last jump at 29.3 Å, the other two jumps observed in the polarizability (Figure 4.4.1) and in the total energy (Figure 4.2.1) show a clearly correlated sudden change in the current. This points towards a remarkable effect of a few atoms (or even a single atom), whose motion influences the overall optical response of the dimer (containing 760 atoms in our case). This observation can be of utmost importance in the control and manipulation of optical signal in subnanometric junctions which are clearly affected by this type of physical processes at the atomic scale.

To establish a more direct connection between the computed current as a function of the gap separation within the junction and the well-known quantization of transport in metal nanocontacts, in the inset panel of Figure 4.4.4 we show the current for the CTP while retracting (left axis of the graph) plotted in relationship with the neck cross-section (right axis of the graph).

The neck formation during the retracting process opens the question of how to measure the neck cross-section. In particular, it is not obvious how to compare the cross-sections of necks with similar structures. Here we decided to use the distribution of the ground-state electron density as means of measuring the neck cross-section for an arbitrary structure. The density is computed in an (x, y) plane passing through the middle of the junction and the neck cross-section A_{cs} is obtained as the area where the electron density is larger than a given threshold

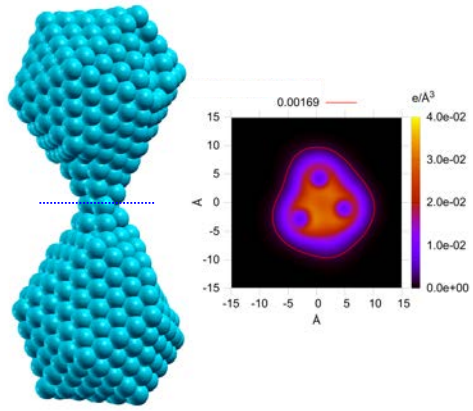

Figure 4.4.5: The neck section is calculated by analyzing the electron density in a (x, y) plane cutting the center of the neck. The right panel shows the 2D electron density distribution in that plane (blue dashed line). The red solid line represent the isocontour corresponding to a 0.00169 $e/\text{Å}^3$ threshold density. The cross-section is defined as the area of the region limited by such isocontour. We can clearly see that the neck cross-section is formed in this case by three Na atoms.

value ρ_{th} (see Figure 4.4.5). In other words, we use the integral

$$\begin{aligned} A_{cs} = &\quad \int\int dxdy \;\; f(\mathbf{r}) \\ \text{where} &\quad f(\mathbf{r}) = 1 \qquad \text{if } |\rho(\mathbf{r})| > \rho_{th}, \\ \text{and} &\quad f(\mathbf{r}) = 0 \qquad \text{if } |\rho(\mathbf{r})| < \rho_{th}. \end{aligned} \tag{4.5}$$

The value of ρ_{th} is arbitrary and was chosen here so that the radius of an isolated Na atom is 2.88 Å, a reasonable value if we compare to Na bulk density (characterized by Wigner-Seitz radius $r_s \sim$2.12 Å) and we take into account the spillage of charge towards vacuum in a finite object. In any case, the specific value of the cross-section assigned to a particular neck structure is irrelevant (as far as *reasonable*), the importance of this method is the ability to continuously monitor the cross-section change as the structure evolves.

As can be seen in Figure 4.4.4, there is an almost perfect correlation between the changes in the current and the evolution of the neck cross-section. Such correlation has been already well-established in the case of low-frequency driving-fields being applied to the necks. It has been observed in the formation of metal nanocontacts in Scanning Tunneling Microscopy (STM) and break-junctions experiments, and corroborated by some calculations [158]. Our Figure 4.4.4 goes one step beyond, establishing such correlation at optical frequencies. With this

additional piece of information, we can now summarize the results described in this section by unambiguously establishing the following cause-effect relationships: plastic deformation of the neck during elongation → cross-section reduction → abrupt drop of the current → decrease of the intensity of the CTP mode. This process is sometimes accompanied by small shifts of the position of the resonance peak. Finally, as mentioned above, more disordered structures translate into broader and dimmer CTP resonances.

4.5 Conclusions

In summary, we have shown how atomic-scale structural reorganizations are crucial to determine the optical properties of plasmonic cavities. Besides the importance of jump-to-contact events, that can almost completely eliminate any signature of the plasmonic tunneling regime, the effects are particularly dramatic when a metal nanocontact is formed across the cavity. This is due to the strong dependence of the plasmonic response of the system on the quantized current flowing through the connecting neck.

The mechanical response of atom-sized necks is characterized by sudden rearrangements of the atomic structure, which often involve just a few atoms in the thinner part of the contact. Since the electron transport through thin metal nanocontacts is quantized, the corresponding changes of the current flowing across the junction are necessarily discontinuous. Our calculations demonstrate that this common observation under small applied dc biases can be extrapolated to the optical frequencies of the plasmon resonances of the cavity, at least for the short ballistic contacts considered here. These jumps in the current translate onto abrupt changes in the plasmonic response of the system. Thus, the discontinuous evolution of the spectral position, width and intensity of the CTP mode observed in our simulations is a direct consequence of the transport quantization in the connecting neck.

The correlation is clearly demonstrated, showing that remarkably, optics follows the atoms. This is absolutely important in the design of subnanometric-scale optical modulators that rely on slight changes of the optical response against tiny configurational modifications. In our case we have analyzed relatively small icosahedral sodium clusters, however, we expect to find a similar behavior for other materials suitable for electronic applications, such as gold.

The effect of a single atom in the optical properties of a nanoscopic object as the one reported here, which can be probably extended to somewhat larger objects, has important consequences in optical engineering, molecular electronics, and photochemistry, where the optical response can now be tailored by a few atoms.

Chapter 5

Size Dispersion of the Plasmon Frequency in Metallic Clusters

An anomalous behavior of the plasmonic frequencies in the simple metal clusters has been attracting the attention of experimental and theoretical physicists for several decades. The red-shift of the plasmonic frequency as the size of the clusters diminishes is opposite to the expected size dispersion of the electronic properties. Plasmons in noble metal and semi-conductors blue-shift with smaller cluster size. In this chapter, we present large-scale *ab initio* atomistic calculations and characterization of the plasmonic resonances in sodium and silver clusters up to more than 5000 atoms. These unprecedentedly large calculations were realized using modest computational resources (32 CPUs, 512GB of RAM). The calculations became possible after the improvements of the iterative TDDFT algorithm which were described in section 2.3.2. The improvements of the algorithm were implemented during this work, and are one of the main results of this thesis. Our calculations reproduce the opposite plasmon dispersion versus size of sodium and silver nanoparticles, and reveal that the observed behaviors stems from the competition between the effects of quantum confinement and the material-dependent screening of the electron-electron interaction.

5.1 Experimental Evidence and Classical Picture

The interest in metal clusters is caused by their numerous applications such as sensors construction [185], enhanced spectroscopies [186], photovoltaics [187] and

medicine [188]. Driven by these prospective applications, a vast number of experimental [189–191] and theoretical [115, 192–194] studies have been performed to understand the dependence of the optical absorption spectra on material, shape and size of metal particles.

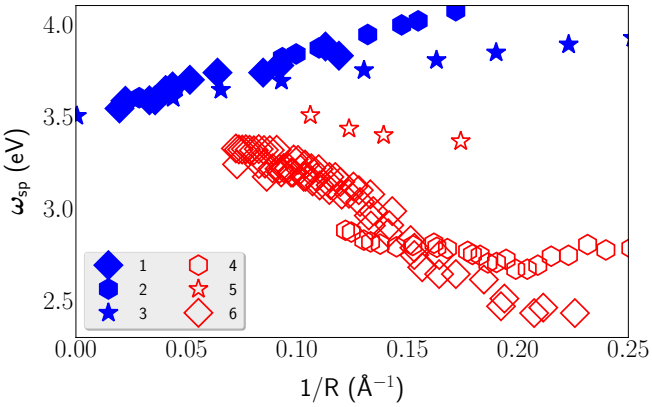

Figure 5.1.1: Experimental data on the frequency of maximal absorption for silver- (1,2,3, blue) and sodium (4,5,6,red) clusters. The data originates from: ◆ 1 – Ref. [189]; ⬢ 2 – Ref. [190]; ★ 3 – Ref. [191]; ◇ 4 – Ref. [195]; ⬡ 5 – Ref. [196]. ☆ 6 – Ref. [197];

Experimentalists found that the frequency of maximal absorption disperses linearly with the inverse characteristic size R^{-1} for both simple metal and noble metal clusters. However, the spectrum blue-shifts for noble metals (Cu, Au, Ag) [190, 193, 198] and red-shifts for simple metals (Li, Na, K, Al) [193, 197, 199, 200], when decreasing the cluster size, for particles much smaller than the wavelength of the exciting light. This size dispersion of the plasmon frequency can be seen in Figure 5.1.1, in which we collected experimental data for sodium and silver clusters.

To address the observed size dispersion from the theoretical point of view, one can resort to classical models within electrodynamics of continuous media [193], two of which [197] are summarized below. According to electrodynamics of continuous media, the optical spectra are determined by matching conditions for the potentials and fields at the cluster surface giving rise to the notion of the surface plasmon (SP). For a spherical particle with sharp boundaries, the frequency of dipolar SP is proportional to the bulk plasmon frequency $\omega_{\mathrm{sp}} = \omega_{\mathrm{p}}/\sqrt{3}$ (if a simple Drude model of dielectric function is assumed) and does not depend on the size of the particle R. (I) Because the bulk plasmon frequency ω_{p} is proportional to the electron density $\omega_p = \sqrt{n}$, one could explain the size dispersion of the SP frequency $\omega_{\mathrm{sp}} = \omega_{\mathrm{sp}}(R)$ by the spill-out of electron density beyond the limits of

the sharp classical sphere [201]. The spill-out of the conduction electrons leads to a more diluted electronic density $\tilde{n}$, which can be described by a size-independent increase d_g of the radius of an effective sphere $\tilde{R} = R + d_g$. In principle, one can assume that this gives rise to a reduction of the average density of conduction electrons in the system that results in a dispersion law

$$\omega_{\rm sp} = \frac{\omega_p}{\sqrt{2+\varepsilon_b}} \left(1 - \frac{3}{2}\frac{d_g}{R}\right), \tag{5.1}$$

(to the first order in $\frac{d_g}{R}$), where the effect of screening due to the presence of *bound* electrons is accounted via a dielectric function ε_b. The simplicity of this model makes it very appealing. However, in a metal particle, one can only expect deviations from the charge neutrality condition right at the surface. This is a problem for the rationale behind this simple argument that is based on the scaling of the bulk plasmon. (II) Alternatively, a similar expression for the SP frequency

$$\omega_{\rm sp} = \frac{\omega_{\rm p}}{\sqrt{2+\varepsilon_b}} \left(1 + \frac{3}{(2+\varepsilon_b)}\frac{d_i}{R}\right), \tag{5.2}$$

was derived within a formalism of the size-dependent dielectric functions by Apell *et al.* [115, 192, 193]. The Apell's parameter d_i is related to the distribution of the induced density $\delta n(\mathbf{r}; \omega_{\rm sp})$, rather than to the ground-state density invoked in explanation (I). Both classical models (I) and (II) imply a sign reversal of their respective parameters d_g or d_i in order to explain the size dispersion of SP frequency in simple metals versus noble metals. The validity of classical models is questionable for clusters containing several dozens of atoms, where quantum effects are expected to be determinant. In the present chapter, we analyze in detail the scaling of the surface plasmon resonance with size for silver and sodium particles using *ab initio* calculations. For this purpose, we analyze a realistic model of both materials, with access to the microscopic distribution of the induced electron density and where the screening of conduction and bound electrons (4d shell in Ag) is automatically included.

5.2 Clusters Structures and Ground-State Calculations Details

For the sake of a consistent comparison, we assume an icosahedral geometry [202, 203] as represented in Figure 5.2.1 for the Ag_{3871} cluster, which is known to be a very stable structural motif for small metal clusters [204]. The initial geometries were generated using the Atomic Simulation Environment (ASE) [19]. In order to get the optimal structure without relaxing the initial geometries (that would

be too much time consuming for the large clusters), we determined an optimal inter-atomic distance L to generate the ideal clusters geometries as close to the relaxed-cluster geometries as possible. The optimal inter-atomic distance L was determined individually for each material (sodium and silver). In the first step, we optimized the geometry of the Ag_{147} cluster using the conjugate-gradient algorithm and forces from the *ab initio* DFT. Using the optimized geometry, we found an effective inter-atomic distance ($L_0 = 5.620$ Bohr) providing the same distance between extremal atoms in the ideal and relaxed geometries. We computed the optical polarizability of the relaxed cluster to be used as the reference. In the second step, we created a series of ideal geometries of Ag_{147} cluster by varying the inter-atomic distance L around the optimal value L_0. Comparing the corresponding series of optical polarizability spectra we confirmed the best match with the relaxed reference is for the polarizability calculated with the inter-atomic distance L_0 determined from the extremal-atoms distance in the first step. The procedure was repeated for the sodium cluster Na_{147}. The optimal inter-atomic distance for sodium is $L_0 = 7.095$ Bohr. The obtained effective bond-length were used to generate the idealized geometries of the other cluster sizes. The ideal geometries were used in the TDDFT calculations of the optical polarizability. All the optical polarizability calculations done in this work (except the analysis in section 5.3.3) were done with these inter-atomic distances. We checked additionally that the deviation of the SP of the unrelaxed structures compared to the relaxed geometry for the larger clusters (up to the Ag_{1415}) is rather small (few meV). The electronic structure calculations of the Na and Ag clusters were performed using standard DFT as implemented in the SIESTA code [1, 2]. The resulting Kohn-Sham orbitals and energies were used as an input for the TDDFT calculations of the optical response using the iterative scheme described in section 2.3.

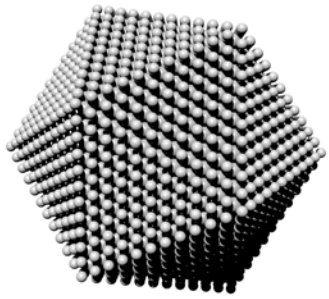

Figure 5.2.1: Silver cluster containing 3871 atoms (ghost atoms are not shown) presenting the icosahedral geometry we used in this work.

We used the GGA by Wu-Cohen (WC) [36] for Ag clusters and by Perdew, Burke and Ernzerhof (PBE) [35] for Na clusters, norm-conserving pseudopotentials to effectively account for the removed core electrons [122], and a DZP basis of NAOs generated using an energy shift of 100 meV [52]. The fineness of the real-space grid used to compute the Hartree and exchange-correlation contributions to the energy and Hamiltonian

corresponds to a plane-wave cut-off [2] of 250 Ry for both elements. In order to get a better dispersion trend for large sodium clusters, it is important to add a layer of ghost atoms [44, 205]. This layer of ghost atoms added in the calculations corresponds to a fictitious external layer of atoms. This allows a better description of the smooth decay of the electron density into the vacuum. For the sake of consistency, we added as well a layer of ghost atoms for silver clusters.

5.3 Size Dispersion from Atomistic *Ab initio* Theory

Quantum mechanical descriptions of plasmonic resonances were repeatedly demonstrated in the past. There have been several calculations within the jellium model [201, 206, 207] and later also with fully atomistic calculations [208–210]. For sodium clusters, a standard jellium model can reproduce the experimental trend for the size dispersion of the SP frequency, while for silver it is necessary to add a polarizable background [207]. The atomistic calculations of plasmonic resonances were done both with linear-response and wave-packet propagation methods [206, 211].

In this section, we analyze the size dispersion trends in silver and sodium clusters from an *ab initio* point of view, using atomistic and jellium models. For both models, we used the framework of Kohn-Sham TDDFT as described in the chapter 2. The atomistic calculations are done with the improved version of the linear-response method described in section 2.3 and Refs. [4, 44] that allows us to treat particles of unprecedented sizes [212].

For comparison purposes, jellium calculations were performed using the wave packet propagation methods described in Ref. [213]. The Wigner-Seitz radii of $r_s = 4.0$ and 3.02 Bohr are used for sodium and silver clusters correspondingly. The radius of the jellium positive background $R^+ = r_s N^{1/3}$ is chosen according to the number of atoms N for both materials. For silver clusters, a polarizable background is added to represent the screening of the electromagnetic field inside the cluster caused by 4d electrons. The polarizable background occupies a sphere of the radius $R_{\mathrm{pb}} = R^+ - 2.4$ Bohr within which a dielectric constant $\varepsilon_b = 4.58$ is assumed. We used LDA by Gunnarsson-Lundqvist [37] in the jellium model.

The maximum of the dipole polarizability (eqn. 2.91) of the metal cluster arises due to the SP resonance [44] and we determine the SP frequencies ω_{sp} as the location of these maxima as function of the cluster size.

The polarizability $\alpha(\omega)$ for a set of sodium and silver clusters is gathered in Figure 5.3.1. We can easily anticipate the opposite size dependence of the SP frequency ω_{sp} in sodium and silver. In Figure 5.3.2, we show the dependence of the SP frequency ω_{sp} on the cluster size both for the atomistic icosahedral clusters

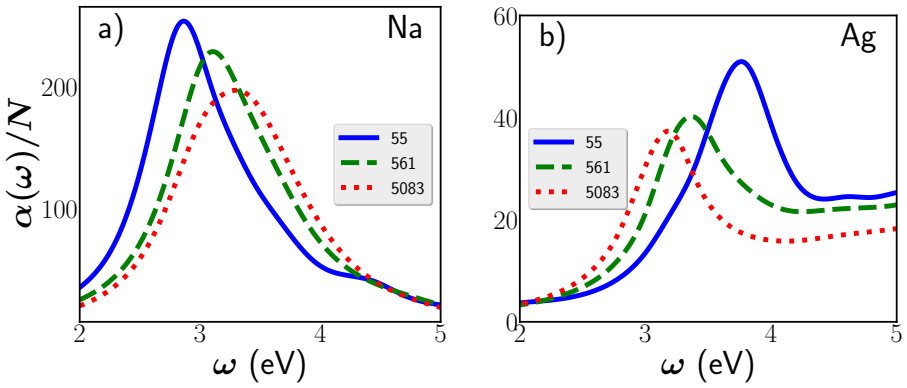

Figure 5.3.1: Optical polarizability per atom from our *ab initio* atomistic calculation for sodium (panel a) and silver (panel b) clusters. Clusters contain 55 (solid line), 561 (dashed line) and 5083 (dotted line) atoms.

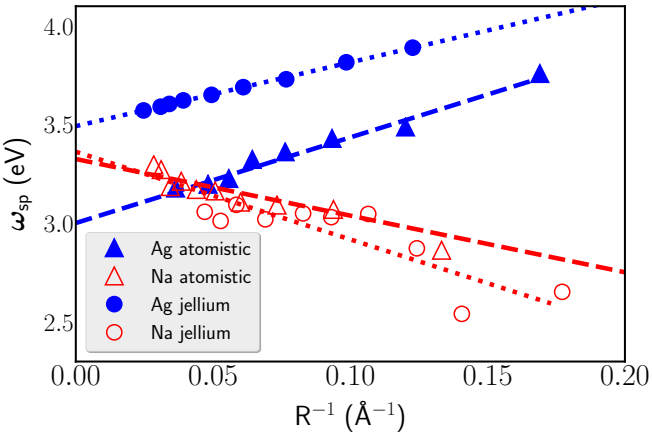

Figure 5.3.2: Theoretical results on the size dispersion of sodium and silver clusters. The SP frequency ω_{sp} dispersion for silver (blue) and sodium (red) is shown for *ab initio* atomistic (dots) and jellium (triangles) simulations. Cluster size is taken as the radius of the positive background R^+ in jellium calculations, and as the radius of a sphere of the same volume as that of each our cluster. The volume of each cluster is computed as the volume of one icosahedron with an edge length equal to the distance between two atoms defining the cluster's edge plus one interatomic distance between nearest-neighbor atoms.

and jellium spherical clusters. Comparing the Figures 5.1.1 and 5.3.2, we see that the theoretical results follow the experimentally observed trends despite the usage of simple semi-local density functionals. Therefore, we obtain a computationally

affordable, atomistic quantum mechanical model for a further analysis.

5.3.1 Electron-Electron Interaction and the SP Frequency

In a first analysis, we characterize the size dispersion of the maximum of the optical response as a function of the strength of the electron-electron (e-e) interaction between the electrons building up the induced density. In order to do so, we modify the TDDFT interaction kernel K, described in section 2.3.3 with a coupling constant λ

$$k = \lambda(f_{\mathrm{H}} + f_{\mathrm{xc}}), \tag{5.3}$$

where the Hartree kernel $f_{\mathrm{H}} = |\mathbf{r} - \mathbf{r}'|^{-1}$ is the bare Coulomb interaction and the exchange-correlation kernel $f_{\mathrm{xc}}[n]$ gives the modification of the exchange-correlation potential in response to a density change as explained in chapter 2. We denote the position of the λ-dependent polarizability maximum as $\omega_{\mathrm{sp}}(R, \lambda)$. Notice that for $\lambda = 1$ we have the plasmon resonances presented in Figure 5.3.2. In the limit $\lambda = 0$, we are mainly analyzing the effect of quantum confinement (QC) on the electron states as a function of the cluster size. The SP frequencies $\omega_{\mathrm{sp}}(R, \lambda)$, are presented in Figure 5.3.3 as a function of the number of atoms N for sodium and silver clusters, on panels (a) and (b) correspondingly.

Without e-e interaction, i.e. with a zero coupling constant $\lambda = 0$, the size dispersion in sodium and silver clusters becomes similar: the optical absorption maximum blue-shifts as we move to smaller cluster sizes, as we expected from QC effects (see Figure 5.3.3). Notice that this size dispersion is opposite to that observed in reality for Na, but qualitatively corresponds to that of Ag. In the limit $N \to \infty$, the SP frequency strives to a small non-zero value (~ 0.1 eV for both elements) which is below the broadening constant 0.15 eV used in the calculations. However, already a small e-e interaction significantly modifies the SP frequencies in sodium [see Figure 5.3.3 (a)]. A small coupling constant $\lambda = 0.2$ is strongly blue-shifting the SP frequencies, albeit still not reversing the size dispersion trend. However, a larger coupling constant $\lambda = 0.6$ results in a qualitatively correct, sodium-like behavior of the size dispersion trend. An artificially stronger e-e interaction $\lambda = 2$ makes the slope of the dispersion only steeper. Moreover, there is almost no change caused by explicit 2p electrons, which we demonstrated by including them into a semi-core shell and using a pseudo-potential modified accordingly.

In contrast to sodium, even the full e-e interaction $\lambda = 1$ or an artificially-increased e-e interaction $\lambda = 2$ makes the slope of the size dispersion in silver clusters less steep, but does not reverse the trend caused by QC [see Figure 5.3.3 (b)]. This comparison leads to the conclusion that QC is the determinant factor behind the size dispersion observed in silver.

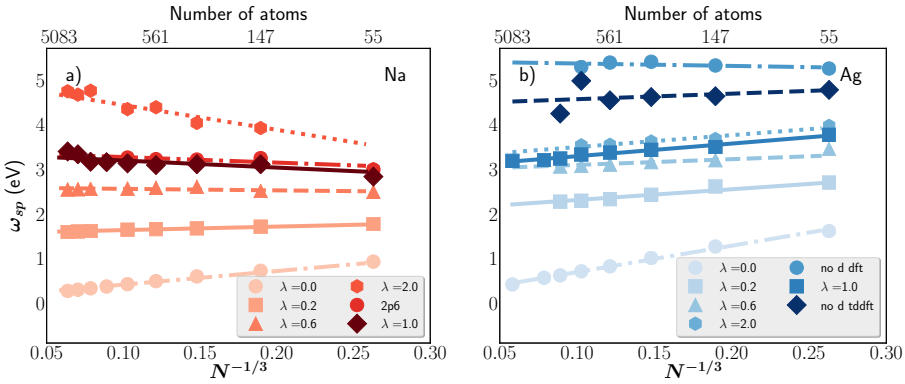

Figure 5.3.3: Size dispersion of the SP frequency as a function of competing factors from our atomistic TDDFT. Notice the different scales along vertical axis in this Figure and Figures 5.1.1 and 5.3.2. For sodium (panel a) and silver (panel b), we show the size dispersion as the function of e-e coupling strength, represented by a coupling constant λ. We show also the trend taking into account the 2p6 electrons for sodium, and removing the 4d electrons for silver with a coupling constant $\lambda = 1$.

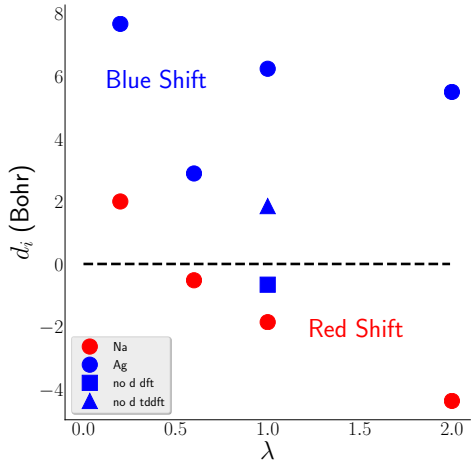

Figure 5.3.4: Variation of the parameter d_i calculated with equation (5.7) using the data from Figure 5.3.3 as function of the coupling constant λ. The change of sign is clearly visible for Na (red dots), but no changes are observed in the case of Ag (blue dots). When calculating d_i for Ag without d-electrons, then the parameter change of sign (blue square). This indicates that eliminating the screening caused by the 4d-shell allows the plasmon dispersion to be dominated by the effect of the Coulomb interaction.

Using equation 5.2, we can easily extract the Apell's parameter d_i from the slope of the lines in Figure 5.3.3. Since the radius R of the icosahedral particles is not well defined, we can express eqn. (5.2) as function of the number of atoms N that we perfectly know noting that $R = r_s N^{1/3}$

$$\omega_{\rm sp}(N^{-1/3}) \quad = \quad \frac{\omega_{\rm p}}{\sqrt{2+\varepsilon_{\rm b}}} - \frac{3\omega_{\rm p}}{r_{\rm s}\left(2+\varepsilon_{\rm b}\right)^{3/2}} d_i N^{-1/3}, \tag{5.4}$$

then

$$\omega_{\rm sp} = aN^{-1/3} + b, \tag{5.5}$$

where

$$a = -\frac{3\omega_{\rm p}}{r_{\rm s}\left(2+\varepsilon_{\rm b}\right)^{3/2}} d_i, \quad b = \frac{\omega_{\rm p}}{\sqrt{2+\varepsilon_{\rm b}}}, \tag{5.6}$$

d_i is then easily obtained

$$d_i = -\frac{2+\varepsilon_{\rm b}}{3}\frac{a}{b} r_{\rm s}. \tag{5.7}$$

The extracted values of d_i (using $\varepsilon_{\rm b} = 1.0$ and $\varepsilon_{\rm b} = 4.58$ for Na and Ag respectively) are represented in Figure 5.3.4 as function of the coupling constant λ. A large value of d_i indicates a strong energy shift with the size, if $d_i < 0$, then the energy of the surface plasmon will be red shifted when N decreases, while it will be blue shifted if $d_i > 0$.

For sodium, we clearly see, that for weak e-e interaction $\lambda < 0.5$, the surface plasmon frequency blue-shifts for smaller clusters as one would expect from QC. However, when the interaction is stronger ($\lambda > 0.5$), the energy is red-shifted as the size of cluster decreases as it is actually observed experimentally. The variation of d_i as function of λ is nearly linear (except for $\lambda \ll 1$). In contrast to sodium, silver does not reverse trend when λ increases (blue dots in Figure 5.3.4). In fact d_i reaches a minimum value for $\lambda = 0.6$, and then increases again. The minima for silver can be explained by the screening caused by 4d electrons which is modified by the coupling constant λ. When the e-e interaction increases, the strength of the inner dipoles created by the d electrons increases, opposing a stronger force to the surface dipole created by the 5s electrons and therefore diminishing the effect of the bare Coulomb interaction.

The reason for the very different effect of the Coulomb interaction in the response of Na clusters can be immediately seen in the maps of the induced density $\delta n(\mathbf{r}; \omega_{\rm sp})$. Figure 5.3.5 shows the induced density in a plane bisecting

the Na_{2869} and Ag_{2869} clusters [panels (a) and (b) correspondingly]. In the case of sodium, the induced density is predominantly concentrated on the cluster surface, while there is a substantial amount of induced density located in the interior of the silver cluster. The induced density in the interior of the silver cluster is mostly caused by the strongly bound 4d electrons. The resonance frequency of these 4d electrons is higher than the SP frequency and, for this reason, their polarization appears with opposite phase with respect to that of the conduction electrons, leading to the screening of the Coulomb interaction among conduction electrons.

To quantify the effect of 4d electrons in the size dispersion, we performed yet another set of calculations switching off the contribution of 4d electrons. For this purpose, we tried two methods. In the first method, we excluded the 4d electrons from the valence shell and treated them as core electrons at the level of pseudo-potential, i.e. fully removing them from the DFT/TDDFT calculations. The corresponding size dispersions of the SP frequency are shown in Figure 5.3.3 with blue circles on panel (b), while the corresponding polarizabilities are shown in Figure 5.3.6, panel (a). In the second method, we removed the 4d electrons at the TDDFT level. For this purpose, before performing the TDDFT iterations, we excluded the KS eigenstates with a predominant 4d character in the formation of the non-interacting response functions χ_0. The selection of KS states was made according to the partial density of states. The corresponding size dispersions of the SP frequency are shown in Figure 5.3.3, with dark-blue diamonds on the panel (b), while the corresponding polarizabilities are shown in Figure 5.3.6, panel (b). In both cases the energy of the SP resonance increases substantially with respect to the calculations including the 4d electrons. With the first method, the SP frequency shift is slightly red-shifted, giving the opposite trend of "normal" silver, as shown by the blue square of Figure 5.3.4. In contrast to the first method, the second method of eliminating the 4d states leaves the dispersion trend qualitatively the same as for the "true" silver (see blue triangle in Figure 5.3.4). The polarizability of the silver clusters with the removed 4d electrons at TDDFT level [Figure 5.3.6, panel (b)] exhibits the slight decrease of the SP frequency for small clusters, while for larger clusters the SP resonance becomes split with the low-frequency resonance strongly red-shifted. The strong mode splitting hampers the determination of the size-dispersion trend. Previously, we determined the SP frequency as the frequency of the most intense peak in the polarizability. Continuing to do so for the polarizability in Figure 5.3.6, we observe a slightly weaker red shift of the SP frequency which does not reverse the trend of the real silver clusters.

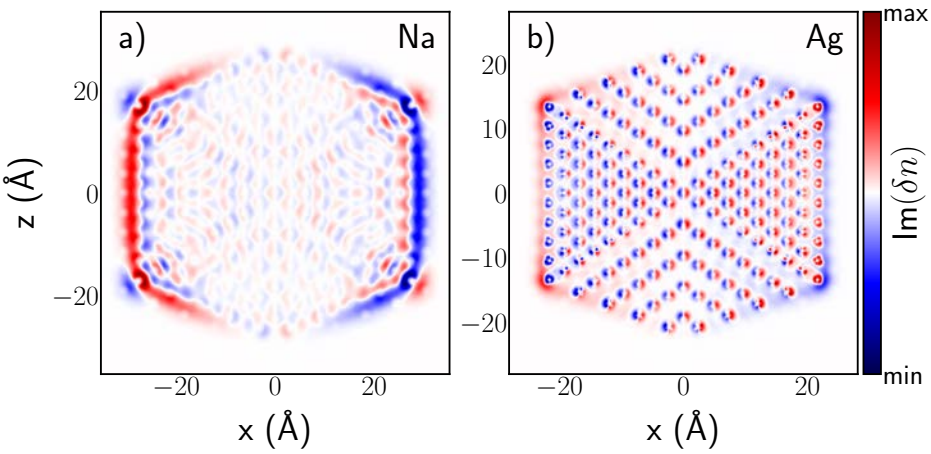

Figure 5.3.5: Distribution of the imaginary part of induced density change $\delta n(\mathbf{r}; \omega_{\text{sp}})$ for (a) sodium and (b) silver clusters containing 2869 atoms (10 atomic layers).

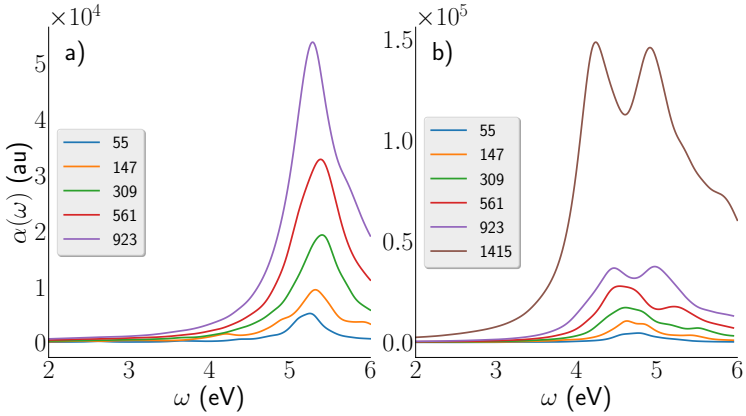

Figure 5.3.6: Imaginary part of the polarizability along the xx axis for silver clusters without d electrons. Panel (a) shows the polarizability when the 4d electrons have been excluded from the pseudo-potential (at the DFT level), while in (b) the eigenfunctions with larger contributions from 4d orbitals have been excluded from the response functions χ_0 (i.e, only at the TDDFT level).

5.3.2 Centroid of Charge at the Cluster Surface

As we mentionned in section 5.1, we can describe phenomenologically the size dispersion of the SP frequency $\omega_{\text{sp}}(R)$ within a formalizm of size-dependent dielectric functions [115] using a size-independent parameter d_i (see eqn. 5.2). The

sign of the parameter d_i defines the trend of the frequency shift: if $d_i < 0$, the SP frequency $\omega_{\rm sp}$ is red-shifted when R decreases (as shown by the red lines of Figure 5.3.2), and vice versa. Apell *et al.* [115] have shown that the parameter d_i is proportional to the centroid C of the distribution of induced charge at the surface

$$d_i = R - C, \quad \text{where} \quad C = \Re \frac{\int \mathbf{r}\delta n(\mathbf{r};\omega_{\rm sp})d^3r}{\int \delta n(\mathbf{r};\omega_{\rm sp})d^3r}. \tag{5.8}$$

Therefore, using the spatial distribution of the induced density calculated from our *ab initio* calculations (for example the colormaps show in Figure 5.3.5), we could calculate the value of d_i. Since the radius of the icosahedral particles is not well defined, it is easier to use the number of atoms, inserting the Wigner-Seitz radius of the cluster $R = r_s N^{1/3}$ in the last equation, $C = r_s N^{1/3} - d_i$.

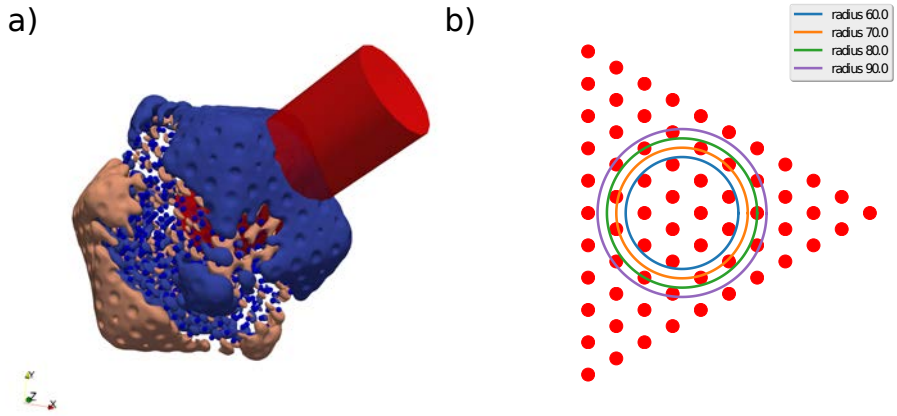

Figure 5.3.7: The integration volume and the diameter of the cylinders over the facet used to compute the centroid of charge C out of the atomically resolved induced density $\delta n(\mathbf{r};\omega_{\rm sp})$. Panel (a) shows the spatial distribution of the imaginary part of the density change for the Na_{923} cluster. The red cylinder represents the integration volume. Blue and brownish iso-surfaces stand for opposite signs of the induced density. Panel (b) shows the position of the atoms on the triangular facet for the Na_{1415} (red dots). The 4 circles represent the cylinders used for the integration.

Because the number of atoms N is the parameter in our atomistic calculations, we can linearly fit the calculated centroid of charge C and extract the effective Wigner-Seitz radius r_s and the parameter d_i simultaneously. The integrations for the calculation of the centroid of charge C should be performed in a suitable volume to avoid the edges and tips of the icosahedral clusters. Because, the

surface of the icosahedral clusters consists of triangular facets, we chose to apply the external field perpendicular to a given facet. We then integrate the induced density inside a cylinder parallel to the external field and with its axis passing through the center of the facet. We used cylinder radii between 60% and 90% of the radius of the circle inscribed in the triangular facet as shown in Figure 5.3.7 (b) to avoid issues with the facet boundaries and limit any edge effects from modifying the results.

species \ kernel strength λ		0.0	0.2	0.6	1.0	2.0
Na d_i (Bohr)	Polarizability	115.70	2.0	−0.52	−1.86	−4.38
	Centroid	–	3.86	1.38	−1.41	–
Ag d_i (Bohr)	Polarizability	398.30	7.67	2.89	6.24	5.50

Table 5.1: The dispersion parameter d_i obtained both, from the scaling of the computed plasmon resonances polarizabilities and, in the case of sodium, from the centroid of the induced charge density for $\lambda = 0.2, 0.6, 1.0$.

In the direction perpendicular to the facet, the integration volume defined by the cylinder starts from the center of the cluster and extends beyond the spatial support of the basis functions [Figure 5.3.7 (a)]. Panels (a) and (b) of Figure 5.3.8 show the real and imaginary part of the induced density $\delta n(\mathbf{r};\omega)$ along the cylinder axis for the systems of interest (for clusters composed of 1415 atoms). Panels (c-f) of the same Figure represent the density change centroid C as function of the number of atoms $N^{1/3}$. Panel (c) shows data for sodium clusters. As one can see, there is a clear linear relationship between the centroid of charge and the number of atoms. This indicates that, as we have seen already in the plot of Figure 5.3.5, the induced density of Na is centered at the surface of the clusters. It is then easy to extract the Wigner-Seitz radius r_s (from the slope of the line) and the d_i parameter (value of the centroid at $N = 0$). We calculated 3.75 Bohr for r_s and −1.41 Bohr for d_i. These values are comparable to those that we got from the dispersion of the SP frequency in Figure 5.3.2 ($d_i = -1.86$ Bohr). As one can see on panel (d) of Figure 5.3.8, the case of silver is more complex. The value of the centroid C are strongly dependent on the radius of the cylinder. The centroids C are scattered and no linear behavior can be extracted. Therefore, no meaningful values for r_s and d_i could be extracted via the centroid of charge for silver clusters with any diameters of the integration cylinders. The unsteady values of the centroid C are caused by the more complex spatial distribution of the induced density in silver clusters. In particular, the induced charge density $\delta n(\mathbf{r};\omega_{\mathrm{sp}})$ extends deep inside the bulk of the cluster. This is mainly due to the presence of the bound 4d electrons that polarize along the

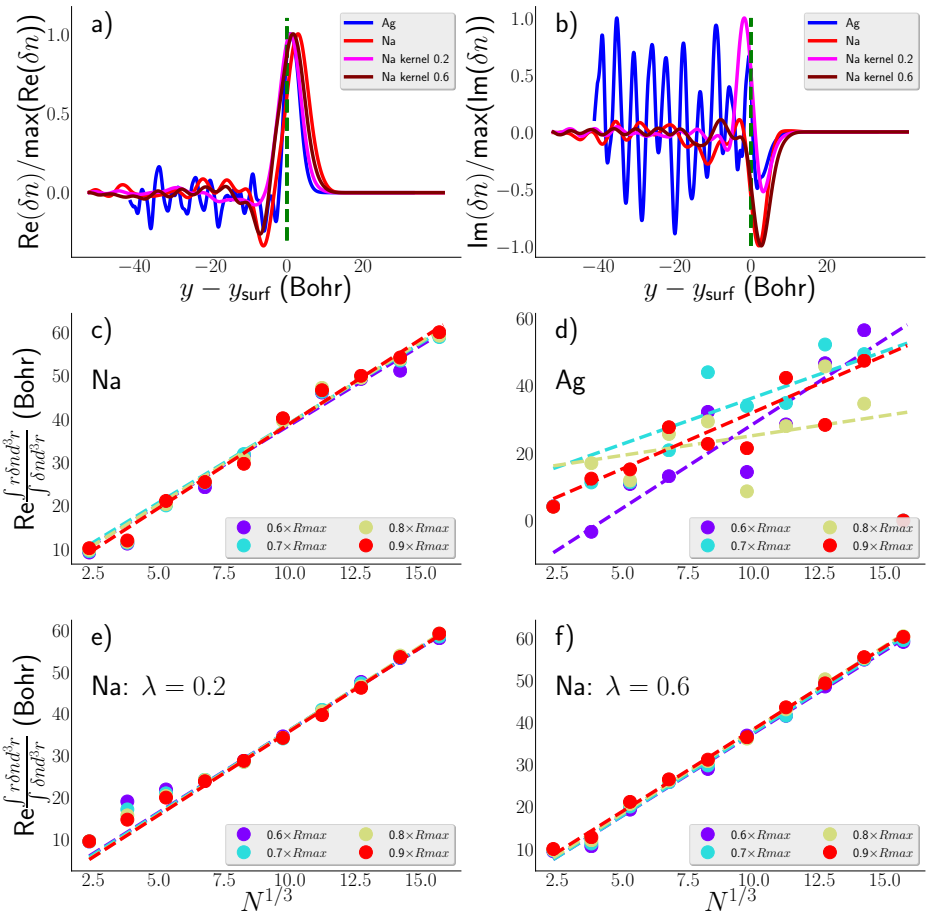

Figure 5.3.8: Analysis of *ab initio* induced density $\delta n(r;\omega_{\mathrm{sp}})$. Panels (a) and (b) show the values of the real and imaginary part, correspondingly, of an average induced density along the axis $\hat{n}$ of the integration domain as function of the position in the cluster (normalized to the cluster "surface"). Panels (c-f) show the linear relation between the centroid of charge and the number of atoms (eqn. 5.8) for different cylinder radii for the following systems, sodium, silver, sodium with 20% of kernel interaction and sodium with 60% of the kernel interaction. As can be seen clearly from the results in panel (d), for Ag is not possible to define a meaningful centroid of charge because the induced charge extends deep inside the bulk of the cluster

whole structure screening the field created by the accumulations of conduction electrons at the cluster surfaces. We extracted as well the trend of the frequency

shift of sodium with weaker electron-electron interactions (Figure 5.3.3). Panels (e) and (f) of Figure 5.3.8 show the corresponding change of the centroid for $\lambda = 0.2$ and $\lambda = 0.6$. In these cases the sign of the extracted d_i is opposite to the fully-interacting case [$\lambda = 1.0$, see panel (a) in Figure 5.3.8]. The values of the d_i parameter are collected in table 5.1. The values of the d_i parameter extracted from the SP dispersion or from the centroid of charge C behave similarly with the charge of the coupling constant λ. For instance, the d_i parameter is positive for the small value of the e-e interaction $\lambda = 0.2$ and becomes negative at the full coupling $\lambda = 1$ for both methods of calculation. However, at the intermediate coupling strength, the sign of the d_i parameters differ depending on the method of calculation.

From the analysis presented here we can conclude that, as pointed out by Apell *et al.* [115, 192] and other authors, there is some levels of correlation between the position of the centroid of induced charge relative to the surface and the sign of the dispersion of the SP resonance with size. However, we could only establish such relation for sodium and artificial variants of sodium where the strength of the Coulomb interaction has been modified. In the case of Ag, the complexity of the induced charge distribution precludes a meaningful definition of the centroid of charge. The main difficulty is related to the presence of bound electrons (4d shell), which are not free to move across the cluster, in addition to conduction electrons similar to those present in simple metal clusters. The screening charge associated with 4d electrons extends deep into the bulk of the cluster and, as a consequence, the centroid of charge is not anymore solely linked to the surface position. For Ag we tried to make a partition into "bound-electron" and "conduction-electron" contributions to the induced charge in order to estimate the centroid of induced charge of the free-carriers using only the last component. However, this turned out to be rather cumbersome. Therefore, we are forced to conclude that the centroid of induced charge density is an ill-defined concept for silver nanoparticles.

5.3.3 Impact of the Average Inter-Atomic Distance

To get additional understanding of the SP dispersion trend within our atomistic models, we tested the effect of the inter-atomic distance L on the SP dispersion. In Figures 5.3.9 and 5.3.10, we gathered the polarizability curves and the SP dispersion trends for sodium and silver clusters correspondingly. The inter-atomic distance L plays a role in the SP dispersion trend, but it does not reverse the trend. We used three inter-atomic distance L, 5.62, 7.095 and 8.2 Bohr and computed the SP dispersion for the series of small clusters $55 \leq N \leq 923$, where N is the number of atoms. The value $L = 5.62$ Bohr is matching the optimal inter-atomic distance of silver, while the value $L = 7.095$ Bohr is matching the optimal inter-atomic distance for sodium. The value $L = 8.2$ Bohr corresponds

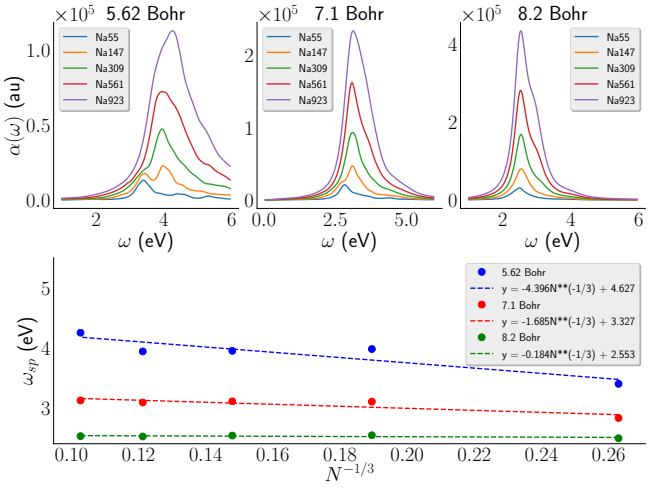

Figure 5.3.9: Impact of the inter-atomic distance L on the SP frequency dispersion trend for sodium. Top row panels show the optical polarizabilities, while the bottom panel shows the SP frequencies as function of the number of atoms $N^{-1/3}$ in the cluster.

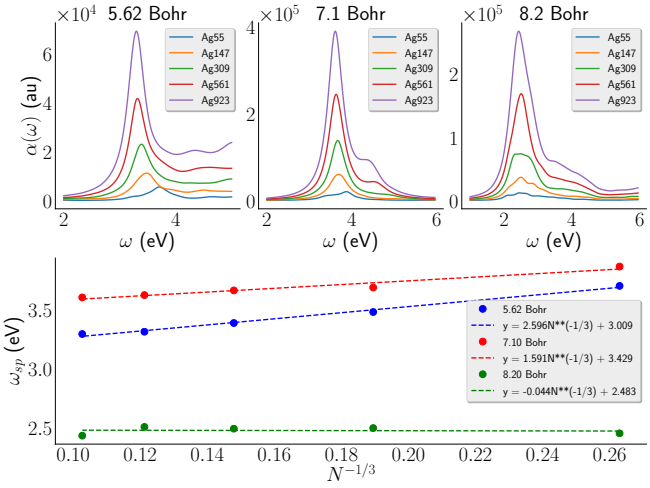

Figure 5.3.10: Impact of the inter-atomic distance L on the SP frequency dispersion trend for silver. Top row panels show the optical polarizabilities, while the bottom panel shows the SP frequencies as function of the number of atoms $N^{-1/3}$ in the cluster.

to the extreme dilution of the electron density. For this inter-atomic distance, the SP frequency dispersion is flat for both materials. When the clusters get compressed ($L = 7.095$ and 5.62 Bohr), the SP frequency dispersion becomes visible. However, there is no sign-change in the dispersion trend neither for silver nor for sodium clusters.

5.4 Conclusions

Thanks to improvements in our iterative TDDFT code that have been implemented during this thesis, we were able to calculate the polarizability and the induced charge density distribution for metallic clusters of sizes ranging from a few atoms up to more than 5000 atoms. The software enhancement allowed us to study the SP frequency dispersion in such large metallic clusters with atomistic *ab initio* methods for the first time. The calculations presented here prove that current *ab initio* TDDFT can be used to successfully describe and gain an understanding on the plasmonic properties of nanostructures of different chemical compositions. In particular, we have revealed the competition between the size dispersion determined by quantum confinement and by Coulomb interaction, the former dominating in Ag due to the d-screening that weakens effective e-e interactions.

Comparing the pictures provided by the classical and quantum mechanical theories, we see that most of the classical explanations are based on some surface models (of the average electron density or of the distribution of the screening charge at the surface). In our quantum mechanical approach, we explain the different size dispersion of Na and Ag as a result of the competition between QC effect and the strength of the Coulomb interaction between conducting electrons. The Coulomb interaction is weakened by the screening created by the bound 4d electrons in the case of silver clusters. Our calculations in the non-interacting and weakly interacting ($\lambda \ll 1$) testify that the crucial effect governing the size dispersion is QC. Moreover, the classical microscopic picture of the induced density clumping at the surface can be confirmed only for sodium clusters.

We think that the detailed input provided by *ab initio* calculations will contribute to increase our understanding of the main ingredients determining the energy position and other characteristic of the surface plasmon resonances, guiding the design of plasmonic particles by controlling their composition or their coating. The methods we used in this work are sufficiently general and can be applied to both metallic and semi-conductor clusters with arbitrary composition.

Chapter 6

Valence Electron Energy Loss Spectroscopy: an *Ab Initio* Approach

The application of electron microscopy for the characterization of nanoparticles has greatly improved our knowledge of the objects at the nanoscale. The interpretation of the images generated in electron microscopes involves the theory of condensed matter systems which is based on the quantum mechanical description of the electrons inside the material. An atomistic *ab initio* theory is thus a viable, and sometimes necessary, framework for the correct modeling of electron energy loss spectroscopy (EELS). However, because of its high computational complexity, *ab initio* theory is difficult to apply in many experimentally relevant situations involving nanoobjects composed of hundreds or thousands of atoms. In the previous chapters, we studied metal clusters under the perturbation of a spatially homogeneous external electric field. In this chapter, the perturbation will be an electric field generated by an uniformly moving electric charge. The perturbation caused by the uniformly moving electric charge is an excellent model of the electromagnetic field created by the fast probing electrons in an electron microscope. Here, we realize the perturbation within the linear-response TDDFT in order to model the spatially resolved EELS in finite systems. The realized theory of EELS was summarized in section 2.3.6 of this thesis. In this chapter, we applied the theory to a number of experimentally relevant systems. The computed EELS match well the experimentally measured spectra. For instance, the computed EELS of carbon and boron nitride nanotubes and silver clusters show an excellent agreement with the experimental data. Further calcu-

lations of silver clusters and silver cluster dimers permitted to analyze the role of the plasmonic response in EELS within an atomistic *ab initio* approach for finite objects of unprecedented size.

6.1 Motivation

The presence of geometrical features in nanomaterials with dimensions well below the wavelength of optical light strongly limits the relevance of light spectroscopy to study many of their properties. The limited spatial resolution of optical spectroscopy fostered the elaboration of new spectroscopic techniques. One of the alternatives to light spectroscopy is to use electrons instead of photons as done in EELS. Since the wavelength of the electrons can be made much shorter than the one of optical light, EELS leads to subnanometer spatial resolution [214–216] and yet with a very good energy resolution [73, 74]. Furthermore, using sufficiently energetic electron beams it is possible to create high-energy excitations involving core-electrons at individual atoms, thus allowing the analysis of the chemical composition of the sample with high spatial resolution [217, 218]. Because of these exceptional characteristics, EELS is revealed to be a powerful tool for the characterization of nanoparticles such as carbon and boron nitride nanotubes [219–222], structure determination of biological molecules [223], measurement of specimen thickness [217, 224–226], or in the study of the localized surface plasmon in noble metals [227–229]. Plasmonic features are particularly pronounced in silver, making it one of the most used material for nanophotonics applications [13, 230, 231]. Thus, silver clusters and cluster dimers have been widely studied by electron microscopy [232–237]

The range of the energy-loss spectrum up to 50 eV, also called low energy loss, is particularly attractive for nanophotonics applications [238]. In many materials, the main loss resonances in this range correspond to collective oscillations of the conduction or valence electrons, giving rise to the notion of plasmon. In other materials, interband transitions appear directly in the low loss spectrum as a series of peaks or fine structure superimposed on the plasmon peak. In all cases, the low loss spectrum is characteristic of the material exposed to the electron beam and can sometimes be used to identify it. Furthermore, in the low loss regime, by optimizing specimen preparation and EEL spectra collection time, it is possible to dramatically reduce the sample damage and thus, achieve non-destructive measurements characterizing the intrinsic properties of materials in the spirit of other spectroscopy techniques [234].

The theory describing the excitation of low-energy valence electrons in nanoparticles created by moving charges has been already explored at different levels of approximation [73–75, 232]. The most widely used method to calculate the response of a system perturbed by swift electrons consist in calculating the inverse

of the dielectric function ε in momentum space [239–241]

$$\Gamma_{\mathrm{EELS}}(\mathbf{q};\omega) = -\Im\left(\frac{1}{\varepsilon(\mathbf{q};\omega)}\right) \tag{6.1}$$

at a given excitation energy ω and momentum transfer $\mathbf{q}$. The dielectric function $\varepsilon(\mathbf{q};\omega)$ can be obtained using various models such as classical electromagnetism theory [147, 242], quantum jellium [243] or quantum atomistic [220, 244–248]. In this approach, the electron probe is described in momentum space using plane-wave expansion, which is perfectly valid and appropriate for electrons in vacuum, i.e., a wide electron beam. However, in order to simulate a specific beam trajectory, the momentum space approach is not the optimal option. A real space methodology is more appropriate to simulate the response of a microscopic system to the perturbations caused by the atomically precise positioned electron beams. Suitable real-space methods to describe energy loss processes have been proposed using real-time wave-packet propagation techniques. In most cases the probing projectile, either an electron or an ion, is treated as a particle moving along a classical trajectory [243, 249, 250]. More scarce are the methods in which both, probe and target electrons, are treated quantum mechanically using TDDFT and other similar time-dependent approaches [251]. Real-time propagation applied to the target's electrons is, in principle, a universal method to describe electron excitations beyond linear-response. Furthermore, with a suitable implementation, it can be quite efficient and, for example, it has been proposed as a suitable alternative to compute optical response in large systems as already mentioned in chapter 2 and in Refs. [235, 252]. However, one of the main limitations of such approach is the poor energy resolution, which is typically limited by the duration of the entire simulation, and the difficulties to correlate the computed losses with specific resonances and modes of the system. Thus, we found that the combination of our efficient iterative linear-response scheme with the description of the probing electrons as moving point charges provides a very efficient way to describe the EEL spectra of large nanoparticles. In the following, we convincingly show that the linear-response regime is sufficient to successfully address most relevant situations in EELS experiments, and to obtain a good qualitative agreement with experimental results in many cases.

In section 2.3.6, we summarized the equations behind our original real-space implementation of EELS within the linear-response TDDFT. In this chapter, we will apply the new method to a number of experimentally relevant nanoscopic objects. The rest of the chapter is organized as following. In section 6.2, we compare the computed EELS spectra of carbon nanotubes, boron nitride nanotubes and small silver clusters with experimentally acquired EELS. In section 6.3, we discuss the EELS of silver clusters and silver cluster dimers in a more detailed manner, analyzing the spatial distributions of induced densities dependent on sev-

eral parameters such as the beam positioning, velocity of the probing electrons, and the geometrical arrangement of the clusters.

6.2 Validation of the Method

With the intention to validate our method, we compare in this section the EELS signal of three systems obtained with the approach described in the section 2.3.6 to available experimental data. We performed EELS calculations for carbon and boron nitride nanotubes, as well as silver cluster. The ground-state DFT calculations were performed using the SIESTA package [1, 2]. A double-ζ polarized basis set of numerical atomic orbitals generated using an *energy shift* [2] of 25 meV was used for the nanotubes, and of 100 meV for the silver cluster. The core electrons were removed by means of Troullier-Martins pseudo-potentials [122]. We used the Perdew-Burke-Erzenhorf density functional (GGA-PBE) [35] for the nanotubes and the Wu-Cohen density functional (GGA-WC) [36] for the silver cluster. The TDDFT calculations were performed using the Local Density Approximation (LDA) kernel and the probe-electron velocity was fixed at 75 a.u. ($\sim$ 100 keV) for all calculations.

6.2.1 Carbon Nanotube

Carbon nanotubes are quasi-one-dimensional (1D) objects whose structure is obtained after rolling up one or several graphene sheets to form cylinders of nanometric diameter. CNTs possess a number of exceptional properties. Their peculiar electronic structure—metallic versus semiconducting behavior—depends sensitively on the diameter and chirality of the tube [253]. CNT have been studied extensively in the low loss regime to characterize their π and σ plasmonic resonances. Stéphan *et al.* [219] performed such kind of experiments and they have made freely available their measured spectra of CNT [254]. One of the spectra from Stéphan *et al.* is shown in Figure 6.2.1 by the red line. The experimental spectrum was obtained by shooting the electrons near the surface of a single wall CNT of 2.2 nm diameter and of several tens of nm length with an armchair geometry. The kinetic energy of the probing electrons is 100 keV. The electron beam follow a trajectory in grazing incidence over the surface of the CNT and perpendicular to the tube's axis as shown in the inset of Figure 6.2.1 by the blue circle together with the tube structure. This particular spectrum was chosen because of the relatively small diameter of the CNT from which it was obtained. Nevertheless, the size of the tube is still too large for our calculations, therefore, we used a CNT of 1 nm diameter, 5 nm length and with an armchair chirality for a total of 624 atoms. The initial geometry of the CNT was generated with the

ASE suite [19] and then relaxed with the SIESTA package until the remaining internal forces were lower than 0.04 eV/Å.

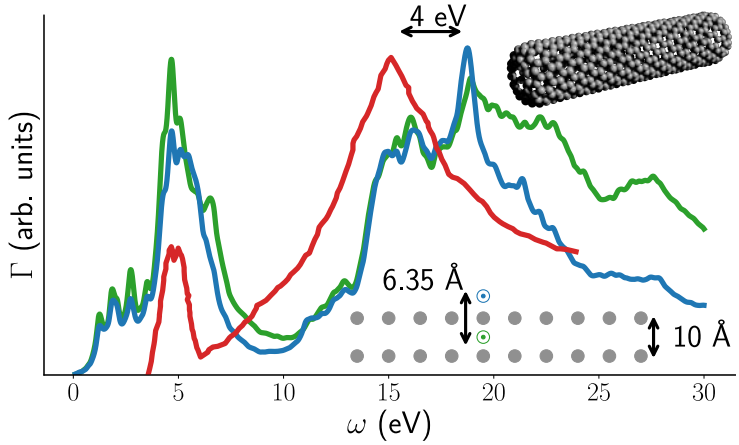

Figure 6.2.1: Comparison of measured and computed EELS for a single-wall carbon nanotube of small diameter. The calculated spectra were obtained for a SWCNT with a diameter of 1 nm, 5 nm length. The spectra were obtained for two trajectories, both perpendicular to the tube's axis. One crossing the tube at its center (green line) and the second in grazing incidence over the surface of the CNT (blue line). The experiments (red line) were performed for a SWCNT of 2.2 nm of diameter and several nm of length and for an external trajectory perpendicular to the tube's axis (similar to the blue trajectory in the scheme). In the top right corner is represented the structure of the tube used for the calculations. In the lower part of the figure, we show the 2D projection of CNT geometry with the positions of electron beams indicated by the green and blue open dots, the trajectories pass across the central region of our finite CNTs. The color coding of the dots match the color coding of the calculated spectra. The energy of the probing electrons was 100 keV in the experiment and in the calculations.

The π and σ plasmons measured by Stéphan *et al.* [219] are located around 4.8 and 15.1 eV respectively, with the high frequency σ plasmon presenting a broader and more intense peak. We computed the EELS spectra for two trajectories, both perpendicular to the tube axis. The first beam trajectory crosses the tube at its center (blue line) while the second passes near the tube surface (green line). The position of the beams relative to the tube are represented in the inset of Figure 6.2.1. The color of the beams matches the one of the spectra. The frequency of the π plasmon is around 5.1 eV for the two computed beam trajectories, which compares very well with the experimental peak position around 4.8 eV. However, the case of the σ plasmon is more complex. When the electron crosses the tube at its center, the σ peak is very broad and has its maximum around 20 eV. For the second trajectory, the resonance is less broad (similar to the experimental one) and shows a clear peak around 18.75 eV. Nevertheless, in

both cases, we observe a frequency shift of around 4-5 eV with respect to the experimental value.

The deviations of the simulation with respect to the experiment have various origins. The most obvious one is the smaller size used for our calculations that differs from the experimental one. The tube used for the measurements performed by Stéphan *et al.* has a diameter twice bigger and a length one order of magnitude larger. Furthermore, the quasiparticle spectrum given by the static version of the functional we utilize here (GGA) is known to have some limitations that are likely to show up also in the TD-GGA calculations of relatively large objects like this finite tubes [255, 256]. In the more technical side, the results might be influenced by the limitations of our DZP basis set of numerical atomic orbitals to represent excitations of such high energy. Finally, we do not take into account the substrate present in experimental measurement nor do we account for the effects of the atomic motion caused by finite temperature. In spite of the problems to reproduce the losses associated with σ peak, we can see that the π peak is well represented and the average shape of the spectrum has a reasonable match with the experimental result.

6.2.2 Boron Nitride Nanotube

Similarly to CNT, the boron nitride nanotubes (BNNTs) are formed by rolling up sheets of hexagonal boron nitride, another layered material with a structure closely related to that of graphene. However, the electronic properties of BNNTs contrast sharply with those of CNTs. They present a more uniform behavior with a wide band-gap (larger than 4 eV), almost independent of diameter and chirality [257, 258]. In this work, we use the experimental measurements of the single wall BNNTs performed by Arenal *et al.* [221]. The experiments were done for 20 nm long and 1 nm diameter single-walled tube. The majority (85%) of the tube sample possess a zigzag chirality [259], but the chirality of the specific tube used for these measurements was not precised in the text. The electron beam crosses the tube approximately in its center. The experimental data were obtained directly from the EELS database [254]. We performed calculations for a shorter tube (5 nm) but with the same diameter as in the experiment (1 nm) and armchair geometry. We use the armchair geometry because previous *ab initio* molecular dynamics simulations have shown that open tips of BNSWNTs with a zig-zag configuration are unstable unlike armchair tubes [260]. Furthermore, For BNNTs, the chirality has little impact on the properties of the tube [257, 258]. Similarly to the CNT calculations, we generated an initial geometry of BNNT in the ASE suite [19]. The edges of the initial geometry (containing 624 atoms) were saturated with hydrogen atoms and further relaxed in SIESTA. Figure 6.2.2 shows the qualitative comparison of the experimental data (red line) with the

EELS spectra obtained from our calculations for two trajectories perpendicular to the tube axis. One trajectory is crossing the tube at its center (green line) and the other is passing near the tube surface (blue line). The inset of Figure 6.2.2 shows the tube geometry along its axis (dark blue dots represent the nitrogen atoms while the orange dots represent the boron atoms) with the position of the electron beams (green and blue open dots). The colors of the beam trajectories match those of the spectra. The comparison of the EELS spectra is rather favorable in

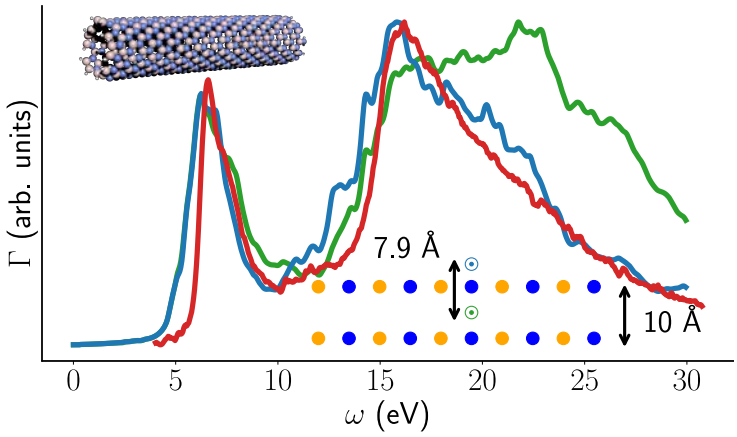

Figure 6.2.2: EELS of BNNT. The experiment is performed for a single-wall BNNT of 1 nm diameter and 20 nm long, while the calculations are performed for single-wall armchair BNNT of the same diameter and 5 nm long. The top left corner shows the geometry of the BNNT used for the calculations. In the lower part of the figure, we show the 2D projection of BNNT geometry with the positions of electron beams indicated by the green and blue open dots. The color coding of the dots match the color coding of the calculated spectra. Unfortunately, it is the green curve which should match best the experimental spectrum (red curve), not the blue as we actually observe. The energy of the probing electrons was 100 keV in the experiment and in the calculations.

this case. Again the low energy peak is well reproduced, as well as the onset of the high energy loss, but the width of the high energy feature on the calculations strongly depends on the trajectory. Surprisingly, although the experimental setup is supposed to correspond to the beam positioning in the center of the tube, we see a significant discrepancy between our corresponding EELS (green solid line) and the these experimental data (red solid line). The discrepancy is clearly visible in the high-frequency range (19-30 eV) and negligible in the low-frequency range (4-15 eV). At the same time, there is a stunning agreement between our EELS for the beam positioning outside the BNNT (blue solid line) and the experimental data in the whole frequency range (4-30 eV). The controversy remains so far unresolved, while the common excuses for the theory (spelled out above in section 6.2.1 in the

case of CNT) still apply in the case of BNNT, the private communication with experimental group leaves little doubt in their confidence in the correct beam positioning and its sufficient collimation. Despite the unfortunate controversy in the high-frequency range, we can clearly identify the main features of the EEL spectra such as π and σ plasmon resonances. The position of the low-frequency π plasmon agrees with experimental measurements within 0.2 eV. The shape of the π plasmon resonance is also in excellent agreement with the experimental data. Moreover, the relative intensities of π and σ resonances agree well between the experimental and theoretical data.

The good agreement, at least in the low energy part of the spectra, with experimental data for the CNT and BNNT is encouraging. In the rest of the chapter, we apply the linear-response TDDFT to the EELS of the silver clusters and silver cluster dimers.

6.2.3 Silver Cluster

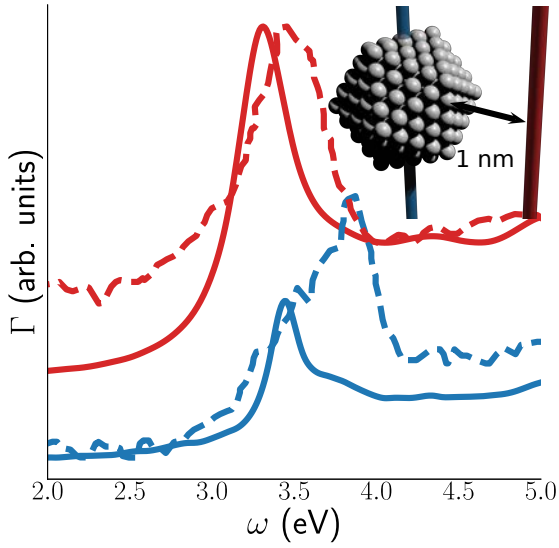

Figure 6.2.3: EELS for large silver clusters. The experimental data for 24 nm diameter silver cluster are represented by dashed lines, while the calculated spectra for icosahedral Ag_{923} cluster are shown by full lines. Two distinct trajectories of the probing electron are shown, one crossing the cluster at its center (blue lines) and the other near the surface of the cluster (red lines). The inset of the figure shows the cluster geometry together with the electron beam trajectories. The colors of the beams are matching the colors of the lines in the plot. The calculated spectra are obtained with 100 keV electrons while the beam energy was not specified for the experimental data.

In this section, we compare our calculations for large silver clusters with the experimental work from J. A. Scholl *et al.* [233] and A. L. Koh *et al.* [234] for the sake of the method's validation. In the work of A. L. Koh *et al.* [234], the EELS spectra of 24 nm diameter silver clusters are reported for two beam trajectories. They analyzed two types of beam trajectories, one that passes right through the center of the cluster, and another trajectory that passes near its surface. In the work of J. A. Scholl *et al.* [233], the EELS spectra are reported for clusters of similar size (of 20 nm diameter) and more beam trajectories ranging from those passing right through the center of the cluster to those passing far outside the cluster and including several intermediate beam positions.

The clusters of 24 nm diameter (containing approximately million atoms) is out of reach currently within our atomistic *ab initio* approach. On the other hand, the larger the object the more amenable for description using classical electromagnetic methods. Therefore, here we focus on clusters containing several hundred atoms that, while can be reasonable described with classical methods and a dielectric function, also present features that require a quantum mechanical treatment, as described in detail in chapter 5. We have chosen Ag_{923} cluster ($\sim$ 3 nm of diameter) of icosahedral shape for our calculations. Despite the fact that this can be a reasonable structural motif for such small cluster, the main motivation to chose the icosahedral structure is the detailed characterization of its optical response presented in chapter 5. Thus, for us, this cluster represents the ideal playground to explore the differences between far-field optical response and the EELS obtained with different trajectories. The cluster geometry has been generated using the ASE package [19], then relaxed with SIESTA [1, 2]. The final geometry is depicted in Figure 6.2.3 together with the examined beam trajectories.

The experimentally measured spectra from Ref. [234] are shown in Figure 6.2.3 with dashed lines, while our simulations are represented with full lines. When the beam is passing near the cluster surface (red lines), the agreement between our calculations and the experimental data is rather good. We can appreciate a slight frequency shift of 0.2 eV of the surface plasmon, otherwise, the resonance is correctly reproduced by our method. Anyway, one should bear in mind that this comparison is also influenced by the size dispersion of the SP resonance presented in chapter 5. However, in case of the crossing trajectory (blue lines), the agreement is less satisfactory. The experiment shows a strong peak at 3.8 eV, which is usually assigned to the bulk plasmon and a shoulder at 3.3 eV corresponding to the surface plasmon, while the calculated EELS still exhibits only a slightly blue-shifted SP resonance at 3.5 eV and a barely discernible shoulder at 3.7 eV which could be related to the strong bulk plasmon response seen in the experiment. The reason for the diminutive bulk resonance could be the differences of geometry of the cluster interior between the 24 nm cluster characterized in the

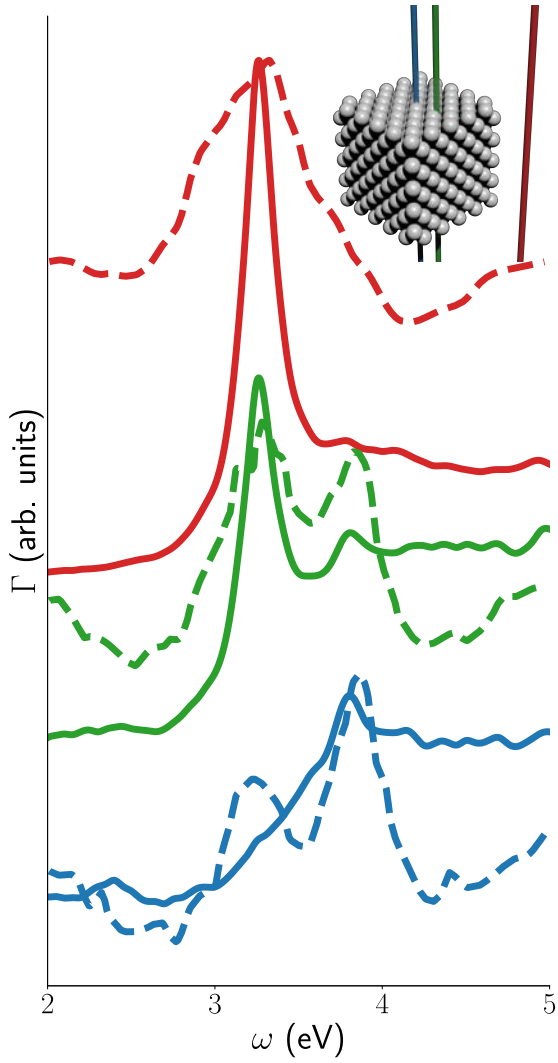

Figure 6.2.4: Experimental (dashed lines) EELS for Ag particles with 20 nm diameter [233], and *ab initio* (full lines) EELS for a silver cube composed of 500 atoms and presenting a FCC lattice. Three distinct trajectories of the electron beam were used both in the experiments and the calculations, one crossing the cluster at its center (blue lines), a second crossing the cluster at half-distance from the surface (green lines) and the last one passing at 1 nm from the surface of the cluster (red lines). The cluster geometry used for the calculations together with the beam trajectories are represented in the figure. The colors of the beams are matching the colors of the lines. Experiments used probing electrons of 300 keV, while 100 keV were used in the calculations.

experiment and the 3 nm icosahedral cluster used in the calculations. Indeed, the surface-to-bulk ratio of these clusters differs by an order of magnitude and one should expect rearrangements in the interior of the 24 nm cluster towards the FCC lattice structure of bulk silver. In order check this conjecture, we calculated the EELS for a small chunk of FCC lattice rather than for the icosahedral geometry. We used a silver cube of 500 atoms, which were cut out from the FCC lattice with the experimental lattice constant of 4.0853 Å [261] and kept non relaxed. In appendix D, we present a deeper analysis of the silver cube. In Figure 6.2.4, we compare the computed EELS of the silver cube with the experimental spectra by Scholl *et al.* [233] for three beam positions. The first one is passing at 1 nm from the cluster surface (red lines), the second beam crosses the cluster but not at its center (green lines), while the last trajectory passes right through the center of the cluster (blue lines). For the first electron beam passing near the surface, the computed spectrum is similar to that of the icosahedral cluster. The SP appears at 3.25 eV in our calculations which is in a good agreement with the corresponding experimental frequency of 3.3 eV. Given that our FCC cube is considerably smaller than the experimental clusters, this good agreement is probably the consequence of a fortunate cancellation of two effects: on the one hand, the blue-shift characteristic of Ag cluster as they become smaller and, on the other hand, the slight red-shift of the SP obtained with the WC-GGA functional (see chapter 5 and Refs. [44]). For the crossing beam arrangements (blue and green lines), the calculated spectra differ significantly from the previous calculations of the icosahedral cluster. Namely, now a clearly discriminated bulk plasmon is excited in the cubic cluster while it was virtually absent for the icosahedral cluster. The bulk plasmon frequency recovered in the calculations is 3.8 eV, which is in excellent agreement with the experimental value of 3.85 eV. When the beam is shot inside the cluster but not at its center (green lines), the simulated spectrum strongly resembles the experimental results. The bulk plasmon is less intense than the SP in our simulation, while they show similar intensity in the experiment. This disagreement can be explained by the size differences between the measured and modeled clusters. Indeed, the cluster used in the simulation is much smaller than the one characterized in experiment. Therefore, the simulated cluster exhibits a relatively weaker bulk plasmon. The computed EELS for the electronic beam crossing the cluster in the middle (blue lines) exhibits a larger disagreement with the corresponding experimental spectrum. Namely, the experimental data show both the bulk plasmon at 3.8 eV as well as an attenuated but still clearly visible SP excitation at 3.3 eV. In contrast to experimental data, the SP resonance is mostly absent in the calculated EELS (however, although no peak is found at the corresponding energy, there is considerable loss at the corresponding energy, i.e. the SP seems to give rise to a shoulder in the spectrum), while the bulk plasmon resonance appears at 3.8 eV. This difference must be due to the perfectly sym-

metric configuration utilized in the theory that strongly reduces the probability to excite the SP mode, and which necessarily differs from that found in a realistic experimental situation.

The comparison of the atomistic *ab initio* EELS and experimental data for silver clusters demonstrates that the SP resonances is well reproduced in the calculations for the beam trajectories passing far from the cluster surface. In contrast to the SP resonances, the bulk plasmons need more care to be reproduced theoretically because the internal structure of the 20 nm clusters must be similar to the bulk arrangement rather than to the icosahedral atomic arrangement characteristic for the small 3 nm clusters affordable in the modeling. Overall, the agreement with the experimental data is good considering the large geometrical differences between the clusters used experimentally and modeled in the calculations.

6.3 Analysis of Silver Clusters and Cluster Dimers EELS spectra

Nanoparticles composed of noble metals are of particular interest for plasmonic applications because they support localized SP resonances, therefore, they have been widely studied with multiple methods, experimentally [229, 233, 234, 262] and theoretically [44, 252, 263]. The presence of d-electrons in the valence band of noble metals screens the SP, damping its intensity and shifting its frequency to lower energy. SP in silver clusters have been examined in several *ab initio* approaches [233, 235]. In particular, recent advances in TDDFT [44, 252, 264] allowed to study the optical excitations in silver clusters consisting of hundreds of atoms. In the rest of this chapter, we analyze the electronic excitations in TEM using the iterative TDDFT for EELS.

6.3.1 Single Icosahedral Silver Clusters

We performed a series of calculations for a set of silver clusters with number of atoms varying from 13 (two shells) up to 923 (seven shells). We assumed icosahedral geometry of the clusters [202, 203] which is known to minimize the total energy for small clusters of many metallic elements [204]. The geometry of the Ag_{923} cluster is shown in the inset of Figure 6.3.2 panel (f). In this analysis, the trajectory of the electron is parallel to one of the edges of the cluster.

In the first series of calculations, the beam trajectory is located at a distance $b' = 1$ nm from the cluster surface as presented by the cartoon in panel (d) of Figure 6.3.1. The distance b between the cluster's center and the trajectory is then $b = b' + D/2$ where D is the diameter of the cluster. The diameter of the

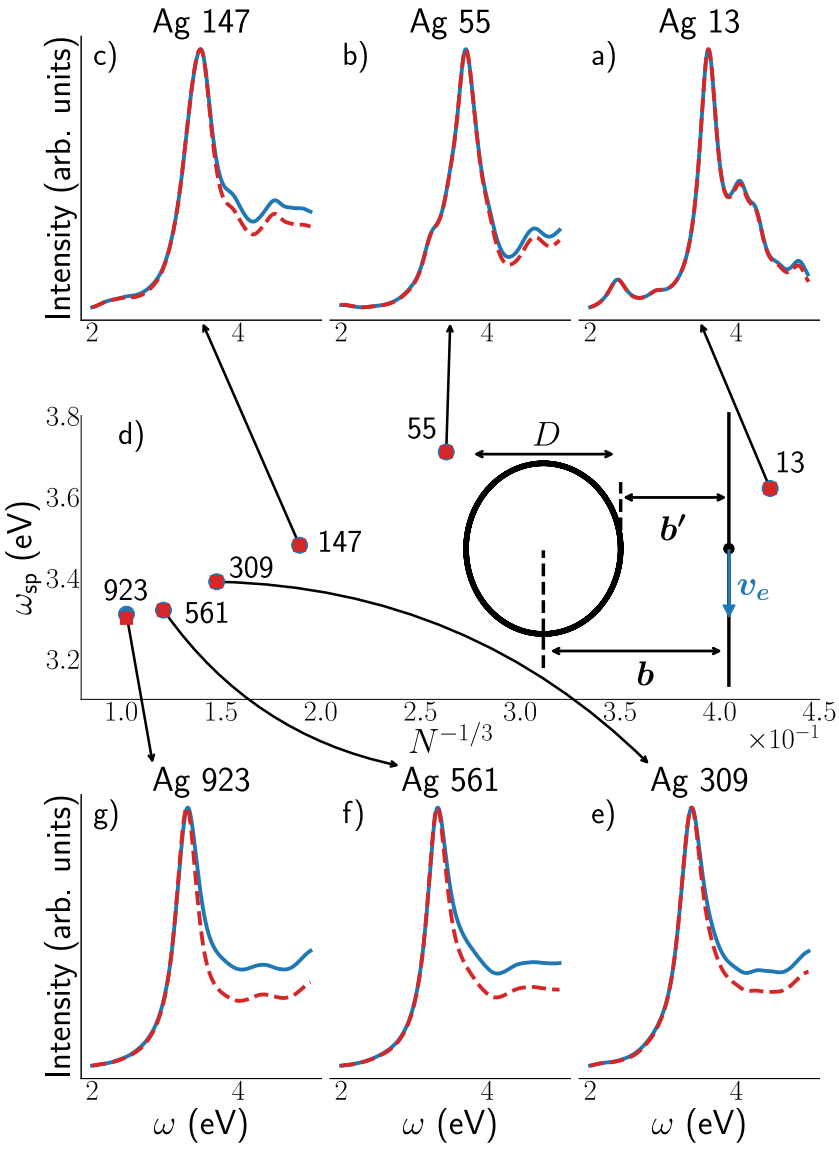

Figure 6.3.1: Panels (a, b, c, e, f, g) show the computed optical polarizability (red dashed lines) and EELS (blue solid lines) for the icosahedral clusters containing 13, 55, 147, 309, 561 and 923 atoms, respectively. The central panel (d) shows the SP frequency extracted from the optical polarizability (red squares) and EELS (blue circles) as function of the number of atoms in the cluster. The black arrows link the dots to them corresponding systems. A scheme of the probing electron trajectory is also shown, $b' = 1$ nm in this case. The electron kinetic energy is 100 keV.

cluster D is measured as a distance between two atoms of opposite edges located at the center of their respective edge. We compare the optical polarizability (eqn. 2.91) shown by red dashed lines with the EELS signal (eqn. 2.124), shown by the blue solid lines. Panels (a, b, c, e, f and g) of Figure 6.3.1 show the optical polarizability and EELS for clusters of different sizes (13, 55, 147, 309, 561 and 923), respectively. Panel (d) shows the dependence of the SP frequency on the cluster size, as obtained from the maxima of the optical polarizabilities and EELS calculations. We see a striking similarity of the optical polarizability and EELS signal, particularly for small clusters shown on panels (a-c). In case of the larger clusters, the distance to size ratio b'/D becomes smaller, increasing the importance of higher multipoles in the response to this specific trajectory and, as expected, reducing the agreement between the optical polarizability and EELS signal. In the high-frequency range, the EELS signal becomes relatively stronger than the optical polarizability, as expected from the excitation of higher multipolar modes, although the overall shape of the spectrum remains maintained. We observe the well known blue shift of the SP frequency $\omega_{\rm sp}$ for Ag clusters with decreasing cluster size. This behavior originates from the dominant effect of quantum confinement [232, 233, 252, 262, 264].

In a second series of calculations, we studied the impact of the electron beam trajectory in the EELS signal for the same set of silver clusters. The beam is kept parallel to the cluster edge as previously, but the distance b between the cluster's center of mass and the beam trajectory is now varying. We performed calculations for the four trajectories shown on panel (f) of Figure 6.3.2. The first trajectory passes right through the center (blue lines) of the cluster ($b = 0.0$ nm), the second trajectory (orange lines) goes inside the cluster, at half-distance between the cluster center and surface ($b = D/4$), the third trajectory (green lines) is situated at the cluster surface ($b = D/2$) and the fourth trajectory (red lines) at 1 nm from the cluster surface ($b = D/2 + 1$ nm), as in the previous calculations in Figure 6.3.1. The spectra corresponding to the beam trajectories are represented on panels (a, b, c, d, e and f) for the clusters 13, 55, 147, 309, 561 and 923 respectively. The color coding of trajectories and spectra matches.

For the electron beam passing outside the cluster (red lines), only one mode responds strongly, independently on the cluster size. As we have seen previously this mode is the SP that blue shifts when the cluster size decreases [Figure 6.3.1 panel (d)]. For the beam passing near the cluster surface (green lines), the SP is still excited in all clusters but other modes appear at higher frequencies. These higher order modes are well differentiated for small clusters (up to Ag_{309}) but give rise to a broad structure for larger clusters. This merging of resonances indicates the quantization of the energy levels as the cluster size diminish, passing from a quasi-continuous to a quantized spectrum one. The beam trajectories passing through the cluster body (orange lines) and through the cluster center

(blue lines) provide very similar responses at high energy, particularly for large clusters. They start to diverge as the cluster size decreases. The main noticeable difference between these two trajectories is for the SP mode. It is weaker when the beam passes right through the center, particularly for the small clusters [panels (b), (c), and (d)], in fact, for clusters smaller than the Ag_{561}, the SP mode is barely excited with this trajectory. The smallest cluster [panel (a)] behaves quite differently than the other ones. The three trajectories that cross the cluster (blue, orange and green lines) give almost identical response, only the spectrum of the last trajectory (red line) which passes far from the cluster is radically different, showing only the single SP peak.

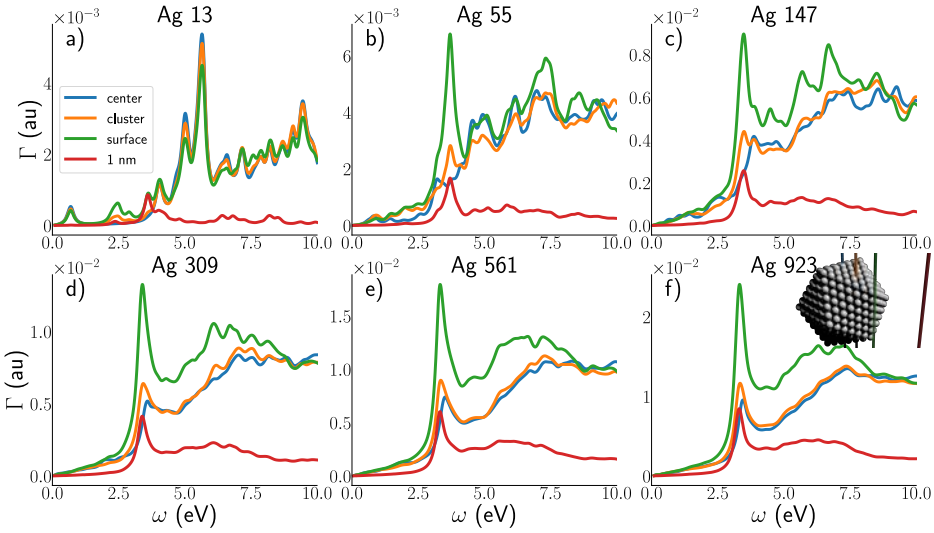

Figure 6.3.2: Calculated EELS for silver cluster of 13, 55, 147, 309, 561 and 923 atoms for four beam trajectories. Blue lines correspond to trajectories passing through the center of the cluster, orange lines to trajectories at half-distance between cluster center and surface, green lines to trajectories passing at the cluster surface and the red lines to trajectories passing far from the cluster surface (1 nm). The trajectories are represented on the inset of panel (f) relative to the Ag_{923} cluster. The kinetic energy of the exciting electrons is 100 keV.

A slight frequency shift of the SP occurs for large clusters (309, 561, 923) as the beam trajectory approaches the silver cluster and penetrates it. For the largest cluster, the SP is excited at 3.3 eV when the beam passes at 1 nm from the cluster surface, but at 3.45 eV when the beam crosses the cluster right at its center (Fig 6.2.3). Inspecting the EELS spectra for the four trajectories presented on panel (f) of Figure 6.3.2, we see that the frequency shift occurs only when the beam passes right through the center of the cluster. For the three other

trajectories, the shift is negligible and the SP frequency locates around 3.3 eV, even when the beam crosses the cluster with an impact parameter of $D/4$.

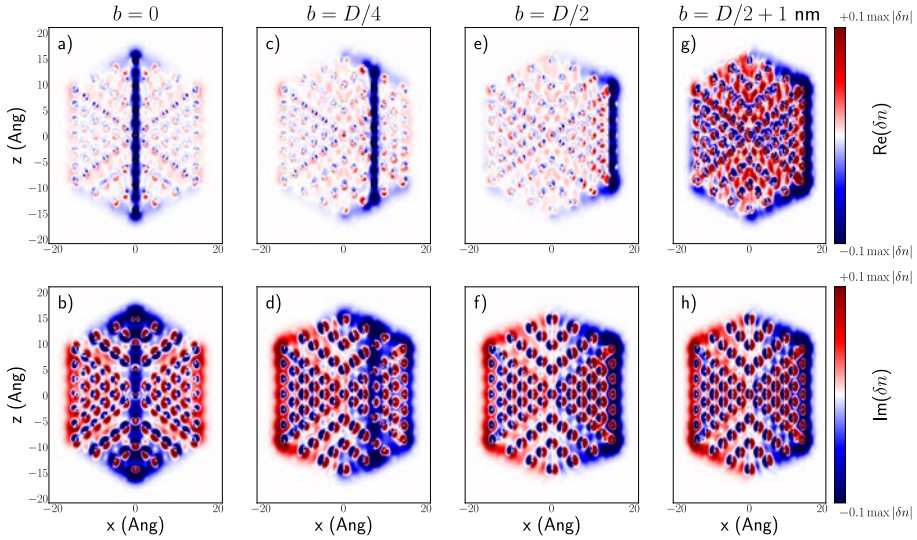

Figure 6.3.3: Real part (top row) and imaginary part (lower row) of the density change distribution for the largest silver cluster with 923 atoms. From the left to the right we have, the trajectory passing through the center of the cluster [panels (a) and (b)], then the trajectory crossing the cluster at half-distance from the edge [panels (c) and (d)], third column show the density for the trajectory passing along an edge of the cluster [panels (e) and (f)], and the last column the trajectory passing at 1 nm from the cluster edge [panels (g) and (h)]. The maximum and minimum values of the color scale are set to 10% of the absolute value of the maximum of the absolute value of the induce density.

In order to get a better understanding of the physics behind this shift we analyzed the induced electron density of the Ag_{923} for the four trajectories at the SP frequencies. The correlation between the appearance of the induced density maps and the symmetry of the modes excited in EELS is not a simple one. This is due to the fact that the external potential $\delta V_{\text{ext}}(\mathbf{r};\omega)$ (eqn. 2.123) in the case of EELS always carries a position-dependent phase that depends on the velocity of the projectile. This is more clearly address in section 6.3.2, where we analyze in detail the dependence of the EEL spectra of Ag clusters on velocity. Thus, neither the real nor the imaginary part reflect fully the symmetry of the imaginary part of the response function χ (see section 2.2.3), which contains the information about the excitation modes in the system. However, at relatively high velocities (here we use $v = 75$ a.u. ~ 100 keV) one expects that the phase variation of the external perturbation $\delta V_{\text{ext}}(\mathbf{r};\omega)$ is small across our nanoparticles. In such

conditions, the inspection of the induced density plots recovers relevance from the point of view of interpreting the symmetry of the excitations associated with a given resonance peak.

Figure 6.3.3 shows the maps of the density change of the Ag_{923} cluster, in a plane cutting the cluster at its center and containing the beam trajectory. The top row [panels (a, c, e, g)] shows the spatial distribution of the real part of the density change, while the bottom row [panels (b, d, f, h)] shows the imaginary part of the induced density. The first column [panel (a) and (b)] displays the density change for the electron beam passing right through the center of the cluster ($b = 0$ nm) at 3.45 eV. The beam trajectory is clearly seen represented by a blue pillar of induced charge (blue color means a deficiency of electrons, i.e., positive charges). The second column of Figure 6.3.3 [panels (c) and (d)] represents the density change for an electron beam passing at a distance $b = D/4$ from the cluster center (the beam trajectory is still clearly visible) at 3.34 eV. In the third column [panels (e) and (f)], the beam is passing just at the edge of the cluster ($b = D/2$) at 3.33 eV and for the fourth column [panels (g) and (h)], the beam is located at 1 nm from the cluster edge ($b = D/2 + 1$ nm) at 3.31 eV. The color scales of Figure 6.3.3 have been saturated at 10% of their respective maximum intensity, in order to identify easily the patterns created by the density change distribution. Thus, no quantitative comparison of their intensity can be done as the color scale changes from panel to panel.

For $b \neq 0$ (second, third and fourth columns), a clear dipolar pattern of the density is present at the cluster surface, which is particularly clear in the imaginary part of the induced density in the lower panels. The dipolar pattern is expected when the electron beam is passing far from the surface [panels (g) and (h)], for which the optical polarizability is almost identical to the EELS [see panel (f) of Figure 6.3.1]. Moreover, the perturbation created by the beam inside the cluster does not forbid the presence of the SP, and the pattern of the density change induced by the charged particles is similar to the one created by an optical excitation. In contrast to optical excitations, the d-electrons near the beam trajectory are affected in a less homogeneous manner by the passage of the charged particles.

When the electron beam crosses the cluster right through its center, the surface dipole is not discernible in the plot [see panel (b) of Figure 6.3.3], and the frequency of the plasmon is shifted by 0.15 eV compared to the other trajectories. For this specific location of the beam, a torus is formed by the induced density at the cluster surface [red color on panel (b)] while a strong lack of electrons occurs at the extremities of the column created by the beam. The charge distributions of the d-electrons is as well strongly affected, forming dipoles with different orientations in the inner part of the cluster. The dominant mode for the central beam position $b = 0$ as already been mentioned in some publications [236, 265]

and referred to as dark surface plasmon (DSP). The name DSP points to the impossibility of exciting the mode with light. The DSP is difficult to observe experimentally because the excited cluster must have a high degree of spatial symmetry and the probe beam must be targeting the center of the cluster with a high precision.

6.3.2 Dependence of EELS on the velocity of the probing electrons

In this section, we study the large silver cluster Ag_{923}, analyzing how the EELS spectra depend on the velocity of the probing electrons. We focus on the central beam position, i.e. the beam passes through the center of the cluster. The normalized EELS are shown in Figure 6.3.4 on panel (a) for the probe-electron velocities of 1 a.u. (blue line), 5 a.u. (orange line), 10 a.u. (green line), 15 a.u. (red line), 20 a.u. (purple line) and 75 a.u. (brown line). The frequencies of EELS maxima $\omega_{\max}$ are shown on panel (b) as function of the velocity of probing electrons.

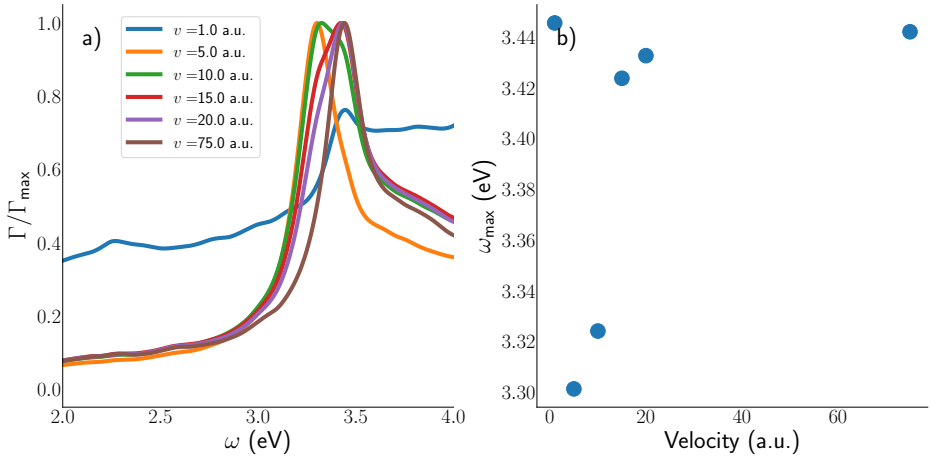

Figure 6.3.4: EELS and resonance frequencies for different probe-electron velocity v. Panel (a) shows the normalized EELS spectra obtained for the Ag_{923} cluster with the probe-electron passing right through the center of the cluster for different velocities v. Panel (b) shows plasmon frequency $\omega_{\max}$ as function of the electron's velocity v.

For $10 < v \leq 75$ a.u., the resonance frequency $\omega_{\max}$ is almost constant and only slightly red shifts as the velocity v diminish. However, the broadening of the plasmon resonance appears to increase as the velocity of the probe decreases. For $v = 10$ a.u., the surface plasmon suddenly and visibly red shifted from 3.47

to 3.37 eV with a strong broadening of the peak. Indeed it is clear that the peak is composed by a main component at the new lower frequency and a shoulder at the resonance frequency observed for higher velocities. Further decrease of the velocity to $v = 5$ a.u. causes only a tiny red shift of the resonance $\omega_{\max}$ by 0.02 eV and a substantial decrease of the effective peak broadening. Finally, for $v = 1$ a.u., the spectrum gets very broad, although an excitation can still be identified at 3.5 eV. The blue shift of $\omega_{\max}$ for $v = 1$ a.u. is curious since it reverses the trend.

The range of the probe-electron velocities is rather wide. In fact, one may argue that the initial assumption about the uniformity of the probe-electron motion is unlikely to hold when this velocity is comparable to the Fermi velocity of the cluster electrons ($v_{\mathrm{F}} \sim 0.635$ a.u. [240]). Leaving aside the impartial critique about the validity of the assumed approximations, we focus on the mathematical origins of the described behavior. The described phenomenology of the EELS velocity dependence suggests the existence of two resonance modes at about 3.37 and 3.47 eV which are excited selectively or collectively, depending on the velocity of the probe-electrons. To directly identify the resonant modes, we will plot the induced density at the frequency of respective maxima for a set of the probe-electron velocities.

The spatial distributions of the induced density δn in the plane cutting the center of the cluster and along the electron beam trajectory are represented in Figure 6.3.5 for all mentioned velocities except $v = 15$ a.u. which bears a close resemblance to the case of $v = 20$ a.u. The first row shows the density change for $v = 1$ a.u., the second row for $v = 5$ a.u., the third row for $v = 10$ a.u., the fourth row for $v = 20$ a.u. and the last row for $v = 75$ a.u. The first column represents the real part of the induced density while the second column shows the imaginary part. The density change distributions are represented at the resonance frequencies $\omega_{\max}$ indicated on panel (b) of Figure 6.3.4. The induced density for two largest velocities are very similar (see panels (g-j) in Figure 6.3.4). The charges are expelled from the center of the cluster, along the beam trajectory, creating a column of positive charges (blue color of the maps meaning a lack of electrons, i.e. positive charges, and the red color an excess of electrons, i.e negative charges), while a torus of negative charges is formed at the surface of the cluster. The induced density exhibits an almost perfect symmetry along the x- and z-axes for the two largest velocities (20 and 75 a.u.). However, we can appreciate a slight deterioration of the symmetry along z-axis, i.e. along the beam direction, for the second large velocity $v = 20$ a.u. For even smaller velocities $v = 10$, 5 and 1 a.u., the symmetry along z-axis vanishes completely. For velocity $v = 10.0$ a.u., the column of positive charges is disturbed, changing sign at the end of the cluster as seen on panel (f) in the imaginary part of the induced density. The real part of the induced density [see panel (e)] shows an

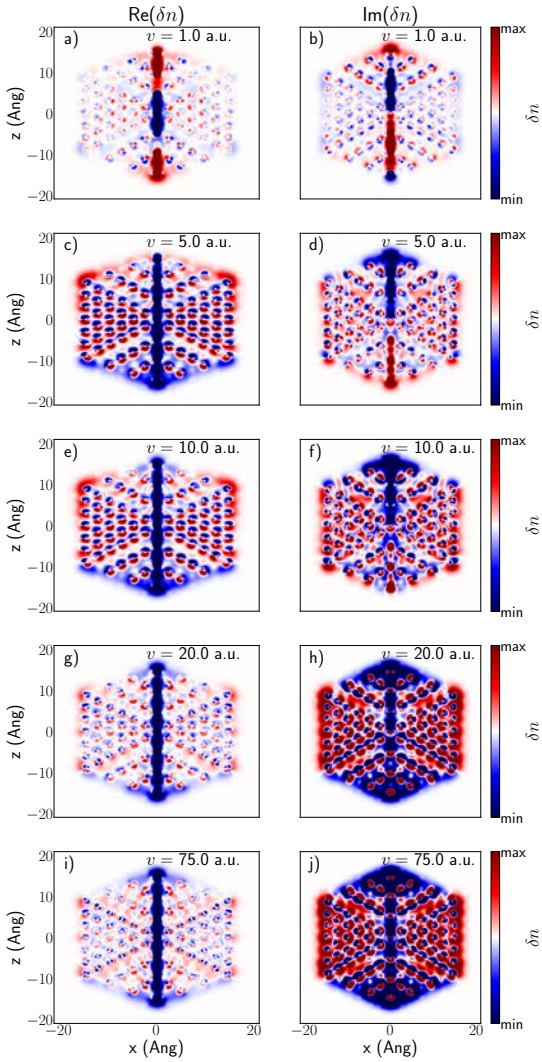

Figure 6.3.5: Maps of the induced density change for the Ag_{923} for an electron beam passing right through the center of the cluster. The first column represents the real part of the density change while the second column represents the imaginary part. Each row represent the induced density for a particular electron velocity at the plasmon frequency ω_{max}, i.e. at the frequency of the maximal EELS response. In the first row the velocity is $v = 1$ a.u., in the second row $v = 5$ a.u., in the next row $v = 10$ a.u., in the fourth row $v = 20$ a.u. and in the last row $v = 75$ a.u.

intense positive density change at the bottom of the cluster while the top is mostly dominated by negative charges. For even smaller velocities [panels (a-d)], the density change inside the cluster is oscillating along z-axis. These oscillations are well visible in the vicinity of the probe-electron beam. The induced density exhibits alternating signs along the beam trajectory. The oscillations are clearly different from the 4d-electron, screening dipole patterns we observed in optical excitations (see chapter 5). These oscillations can be understood by Fourier transforming the external potential $\delta V_{\text{ext}}(\boldsymbol{r};t) = |\mathbf{r} - \mathbf{v}t|^{-1}$ to the frequency domain, in cylindric spatial coordinates

$$\delta V_{\text{ext}}(\boldsymbol{\rho}, z; \omega) = f\left(|\boldsymbol{\rho}|; \omega\right) e^{-i\frac{\omega}{v}z}, \tag{6.2}$$

where z is the coordinate along the electron beam direction, $\boldsymbol{\rho}$ the polar vector perpendicular to z and $f\left(|\boldsymbol{\rho}|; \omega\right)$ is the amplitude of the external potential. Because of the factor $e^{-i(\omega/v)z}$, it is clear that the external potential (6.2) will show oscillation as a function of the velocity v. We can now ask an important question: when the bright or the dark SP will be excited for these highly symmetric trajectories going through the center of the particle?

The answer is quite obvious from eqn. (6.2). When the external potential has an odd number of oscillations across the structure, we will preferentially excite the bright SP. On the contrary, for an even, or zero, number of oscillations the dark SP will be preferentially excited. Intermediate situation, will produce the excitations of the two modes with different relative intensities.

We can now translate this argument to velocities. The first preferential excitation of the bright SP will happen when the condition $(\omega L)/v = \pi$ is satisfied, implying the external potential changes sign when moving from one side to the opposite side of the structure. Here L is the characteristic dimension of the system along the trajectory. Thus, we can obtain the threshold velocity at which we can find a fully-developed dipolar plasmon peak

$$v_{\text{th}} = \frac{\omega L}{\pi}. \tag{6.3}$$

In the present case we have $L \sim 60$ a.u., $\omega \sim 3.4$ eV or 0.125 a.u., and we get $v_{\text{th}} \sim 2.4$ a.u. We should take into account that this is only a rough estimation that does not consider the complex structure of the object on the estimation of the parameter L.

As we decrease v below v_{th}, the external potential at frequency ω, will progressively evolve from having odd to an even number of oscillations across the length of the structure L. This means that for $v < v_{\text{th}}$, the maximum of the EELS spectrum will oscillate between the bright and dark SP. In particular, for $v = 1$ a.u. we can estimate the accumulated phase across the structure to be

$\omega L \sim 7.5 \sim 2.4\pi$. Therefore, we have a full oscillation of the external perturbation and, as a consequence, we find the main loss peak at the frequency of the dark SP.

On the other hand, for $v \gg v_{\text{th}}$ the main mode excited is always the dark SP. For $v = 75$ a.u., we are clearly in this regime (see panels (i) and (j) in Figure 6.3.5) For intermediate velocities $v > v_{\text{th}}$ we should see a continuous transition from EELS maximum at dark SP to bright SP, as clearly seen in Figure 6.3.5.

The velocity dependence of EELS originates in the spatial variation of the Coulomb field created by probe-electrons. In particular, the spatial variation of the slowly moving probe-electrons becomes so short length that this is noticeable in the induced density change of small clusters, containing as little as 1000 atoms.

6.3.3 EELS of Silver Cluster Dimers

In this section, we analyze the EELS of metallic nanogaps that are formed by placing two metallic nanoparticles in a close proximity. In such nanogaps, the coupling of plasmonics modes generates new hybridized solutions that, in the optical response, give rise to a red-shift of dominant resonance with respect to the original resonances of the individual particles [11, 138]. We constructed the cluster dimers using two Ag_{309} clusters in a "tip-to-facet" mutual orientation as shown by the cartoon in Figure 6.3.6 (d). Silver cluster dimers have been studied experimentally [227, 229] using TEM. However, this is the first atomistic *ab initio* study of the EELS in silver cluster dimers to the best of our knowledge.

In Figure 6.3.6, we compare the optical polarizability (eqn. 2.91) and EELS stopping probability (eqn. 2.124) as function of the inter-cluster separation d. The inter-cluster separation d is measured as the distance between closest atoms belonging to different monomers. We varied the inter-cluster separation d between 2 and 12 Å in step of 1 Å. The optical polarizability is shown by the color plot on panel (a). We computed the EELS stopping probability for two beam positions shown by the blue and green dots on panel (d) of Figure 6.3.6. Both probing beams are perpendicular to the dimer axis. The first beam locates at a relatively large distance of 1 nm from the left cluster independently on the separation d. The second beam locates in the midpoint of the dimer independently on the cluster separation d. The EELS stopping probability is shown by the color plots on panels (b) and (c) for the first and second beam locations correspondingly. As expected, the spectra on panels (a) and (b) are rather similar. Both the optical polarizability as well as the EELS stopping probability exhibit the bonding dimer plasmon (BDP) at approximately 3.28 eV for large inter-cluster separation of 12 Å. The BDP slightly red shifts at smaller separation distances down to approximately 5 Å. The red shifting of the BDP is a well-known phenomenon [11, 92, 93]. At even smaller distances of $d = 2 \ldots 5$ Å, a strong red

shift and attenuation occurs due to the tunneling effect. At these separations, the stopping probability reveals a more pronounced mode with a frequency of maximum at approximately 3.4 eV. We demonstrate the similarities between the optical polarizability and stopping probability by comparing them at a given excitation frequency of 3.28 eV and different inter-cluster separations d on panel (d) of Figure 6.3.6. The normalized spectra are very similar up to as large separation distance as 7 Å which is comparable to the beam-cluster distance of 1 nm. The cluster geometries were kept fixed while the different separation distances d were examined. Therefore, the jump-to-contact instability that would occur otherwise (see Ref. [266] and chapter 4) is absent in these calculations.

The stopping probability for the beam position at the midpoint between clusters is shown on panel (c) of Figure 6.3.6. The stopping probability is substantially different to both the optical polarizability [panel (a)] and the stopping probability for the off-dimer incidence [panel (b)]. The midpoint stopping probability exhibits a larger loss into the higher frequency excitations $\omega > 5$ eV. The low-frequency resonance locates at a slightly higher frequency of 3.45 eV instead of 3.28 eV as in the other spectra in the study. Moreover, the low-frequency resonance is not red shifting at the reduced cavity size d. The midpoint stopping probability at the fixed frequency 3.45 eV and for different cavity sizes d is shown by the green dotted line on panel (d). This graph gives further evidence of the surmised difference between the BDP excited in previous cases and the current "mid-point" plasmonic mode. Namely, for the mid-point trajectory the stopping presents a weaker dependence at short distances and vice versa—it diminishes faster as the clusters retreat as compared with the previous two spectra (blue solid line and red dashed line).

In order to get more information on the spectra, we computed the induced density in Cartesian space, at the frequencies of the respective resonances. The imaginary part of the corresponding induced density (eqn. 2.60) and induced electric field (eqn. 2.97) are plotted on panels (a,b,c) and (d,e,f) of Figure 6.3.7, respectively. The cavity size d is chosen to be 5 Å, while the fields are plotted in the plane bisecting the dimer. First column shows the induced density and electric field for the optical excitation at resonance ($\omega_{\rm sp} = 3.28$ eV). The induced density and electric field computed from the EELS spectra with a beam passing far from the dimer surface and at the center of the dimer cavity are shown on the second and third column respectively. Similarly to the spectra in Figure 6.3.6, the maps of the induced density $\delta n(\mathbf{r}; \omega_{\rm sp})$ obtained from the two perturbations (optical and external trajectory) show great resemblances. The direction of the external field and the positions of the electron beams are indicated with red arrows and red dots respectively. The BDP charge distribution can be recognized through the cut done along the dimer axis. Each cluster presents a dipolar charge distribution. A strong charge accumulation at the tip of the cavity occurs, leading to a strong

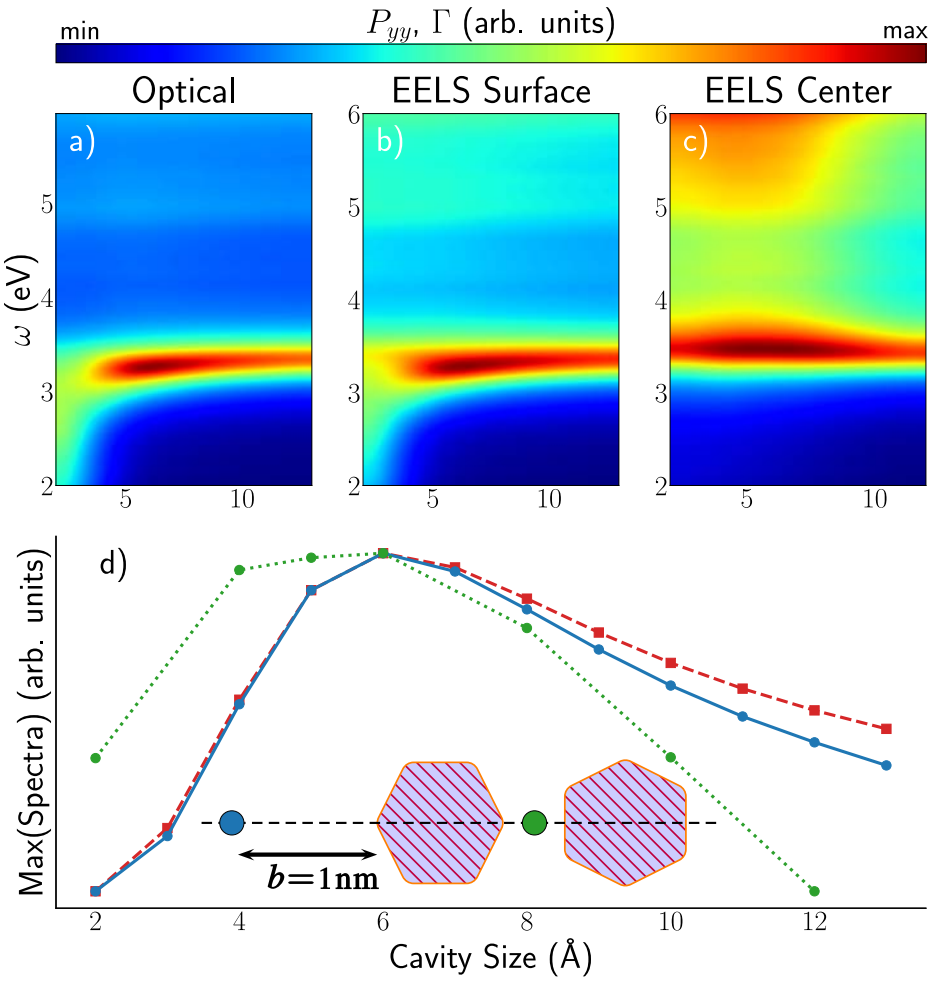

Figure 6.3.6: Calculated optical [panel (a)] and EELS spectra [panel (b) and (c)] as function of the frequency and cavity size for silver cluster dimers containing two clusters composed of 309 atoms. Panel (b) shows the EELS spectra for a beam passing at 1 nm from the dimer surface, while panel (c) for a beam passing right through the cavity center. Panel (d) shows the polarizability and stopping probabilities at a fixed frequency of 3.28 eV for the optical and off-center EELS and 3.45 eV for the mid-point EELS as function of the inter-cluster separation d. For EELS calculations the kinetic energy of the probing electrons is 100 keV. A cartoon representation of the cluster dimer geometry is shown in the inset on panel (d). Further details in the text.

induced field. This enhancement is created due to the collective motion of the cluster electrons which is commonly referred to as "lightning rod effect". The total

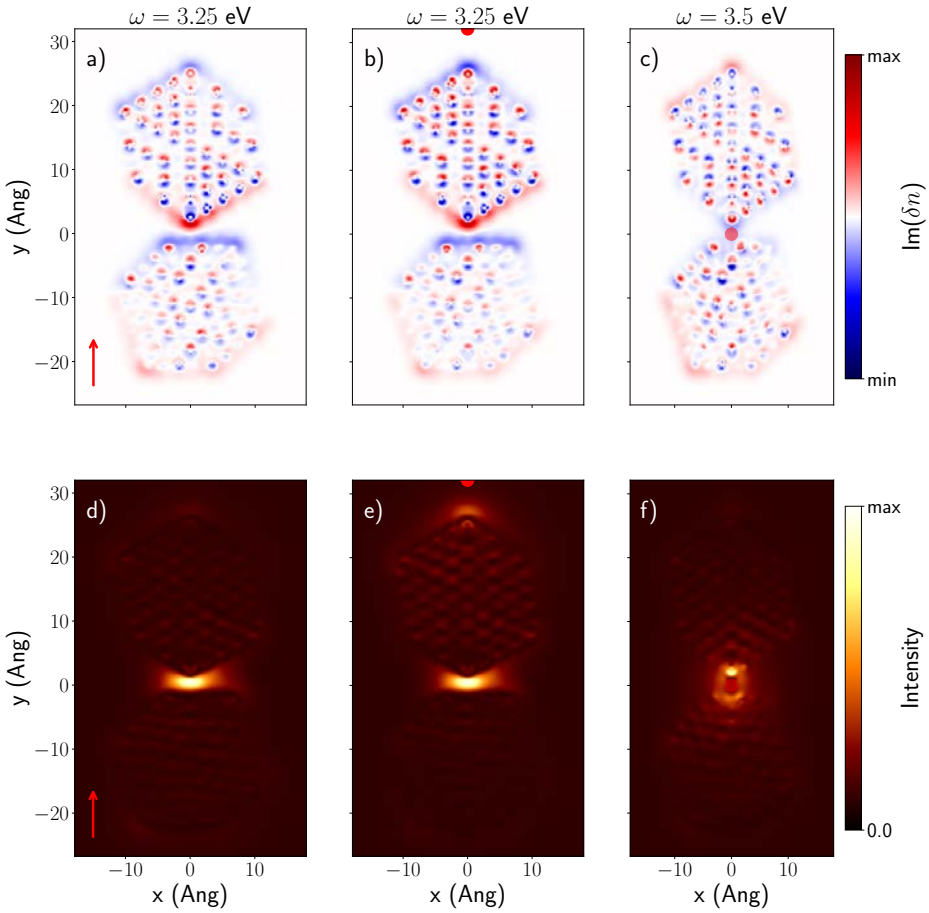

Figure 6.3.7: Imaginary part of induced density change (top row) and intensity of the induced electric field (lower row) maps for optical (first column) and EELS (second and third columns) calculations. The size of the dimer's cavity is 5 Å. For optical calculations [panels (a) and (d)], the red arrow indicates the direction of the external field (parallel to the dimer axis). In second and third column, the position of the beam is indicated by the red dots. Panels (b) and (e) show the density change and electric field for an electron beam passing outside the dimer, while the electron beam is passing right through the center of the cavity in panels (c) and (f).

enhancement can be split into the enhancement due to atomic-size protrusion at the surface of the cluster and due to the plasmon resonance associated with the whole cluster, as we demonstrated previously [83, 146] for sodium clusters and cluster dimers (see chapter 3).

The density map on panel (c) of Figure 6.3.7 permits to identify the mid-point plasmonic mode as a symmetric surface mode with respect to the center of the cavity. The dimer's electrons are expelled from the cavity because of the presence of the beam and they gather at the extremities of the dimer far from the beam. This mode is known as the anti-BDP and is referred as a "dark mode" because it can not be excited with light.

Panels (d,e,f) of Figure 6.3.7 show the moduli of the induced electric field corresponding to the induced density shown on panels (a,b,c). The maxima of the induced field locates in the cavity for all types of excitations. Moreover, we can clearly see a stronger participation of the inner atoms in case (panel e) of the off-cluster EELS as compared to the optical excitation (panel d). In the case of mid-point beam position (panel f), the maximum of the induced field locates closer to the tip atom as compared to the other excitation modes.

It is interesting to note the correlation of the stopping probabilities between the single cluster [panel (d) of Figure 6.3.3] and the dimer [panel (b) of Figure 6.3.7]. We can deduce that the mode observed at 3.45 eV for the single cluster [panels (b) and (e) Figure 6.3.3] is a dark mode.

6.4 Conclusion

In this chapter we have shown that the real-space implementation of electron energy loss spectroscopy presented in section 2.3.6 can correctly predict the interaction of swift electrons with nanoparticles. This method combined with the efficient TDDFT codes MBPT-LCAO or PySCF-NAO permits to compute the EELS spectra of isolated systems containing thousands of atoms. To the best of our knowledge, it is the only implementation of linear-response TDDFT for EELS capable to reach such large sizes using atomistic *ab initio* theory. To validate the implementation, we compared calculations for carbon and boron nitride nanotubes with existing experimental results. The calculated and experimental spectra for the tubes show a qualitatively good agreement. Furthermore, we performed a deeper analysis of silver clusters and silver cluster dimers. First, we have shown that the internal atomic arrangement in the cluster and the trajectory of the electron beam are crucial to get good agreement with experimental results, specifically to excite the bulk plasmon at 3.8 eV. Secondly, we analyzed the response of icosahedral clusters as function of the beam location. For large separation between the beam trajectory and the cluster surface, the EELS spectra were very similar to the polarizability obtained from optical excitation. As the beam approaches the cluster, higher order modes were excited and the signal deviated from the optical one. However, a clear resonance peak corresponding to the bulk plasmon was only observed for clusters whose internal structure recover the correct FCC lattice of Ag. When the electron beam crosses the system

right through its center, a clear resonance corresponding to the excitation of a dark surface plasmon mode was observed for the icosahedral clusters. Finally, we studied the response of a plasmonic cavity formed by two silver clusters in a "tip-to-facet" configuration. By manipulating the beam location, we could excite the bonding dimer plasmon or anti-bonding dimer plasmons. The former excitation is similar to the optical excitations, while the latter dark mode cannot be excited by optical means. This theoretical study emphasizes the uniqueness of the electron energy loss spectroscopy for a detailed characterization of the collective electronic excitation in nanometer-size systems.

Chapter 7

Raman and Infrared Spectroscopy from *Ab Initio* Calculations

Raman and infrared (IR) spectroscopies are vibrational spectroscopy techniques capable of providing molecular finger print information for chemical identification. Both techniques have been widely used in various fields such as chemical analysis, material science and biomedical applications. Recently, the combination of Raman and IR spectroscopies with the plasmonic fields in the vicinity of metallic surfaces, clusters and tips led to the enhanced sensitivity of the spectroscopic techniques. The enhanced sensitivity allows to characterize tiny amounts of matter, down to a few [267, 268] or even a single molecule [108, 268, 269]. To calculate the Raman and IR spectra, we use the well known harmonic approximation method that was already implemented for IR in the Atomic Simulation Environment (ASE) [19] package. We extented this implementation to Raman scattering. In order to calculate the Raman intensity of the vibrational modes of a molecule, one needs to provide the polarizability of the molecules, obtained from TDDFT calculations. Combining SIESTA, ASE, and our TDDFT code, we can calculate the IR and Raman spectra within the *ab initio* atomistic framework. The chapter is organized as follows. In section 7.1.1, we briefly summarize the basics of the Raman spectroscopy and our implementation of the harmonic approximation. In section 7.2, we reproduce the IR and Raman signals for the well-studied CO_2 molecule, while in the section 7.3 we conclude on the method.

7.1 Brief Introduction to Raman Scattering

Raman was awarded the Nobel Prize in 1930 for his discovery of inelastic light scattering from molecules. The phenomenon, which now carries his name, refers to the absorption and reemission of optical photons mediated by the vibrational and rotational modes of the scattering molecules. During Raman scattering, the optical photon changes its frequency while the excess energy excites some vibrational or rotational mode of the molecule [270, 271]. In contrast to Raman (inelastic) scattering, the Rayleigh (elastic) scattering does not change the frequency of the scattered optical photons [272]. We depicted the Rayleigh scattering on panel (a) of Figure 7.1.1 for the sake of comparison with the more complex Raman scattering. The energy carried by the photon $\hbar\omega_0$ gets absorbed by the electrons of the molecule changing their ground state $|g\rangle$ (of energy $\hbar\omega_g$) to an excited state $|e\rangle$ (of energy $\hbar\omega_e$). The state $|e\rangle$ can be considered to be true excited state of the system, in which case we are describing resonant process, or it can be considered a virtual excitation, in which case we are dealing with a non-resonant processes. In the case of the inelastic Raman scattering this gives rise to two possibilities, the so-called resonant and non-resonant Raman processes. It is worth to emphasize already here that the finite-difference numerical approach that we carried out in this chapter, in principle, is only appropriate to study the non-resonant processes. The excited state $|e\rangle$ decays radiatively back to the ground state $|g\rangle$ reemitting the photon of the same energy $\hbar\omega_s = \hbar\omega_0 = \hbar\omega_e - \hbar\omega_g$ although the propagation direction of the reemitted photon can change.

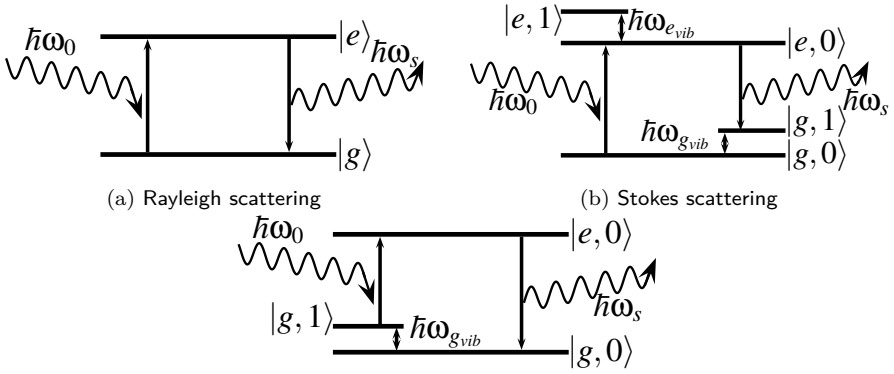

Figure 7.1.1: Rayleigh (a), Stokes (b) and anti-Stokes (c) scattering phenomena

The Raman scattering is mediated by the vibrational (nuclei) degrees of freedom as shown on panel (b) of Figure 7.1.1. The energy spectrum of a molecule

consists of closely spaced (small-gap) levels associated with different vibrational excitations at a given electronic state, e.g., for a molecule in its ground-state and with a single vibrational mode we can label the levels as $|g,0\rangle$, $|g,1\rangle$, ... with the second integer corresponding to the vibrational quantum number. The energy distance between the vibrational levels is $\hbar\omega_{g_{\text{vib}}}$, with $\omega_{g_{\text{vib}}}$ the frequency of the corresponding vibrational mode. Collections of levels associated with different electronic configurations are usually well-separated (wide-gap) in energy, corresponding to the electronic excitation energies. Let us now consider that the system gets excited from its ground-state $|g,0\rangle$ (at low temperature the initial population of other vibrational levels will be negligible) to an excited state of the molecule $|e,n\rangle$ by a photon with energy $\hbar\omega_0$. The molecule can subsequently decay back to its electronic ground state, but in a different vibrational state $|g,m\rangle$. Thus, the molecule is left in a vibrational excited state. Correspondingly the energy of the scattered (emitted) photon $\hbar\omega_s$ is smaller than that of the initial photon $\hbar\omega_0$. The energy difference has gone into the vibrational excitation of the molecule. Therefore, $\hbar\omega_0 - \hbar\omega_s = m \times \hbar\omega_{g_{\text{vib}}}$. The scattering events in which $\omega_s < \omega_0$ are called Stokes scattering [270, 272].

Besides the Stokes scattering $\omega_s < \omega_0$, there is a possibility for the reemitted photon to carry higher energy $\hbar\omega_s$ than the energy of the absorbed photon $\hbar\omega_0$. The so-called anti-Stokes scattering is less probable than the Stokes scattering. We depicted the energy diagram of a simplest anti-Stokes scattering event on panel (c) of Figure 7.1.1. Because of the Bolzmann distribution, the molecule could be in a vibrationally excited ground state $|g,n\rangle$ while absorbing the incoming photon of energy $\hbar\omega_0$ and getting excited to the excited state $|e,m\rangle$. If the excited state $|e,m\rangle$ decays radiatively into the ground-state of the system with a lower level of vibration excitation $|g,j\rangle$ with $j < n$, for example to the vibrational ground state $|g,0\rangle$, then the emitted photon will have larger energy $\hbar\omega_s > \hbar\omega_0$ than the initial photon.

The energy difference $\Delta\omega = \hbar\omega_s - \hbar\omega_0$ is the quantity tracked down in the Raman scattering experiments. The probability of Raman scattering depends critically on the energy difference $\Delta\omega$. The scattering probability peaks at certain resonant frequencies determined by the vibrational spectrum of the molecule. We computed the vibrational frequencies and Raman scattering cross-section within harmonic approximation for the restoring forces acting on the molecular nuclei. The harmonic approximation is summarized in the following section.

7.1.1 Harmonic Approximation in Vibrational Spectroscopies

Vibrational spectroscopies can be explained within the Born-Oppenheimer approximation [270] (see also chapter 1). The many-body wave function describing the coupled motion of electrons and nuclei is separated into nuclear and electronic

wave functions within the Born-Oppenheimer approximation. Because the nuclei are much heavier than the electrons, in most cases they can be further treated as classical particles. In the ground state, the nuclei and electrons are at equilibrium. At equilibrium, the nuclei assume some positions dictated by the minimum energy principle in which the internal forces compensate. If a nucleus position is perturbed, then a collective back-action of other nuclei and electrons will exert a restoring force. The restoring forces are *harmonic*, i.e. linearly proportional to the spatial perturbations in the limit of *small displacements*. Obviously, there are at most $3N-3$ spring constants, describing vibrations in a N-atom molecule. For vibrational spectroscopy, we would like to determine the linearly independent vibrations of the whole molecule rather than the spring constants of each atom. The following description is based on the work from Ref. [273].

In the harmonic approximation, the vibrational eigenmodes are determined by solving an eigenvalue problem [271, 273]

$$\begin{aligned} &\sum_{\alpha=1}^{3N} \left(H_{j\alpha} - \lambda_q M_{j\alpha}\right) X_{\alpha q} = 0, \quad j \in [1, 3N] \quad \lambda_q = (2\pi\nu_q)^2, \\ &\sum_{\alpha,l=1}^{3N} X_{\alpha q} M_{\alpha l} X_{lj} = \delta_{qj}, \quad M_{\alpha l} = \delta_{\alpha l} m_n, \quad n = [l/3] + 1. \end{aligned} \tag{7.1}$$

In eqn. (7.1), H is the dynamical or Hessian matrix of the system, m_n is the mass of the nth atom. The eigenvectors $X_{\alpha q}$ and eigenfrequencies ν_q represent the linearly independent vibration modes of the molecule. A displacement $U_{\alpha q}$ in the direction of the ith eigenvector can be written as

$$U_{\alpha q} = Q_q X_{\alpha q}, \tag{7.2}$$

where Q_q is referred to as a normal mode coordinate, assuming that $X_{\alpha q}$ is properly normalized. The scattering cross-sections of IR and Raman spectroscopies depend on derivatives of the dipole moment μ and the dynamical polarizability P with respect to the normal modes Q_q, correspondingly. If the derivatives of a physical property A are already known with respect to the Cartesian atomic coordinates R_α, then the required derivative dA/dQ_q is obtained by the chain rule $\frac{dA}{dQ_q} = \sum_{\alpha=1}^{3N} \frac{\partial A}{\partial R_\alpha} X_{\alpha q}$. The first-order IR intensity of the q-th mode is given by [271]

$$I_q^{IR} = \frac{\mathscr{N}\pi}{3c} \left| \frac{d\mu}{dQ_q} \right|^2, \tag{7.3}$$

where $\mathscr{N}$ is the particle density, c is the velocity of light and μ is the electric dipole moment of the molecule. The square of the derivative $|d\mu/dQ_q|^2$ is the

only molecular property entering the formula (7.3). Therefore, it is often referred to as the absolute IR intensity. The dipole moment is a property of the electronic ground state and it can be easily estimated within DFT. If the IR intensity (7.3) are measured at normal conditions—temperature 0°C and pressure 1 atm, then it is related to the absolute IR intensity as following: 1 $(\mathrm{D/\AA})^2$ amu^{-1} = 171.65 cm^{-2} atm^{-1}.

The evaluation of Raman-scattering intensities is slightly more complicated. Following Refs. [273, 274], the first-order differential Raman cross-section for the Stokes component of the ith eigenmode far from electronic resonances is given by

$$\frac{d\sigma_q}{d\Omega} = \frac{(2\pi\nu_S)^4}{c^4} \left| \mathbf{e_S} \frac{\partial P}{\partial Q_q} \mathbf{e_L} \right|^2 \frac{h(n_q^b + 1)}{8\pi^2 \nu_q}, \tag{7.4}$$

$$\text{with} \quad n_q^b = \left[e^{\frac{h\nu_q}{kT}} - 1 \right]^{-1}. \tag{7.5}$$

In eqn. (7.4), ν_S is the frequency of the scattered light, $\mathbf{e_S}$ and $\mathbf{e_L}$ are the unit vectors of the electric field direction (polarization) for the scattered and the incident light, P is the polarizability tensor obtained from TDDFT calculations (see eqn. (2.91)), and n_q^b is the Bose-Einstein statistical factor. Since molecules in the gas phase may be oriented randomly, this expression has to be appropriately averaged. The result of this averaging procedure depends on the relative orientations of the direction and polarization of the incident and scattered beams. In most of the experiments, the direction of the incident beam, the polarization direction of this beam and the direction of observation are perpendicular to each other. Under these circumstances, one yields a Raman cross section

$$\frac{d\sigma_q}{d\Omega} = \frac{(2\pi\nu_S)^4}{c^4} \frac{h(n_q^b + 1)}{8\pi^2 \nu_q} \frac{I_q^{\mathrm{Ram}}}{45}, \tag{7.6}$$

where the *Raman scattering activity* I_q^{Ram} is the only quantity depending on the intrinsic molecular properties

$$I_q^{\mathrm{Ram}} = 45\langle \frac{d\alpha}{dQ_q} \rangle^2 + 7 \left(\frac{d\beta}{dQ_q} \right)^2 = 45\langle \alpha' \rangle^2 + 7\beta'^2. \tag{7.7}$$

The derivative $\langle \alpha' \rangle$ is the mean polarizability derivative

$$\langle \alpha' \rangle^2 = \left[\frac{1}{3} \left(P'_{xx} + P'_{yy} + P'_{zz} \right) \right]^2, \tag{7.8}$$

and the derivative β' is an anysotropy parameter of the polarizability tensor, respectively

$$\beta'^2 = \frac{1}{2}\left[\left(P'_{xx} - P'_{yy}\right)^2 + \left(P'_{xx} - P'_{zz}\right)^2 + \left(P'_{yy} - P'_{zz}\right)^2 + 6\left(P'^2_{xy} + P'^2_{xz} + P'^2_{yz}\right)\right]. \tag{7.9}$$

Primes denote derivatives with respect to the normal mode coordinate $P'_{ij} = \frac{\partial P_{ij}}{\partial Q_q}$. The optical polarizability P_{ij} is computed at a given frequency, being the only frequency entering in the calculation, this is justified by the fact that the vibrational energies are usually negligible as compared to the electronic excitation energies. All the equations given above are derived within the double harmonic approximation. Thus, the higher-order changes of the energy, dipole moment, and polarizability with respect to the normal-mode coordinate Q are neglected.

7.1.2 Implementation of the Harmonic Approximation

The theory summarized above was implemented using the finite-differences method to compute the derivatives of the dipole moment μ and the optical polarizability $P(\omega = 0)$ with respect to the normal coordinates Q_q. The necessary calculations were organized using ASE, SIESTA (DFT) and PySCF-NAO (TDDFT) packages. ASE is used as a driver, ordering necessary calculations, gathering the data and combining it into the scattering cross-sections (7.3) and (7.7). At the beginning, we determine the ground-state geometry with a small tolerance on the remaining internal forces and the same DFT parameters that will be used later across the other calculations. The equilibrium geometry is the only input data used in the calculation of the vibrational modes and their respective Raman intensity.

In the next step, the six small displacements are applied for each atom to determine the force constants H and the derivatives of dipole moment μ' and the optical polarizability tensor P'_{ij}. The whole calculation is similar to the usual normal-mode determination in the vibrational spectroscopy. It consist of $6N+1$ independent DFT+TDDFT calculations with slightly different molecular geometries. The calculations can be rather time-consuming (especially TDDFT calculations of the optical polarizability). Therefore, the independence of the calculations can be optionally preserved. Moreover, the generated data are stored in separate files for each of the $6N+1$ DFT and TDDFT calculations. In the last step, the stored data are read from files, the normal vibrational modes (eqn. 7.1) are identified, and the calculated dipole moment and polarizabilities are combined into the IR and Raman scattering cross-section. An example of Python script is shown in Figure E.2.1 of appendix E.2.

7.2 Vibrational Spectra of the CO_2 Molecule

In order to check the implementation described in the previous section, we computed the vibrational modes and their IR and Raman intensities of a CO_2 molecule. CO_2 is a good molecule for such check since it is composed only of three atoms, therefore, just 19 calculations (DFT+TDDFT) are necessary in order to get its vibrational modes, and each calculation takes a few minutes to complete. Furthermore, the vibrational modes of CO_2 have been extensively studied and are well understood [275–277]. Linear triatomic molecules such as CO_2 possess four vibrational modes but only three fundamental vibration frequencies because two modes are degenerate. As its name indicates, the symmetric stretching mode is fully symmetric, thus, it is inactive in IR spectra and active in Raman spectra. The asymmetric stretching vibration and the degenerate bending vibrations are IR active and Raman inactive.

To compute the vibrational modes, we first must relax the molecule with care. This step was performed using the SIESTA suite. Once an equilibrium geometry has been found, we can start to run the vibrational calculations (an example of script is shown in appendix E.2). In the ground-state calculations, the core electrons were removed by means of Troullier-Martins pseudo-potentials [122]. We used the Perdew-Burke-Erzenhorf density functional (GGA-PBE) [35] for geometry relaxations and force constants calculations. A double-ζ polarized basis set of numerical orbitals generated using an energy shift of 10 meV was used. The fineness of the real-space grid used to compute the Hartree and exchange-correlation contribution to the energy and Hamiltonian corresponds to a plane-wave cut-off of 450 Ry. Another parameter that has a dramatic impact on the accuracy of the method, is the atomic displacement `delta`. While choosing an appropriate value, one must find a compromise between the smallness necessary for the harmonic approximation to remain valid and having a sufficiently large variation of the computed magnitudes to obtain meaningful numerical derivatives. For this particular calculations, optimal frequencies were obtained for `delta=0.015`Å.

Quantum Espresso (QE) [278] calculations of the vibrational modes of CO_2 were performed as a reference for our calculations. We used PBE functional as in our calculations to determine the frequencies of vibrational modes and IR intensities. The Raman intensities were computed with Perdew-Zunger LDA functional, because this is the only possibility allowed in QE. The results are gathered in table 7.1. The vibrational frequencies differ by less than 23 cm^{-1} (2%) and somewhat more (125 cm^{-1} or 9%) comparing to experimental data [277]. The bending and asymmetric stretching modes are IR-active and Raman-silent, while the symmetric stretching mode is Raman active and IR-silent in both implementations, as expected.

We demonstrated that it is feasible to use the iterative TDDFT also in the cal-

Modes		1 bending	2 stretching	3 asymmetric stretching
ω (cm^{-1})	exp	667.00	1330.00	2349.00
	ASE	619.30	1248.40	2244.40
	QE	608.45	1271.13	2223.67
IR ($(D/Å)^2$ amu^{-1})	ASE	0.43	0.00	11.99
	QE	0.45	0.02	12.33
Raman ($Å^4$ amu^{-1})	ASE	0.00	24.57	0.00
	QE	0.00	23.82	0.00

Table 7.1: CO_2 vibrational modes with their respective IR and Raman intensities. First row compares the frequencies of the three vibrational modes from experimental data [277], our implementation and Quantum Espresso [278] calculations. The second row shows the IR intensities of the corresponding modes while the third row shows the Raman intensities.

culation of the Raman scattering intensities. In the current section, we achieved a proof-of-principle implementation. Moreover, this method could be used for more complex simulations. We explored the possibility to apply this method to simulate surface-enhanced Raman spectroscopy (SERS) [279] and tip enhanced Raman spectroscopy (TERS) [280] by placing a molecule inside a cavity formed by metallic clusters (such as the one show in chapter 3, 4 and 6). However, for such systems, where the vibrational modes are localized in one small portion of the total system, the finite differences approach presented here did not provide sufficient accuracy to determine meaningful Raman scattering cross-section. The next step would be to develop some scheme (based on Mulliken population analysis [44, 281]) to project the result onto the region of interest, thus, increasing the resolution of the calculations. Unfortunately, this has proven to be a difficult task so far.

7.3 Conclusions

In this chapter, we gave an account on yet another type of spectroscopy—the vibrational scattering spectroscopy. Vibrational spectroscopies explore relatively small energy changes of a molecule caused by the oscillations of molecular nuclei. The infrared and Raman spectroscopies are widely used vibrational spectroscopies, which can serve as very sensitive detectors for molecules. Coupling of the infrared and Raman spectroscopies with near-field plasmonic enhancement in the vicinity of surfaces, tips or clusters allows to increase sensitivity of the detection up to a single-molecule level. Theoretically, the vibrational spectroscopies can be simulated in atomistic *ab initio* frameworks, using a plausible harmonic approx-

imation to get the restoring forces felt by the nuclei slightly displaced from their equilibrium positions. In fact, the calculation of vibrational frequencies is part of many *ab initio* DFT packages. However, the estimation of scattering cross-sections involves more steps, particularly the Raman scattering. To estimate the probability of non-resonant Raman scattering one can track changes of the optical polarizability along the normal mode vibrations. One of the advantages of this implementation of Raman spectroscopy, is its potential capacity to calculate the Raman intensities of the vibrational modes of large systems made possible by the efficiency of our iterative TDDFT implementation.

Chapter 8

Conclusions

As J.D. Wilson and C.A. Hernández-Hall state in Ref. [282]: "*Experimental measurement is the cornerstone of the scientific method, which holds that no theory or model of nature is tenable unless it predicts are in accord with experiment.*" However, not all the characterization of condensed matter systems can be done exclusively with experimental measurements. The kind of experiments necessary are often time consuming, difficult to perform and to reproduce, requiring costly instrumentations and can even be dangerous for the operator. Furthermore, there is simply not enough researchers, time and resources to explore experimentally the vast potential of modern science. Simulations are revealed to be crucial to accelerate the progress in science, and particularly in nanosciences. Simulations allow to run "virtual" experiments that are sometimes faster and cost less than "real" experiments, permitting to select potential materials and the conditions required to obtain the desired effects. Modeling is also often necessary to validate an experiment and to better understand the physical phenomena observed. Beyond the simple reproduction of experimental measurements, simulations permit to examine unphysical conditions and non-existing materials. By studying the impossible, we can get a better understanding of what is possible.

In this thesis we focused on a particular kind of modeling, the simulation of electrons in matter and their interaction with the environment using atomistic *ab initio* theory. Specifically, we modeled the behavior of plasmons in nanostructures composed of different materials using density functional theory (DFT) and time-dependent DFT (TDDFT). The foundations of DFT and TDDFT are summarized in chapter 2 together with a detailed description of the methods to realize linear-response TDDFT calculations with numerical atomic orbitals (NAO). To apply the atomistic TDDFT to the metallic clusters containing sometimes thousands of atoms, several improvements and extensions were realized in the TDDFT

code MBPT-LCAO, its successor PySCF-NAO and in the ASE suite. Below, we list the major extensions and technical improvements realized during this work.

- Implementation of the real-space Electron Energy Loss Spectroscopy;
- Improvement of the iterative procedure that permitted unprecedentedly large calculations;
- Efficient computation of the induced electric field in Cartesian coordinates;
- Implementation of the Raman scattering spectroscopy for molecules;
- Parallelization of several parts of the code, most notably of the iterative procedure, for its use on Graphical Processing Units (GPU);
- Other technical improvements such as support of Hierarchical Data Format (HDF) and optimization of the random access memory use.

The contributions listed above allowed to model the electronic excitations in several scenarios relevant for modern nanoscience and previously unexplored in *ab initio* simulations. The simulations performed during this work are summarized below.

In chapter 3, by means of first-principles atomistic TDDFT calculations we demonstrated [44, 83, 146, 264, 266] that the distribution of the near-field close to plasmonic nanoparticles exhibits subnanometric hot spots. The hot spots reflect the atomic-scale features at the nanoparticle surface. These features consist of vertices and edges at the contact of the crystallographic facets of the particles. In particular, for the plasmonic dimer, we have shown that the field localization and enhancement inside the plasmonic nanogaps can be very different depending on whether the distribution of the atoms at the gap define a flat surface, or present atomic-scale tip-like protrusions. We obtained that the far-field also depends on the atomic configuration but in a less marked manner.

Our findings provide new insights into the limits of plasmonic localization. The presence of atomic-size features, e.g., formed by edges and vertices between crystalline facets in a nanoparticle, gives rise to near-fields localized in regions of a few Ångstroms, i.e., literally of atomic size. This effect can be related to the classical divergence of a field due to the presence of sharp edges. Indeed, the vertex ending by a single atom, as the one considered in this thesis, would be the example of the sharpest possible tip. Furthermore, the field enhanced at the atomic-scale hot spots is intensified by the presence of the overall plasmonic background enhancement, following a cascade effect. Based on this parallelism, we can establish an atomic-scale analogy with the macroscopic plasmonic lens of self-similar antennas [135, 146].

We compared classical simulations of small metal clusters with our *ab initio* atomistic simulations and found that the predictions of the former can be significantly improved when the atomic-scale geometrical features are taken into account [146]. Nevertheless, only full *ab initio* atomistic calculations are able to provide a fair description of the response of the system under external perturbation [83, 283], when quantum phenomena play an important role. As demonstrated in section 3.3 of chapter 3, in a realistic nanogap, the key features of the field enhancement can easily reach the atomic-scale. Therefore, a description of the plasmonic response based on smooth interface profiles, either classical or quantum, might not be able to address this atomic-scale near-field regime. To understand and optimize certain experimental situations operating in the subnanometer-scale, it might be mandatory to develop computational schemes that account for the atomistic structural details and basic quantum mechanical effects. Such sensitivity to the atomic details of a structure could explain the lack of reproducibility between apparently similar experiments [267], but could also provide a hint for further optimization of morphologies. The dependence of the far-field optical spectroscopy on the atomic-scale features at the nanoparticle(s) surface, is a remarkable finding that might provide new insights into the limits of plasmon localization, and has important consequences for the limits of optical resolution in field-enhanced spectroscopies [284, 285] and microscopies [126, 128, 141].

Chapter 4 describes how atomic-scale structural reorganizations are crucial to determine the optical properties of plasmonic cavities [266]. Besides the importance of jump-to-contact events, which can almost completely eliminate any signature of the plasmonic tunneling regime, the effects are dramatic when a metal nanocontact is formed across the cavity. This is due to the strong dependence of the plasmonic response of the system on the quantized current flowing through the connecting neck.

The mechanical response of atom-sized necks is characterized by sudden rearrangements of the atomic structure which frequently involve just a few atoms in the thinner part of the contact. Since the electron transport through thin metal nanocontacts is quantized, the corresponding changes of the current flowing across the junction are necessarily discontinuous. Our calculations demonstrate that this common observation under small applied dc biases can be extrapolated to the optical frequencies of the plasmon resonances of the cavity, at least for the short ballistic contacts considered here. These jumps in the current translate onto abrupt changes in the plasmonic response of the system. Thus, the discontinuous evolution of the spectral position, width and intensity of the charge transfer plasmon mode observed in our simulations is a direct consequence of the transport quantization in the connecting neck.

The correlation is clearly demonstrated, showing that remarkably, optics follows the atoms. This is absolutely important in the design of subnanometric-scale optical modulators that rely on slight changes of the optical response against tiny configurational modifications. In our case, we have analyzed structures inside plasmonic cavities formed by relatively small icosahedral sodium clusters, however, we expect to find a similar behavior for other materials suitable for electronic applications, such as gold.

The effect of single-atom motion on the optical properties of a nanoscopic object as the one reported in chapter 4, which can be probably extended to somewhat larger objects, has important consequences in optical engineering, molecular electronics, and photochemistry, where the optical response could be tailored by a few atoms.

Thanks to improvements to the software that have been implemented during this thesis, we were able to calculate the polarizability and the induced charge density for metallic clusters of sizes ranging from a few atoms up to more than 5000 atoms as presented in chapter 5. This allowed us to study the size dispersion of surface plasmon frequency of these large systems with atomistic *ab initio* methods for the first time. The calculations presented in chapter 5 prove that current *ab initio* theories can be used to successfully describe and gain understanding on the plasmonic properties of nanostructures of different chemical compositions. In our simulations, we studied the surface plasmon resonances in silver and sodium clusters comparing their dependence on the cluster sizes. In particular, we have revealed the competition between the size dispersion determined by the quantum confinement (QC) and the Coulomb interaction, the former dominating in silver clusters due to the screening of the d-electrons that weakens the effective electron-electron interaction.

Comparing the pictures provided by the classical and quantum mechanical theories, we see that most of the classical explanations are based on some surface models (either of the modifications of the average electron density or of the distribution of the induced density close to the surface). In our quantum mechanical approach, we can explain the different size dispersion of Na and Ag as a result of the competition between QC and the strength of the Coulomb interaction between conducting electrons. The latter is weakened due to the screening caused by the bound d-electrons in the case of silver clusters. Our calculations in the non-interacting case testify that the crucial effect governing the size dispersion is QC. Moreover, the classical microscopic picture of the induced density clumping at the surface can be confirmed only for sodium clusters.

The improved *ab initio* picture, will help guiding the design of plasmonic particles by controlling their composition or their coating.

In chapter 6, we study the electron energy loss spectra (EELS) of carbon nanotubes, boron nitride nanotubes, silver clusters and silver dimers. There are several experimental studies of the mentioned systems. We find a qualitative agreement between our calculations and experimental data in all the cases. The good agreement between theory and experiment in the characterization of such chemically different systems as metallic clusters and organic compounds confirms the chemical sensitivity of the implemented method. The method of computing EELS includes several approximations. Firstly, the probe electrons are modeled as classical point particles moving uniformly in a straight-line trajectory and perturbing the probed condensed matter system via the instantaneous Coulomb interaction. Secondly, the induced density of the perturbed condensed matter system is modeled within the linear-response TDDFT, using the iterative methods similar to those utilized to explore the optical spectroscopy of nanobjects in chapters 3, 4 and 5.

Similarly to the optical spectroscopy, in most cases EELS is capable to excite the dipolar modes in the probed quantum system. However, the EELS proves to be more versatile than optical spectroscopy. For instance, EELS signal strongly depends on the probing beam positioning. We demonstrate the dependence of the EELS on the beam positioning unambiguously in our calculations both for nanotubes and metal clusters. Besides the dipolar excitations, EELS is sensitive to the higher multipolar modes. Such higher multipolar modes are usually called dark modes because they are normally inaccessible using optical (light) spectroscopy. In our calculations, we demonstrate the excitation of dark surface plasmon modes in silver clusters and silver cluster dimers. The conditions for the dark surface plasmon mode to dominate in EELS are a central positioning of the probing electron beam and the spatial symmetry of the probed system. Under these conditions, the dipolar modes are not (or weakly) excited and the dark modes dominate the loss spectra. Unfortunately, these conditions (particularly the requirement of high symmetry) might be difficult to achieve with sufficient accuracy in experimental setups, which explains the scarcity of the experimental studies of dark modes.

The iterative TDDFT applied to EELS permitted to characterize finite systems containing several hundreds of atoms. Our implementation is the only *ab initio* atomistic framework capable to cope with such large quantum systems to the best of our knowledge. However, the experimentally characterized systems are typically much bigger than we can afford in the calculations and we needed to design carefully our calculations to obtain qualitatively correct and quantitatively reasonable results. For instance, we compared our calculations against the experimental measurements for some 20 nm silver clusters, containing about one million atoms. A direct *ab initio* determination of the cluster geometry for such a large cluster is currently impossible. However, since the surface to volume

ratio of the computed and measured clusters differs by an order of magnitude, it is reasonable to assume that the internal structure of such large clusters is similar to the lattice of bulk silver rather than to the icosahedral geometry that we have used to model small clusters. A comparison of the calculated EELS against experimental data indicate that this implication is correct. Namely, the experimental EELS for central incidence shows a bulk plasmonic resonance at 3.8 eV in very good agreement with the experimental observation. This resonance frequency differs significantly from the surface plasmon frequency at about 3.3 eV. On the theoretical side, the EELS for icosahedral clusters show only a slightly blue-shifted resonance at 3.4 eV, while the EELS for a cubic chunk of silver preserving the bulk lattice shows the plasmonic resonance at 3.8 eV, matching the experimental spectra more accurately.

In chapter 7, we gave an account on yet another type of spectroscopy—vibrational scattering spectroscopy. Vibrational spectroscopy originates in relatively small energy changes of a molecule caused by the nuclear motion, i.e., the excitation of vibrations. Infrared and Raman spectroscopies are widely used vibrational spectroscopies, which can serve as a very sensitive detectors for specific molecules. Theoretically, vibrational spectroscopies can be simulated in atomistic *ab initio* frameworks, using the harmonic approximation to obtain the restoring forces felt by the nuclei slightly displaced from their equilibrium positions. In fact, the calculation of vibrational frequencies is part of many *ab initio* DFT packages. However, the estimation of scattering cross-sections involves more steps, particularly for Raman scattering. To estimate the probability of non-resonant Raman scattering, one can track the changes of the optical polarizability along the normal mode vibrations. The calculations of optical polarizability can be relatively fast with our iterative TDDFT, allowing to estimate polarizabilities of molecules in the vicinity of relatively large metallic clusters to account for the enhanced Raman spectroscopy. In this chapter, however, we demonstrate only proof-of-principle calculations of Raman (and infrared) cross sections for small molecules, speculating on how the harmonic approximation could be extended to simulate directly the enhanced Raman spectroscopies necessary for the detection of single-molecule signal.

Nanophotonics is a key in the development of many new technologies. We believe that atomistic *ab initio* theoretical approaches are necessary to properly describe processes at the atomic scale as those presented in this work. We presented a theoretical study of several types of spectroscopies at the DFT and TDDFT levels of theory. Several methods were developed and improved during the thesis, allowing to realize many calculations that were impossible before this work. We believe that the extensions of the implemented methods towards

higher accuracy (using improved DFT functionals) and towards accounting for yet unexplored physical observables and situations will contribute to advances in nanophotonics and in a broader scope, in nanosciences.

Appendices

Appendix A

The SIESTA program

The following appendix is based on the description of the SIESTA program from Federico Marchesin's PhD thesis [286]. SIESTA is both a method and computing code inspired by the *ab initio* Tight-Binding (TB) technique developed by Sankey and Niklewski [287] which became a popular *ab initio* code for electronic structure calculations [1, 2, 44, 83, 205, 266]. SIESTA is an *ab initio* DFT code designed to perform electronic ground-state calculations for periodic and finite systems. The use of localized basis sets and linear-scaling algorithms results in a highly efficient code for electronic structure and molecular dynamics simulations. Starting with version 4.0 in spring 2016, the SIESTA package became GPL (General Public Licence) and also adopted a modern approach for developing open-source software [288].

In this appendix, as a short introduction to the program, we will show one example of SIESTA input file and explain some selected parameters. Although the thesis is mainly focused to the study of optical properties, quality of the ground-state calculations are of fundamental importance as it directly influences the response of the system to an external perturbation. Two of the most influential parameters will be discussed separately in sections A.2 (basis set multiplicity) and A.3 (energy shift).

A.1 SIESTA Input File

An example of SIESTA input file is shown in Figure A.1.1. The input file corresponds to a simple diatomic silver system. The meaning of all parameters is explained in the SIESTA documentation [289]. Below, we discuss only five parameters that are essential for the quality of a subsequent TDDFT calculation.

- *MeshCutOff*: parameter defining the fineness of the 3D real-space grid. Although the real-space quantities are not directly imported in our implementation of TDDFT, the number of grid points affects the overall quality of the numerically computed matrix elements and thus the quality of the whole DFT output—Kohn-Sham states, molecular geometries etc.

- *DM.Tolerance*: parameter controlling the convergence of the density matrix (DM) during the Kohn-Sham self-consistent loop. It is important to use a small value (less than 10^{-4}) and also to ensure the actual convergence of the self-consistent loop to achieve reproducibility of the TDDFT calculations.

- *PAO.BasisSize*: parameter to set the basis set multiplicity of pseudo-atomic orbitals (PAO). The multiplicity defines a set of atomic orbitals. In this work, we were using mostly the default double-ζ polarized (DZP) basis set. DZP basis set is sufficient to reproduce qualitatively most of features of optical response. To improve quantitatively the results, user might want to increase the basis set multiplicity at the cost of some computational performance loss. More details on this parameter are provided in section A.2.

- *PAO.EnergyShift*: parameter to control the spatial extend of atomic orbitals globally. The energy shift parameter is designed to control the extend of all atomic orbitals at once, but appropriately for each radial orbital. Smaller energy shifts lead to more extended orbitals which is better for the quality of the basis set but worser for the computational performance. In this work, we normally used longer-than-default orbitals. Further details are available in section A.3.

- *COOP.Write*: boolean parameter causing to export the Kohn-Sham Hamiltonian and eigenstates at the end of the Kohn-Sham self-consistent loop. This data is used in the subsequent linear-response TDDFT calculations. Therefore, it must be set to True in most of our SIESTA calculations.

```
SystemName          Ag2
SystemLabel         siesta

NumberOfAtoms     2
NumberOfSpecies   1

%block ChemicalSpeciesLabel
  1  47  Ag
%endblock ChemicalSpeciesLabel

AtomicCoordinatesFormat Ang
%block AtomicCoordinatesAndAtomicSpecies
  -0.00000  0.00000  -0.00000   1
   2.40600  0.00000  -1.48699   1
%endblock AtomicCoordinatesAndAtomicSpecies

XC.functional     GGA
XC.authors     WC

MD.TypeOfRun     CG
MD.NumCGsteps     400
MD.MaxForceTol     0.02   eV/Ang

MeshCutOff     250   Ry

DM.MixingWeight     0.01
DM.Tolerance     0.0001
DM.NumberKick     40
DM.NumberPulay     4
DM.KickMixingWeight     0.15
DM.UseSaveDM    .True.
DM.MixSCF1      .True.

SolutionMethod     Diagon
MaxSCFIterations     1500

PAO.BasisType     split
PAO.EnergyShift     100   meV
PAO.BasisSize     DZP

WriteCoorXmol     .True.

### Exports .DIM and .PLD files
WriteDenchar     .True.

### Exports .WFSX, .HSX
COOP.Write     .True.
```

Figure A.1.1: SIESTA input file for two silver atoms.

A.2 Basis Set Multiplicity

SIESTA uses a linear combination of atomic orbitals to expand the Kohn-Sham eigenstates

$$\psi_n(\mathbf{r}) = \sum_a X_a^n f^a(\mathbf{r}). \tag{A.1}$$

The expansion coefficients X_a^n are determined in the Kohn-Sham self-consistent loop (see chapter 2). The atomic orbitals $f^a(\mathbf{r})$ are given by a product of radial functions and spherical harmonics. The size of the basis, i.e. the number of orbitals per atom included in the calculation can be tuned by the user (*block PAO.Basis* as in Figure B.0.1). However, to facilitate the use, a parameter sets the number of Atomic Orbital (AO) generated by the program. Different types of basis sets can be easily chosen by the user: single, double or triple ζ (SZ, DZ, TZ). Polarized orbitals can be added in the same fashion: single, double or triple-ζ polarized (SZP, DZP, TZP). The SZ basis set is the minimal basis set available. It has one single radial function per angular momentum channel, i.e. carbon atom's valence orbital $2s2p$ is described by four functions, one for the s-type orbital and three for the p-type orbital. By adding a second function per channel the DZ basis set is obtained. In this case a carbon atom is described with 8 atomic functions. The default basis set in SIESTA is the DZP, which adds polarization orbitals, i.e. orbitals with a higher angular momentum component. For instance, in case of the carbon atom described by a DZP basis, five d-type extra orbitals are added to the DZ basis set. Thus, valence electrons are described with a total of 13 functions per carbon atom when using the DZP basis set.

As we add orbitals, the basis set becomes more accurate. A larger basis set is usually providing a more accurate and reliable results due to the better completeness of the high-ζ basis sets. However, these larger basis set are naturally more computationally demanding and there is typically a trade-off between the accuracy and computational performance of the calculation. SIESTA's default DZP basis set is a good compromise between accuracy and computational performance. Therefore, it is used in most of the calculations in this work.

A.3 Energy Shift Parameter

The radial orbitals in SIESTA are given on a numerical grid. The atomic orbitals defined on a radial grid are usually referred as numerical atomic orbitals (NAO). Moreover, the pseudo-potentials are obligatory in SIESTA and, by analogy, the atomic orbitals are referred as pseudo-atomic orbitals (PAO). The shape of PAOs is determined by solving a radial Schrödinger equation and they are

strictly zero beyond a radial distance. The orbitals' confinement can be controlled by the *PAO.EnergyShift* parameter rather than the value of the cutoff radius itself. Solving the radial part of the Schrödinger equation. SIESTA adds the energy shift to the precise eigenenergy of an orbital, causing the outward solution to cross the abscissa axis rather than to strive to zero at infinity $r \to \infty$. The cross point is taken as the radial cutoff beyond which the radial orbital is not represented. This is similar to define a spherical box with infinite walls at the radial cutoff. Usually, a common energy shift is fixed for all the chemical species avoiding the task to define different cutoff radii for different atoms and angular momenta. The higher is the energy shift, the more contracted are the generated orbitals. Left panel of Figure A.3.1 shows the 2p orbitals of carbon generated using an energy shift of 50 meV (red line) and 100 meV (blue line), the right panel shows the same comparison but for the polarization orbital with *d*-symmetry. Obviously, the extension of the orbitals affects the results of the cal-

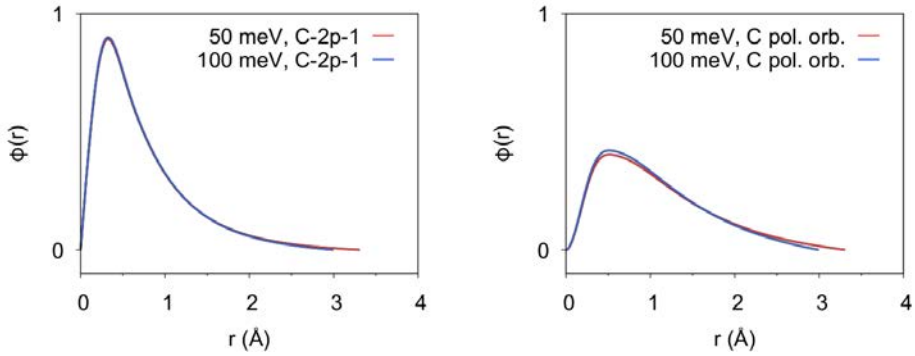

Figure A.3.1: The effect of the energy shift parameter on the shape of the radial orbitals. Smaller energy shift leads to more extended orbitals, from Ref. [286].

culation. More extended orbitals (small energy shift) provide in principle more accurate results, however, calculations will be more costly. Thus, it is important to perform convergence studies in order to make sure that reasonable values of the *PAO.EnergyShift* parameter are used.

Appendix B

TDDFT Calculations Example: Silver Clusters

In this appendix, we describe optical calculations of the series of icosahedral silver clusters presented in chapter 5. Once the geometry of the system is defined, the first step to perform is the calculations of the ground-state using SIESTA. We show our SIESTA input file in Figure B.0.1. Not all the data to be used in a subsequent linear-response TDDFT is exported by default, therefore it is mandatory to set the flag and `COOP.Write` to `True`. The main parameters of the SIESTA input are described in appendix A.

Once the ground-state calculations are finished, we used MBPT-LCAO [3–5] to compute the polarizability of the clusters. The input file for MBPT-LCAO for these specific calculations is shown in Figure B.0.2. These are the most optimal parameters which will give the best performance (CPU time and RAM usage) while not compromising the accuracy of the results. A more complete description of the parameters of MBPT-LCAO can be found on a wiki page [290]. The polarizability along the xx-axis for this series of silver clusters (from 13 to 2057 atoms) is shown in Figure B.0.3. The data (running time and memory consumption) extracted from these calculations were used for the Figures 2.3.1 and 2.3.2 in the main text of the thesis. The input files for these calculations can be downloaded from Ref. [291].

```
%block PAO.Basis
  Ag    2
  n=5  0  2  P  E 50.0 7.0
    0.000  0.000
  n=4  2  2     E 50.0 4.0
    0.000  0.000
  Ags  1
  n=5  0  1  P  E 50.0 7.0
    0.000
%endblock PAO.Basis

SystemLabel                siesta

%include "geometry.siesta.fdf"

MD.TypeOfRun     CG
XC.functional     GGA
XC.authors     WC
MD.NumCGsteps     400

MD.MaxForceTol     0.02   eV/Ang

MeshCutOff     250   Ry
DM.MixingWeight     0.01
DM.Tolerance     0.0001
DM.NumberKick     40
DM.NumberPulay     4
DM.KickMixingWeight     0.15
SolutionMethod     Diagon
MaxSCFIterations     1500
PAO.BasisType     split

DM.UseSaveDM    .True.
DM.MixSCF1      .True.

PAO.EnergyShift     100   meV
PAO.BasisSize     DZP
WriteCoorXmol     .True.
WriteDenchar     .True.
COOP.Write     .True.
```

Figure B.0.1: SIESTA input file for silver clusters

```
prod_basis_type     AC_DIRECT
biloc_interm_storage  SM
prod_basis_procedure   ONLY-PB
solver_type     3

gmres_eps     0.003
gmres_itermax     200
gmres_restart     250
gmres_verbose     20

xc_ord_lebedev     14
xc_ord_gl     48

eigmin_local     1e-04
eigmin_bilocal     1e-06

d_omega_win1     0.05
freq_eps_win1     0.15
omega_min_tddft     0.0
omega_max_tddft     5.0
omega_max_win1      5.0

ext_field_direction     1.0  0.0  0.0
dr   0.2    0.2    0.2

chi0_v_algorithm     13
para_type  MATRIX
save_temp   1

comp_dens_chng_and_polarizability     1
store_dens_chng     1
enh_given_volume_and_freq     0
diag_hs     0
check_basis  0
no_wfsx     0
plot_freq    3.6

ihartree       1
iexchange      1
icorrelation   1

do_tddft_iter    1

tddft_iter_solver_op    N
gwa_initialization      SIESTA_PB

kernel_algorithm      BCRS
bcrs_mv_block_size    15
```

Figure B.0.2: MBPT-LCAO input file for silver clusters

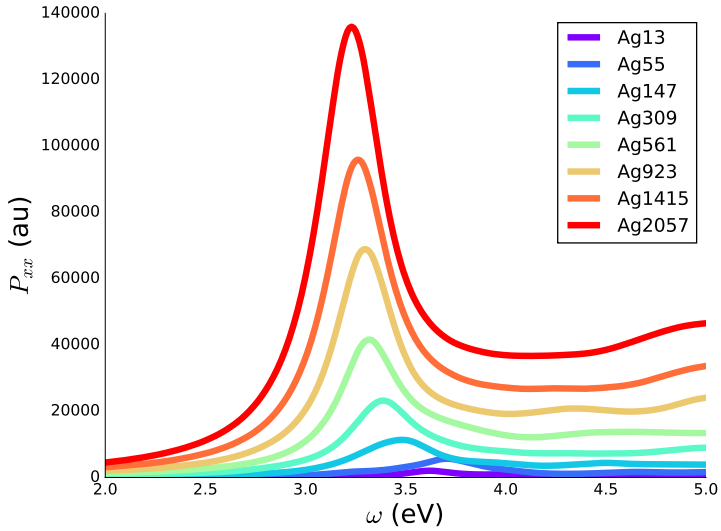

Figure B.0.3: Polarizability of silver clusters from 13 (purple) to 2057 (red) atoms calculated using SIESTA and MBPT-LCAO programs.

Appendix C

PySCF-NAO Script Examples

The code shown in Figure C.0.1 can be used to calculate the optical polarizability of a molecule in a dipole approximation. The script should be executed in the same folder where the preceding SIESTA calculation is finished. The SIESTA calculation should export certain data that are not exported by default for the TDDFT calculation to start successfully. For example, the Kohn-Sham eigenvalues will be taken from an XML output. The Kohn-Sham eigenstates will be taken from the WFSX binary files. In order to demand the export of the data used by PySCF-NAO, one should add the following options to the SIESTA fdf file

```
XML.Write       .True.
COOP.Write      .True.
```

The Python script in Figure C.0.1 was used to compute the optical polarizability of the silver icosahedral clusters on panel (a) of Figure 2.3.4. After the unavoidable import commands, a `tddft_iter` object is constructed. The object is versatile, but the presence of option `label` tells to import the data from SIESTA files defined by the `SystemLabel=siesta`. The other options present in the constructor of the `tddft_iter` object are suitable for a pseudo-potential starting points which is the case for any SIESTA calculation. During the execution of the constructor, the data will be imported, the SIESTA's atomic orbitals will be remapped to logarithmic grids, the product basis will be constructed and the matrix elements of TDDFT kernel will be computed. Later in the script, the non-interacting and interacting polarizabilities will be computed and stored into text files for a set of frequencies by calling appropriate methods of the class

tddft_iter.

```
from __future__ import print_function, division
import numpy as np
import sys
from pyscf.nao import tddft_iter

from ase.units import Ry, eV, Ha
from timeit import default_timer as timer

# initialize tddft calculations: calculate vertices and kernel
t1 = timer()
td = tddft_iter(label="siesta", iter_broadening=0.15/Ha, xc_code='LDA,PZ',
            level=0, tddft_iter_tol=1e-3, tol_loc=1e-4, tol_biloc=1e-6)
t2 = timer()
print("time tddft_iter = ", t2-t1)

# non interacting polarizability first
omegas = np.arange(1.0, 6.05, 0.05)/Ha + 1j*td.eps
t3 = timer()
pxx = -td.comp_polariz_nonin_xx(omegas).imag
t4 = timer()
print("time chi0 = ", t4-t3)

data = np.zeros((omegas.shape[0], 2))
data[:, 0] = omegas.real*Ha
data[:, 1] = pxx
np.savetxt('polarizability_nonin_siesta.pxx.txt', data)

# calculate interacting polarizability
t5 = timer()
pxx = -td.comp_polariz_inter_xx(omegas).imag

t6 = timer()
print("time chi = ", t6-t5)
data = np.zeros((omegas.shape[0], 2))
data[:, 0] = omegas.real*Ha
data[:, 1] = pxx
np.savetxt('polarizability_inter_siesta.pxx.txt', data)

print("nb call:")
print("rf0_ncalls = {0}, matvec_ncalls = {1}".format(td.rf0_ncalls,
                                                     td.matvec_ncalls))
t7 = timer()
print("total time = ", t7-t1)
```

Figure C.0.1: Python script for PySCF-NAO. In the script, we organize the calculation of the optical polarizability component $P_{xx}(\omega)$ for a set of frequencies, using the data from a preceding SIESTA run.

Appendix D

Analysis of EELS Spectra for a Silver Cube

In chapter 6, we have seen that the experimental bulk plasmon frequency [233, 234] at 3.8 eV is possible to reproduce in the calculation for a cubic chunk of bulk silver, while the calculation for an icosahedral geometry delivers the frequency of EELS maximum at 3.45 eV. In this appendix, we show more calculations for the cubic chunk of bulk silver for different beam trajectories.

In Figure D.0.1 the EELS spectra of five beam trajectories are shown. Four of the trajectories are oriented along the z-axis (full lines), perpendicular to the facet they cross. The fifth trajectory is directed along the cube diagonal (dashed line) as shown by the inset of the Figure. The first trajectory (blue line) the beam crosses the cluster through its center ($b = 0$ nm). The second trajectory (orange line) bisects the cluster at half distance to the surface ($b = D/4$). The third trajectory (green line) is passing just near the surface of the cluster ($b = D/2$). While the last trajectory is passing at 1 nm from the cluster surface ($b = D/2+1$ nm). When the beam is directed along the z-axis (full lines), two modes are excited. The SP at 3.25 eV, except when the beam is passing right through the center of the cluster (blue line), and the bulk plasmon at 3.8 eV, except when the beam is far from the cluster (red line). The fact that the SP is not excited when the beam passes right through the center can be justified by invoking the symmetry of the external potential in the relevant range of frequencies. While it is obvious that the bulk plasmon can not be excited if the beam is not crossing the particle. The presence of the bulk plasmon for the silver cube is the main difference with the icosahedral geometry for which no excitations were observed at 3.8 eV (Figure 6.3.2). Yet, when the beam is directed along the diagonal of the cube (dashed blue line), but still passing through the center of the cluster,

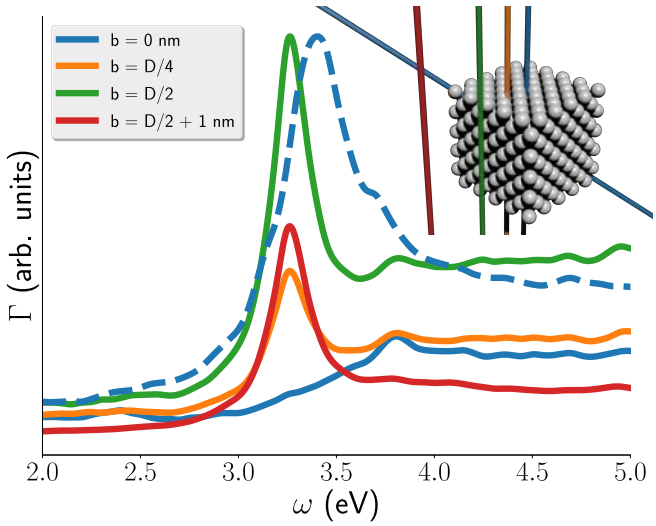

Figure D.0.1: Computed EELS spectra of a silver cube composed of 500 atoms with an edge length of $D \sim 20$ Å and a FCC lattice. The spectra were obtained for five beam trajectories. Four of them along the z-axis (full lines) and the fifth one along the diagonal of the cube (dashed line). Four impact parameters were used. The first one (blue lines) crossing the cluster right through its center ($b = 0$ nm). The second (orange line) passing at half-distance between the cluster center and its surface ($b = D/4$). The third trajectory (green line) passing just at the surface of the cluster ($b = D/2$). The last one (red line) passing at 1 nm from the cluster surface ($b = D/2 + 1$ nm). The cluster geometry used for the calculations together with the beam trajectories are represented in the figure. The colors of the beams are matching the colors of the lines. The kinetic energy of the probing electrons is 100 keV.

the bulk plasmon does not give rise to a well-developed peak, but it seems to appear a slightly red-shifted shoulder of the main resonance. Instead an intense peak rises at 3.4 eV, blue shifted of 0.15 eV compared to the SP. This is the exact same behavior that for the icosahedral clusters which was explained in section 6.3.1. This comparison of EELS spectra for silver cube and icosahedral clusters demonstrate that we are capable to reveal the bulk plasmon from *ab initio* method in silver. It also shows that the intensity of the bulk plasmon is greatly sensitive to the cluster internal structure and to the beam position and orientation.

Appendix E

PySCF-NAO Calculator and Raman Scattering implementations in ASE

The atomic simulation environment (ASE) [19] is a software package written in the Python programming language with the aim of setting up, steering, and analyzing atomistic simulations. In ASE, tasks are fully scripted in Python. The powerful syntax of Python combined with the NumPy library make it possible to perform complex simulations. For example, a sequence of calculations may be performed with the use of a simple "for-loop" construct. Calculations of energy, forces, stresses and other quantities are performed through interfaces to many external electronic structure codes or force fields using a uniform interface. On top of this calculator interface, ASE provides modules for performing many standard simulation tasks such as structure optimization, molecular dynamics, handling of constraints, and many other modules.

E.1 SIESTA-PySCF Calculator

During this thesis, the SIESTA calculator had been greatly improved by Mads Englund (mads_engelund001@ehu.es) whom I helped and I added some more functionalities to the calculator. The main functionality I added is the the computation of optical polarizability using PySCF-NAO package. An example of script that can be used to compute the polarizability using the combination of SIESTA-PySCF-ASE in Python is show in Figure E.1.1.

```
from ase.units import Ry, eV, Ha
from ase.calculators.siesta import Siesta
from ase import Atoms
import numpy as np

# Define the geometry of the molecule
Na8 = Atoms('Na8',
            positions=[[-1.90503810, 1.56107288, 0.00000000],
                       [1.90503810, 1.56107288, 0.00000000],
                       [1.90503810, -1.56107288, 0.00000000],
                       [-1.90503810, -1.56107288, 0.00000000],
                       [0.00000000, 0.00000000, 2.08495836],
                       [0.00000000, 0.00000000, -2.08495836],
                       [0.00000000, 3.22798122, 2.08495836],
                       [0.00000000, 3.22798122, -2.08495836]],
            cell=[20, 20, 20])

# enter SIESTA input
siesta = Siesta(
    mesh_cutoff=150 * Ry,
    basis_set='DZP',
    pseudo_qualifier='',
    energy_shift=(10 * 10**-3) * eV,
    fdf_arguments={
        'SCFMustConverge': False,
        'COOP.Write': True,
        'WriteDenchar': True,
        'PAO.BasisType': 'split',
        'DM.Tolerance': 1e-4,
        'DM.MixingWeight': 0.01,
        'MaxSCFIterations': 300,
        'DM.NumberPulay': 4,
        'XML.Write': True})


Na8.set_calculator(siesta)

# run DFT calculation with SIESTA
e = Na8.get_potential_energy()

# run TDDFT calculations using PYSCF
siesta.pyscf_tddft(label="siesta", jcutoff=7, iter_broadening=0.15/Ha,
        xc_code='LDA,PZ', tol_loc=1e-6, tol_biloc=1e-7,
        freq = np.arange(0.0, 5.0, 0.05))
```

Figure E.1.1: Python script that compute the ground-state (SIESTA) and the polarizability (PySCF) of a molecule using the ASE package. The calculated polarizability tensor can be found in the variable `siesta.results["polarizability inter"]`.

E.2 Raman Intensity with ASE, SIESTA, PySCF-NAO

The ASE package has a `vibration` module that can be used to compute the vibrational frequencies using finite difference method and the infrared intensities as presented in chapter 7. In chapter 7, we discussed how the Raman scattering intensity can be estimated theoretically within the harmonic approximation. Here, in Figure E.2.1, we show a Python script used to compute the Raman spectra of a molecule. Several packages must be orchestrated to perform this calculation. The presented script relies on ASE, SIESTA and PySCF-NAO to compute the Raman intensities. During the execution of the script, a set of $6N + 1$ DFT/TDDFT calculations will be performed, where N is the number of atoms to be displaced.

The script presented on Figure E.2.1 is used to calculate the Raman spectra of a molecule, it does not need any input files since ASE will take care to run SIESTA and PySCF. The output of the script consists both of a formatted report on the vibrational modes and Raman intensities as well as of a set of pickle files (binary, Python-readable) containing the data gathered after each of the DFT/TDDFT calculations. The calculation of Raman intensities can be easily parallelized. To parallelize the calculation, we use the option `indices` to indicate a subset of atoms which must be treated during the construction of the class `SiestaRaman`. The method `.run()` executes DFT/TDDFT calculations producing the binary pickle output files. If the expected pickle file exists already, then the corresponding DFT/TDDFT calculation is skipped and the necessary data are just read from the file. Such design makes the calculation of Raman spectra parallelizable and restartable.

```
from ase.units import Ry, eV, Ha
from ase.calculators.siesta import Siesta
from ase.calculators.siesta.siesta_raman import SiestaRaman
import ase.io as io
import numpy as np

# Load the relaxed geometry of the molecule
mol = io.read("path_to_relax_geo.xyz")

# enter siesta input
siesta = Siesta(
    mesh_cutoff=450 * Ry,           # Large meshcutoff
    basis_set='DZP',
    xc="GGA",
    pseudo_qualifier='gga',
    energy_shift=(10 * 10**-3) * eV,
    fdf_arguments={'SCFMustConverge': False,
                   'COOP.Write': True,       # necessary for TDDFT
```

```
19                     'WriteDenchar': True,      # necessary for TDDFT
20                     'PAO.BasisType': 'split',
21                     "PAO.SoftDefault": True,   # can help to get better accuracy
22                     'DM.Tolerance': 1e-4, 'DM.MixingWeight': 0.01,
23                     'MaxSCFIterations': 1500,
24                     'DM.NumberPulay': 4, "MD.MaxForceTol": 0.01,
25                     "MD.NumCGsteps": 0,        # No relaxation
26                     "DM.UseSaveDM": True,      # better to use previous density matrix
27                                                # to speed up siesta calculation
28                     'XML.Write': True          # necessary for TDDFT
29 })
30
31
32 mol.set_calculator(siesta)
33 list_atoms_disp = [0, 1, 2]          # list of the atoms to displace in order to
34                                      # compute the vibrational modes
35
36 ram = SiestaRaman(mol, siesta, label="siesta", jcutoff=7,
37                   iter_broadening=0.15/Ha,
38                   xc_code='LDA,PZ',                      # better to have good tolerance
39                   tol_loc=1e-6, tol_biloc=1e-7,          # keep in mind that this method is
40                   freq = np.arange(0.0, 4.0, 0.05)       # correct only far from resonnance
41                   delta = 0.01, indices=list_atoms_disp)
42
43 ram.run()                                               # run calculations
44 ram.summary(intensity_unit_ram='A^4 amu^-1')            # print summary
45 ram.write_spectra(start=200,                            # write continuous
46         intensity_unit_ram='A^4 amu^-1')                # spectra to file
```

Figure E.2.1: Python script to compute the Raman spectrum of a molecule. This script uses the `Siesta` calculator to perform DFT/TDDFT calculations for a set of perturbed molecular geometries around the equilibrium geometry given by reading an xyz file (other formats are accepted) at the beginning of the script. The list of the atoms to displace is given by the parameter `indices=list_atoms_disp` in line 41. By default, all the atoms of the molecule are displaced. This parameter can be used to parallelize the calculations over the atoms. Each computer running the calculations for the motions of one or few atoms.

Appendix F

Iterative Procedure: GPU Parallelization

We gratefully acknowledge the support of NVIDIA Corporation with the donation of the Tesla K40 GPU used for this research.

As we explained in the section 2.3.2.2, the most expensive part of the program, particularly for large systems, is the χ_0 algorithm that scales as $O(N^3)$ with the number of electron N. Even by using OpenMP and the Intel MKL [292] library for the basic linear algebra subroutine (BLAS) [293], the calculations are still very heavy because of the large matrix-matrix multiplications. It can be advantageous to use graphical processing units (GPU) to accelerate scientific software [294]. Nowadays, after more than a decade of development, this technology is becoming more mature and easy to use. We choose the CUDA [295] environment from NVIDIA since it is one of the most advanced for scientific computing with GPU. Particularly, we did a heavy use of the cuBLAS library to replace the BLAS routines by their GPU versions. In the columns below, we compare the routine chi0_13_matrix (left column) and its GPU version chi0_13_matrix_gpu (right column). These subroutines are the implementation of the equation (2.88). For simplification, we show only the code corresponding to the calculations of the real part of the matrix. The imaginary part is calculated with a similar code.

To illustrate the performance of the code, we performed the same calculation with both BLAS and cuBLAS parallelization methods. We used a silver dimer composed of 618 atoms of silver and 504 silver ghost atoms for a total of 1122 atoms (see section 6.3.3 in chapter 6). The calculation was performed on a relatively old machine with 16 Intel Xeon CPU E5620 at 2.40GHz with 12 MB of cache. This CPU is relatively old (2010). We added to this machine two recent GPUs GeForce GTX 1050 Ti that are low-end GPU. Only one GPU was used

during the calculation.

MATRIX parallelization: OpenMP and GEMM Blas routine.

```
!$OMP PARALLEL DEFAULT(NONE) &
!$OMP SHARED(aux, VV, vKS_re) &
!$OMP PRIVATE(n,i, j, si, fi)
!$OMP DO
do n = 1, aux%nloop
  si = aux%si(n, :); fi = aux%fi(n, :);
  do j = lbound(aux%Vertex_array(n)%array, 2), &
         ubound(aux%Vertex_array(n)%array, 2)
  do i = lbound(aux%Vertex_array(n)%array, 1), &
         ubound(aux%Vertex_array(n)%array, 1)
    VV(si(1)+i-1, si(2)+j-1) = &
      sum(aux%Vertex_array(n)%array(i, j, :)* &
      vKS_re(si(3):fi(3)))
  enddo
  enddo
enddo
!$OMP ENDDO
!$OMP ENDPARALLEL
call sgemm('N', 'N', norb, nocc, norb, 1E0, &
  VV, norb, aux%X4, norb, 0E0, XVV, norb)
call sgemm('T', 'N', nvirt, nocc, norb, 1E0, &
  aux%X_aF, norb, XVV, norb, 0E0, XXVV_re, nvirt);

!$OMP PARALLEL DEFAULT(NONE) &
!$OMP SHARED(aux, omega, eps, XXVV_re, XXVV_im, nocc) &
!$OMP SHARED(nvirt, vm) &
!$OMP PRIVATE(E, F, XVXz_FE, Emf, odiff)
!$OMP DO
do E=vm,aux%nocc;
  XXVV_re(1:E-vm+1, E) = 0;
  XXVV_im(1:E-vm+1, E) = 0;
enddo
!$OMP ENDDO

!$OMP DO
do F=1,aux%nvirt
  do E=1,min(F+aux%norbs-aux%nvirt,aux%nocc)
    odiff = aux%n2occ(aux%Fmin+F-1) - aux%n2occ(E)
    EmF = aux%DFT_E_occ(E) - aux%DFT_E_virt(F);
    XVXz_FE = cmplx(XXVV_re(F,E), XXVV_im(F,E))
    XVXz_FE = XVXz_FE*(odiff/cmplx(omega-EmF,eps) - &
      odiff/cmplx(omega+EmF,eps))
    XXVV_re(F,E) = real(XVXz_FE);
    XXVV_im(F,E) = aimag(XVXz_FE);
  enddo
enddo
!$OMP ENDDO
!$OMP ENDPARALLEL

call sgemm('N', 'N', norb, nocc, nvirt, 1E0, &
  aux%X_aF, norb, XXVV_re, nvirt, 0E0, XVV, norb);
call sgemm('N', 'T', norb, norb, nocc, 1E0, &
  XVV, norb, aux%X4, norb,0E0, VV, norb);
chi0_vKS(1:nprod) = 0
do n = 1, aux%nloop
  si = aux%si(n, :); fi = aux%fi(n, :);
  do k = lbound(aux%Vertex_array(n)%array, 3), &
      ubound(aux%Vertex_array(n)%array, 3)
  do j = lbound(aux%Vertex_array(n)%array, 2), &
      ubound(aux%Vertex_array(n)%array, 2)
  do i = lbound(aux%Vertex_array(n)%array, 1), &
      ubound(aux%Vertex_array(n)%array, 1)
    chi0_vKS(si(3) + k-1) = chi0_vKS(si(3) + k-1) + &
      aux%Vertex_array(n)%array(i, j, k)*VV(si(1)+i-1, &
      si(2)+j-1)
  enddo
  enddo
  enddo
enddo
```

MATRIX_GPU parallelization: OpenMP and CUDA.

```
!$OMP PARALLEL DEFAULT(NONE) &
!$OMP SHARED(aux, VV, vKS_re) &
!$OMP PRIVATE(n,i, j, si, fi)

!$OMP DO
do n = 1, aux%nloop
  si = aux%si(n, :); fi = aux%fi(n, :);
  do j = lbound(aux%Vertex_array(n)%array, 2), &
      ubound(aux%Vertex_array(n)%array, 2)
  do i = lbound(aux%Vertex_array(n)%array, 1), &
      ubound(aux%Vertex_array(n)%array, 1)
    VV(si(1)+i-1, si(2)+j-1) = &
      sum(aux%Vertex_array(n)%array(i, j, :)*vKS_re(si(3):fi(3)))
  enddo
  enddo
enddo
!$OMP ENDDO
!$OMP ENDPARALLEL

call chi0_mv_noxv_set_first_vv(VV, norb)
call chi0_mv_noxv_step1_re_gpu(norb, nocc, nvirt, Fmin)
call chi0_mv_noxv_step2_gpu(omega, eps, norb, nocc, nvirt, Fmin)
VV= 0
call chi0_mv_noxv_step3_re_gpu(VV, norb, nocc, nvirt, Fmin)
call chi0_mv_noxv_get_last_VV(VV, norb)
V = 0
!$OMP PARALLEL DEFAULT(NONE) &
!$OMP SHARED(V, aux, VV) &
!$OMP PRIVATE(n,k) &
!$OMP PRIVATE(si, fi)

!$OMP DO REDUCTION(+: V)
do n = 1, aux%nloop
  si = aux%si(n, :); fi = aux%fi(n, :);
  do k = lbound(aux%Vertex_array(n)%array, 3), &
      ubound(aux%Vertex_array(n)%array, 3)
    V(si(3) + k-1) = V(si(3) + k-1) + &
    sum(aux%Vertex_array(n)%array(:, :, k)*VV(si(1):fi(1), si(2):fi(2)))
  enddo
enddo
!$OMP ENDDO
!$OMP ENDPARALLEL

chi0_vKS(1:nprod) = chi0_vKS(1:nprod) + cmplx(0.0, V(1:nprod), 4);
```

The first loop is the calculation of the coefficient $\alpha^{cd} = V_\nu^{cd} z^\nu$ that was explained in the section 2.3.2.2. In fact this loop is very fast compared to the other part of the routine, for the CPU version it represents less than 1% of the full time of the χ_0 routine, therefore we chose to keep it with OpenMP in the GPU version in order to save memory on the GPU.

```
do n = 1, aux%nloop
  si = aux%si(n, :); fi = aux%fi(n, :);
  do j = lbound(aux%Vertex_array(n)%array, 2), ubound(aux%Vertex_array(n)%array, 2)
  do i = lbound(aux%Vertex_array(n)%array, 1), ubound(aux%Vertex_array(n)%array, 1)
    VV(si(1)+i-1, si(2)+j-1) = sum(aux%Vertex_array(n)%array(i, j, :) &
        *vKS_re(si(3):fi(3)))
  enddo
  enddo
enddo
```

For the GPU version, this loop takes 5.6% of the time spend in the algorithm, but since it is possible to overlap this loop with calculations performed on the GPU, its impact is reduced. Then, there are two matrix multiplications

```
call sgemm('N', 'N', norb, nocc, norb, 1E0, VV, norb, aux%X4, norb, 0E0, XVV, norb)
call sgemm('T', 'N', nvirt, nocc, norb, 1E0, aux%X_aF, norb, XVV, norb, 0E0, &
           XXVV_re, nvirt);
```

The `aux%X4` variable contains the occupied-states eigenvector, while `aux%X_aF` contains the virtual-states Kohn-Sham eigenvectors. These two matrix operations are very heavy for large systems and in our example they represent 60.6% of the χ_0 routine in the CPU case. Therefore, we start the GPU parallelization with these routines

```
call chi0_mv_noxv_set_first_vv(VV, norb)
call chi0_mv_noxv_step1_re_gpu(norb, nocc, nvirt, Fmin)
```

The routine `chi0_mv_noxv_set_first_vv` transfer the α^{cd} (noted `VV` in the code) matrix to the GPU in order to start the calculations

```
extern "C" void chi0_mv_noxv_set_first_vv_(float *VV_re, int *norbp)
{
  int norb = *norbp;
  checkCudaErrors(cublasSetMatrixAsync(norb, norb, sizeof(float), VV_re, norb,
                  VV_mat_d, norb, 0));
}
```

One of the bottle necks of GPU computing is the data transfer between the host (CPU) and the device (GPU). In order to minimize this data transfer, all the matrices that are constant in this routine are send to the device before the start of the iterative procedure. Only the matrix VV is in fact send

to the device and then send back to the host at each iteration. The routine `chi0_mv_noxv_step1_re_gpu` performs the two GEMM operations on the GPU. It is defined as following

```
extern "C" void chi0_mv_noxv_step1_re_gpu_(int *norbp, int *noccp, int *nvirtp,
                                           int *Fminp)
{
  int norb = *norbp, nocc = *noccp, nvirt = *nvirtp, Fmin=*Fminp;
  float alpha, beta;
  alpha = 1.0;
  beta = 0.0;

  cublasSgemm(handle_mat, CUBLAS_OP_N, CUBLAS_OP_N, norb, nocc, norb, &alpha,
            VV_mat_d, norb,aux_X4_mat_d, norb, &beta, XVV_mat_d, norb);
  cublasSgemm(handle_mat, CUBLAS_OP_T, CUBLAS_OP_N, nvirt, nocc, norb, &alpha,
            &aux_X4_mat_d[(Fmin-1)*norb], norb, XVV_mat_d, norb, &beta,
            XXVV_mat_re_d, nvirt);
}
```

The same routine is implemented for the imaginary part. The next step is the division by the energy denominator $\frac{XXVV}{\omega-(E-F+i\varepsilon)}$

```
do E=vm,aux%nocc;
  XXVV_re(1:E-vm+1, E) = 0;
  XXVV_im(1:E-vm+1, E) = 0;
enddo

do F=1,aux%nvirt
  do E=1,min(F+aux%norbs-aux%nvirt,aux%nocc)
    odiff = aux%n2occ(aux%Fmin+F-1) - aux%n2occ(E)
    EmF = aux%DFT_E_occ(E) - aux%DFT_E_virt(F);
    XVXz_FE = cmplx(XXVV_re(F,E), XXVV_im(F,E))
    XVXz_FE = XVXz_FE*(odiff/cmplx(omega-EmF,eps)-odiff/cmplx(omega+EmF,eps))

    XXVV_re(F,E) = real(XVXz_FE);
    XXVV_im(F,E) = aimag(XVXz_FE);
  enddo
enddo
```

This step is also very fast, for the CPU version it takes only 0.34% of the runtime. Even if this operation is very fast, we decided to perform it on the GPU device in case of the GPU parallelization in order to avoid data transfer. The GPU version of the previous routine look as following

```
__global__ void calc_XXVV_mat_mat(float *XXVV_mat_re, float *XXVV_mat_im,
  double *aux_n2occ, float *aux_DFT_E_mat_occ, float *aux_DFT_E_mat_virt,
  double omega, double eps, int norbs, int nocc, int nvirt, int Fmin)
{
  int i = blockIdx.x * blockDim.x + threadIdx.x; //nocc
  int j = blockIdx.y * blockDim.y + threadIdx.y; //nvirt
```

```
  double odiff = 0.0, Re = 0.0, Im = 0.0;
  float EmF = 0.0, old_Re = 0.0, old_Im = 0.0;
  double d1 = 0.0, d2 = 0.0;

  if (j < nvirt)
  {
  if (MIN(j + norbs-nvirt, nocc) >= 0)
    {
    if (i<MIN(j + norbs-nvirt, nocc))
    {
      odiff = aux_n2occ[Fmin+j-1] - aux_n2occ[i];
      EmF = aux_DFT_E_mat_occ[i] - aux_DFT_E_mat_virt[j];
      d1 = (omega-EmF)*(omega-EmF) + eps*eps;
      d2 = (omega+EmF)*(omega+EmF) + eps*eps;
      Re = ((omega-EmF)*d2 - (omega+EmF)*d1)/(d1*d2);
      Im = eps*((d1-d2)/(d2*d1));
      old_Re = XXVV_mat_re[i*nvirt + j];
      old_Im = XXVV_mat_im[i*nvirt + j];
      XXVV_mat_re[i*nvirt + j] = old_Re*odiff*Re - old_Im*odiff*Im;
      XXVV_mat_im[i*nvirt + j] = old_Re*odiff*Im + old_Im*odiff*Re;
     }
   }
 }
}
```

This routine is launched with the following line

```
  calc_XXVV_mat_mat<<<dimGrid, dimBlock>>>(XXVV_mat_re_d, XXVV_mat_im_d, aux_n2occ_mat_d,
          aux_DFT_E_mat_occ_d, aux_DFT_E_mat_virt_d, omega,eps, norb, nocc, nvirt, Fmin);
```

After this part, there is two more matrix multiplications similar to the previous one (as the GPU one).

```
  call sgemm('N', 'N', norb, nocc, nvirt, 1E0, aux%X_aF, norb, XXVV_re, nvirt, 0E0, &
             XVV, norb);
  call sgemm('N', 'T', norb, norb, nocc, 1E0, XVV, norb, aux%X4, norb,0E0, VV, norb);
```

This step is the last one done on the GPU device. After these matrix multiplications are finished, we copy the data back to the host resulting matrix.

```
  call chi0_mv_noxv_get_last_VV(VV, norb)
```

Finally, the last step of the algorithm is similar to the first one and is performed on the host (CPU)

```
  do n = 1, aux%nloop
    si = aux%si(n, :); fi = aux%fi(n, :);
    do k = lbound(aux%Vertex_array(n)%array, 3), ubound(aux%Vertex_array(n)%array, 3)
      V(si(3) + k-1) = V(si(3) + k-1) + &
        sum(aux%Vertex_array(n)%array(:, :, k)*VV(si(1):fi(1), si(2):fi(2)))
    enddo
  enddo
```

As can be seen from this appendix, the programming to achieve the GPU parallelization is relatively straightforward with CUDA if large matrix-matrix operations must be parallelized. Table F.1 summarizes the runtime of the algorithm for CPU and GPU versions. The speed-up obtained for this system on this machine is appreciable (~ 12), taken into account that we used rather old CPUs[1] and one of the cheapest GPU[2] at the moment of writing. The speedup obtained with High-end GPU such as the Tesla P100 would be much larger. In this specific application, the usage of low-end GPUs can be seen as a way to improve the potential of old machine for relatively little money (~ 400\$ for two GPUs).

code part	CPU runtimes (h)	GPU runtimes (h)	speed-up
χ_0	55.25	4.61	11.99
Iterative part	61.57	11.54	5.33
Full program	72.29	22.286	3.24

Table F.1: Comparison of runtimes for the Ag_{618} cluster dimer between CPU and GPU parallelization of the χ_0 alogorithm.

[1] 16 Intel Xeon CPU E5620 at 2.40GHz with 12 MB of cache.
[2] GeForce GTX 1050 Ti

List of Publications

[1] M. Barbry, P. Koval, F. Marchesin, R. Esteban, A. G. Borisov, J. Aizpurua, and D. Sánchez-Portal. Atomistic Near-Field Nanoplasmonics: Reaching Atomic-Scale Resolution in Nanooptics. *Nano Letters*, 15(5):3410–3419, may 2015.

[2] F. Marchesin, P. Koval, M. Barbry, J. Aizpurua, and D. Sánchez-Portal. Optical response of metallic nanojunctions driven by single atom motion. *ACS Photonics*, 3(2):269–277, sep 2016.

[3] M. Urbieta, M. Barbry, Y. Zhang, P. Koval, D. Sánchez-Portal, N. Zabala, and J. Aizpurua. Atomic-scale lightning rod effect in plasmonic picocavities: A classical view to a quantum effect. *ACS Nano*, 12(1):585–595, 2018. PMID: 29298379.

[4] P. Koval, M. Barbry, and D. Sánchez-Portal. PySCF-NAO: an efficient and flexible implementation of linear response time-dependent density functional theory with numerical atomic orbitals. *Computer Physics Communication*, (accepted), 2018.

[5] M. Barbry, N. E. Koval, J. Aizpurua, D. Sánchez-Portal, and P. Koval. Size dispersion of the plasmon frequency in metal clusters: ab-initio atomistic description. (In preparation), 2018.

[6] M. Barbry, P. Koval, and D. Sánchez-Portal. An original atomistic ab-initio implementation of electron energy loss spectroscopy. (In preparation), 2018.

Bibliography

[1] D. Sánchez-Portal, P. ; Ordejón, E. Artacho, and J. M. Soler. Density-functional method for very large systems with lcao basis sets. *Int. J. Quantum Chem.*, 65:453–461, 1997.

[2] J. M. Soler, E. Artacho, J. D. Gale, A. García, J. Junquera, P Ordejón, and D. Sánchez-Portal. The siesta method for ab initio order-n materials simulation. *J. Phys.: Condens. Matter*, 14:2745–2779, 2002.

[3] D. Foerster. Elimination, in electronic structure calculations, of redundant orbital products. *The Journal of Chemical Physics*, 128(3):034108, 2008.

[4] Peter Koval, Dietrich Foerster, and Olivier Coulaud. A Parallel Iterative Method for Computing Molecular Absorption Spectra. *Journal of Chemical Theory and Computation*, 6(9):2654–2668, September 2010.

[5] D Foerster, P Koval, and D Sánchez-Portal. An O(N3) implementation of Hedin's GW approximation for molecules. *The Journal of chemical physics*, 135(7):074105, August 2011.

[6] Q. Sun, T. C. Berkelbach, N. S. Blunt, G. H. Booth, S. Guo, Z. Li, J. Liu, J. McClain, E. R. Sayfutyarova, S. Sharma, S. Wouters, and G. Kin-Lic Chan. The Python-based Simulations of Chemistry Framework (PySCF). *ArXiv e-prints*, January 2017.

[7] P. Koval, M. Barbry, and D. Sánchez-Portal. PySCF-NAO: an efficient and flexible implementation of linear response time-dependent density functional theory with numerical atomic orbitals. *Computer Physics Communication*, (accepted), 2018.

[8] R. P. Feynman. There's plenty of room at the bottom. *Journal of Microelectromechanical Systems*, 1(1):60–66, March 1992.

[9] S. J. Oldenburg, R. D. Averitt, S. L. Westcott, and N. J. Halas. Nanoengineering of optical resonances. *Chem. Phys. Lett.*, 288:243 – 247, 1998.

[10] Hongxing Xu, Erik J. Bjerneld, Mikael Käll, and Lars Börjesson. Spectroscopy of single hemoglobin molecules by surface enhanced Raman scattering. *Phys. Rev. Lett.*, 83:4357–4360, 1999.

[11] Isabel Romero, Javier Aizpurua, Garnett W. Bryant, and F. Javier García de Abajo. Plasmons in nearly touching metallic nanoparticles: singular response in the limit of touching dimers. *Opt. Express*, 14:9988–9999, 2006.

[12] Martin Moskovits. Surface-enhanced spectroscopy. *Rev. Mod. Phys.*, 57:783–826, 1985.

[13] Shuming Nie and Steven R. Emory. Probing single molecules and single nanoparticles by surface-enhanced raman scattering. *Science*, 275:1102–1106, 1997.

[14] Harry A Atwater and Albert Polman. Plasmonics for improved photovoltaic devices. *Nat. Mater.*, 9(3):205–213, 2010.

[15] Suljo Linic, Phillip Christopher, and David B Ingram. Plasmonic-metal nanostructures for efficient conversion of solar to chemical energy. *Nat. Mater.*, 10(12):911–921, 2011.

[16] Kevin F MacDonald, Zsolt L Sámson, Mark I. Stockman, and Nikolay I. Zheludev. Ultrafast active plasmonics. *Nat. Photonics*, 3:55–58, 2008.

[17] Nicolas Large, Martina Abb, Javier Aizpurua, and Otto L. Muskens. Photoconductively loaded plasmonic nanoantenna as building block for ultracompact optical switches. *Nano Lett.*, 10:1741–1746, 2010.

[18] Surbhi Lal, Susan E. Clare, and Naomi J. Halas. Nanoshell-enabled photothermal cancer therapy: Impending clinical impact. *Acc. Chem. Res.*, 41(12):1842–1851, 2008.

[19] Ask Hjorth Larsen et al. The atomic simulation environment-a python library for working with atoms. *Journal of Physics: Condensed Matter*, 29(27):273002, 2017.

[20] Claude Cohen-Tannoudji, Bernard Diu, Franck Lalö, and Bernd Crasemann. *Quantum Mechanics*. 1979.

[21] R. M. Dreizler and E K U Gross. *Density Functional Theory: An Approach to the Quantum Many-Body Problem*. 1990.

[22] W. Kohn. Nobel lecture: Electronic structure of matter—wave functions and density functionals. *Rev. Mod. Phys.*, 71:1253–1266, Oct 1999.

[23] A. Szabo and N.S. Ostlund. *Modern Quantum Chemistry: Introduction to Advanced Electronic Structure Theory*. Dover Books on Chemistry. Dover Publications, 1989.

[24] I.N. Levine. *Quantum chemistry*. Allyn and Bacon chemistry series. Allyn and Bacon, 1983.

[25] W. Tobocman. Many-body perturbation theory. *Phys. Rev.*, 107:203–208, Jul 1957.

[26] R J Bartlett. Many-body perturbation theory and coupled cluster theory for electron correlation in molecules. *Annual Review of Physical Chemistry*, 32(1):359–401, 1981.

[27] R. O. Jones and O. Gunnarsson. The density functional formalism, its applications and prospects. *Rev. Mod. Phys.*, 61:689–746, Jul 1989.

[28] Robert G. Parr and Weitao Yang. *Density-Functionnal Theory of Atoms and Molecules*. Oxford University Press, 1989.

[29] Julien Toulouse. *Introduction to density-functional theory*. 2017.

[30] N.H. March. *Theory of the Inhomogeneous Electron Gas*. Springer US, 1983.

[31] P. Hohenberg and W. Kohn. Inhomogeneous electron gas. *Phys. Rev.*, 136:B864–B871, Nov 1964.

[32] W. Kohn and L. J. Sham. Self-consistent equations including exchange and correlation effects. *Phys. Rev.*, 140:A1133–A1138, Nov 1965.

[33] W. Kohn and L. J. Sham. *Phys. Rev.*, 140:A1133–A1138, 1965.

[34] J. P. Perdew and A. Zunger. *Phys. Rev. B*, 23:5048–5079, 1981.

[35] John P. Perdew, Kieron Burke, and Matthias Ernzerhof. Generalized gradient approximation made simple. *Phys. Rev. Lett.*, 77:3865–3868, Oct 1996.

[36] Zhigang Wu and R. E. Cohen. More accurate generalized gradient approximation for solids. *Phys. Rev. B*, 73:235116, Jun 2006.

[37] O. Gunnarsson and B. I. Lundqvist. Exchange and correlation in atoms, molecules, and solids by the spin-density-functional formalism. *Phys. Rev. B*, 13:4274–4298, May 1976.

[38] Erich Runge and E. K. U. Gross. Density-functional theory for time-dependent systems. *Phys. Rev. Lett.*, 52:997–1000, Mar 1984.

[39] C. A. Ullrich, U. J. Gossmann, and E. K. U. Gross. Time-dependent optimized effective potential. *Phys. Rev. Lett.*, 74:872–875, Feb 1995.

[40] Carsten A. Ullrich, Kieron Burke, Miguel A.L. Marques, Carsten A. Ullrich, Fernando Nogueira, Angel Rubio, and Kieron Burke andEberhard K. U. Gross. *Time-Dependent Density Functional Theory*. 2006.

[41] K. Yabana and G. F. Bertsch. Time-dependent local-density approximation in real time. *Phys. Rev. B*, 54:4484–4487, Aug 1996.

[42] Argyrios Tsolakidis, Daniel Sánchez-Portal, and Richard Martin. Calculation of the optical response of atomic clusters using time-dependent density functional theory and local orbitals. *Physical Review B*, 66(23):235416, December 2002.

[43] M Petersilka, Uj Gossmann, and Ek Gross. Excitation energies from time-dependent density-functional theory. *Physical Review Letters*, 76(8):1212–1215, February 1996.

[44] Peter Koval, Federico Marchesin, Dietrich Foerster, and Daniel Sánchez-Portal. Optical response of silver clusters and their hollow shells from linear-response TDDFT. *Journal of Physics: Condensed Matter*, 28(21):214001, jun 2016.

[45] Alexander M. Kalsin, Marcin Fialkowski, Maciej Paszewski, Stoyan K. Smoukov, Kyle J. M. Bishop, and Bartosz A. Grzybowski. Electrostatic self-assembly of binary nanoparticle crystals with a diamond-like lattice. *Science*, 312(5772):420–424, 2006.

[46] Douglas A. Stuart, Jonathan M. Yuen, Nilam Shah, Olga Lyandres, Chanda R. Yonzon, Matthew R. Glucksberg, Joseph T. Walsh, and Richard P. Van Duyne. In vivo glucose measurement by surface-enhanced raman spectroscopy. *Analytical Chemistry*, 78(20):7211–7215, 2006. PMID: 17037923.

[47] Mark Fox. *Optical Properties of Solids*. Oxford University Press, 2010.

[48] Stephan Link and Mostafa A. El-Sayed. Spectral properties and relaxation dynamics of surface plasmon electronic oscillations in gold and silver nanodots and nanorods. *J. Phys. Chem. B*, 103(40):8410–8426, 1999.

[49] Rongchao Jin, YunWei Cao, Chad A. Mirkin, K. L. Kelly, George C. Schatz, and J. G. Zheng. Photoinduced conversion of silver nanospheres to nanoprisms. 294:1901–1903, 2001.

[50] P. Koval, D. Foerster, and D. Sánchez-Portal. Fully self-consistent *gw* and quasiparticle self-consistent *gw* for molecules. *Phys. Rev. B*, 89:155417, Apr 2014.

[51] M. P. Ljungberg, P. Koval, F. Ferrari, D. Foerster, and D. Sánchez-Portal. Cubic-scaling iterative solution of the bethe-salpeter equation for finite systems. *Phys. Rev. B*, 92:075422, Aug 2015.

[52] E. Artacho, D. Sánchez-Portal, P Ordejón, A García, and J. M. Soler. Linear-scaling ab-initio calculations for large and complex systems. *Phys. Status Solidi B*, 215:809–817, 1999.

[53] Javier Junquera, Óscar Paz, Daniel Sánchez-Portal, and Emilio Artacho. Numerical atomic orbitals for linear-scaling calculations. *Phys. Rev. B*, 64:235111, Nov 2001.

[54] Nelson H. F. Beebe and Jan Linderberg. Simplifications in the generation and transformation of two-electron integrals in molecular calculations. *International Journal of Quantum Chemistry*, 12(4):683–705, 1977.

[55] C.-K Skylaris, L Gagliardi, N.C Handy, A.G Ioannou, S Spencer, and A Willetts. On the resolution of identity coulomb energy approximation in density functional theory. *Journal of Molecular Structure: THEOCHEM*, 501:229 – 239, 2000.

[56] E.J. Baerends, D.E. Ellis, and P. Ros. Self-consistent molecular hartree-fock-slater calculations i. the computational procedure. *Chemical Physics*, 2(1):41 – 51, 1973.

[57] G. te Velde, F. M. Bickelhaupt, E. J. Baerends, C. Fonseca Guerra, S. J. A. van Gisbergen, J. G. Snijders, and T. Ziegler. Chemistry with adf. *Journal of Computational Chemistry*, 22(9):931–967, 2001.

[58] M. E. Casida. *Recent Advances in Density Functional Theory.* D. P. Chong (World Scientific, Singapore), 1995.

[59] S.J.A. van Gisbergen, J.G. Snijders, and E.J. Baerends. Implementation of time-dependent density functional response equations. *Computer Physics Communications*, 118(2):119–138, 1999.

[60] Victor P. Vysotskiy and Lorenz S. Cederbaum. On the cholesky decomposition for electron propagator methods: General aspects and application on c60. *The Journal of Chemical Physics*, 132(4):044110, 2010.

[61] Dietrich Foerster. On an "interaction by moments" property of four center integrals. pages 1–4, dec 2006.

[62] D. Foerster. Elimination, in electronic structure calculations, of redundant orbital products. *The Journal of Chemical Physics*, 128(3), 2008.

[63] Valérie Frayssé, Luc Giraud, Serge Gratton, and Julien Langou. Algorithm 842: A set of gmres routines for real and complex arithmetics on high performance computers. *ACM Trans. Math. Softw.*, 31(2):228–238, June 2005.

[64] Yousef Saad. *Iterative Methods for Sparse Linear Systems Second Edition.* Second edi edition, 2003.

[65] Ilse C. F. Ipsen and Carl D. Meyer. The idea behind krylov methods. *The American Mathematical Monthly*, 105(10):889–899, 1998.

[66] Eric Jones, Travis Oliphant, Pearu Peterson, et al. SciPy: Open source scientific tools for Python, 2001–.

[67] John Nickolls, I A N Buck, and Michael Garland. Scalable Parallel Programming with CUDA. *ACM QUEUE*, (April), 2008.

[68] Carole Van Caillie and Roger D. Amos. Geometric derivatives of density functional theory excitation energies using gradient-corrected functionals. *Chemical Physics Letters*, 317(1-2):159–164, 2000.

[69] Timothy J. Giese and Darrin M. York. Density-functional expansion methods: Evaluation of LDA, GGA, and meta-GGA functionals and different integral approximations. *Journal of Chemical Physics*, 133(24), 2010.

[70] V. U. Nazarov and G. Vignale. Optics of semiconductors from meta-generalized-gradient-approximation-based time-dependent density-functional theory. *Physical Review Letters*, 107(21), 2011.

[71] E. Betzig, P. L. Finn, and J. S. Weiner. Combined shear force and near-field scanning optical microscopy. *Applied Physics Letters*, 60(20):2484–2486, 1992.

[72] Achim Hartschuh. Tip-enhanced near-field optical microscopy. *Angewandte Chemie International Edition*, 47(43):8178–8191.

[73] F. J. García de Abajo. Optical excitations in electron microscopy. *Rev. Mod. Phys.*, 82:209–275, Feb 2010.

[74] S. Lazar, G.A. Botton, and H.W. Zandbergen. Enhancement of resolution in core-loss and low-loss spectroscopy in a monochromated microscope. *Ultramicroscopy*, 106(11):1091 – 1103, 2006. Proceedings of the International Workshop on Enhanced Data Generated by Electrons.

[75] T. L. Ferrell and P. M. Echenique. Generation of surface excitations on dielectric spheres by an external electron beam. *Phys. Rev. Lett.*, 55:1526–1529, Sep 1985.

[76] Python Software Foundation. ctypes - a foreign function library for python.

[77] J. J. Mortensen, L. B. Hansen, and K. W. Jacobsen. Real-space grid implementation of the projector augmented wave method. *Phys. Rev. B*, 71:035109, Jan 2005.

[78] Steven Boker, Michael Neale, Hermine Maes, Michael Wilde, Michael Spiegel, Timothy Brick, Jeffrey Spies, Ryne Estabrook, Sarah Kenny, Timothy Bates, Paras Mehta, and John Fox. Openmx: An open source extended structural equation modeling framework. *Psychometrika*, 76(2):306–317, Apr 2011.

[79] Jesús I. Mendieta-Moreno, Ross C. Walker, James P. Lewis, Paulino Gómez-Puertas, Jesús Mendieta, and José Ortega. fireball/amber: An efficient local-orbital dft qm/mm method for biomolecular systems. *Journal of Chemical Theory and Computation*, 10(5):2185–2193, 2014. PMID: 26580543.

[80] S. van der Walt, S. C. Colbert, and G. Varoquaux. The numpy array: A structure for efficient numerical computation. *Computing in Science Engineering*, 13(2):22–30, March 2011.

[81] Travis E. Oliphant. Python for scientific computing. *Computing in Science & Engineering*, 9(3):10–20, 2007.

[82] K. Jarrod Millman and Michael Aivazis. Python for scientists and engineers. *Computing in Science & Engineering*, 13(2):9–12, 2011.

[83] M. Barbry, P. Koval, F. Marchesin, R. Esteban, A. G. Borisov, J. Aizpurua, and D. Sánchez-Portal. Atomistic Near-Field Nanoplasmonics: Reaching Atomic-Scale Resolution in Nanooptics. *Nano Letters*, 15(5):3410–3419, may 2015.

[84] R. Averitt, D. Sarkar, and N. Halas. Plasmon resonance shifts of au-coated au$_2s$ nanoshells: Insight into multicomponent nanoparticle growth. *Phys. Rev. Lett.*, 78:4217–4220, Jun 1997.

[85] J. Aizpurua, P Hanarp, D. Sutherland, M. Kall, G. W. Bryant, and F. J. García de Abajo. Optical properties of gold nanorings. *Phys. Rev. Lett.*, 90:057401, 2003.

[86] J. Aizpurua, Garnett W. Bryant, Lee J. Richter, F. J. García de Abajo, Brian K. Kelley, and T. Mallouk. Optical properties of coupled metallic nanorods for field-enhanced spectroscopy. *Phys. Rev. B*, 71:235420, 2005.

[87] Lukas Novotny. Effective wavelength scaling for optical antennas. *Phys. Rev. Lett.*, 98:266802, 2007.

[88] Jens Dorfmüller, Ralf Vogelgesang, R. Thomas Weitz, Carsten Rockstuhl, Christoph Etrich, Thomas Pertsch, Falk Lederer, and Klaus Kern. Fabry-Pérot resonances in one-dimensional plasmonic nanostructures. *Nano Lett.*, 9:2372–2377, 2009.

[89] Alison M. Funston, Carolina Novo, Tim J. Davis, and Paul Mulvaney. Plasmon coupling of gold nanorods at short distances and in different geometries. *Nano Lett.*, 9:1651–1658, 2009.

[90] Feng Hao, Colleen L. Nehl, Jason H. Hafner, and Peter Nordlander. Plasmon resonances of a gold nanostar. *Nano Lett.*, 7(3):729–732, 2007.

[91] Sergey M. Novikov, Ana Sánchez-Iglesias, Mikolaj K. Schmidt, Andrey Chuvilin, Javier Aizpurua, Marek Grzelczak, and Luis M. Liz-Marzán. Gold spiky nanodumbbells: Anisotropy in gold nanostars. *Part. Part. Syst. Charact.*, 31(1):77–80, 2014.

[92] K.-H. Su, Q.-H. Wei, X. Zhang, J. J. Mock, D. R. Smith, and S. Schultz. Interparticle coupling effects on plasmon resonances of nanogold particles. *Nano Lett.*, 3:1087–1090, 2003.

[93] W. Rechberger, A. Hohenau, A. Leitner, J. R. Krenn, B. Lamprecht, and F. R. Aussenegg. Optical properties of two interacting gold nanoparticles. *Opt. Commun.*, 220:137 – 141, 2003.

[94] Jonathan A. Fan, Chihhui Wu, Kui Bao, Jiming Bao, Rizia Bardhan, Naomi J. Halas, Vinothan N. Manoharan, Peter Nordlander, Gennady Shvets, and Federico Capasso. Self-assembled plasmonic nanoparticle clusters. *Science*, 328(5982):1135–1138, 2010.

[95] Mario Hentschel, Michael Saliba, Ralf Vogelgesang, Harald Giessen, A. Paul Alivisatos, and Na Liu. Transition from isolated to collective modes in plasmonic oligomers. *Nano Lett.*, 10(7):2721–2726, 2010.

[96] K. Lance Kelly, Eduardo Coronado, Lin Lin Zhao, and George C. Schatz. The optical properties of metal nanoparticles: The influence of size, shape, and dielectric environment. *J. Phys. Chem. B*, 107:668–677, 2003.

[97] M. Pelton, J. Aizpurua, and G. Bryant. Metal-nanoparticle plasmonics. *Laser Photonics Rev.*, 2:136–159, 2008.

[98] M. Schnell, A. García-Etxarri, A. J. Huber, K. Crozier, J. Aizpurua, and R. Hillenbrand. Controlling the near-field oscillations of loaded plasmonic nanoantennas. *Nat. Photonics*, 3:287–291, 2009.

[99] Naomi J. Halas, Surbhi Lal, Wei-Shun Chang, Stephan Link, and Peter Nordlander. Plasmons in strongly coupled metallic nanostructures. *Chem. Rev.*, 111:3913–3961, 2011.

[100] P. Mühlschlegel, H.-J. Eisler, O. J. F. Martin, B. Hecht, and D. W. Pohl. Resonant Optical Antennas. *Science*, 308:1607–1609, 2005.

[101] Lukas Novotny and Niek van Hulst. Antennas for light. *Nat. Photonics*, 5:83–90, 2011.

[102] Johannes Kern, Swen Großmann, Nadezda V. Tarakina, Tim Häckel, Monika Emmerling, Martin Kamp, Jer-Shing Huang, Paolo Biagioni, Jord C. Prangsma, and Bert Hecht. Atomic-scale confinement of resonant optical fields. *Nano Lett.*, 12:5504–5509, 2012.

[103] Daniel R. Ward, Falco Hüser, Fabian Pauly, Juan Carlos Cuevas, and Douglas Natelson. Optical rectification and field enhancement in a plasmonic nanogap. *Nat. Nanotechnol.*, 5:732–736, 2010.

[104] Mengtao Sun and Hongxing Xu. A novel application of plasmonics: Plasmon-driven surface-catalyzed reactions. *Small*, 8(18):2777–2786, 2012.

[105] Phillip Christopher, Hongliang Xin, Andiappan Marimuthu, and Suljo Linic. Singular characteristics and unique chemical bond activation mechanisms of photocatalytic reactions on plasmonic nanostructures. *Nat. Mater.*, 11(12):1044–1050, 2012.

[106] Shaunak Mukherjee, Florian Libisch, Nicolas Large, Oara Neumann, Lisa V. Brown, Jin Cheng, J. Britt Lassiter, Emily A. Carter, Peter Nordlander, and Naomi J. Halas. Hot electrons do the impossible: Plasmon-induced dissociation of h2 on au. *Nano Lett.*, 13(1):240–247, 2013.

[107] Guillaume Baffou and Romain Quidant. Nanoplasmonics for chemistry. *Chem. Soc. Rev.*, 43:3898–3907, 2014.

[108] Katrin Kneipp, Yang Wang, Harald Kneipp, Lev Perelman, Irving Itzkan, Ramachandra Dasari, and Michael Feld. Single molecule detection using surface-enhanced raman scattering (sers). *Phys. Rev. Lett.*, 78:1667–1670, Mar 1997.

[109] Ekmel Ozbay. Plasmonics: Merging photonics and electronics at nanoscale dimensions. *Science*, 311(5758):189–193, 2006.

[110] Jer-Shing Huang, Thorsten Feichtner, Paolo Biagioni, and Bert Hecht. Impedance matching and emission properties of nanoantennas in an optical nanocircuit. *Nano Lett.*, 9(5):1897–1902, 2009.

[111] R. G. Parr and Y. Weitao. *Density-functional theory of atoms and molecules*. Oxford University Press, Oxford, 1989.

[112] Peter J. Feibelman. Microscopic calculation of electromagnetic fields in refraction at a jellium-vacuum interface. *Phys. Rev. B*, 12:1319–1336, 1975.

[113] A. Liebsch and W. L. Schaich. Influence of a polarizable medium on the nonlocal optical response of a metal surface. *Phys. Rev. B*, 52:14219–14234, 1995.

[114] T. V. Teperik, P. Nordlander, J. Aizpurua, and A. G. Borisov. Robust subnanometric plasmon ruler by rescaling of the nonlocal optical response. *Phys. Rev. Lett.*, 110:263901, 2013.

[115] R Carmina Monreal, Tomasz J Antosiewicz, and S Peter Apell. Competition between surface screening and size quantization for surface plasmons in nanoparticles. *New Journal of Physics*, 15(8):83044, 2013.

[116] Christian F. A. Negre, Eduardo M. Perassi, Eduardo A. Coronado, and Christián G. Sánchez. Quantum dynamical simulations of local field enhancement in metal nanoparticles. *J. Phys.: Condens. Matter*, 25:125304, 2013.

[117] K. Iida, M. Noda, K. Ishimura, and K. Nobusada. First-principles computational visualization of localized surface plasmon resonance in gold nanoclusters. *J. Phys. Chem. A*, 118:11317–11322, 2014.

[118] Jorge Zuloaga, Emil Prodan, and Peter Nordlander. Quantum description of the plasmon resonances of a nanoparticle dimer. *Nano Lett.*, 9:887–891, 2009.

[119] D. C. Marinica, A. K. Kazansky, P. Nordlander, J. Aizpurua, and A. G. Borisov. Quantum plasmonics: Nonlinear effects in the field enhancement of a plasmonic nanoparticle dimer. *Nano Lett.*, 12:1333–1339, 2012.

[120] Pu Zhang, Johannes Feist, Angel Rubio, Pablo García-González, and F. J. García-Vidal. Ab initio nanoplasmonics: The impact of atomic structure. *Phys. Rev. B*, 90:161407, Oct 2014.

[121] The initial structure of the Na_{380} cluster was download from the Cambridge Cluster Database, D. J. Wales, J. P. K. Doye, A. Dullweber, M. P. Hodges, F. Y. Naumkin, F. Calvo, J. Hernández-Rojas and T. F. Middleton, URL http://www-wales.ch.cam.ac.uk/CCD.html.

[122] N. Troullier and José Luís Martins. Efficient pseudopotentials for plane-wave calculations. *Phys. Rev. B*, 43:1993–2006, Jan 1991.

[123] Joel Gersten and Abraham Nitzan. Electromagnetic theory of enhanced raman scattering by molecules adsorbed on rough surfaces. *J. Chem. Phys.*, 73(7):3023–3037, 1980.

[124] Lukas Novotny, Randy Bian, and X. Xie. Theory of nanometric optical tweezers. *Phys. Rev. Lett.*, 79:645–648, Jul 1997.

[125] Fei Le, Daniel W. Brandl, Yaroslav A. Urzhumov, Hui Wang, Janardan Kundu, Naomi J. Halas, Javier Aizpurua, and Peter Nordlander. Metallic nanoparticle arrays: A common substrate for both surface-enhanced Raman scattering and surface-enhanced infrared absorption. *ACS Nano*, 2:707–718, 2008.

[126] R. Zhang, Y. Zhang, Z. C. Dong, S. Jiang, C. Zhang, L. G. Chen, L. Zhang, Y. Liao, J. Aizpurua, Yi Luo, J. L. Yang, and J. G. Hou. Chemical mapping of a single molecule by plasmon-enhanced raman scattering. *Nature*, 498(7452):82–86, 2013.

[127] J. L. Payton, S. M. Morton, Moore J. E., and L. Jensen. A discrete interaction model/quantum mechanical method for simulating surface-enhanced raman spectroscopy. *J. Chem. Phys.*, 136:214103, 2012.

[128] Taka-aki Yano, Taro Ichimura, Shota Kuwahara, Fekhra HDhili, Kazumasa Uetsuki, Yoshito Okuno, Prabhat Verma, and Satoshi Kawata. Tip-enhanced nano-raman analytical imaging of locally induced strain distribution in carbon nanotubes. *Nat. Commun.*, 4:2592, 2013.

[129] Tanja Deckert-Gaudig and Volker Deckert. Ultraflat transparent gold nanoplates–ideal substrates for tip-enhanced Raman scattering experiments. *Small*, 5:432–436, 2009.

[130] J. L. Payton, S. M. Morton, Moore J. E., and L. Jensen. A hybrid atomistic electrodynamics-quantum mechanical approach for simulating surface-enhanced raman scattering. *Acc. Chem. Res.*, 47:88–99, 2014.

[131] Felix Benz, Mikolaj K. Schmidt, Alexander Dreismann, Rohit Chikkaraddy, Yao Zhang, Angela Demetriadou, Cloudy Carnegie, Hamid Ohadi, Bart de Nijs, Ruben Esteban, Javier Aizpurua, and Jeremy J. Baumberg. Single-molecule optomechanics in "picocavities". *Science*, 354(6313):726–729, 2016.

[132] G Mie. Contributions to the optics of turbid media, particularly of colloidal metal solutions. *Ann. Phys.(Leipzig)*, 25:377–445, 1908.

[133] J. Friedel. Xiv. the distribution of electrons round impurities in monovalent metals. *Philos. Mag.*, 43(337):153–189, 1952.

[134] Olivier J. F. Martin and Christian Girard. Controlling and tuning strong optical field gradients at a local probe microscope tip apex. *App. Phys. Lett.*, 70(6):705–707, 1997.

[135] K. Li, M. I. Stockman, and D. J. Bergman. Self-similar chain of metal nanospheres as an efficient nanolens. *Phys. Rev. Lett.*, 91:227402, 2003.

[136] V. G. VKravets, G. Zoriniants, C. P. Burrows, F. Schedin, C. Casiraghi, P. Klar, A. K. Geim, W. L. Barnes, and A. N. Grigorenko. Cascaded optical field enhancement in composite plasmonic nanostructures. *Phys. Rev. Lett.*, 105:246806, 2010.

[137] Christiane Höpener, Zachary J. Lapin, Palash Bharadwaj, and Lukas Novotny. Self-similar gold-nanoparticle antennas for a cascaded enhancement of the optical field. *Phys. Rev. Lett.*, 109:017402, 2012.

[138] P. Nordlander, C. Oubre, E. Prodan, K. Li, and M. I. Stockman. Plasmon hybridization in nanoparticle dimers. *Nano Lett.*, 4:899–903, 2004.

[139] Ruben Esteban, Andrei G. Borisov, Peter Nordlander, and Javier Aizpurua. Bridging quantum and classical plasmonics with a quantum-corrected model. *Nat. Commun.*, 3:825, 2012.

[140] O. Pérez-González, N. Zabala, A. G. Borisov, N. J. Halas, P. Nordlander, and J. Aizpurua. Optical spectroscopy of conductive junctions in plasmonic cavities. *Nano Lett.*, 10:3090–3095, 2010.

[141] T. Deckert-Gaudig and V. Deckert. Ultraflat transparent gold nanoplates–ideal substrates for tip-enhanced raman scattering experiments. *Small*, 16:432–436, 2009.

[142] F. J. García de Abajo. Optical excitation in electron microscopy. *Rev. Mod. Phys.*, 82:209–275, 2010.

[143] Kevin J. Savage, Matthew M. Hawkeye, Ruben Esteban, Andrei G. Borisov, Javier Aizpurua, and Jeremy J. Baumberg. Revealing the quantum regime in tunnelling plasmonics. *Nature*, 491:574–577, 2012.

[144] R. Esteban, A. Zugarramurdi, P. Zhang, P. Nordlander, F. J. García-Vidal, A. G. Borisov, and J. Aizpurua. A classical treatment of optical tunneling in plasmonic gaps: extending the quantum corrected model to practical situations. *Faraday Discuss.*, 178:151–183, 2015.

[145] Kenji Iida, Masashi Noda, Kazuya Ishimura, and Katsuyuki Nobusada. First-principles computational visualization of localized surface plasmon resonance in gold nanoclusters. *J. Phys. Chem. A*, 118(47):11317–11322, 2014. PMID: 25367153.

[146] Mattin Urbieta, Marc Barbry, Yao Zhang, Peter Koval, Daniel Sánchez-Portal, Nerea Zabala, and Javier Aizpurua. Atomic-scale lightning rod effect in plasmonic picocavities: A classical view to a quantum effect. *ACS Nano*, 12(1):585–595, 2018. PMID: 29298379.

[147] F. J. García de Abajo and A. Howie. Retarded field calculation of electron energy loss in inhomogeneous dielectrics. *Phys. Rev. B*, 65:115418, Mar 2002.

[148] U. Kreibig and C.v. Fragstein. The limitation of electron mean free path in small silver particles. *Z. Phys.*, 224(4):307–323, 1969.

[149] A. Moroz. Electron mean free path in a spherical shell geometry. *J. Phys. Chem. C*, 112(29):10641–10652, 2008.

[150] N. Chernov. Lyapunov instability of the boundary-driven chernov-lebowitz model for stationary shear flow. *J. Stat. Phys.*, 88:825–842, 1997.

[151] U. Hohenester. Simulating electron energy loss spectroscopy with the mnpbem toolbox. *Comput. Phys.*, 185(3):1177 – 1187, 2014.

[152] B. Ding, Z. Deng, H. Yan, S. Cabrini, R. N. Zuckermann, and J. Bokor. Gold nanoparticle self-similar chain structure organized by dna origami. *J. Am. Chem. Soc.*, 132:3248–3249, 2010.

[153] M. Danckwerts and L. Novotny. Optical frequency mixing at coupled gold nanoparticles. *Phys. Rev. Lett.*, 98:026104, 2007.

[154] Yu Luo, A. I. Fernandez-Dominguez, Aeneas Wiener, Stefan A. Maier, and J. B. Pendry. Surface plasmons and nonlocality: A simple model. *Phys. Rev. Lett.*, 111:093901, 2013.

[155] A. Varas, P. García-González, F. J. García-Vidal, and A. Rubio. Anisotropy effects on the plasmonic response of nanoparticle dimers. *J. Phys. Chem. Lett.*, 6:1891–1898, 2015.

[156] Fangfang Wen, Yue Zhang, Samuel Gottheim, Nicholas S. King, Yu Zhang, Peter Nordlander, and Naomi J. Halas. Charge transfer plasmons: Optical frequency conductances and tunable infrared resonances. *ACS Nano*, 9:6428–6435, 2015.

[157] T. P Rossi, A. Zugarramurdi, M. Puska, and R. M. Nieminen. Quantized evolution of the plasmonic response in a stretched nanorod. 2015.

[158] N. Agraït, A. Levy-Yeyati, and J. M. van Ruitenbeek. Quantum properties of atomic-sized conductors. *Phys. Reps.*, 377:81–380, 2003.

[159] U. Landman, W. D. Luedtke, N. A. Burnham, and R. J. Colton. Atomistic mechanisms and dynamics of adhesion, nanoindentation and fracture. *Science*, 248:454–461, 1990.

[160] Y. Kondo and K. Takayanagi. Synthesis and characterization of helical multi-shell gold nanowires. *Science*, 289:606–608, 2000.

[161] V. Rodrigues, T. Fuhrer, and D. Ugarte. Signature of atomic structure in the quantum conductance of gold nanowires. *Phys. Rev. Lett.*, 85:4124–4127, 2000.

[162] D. Stöffler, S. Fostner, P. Grütter, and R. Hoffmann-Vogel. Scanning probe microscopy imaging of metallic nanocontacts. *Phys. Rev. B*, 85:033404, Jan 2012.

[163] B. Bhushan, J. N. Israelachvili, and U. Landman. Nanotribology: Friction, wear and lubrication at the atomic scale. *Nature*, 374:607–616, 1995.

[164] U. Landman, W. D. Luedtke, and J. Gao. Atomic-scale issues in tribology: Interfacial junctions and nano-elastohydrodynamics. *Langmuir*, 12:4514–4528, 1996.

[165] J. I. Pascual, J. Méndez, J. Gómez-Herrero, A. M. Baró, N. García, and V. T. Binh. *Phys. Rev. Lett.*, 71:1852–1855, 1993.

[166] L. Olesen, E. Laegsgaard, I. Stensgaard, F. Besenbacher, J. Schiøtz, P. Stoltze, K. W. Jacobsen, and J. K. Nørskov. Quantized conductance in an atom-sized point contact. *Phys. Rev. Lett.*, 72:2251–2254, Apr 1994.

[167] J. A. Torres and J. J. Sáenz. Conductance and mechanical properties of atomic-size metallic contacts: a simple model. *Phys. Rev. Lett.*, 77:2245–2248, 1996.

[168] D. R. Ward, N. K. Grady, C. S. Levin, N. J. Halas, Y. Wu, P. Nordlander, and D. Natelson. Electromigrated nanoscale gaps for surface-enhanced raman spectroscopy. *Nano Lett.*, 7:1396–1400, 2007.

[169] A Emboras, , J. Niegemann, P. Ma, Ch. Haffner, M. Luisier, Ch. Hafner, T. Schimmel, and J. Leuthold. Single atom plasmonic switch. 2015.

[170] P. Koval, D Foerster, and O. Coulaud. *J. Chem. Theory Comput.*, 6:2654–2668, 2010.

[171] P Koval, D Foerster, and O. Coulaud. *Phys. Status Solidi B*, 247:1841–1848, 2010.

[172] D. Foerster and P Koval. *J. Chem. Phys.*, 131:044103, 2009.

[173] J. N Murrell and R. E. Mottram. *Mol. Phys.*, 69:571–585, 1990.

[174] J. B. Pethica and A. P. Suttom. On the stability of a tip and flat at very small separations. *J. Vac. Sci. Technol.*, A6:2494, 1988.

[175] M. R. Sørensen, M. Brandbyge, and K. W. Jacobsen. Mechanical deformation of atomic-scale metallic contacts: structure and mechanisms. *Phys. Rev. B*, 57:3283–3294, 1998.

[176] Pavel Jelínek, Rubén Pérez, José Ortega, and Fernando Flores. First-principles simulations of the stretching and final breaking of al nanowires: Mechanical properties and electrical conductance. *Phys. Rev. B*, 68:085403, Aug 2003.

[177] Daniel Sánchez-Portal, Carlos Untiedt, José M. Soler, Juan J. Sáenz, and Nicolás Agraït. Nanocontacts: Probing electronic structure under extreme uniaxial strains. *Phys. Rev. Lett.*, 79:4198–4201, 1997.

[178] E. Prodan, P. Nordlander, and N. J. Halas. Electronic structure and optical properties of gold nanoshells. *Nano Lett.*, 3:1411–1415, 2003.

[179] Werner A. Hofer, Adam S. Foster, and Alexander L. Shluger. Theories of scanning probe microscopes at the atomic scale. *Rev. Mod. Phys.*, 75:1287–1331, Oct 2003.

[180] H. Ohnishi, Y. Kondo, and K. Takayanagi. Quantized conductance through individual rows of suspended gold atoms. *Nature*, 395:780–783, 1998.

[181] A. I. Yanson, G. Rubio Bollinger, H. E. van den Brom, N. Agraït, and J. M. van Ruitenbeek. Formation and manipulation of a metallic wire of single gold atoms. *Nature*, 395:783, 1998.

[182] Daniel Sánchez-Portal, Emilio Artacho, Javier Junquera, Pablo Ordejón, Alberto García, and José M. Soler. Stiff monatomic gold wires with a spinning zigzag geometry. *Phys. Rev. Lett.*, 83:3884–3887, 1999.

[183] G. Rubio-Bollinger, S. R. Bahn, N. Agraït, K. W. Jacobsen, and S. Vieira. Mechanical properties and formation mechanisms of a wire of single gold atoms. *Phys. Rev. Lett.*, 87:026101, 2001.

[184] S. Datta. *Electronic Transport in Mesoscopic Systems*. Cambridge University Press, 1995.

[185] Ahmed Abdelhalim, Maximilian Winkler, Florin Loghin, Christopher Zeiser, Paolo Lugli, and Alaa Abdellah. Highly sensitive and selective carbon nanotube-based gas sensor arrays functionalized with different metallic nanoparticles. *Sensors and Actuators, B: Chemical*, 220:1288–1296, 2015.

[186] Zheng Zeng, Yiyang Liu, and Jianjun Wei. Recent advances in surface-enhanced raman spectroscopy (SERS): Finite-difference time-domain (FDTD) method for SERS and sensing applications, 2016.

[187] Yong Siou Chen, Hyunbong Choi, and Prashant V. Kamat. Metal-cluster-sensitized solar cells. A new class of thiolated gold sensitizers delivering efficiency greater than 2%. *Journal of the American Chemical Society*, 135(24):8822–8825, 2013.

[188] Alexander S Urban, Sol Carretero-Palacios, Andrey a Lutich, Theobald Lohmüller, Jochen Feldmann, and Frank Jäckel. Optical trapping and manipulation of plasmonic nanoparticles: fundamentals, applications, and perspectives. *Nanoscale*, 6(9):4458–74, may 2014.

[189] K. P. Charlé, W. Schulze, and B. Winter. The size dependent shift of the surface plasmon absorption band of small spherical metal particles. *Zeitschrift für Physik D Atoms, Molecules and Clusters*, 12(1):471–475, 1989.

[190] K.-P. Charlé, L. König, S. Nepijko, I. Rabin, and W. Schulze. The surface plasmon resonance of free and embedded ag-clusters in the size range 1,5 nm $<$ d $<$ 30 nm. *Crystal Research and Technology*, 33(7-8):1085–1096, 1998.

[191] V. Kasperovich and V. V. Kresin. Ultraviolet photoabsorption spectra of silver and gold nanoclusters. *Philosophical Magazine Part B*, 78(4):385–396, 1998.

[192] P. Apell and Å. Ljungbert. Red shift of surface plasmons in small metal particles. *Solid State Communications*, 44(9):1367–1369, dec 1982.

[193] U. Kreibig and M. Vollmer. *Optical properties of metal clusters*. Number v. 25 in Springer series in materials science. Springer, 1995.

[194] M A Garcia. Surface plasmons in metallic nanoparticles: fundamentals and applications. *Journal of Physics D: Applied Physics*, 44(28):283001, 2011.

[195] M. Schmidt and H. Haberland. Optical spectra and their moments for sodium clusters, na_n^+, with $3 \leq n \leq 64$. *The European Physical Journal D - Atomic, Molecular, Optical and Plasma Physics*, 6(1):109–118, 1999.

[196] Kathy Selby, Michael Vollmer, Jun Masui, Vitaly Kresin, Walt A. de Heer, and W. D. Knight. Surface plasma resonances in free metal clusters. *Phys. Rev. B*, 40:5417–5427, Sep 1989.

[197] Thomas Reiners, Christoph Ellert, Martin Schmidt, and Hellmut Haberland. Size dependence of the optical response of spherical sodium clusters. *Phys. Rev. Lett.*, 74:1558–1561, Feb 1995.

[198] O Yeshchenko, I Dmitruk, a Dmytruk, and a Alexeenko. Influence of annealing conditions on size and optical properties of copper nanoparticles embedded in silica matrix. *Materials Science and Engineering: B*, 137(1-3):247–254, 2007.

[199] Manfred M Kappes, Martin Schär, Peter Radi, and Ernst Schumacher. On the manifestation of electronic structure effects in metal clusters. *The Journal of Chemical Physics*, 84(3):1863–1875, 1986.

[200] C. Bréchignac, Ph. Cahuzac, N. Kebaïli, J. Leygnier, and A. Sarfati. Collective resonance in large free potassium cluster ions. *Phys. Rev. Lett.*, 68:3916–3919, Jun 1992.

[201] Matthias Brack. The physics of simple metal clusters: self-consistent jellium model and semiclassical approaches. *Reviews of Modern Physics*, 65(3):677–732, jul 1993.

[202] Sheng Peng, Jeffrey M. McMahon, George C. Schatz, Stephen K. Gray, and Yugang Sun. Reversing the size-dependence of surface plasmon resonances. *Proceedings of the National Academy of Sciences*, 107(33):14530–14534, 2010.

[203] T P Martin. Shells of atoms. *Physics Reports*, 273(4):199–241, 1996.

[204] E. G. Noya, J. P.K. Doye, D. J. Wales, and A. Aguado. Geometric magic numbers of sodium clusters: Interpretation of the melting behaviour. *The European Physical Journal D*, 43(1):57–60, Jul 2007.

[205] Sandra García-Gil, Alberto García, Nicolás Lorente, and Pablo Ordejón. Optimal strictly localized basis sets for noble metal surfaces. *Phys. Rev. B*, 79:075441, Feb 2009.

[206] W Ekardt. Size-dependent photoabsorption and photoemission of small metal particles. *Physical Review B*, 31(10):6360–6370, may 1985.

[207] Ansgar. Liebsch. Surface-plasmon dispersion and size dependence of Mie resonance: Silver versus simple metals. *Physical Review B*, 48(15):11317–11328, oct 1993.

[208] K Yabana and G. F. Bertsch. Optical response of small silver clusters. *Physical Review A*, 60(5):3809–3814, 1999.

[209] Hannu Häkkinen. Atomic and electronic structure of gold clusters: understanding flakes, cages and superatoms from simple concepts. *Chemical Society Reviews*, 37(9):1847, 2008.

[210] Christine M. Aikens, Shuzhou Li, and George C. Schatz. From discrete electronic states to plasmons: TDDFT optical absorption properties of Agn (n = 10, 20, 35, 56, 84, 120) tetrahedral clusters. *Journal of Physical Chemistry C*, 112(30):11272–11279, 2008.

[211] Mikael Kuisma, Arto Sakko, Tuomas P. Rossi, Ask H. Larsen, Jussi Enkovaara, Lauri Lehtovaara, and Tapio T. Rantala. Localized surface plasmon resonance in silver nanoparticles: Atomistic first-principles time-dependent density-functional theory calculations. *Physical Review B*, 91(11):115431, mar 2015.

[212] Kenji Iida, Masashi Noda, Kazuya Ishimura, and Katsuyuki Nobusada. First-principles computational visualization of localized surface plasmon resonance in gold nanoclusters. *Journal of Physical Chemistry A*, 118(47):11317–11322, 2014.

[213] A. G. Borisov. Solution of the radial Schrödinger equation in cylindrical and spherical coordinates by mapped Fourier transform algorithms. *Journal of Chemical Physics*, 114(18):7770–7777, 2001.

[214] Ernst Ruska. The development of the electron microscope and of electron microscopy. *Rev. Mod. Phys.*, 59:627–638, Jul 1987.

[215] P. D. Nellist, M. F. Chisholm, N. Dellby, O. L. Krivanek, M. F. Murfitt, Z. S. Szilagyi, A. R. Lupini, A. Borisevich, W. H. Sides, and S. J. Pennycook. Direct sub-angstrom imaging of a crystal lattice. *Science*, 305(5691):1741–1741, 2004.

[216] N. D. Browning, M. F. Chisholm, and S. J. Pennycook. Atomic-resolution chemical analysis using a scanning transmission electron microscope. *Nature*, 366:143, 1993.

[217] R.F. Egerton. *Electron Energy-Loss Spectroscopy in the Electron Microscope*. SpringerLink : Bücher. Springer US, 2011.

[218] C.C. Ahn. *Transmission Electron Energy Loss Spectrometry in Materials Science and the EELS Atlas*. Wiley, 2006.

[219] O. Stéphan, D. Taverna, M. Kociak, K. Suenaga, L. Henrard, and C. Colliex. Dielectric response of isolated carbon nanotubes investigated by spatially resolved electron energy-loss spectroscopy: From multiwalled to single-walled nanotubes. *Phys. Rev. B*, 66:155422, Oct 2002.

[220] A.G. Marinopoulos, L. Wirtz, A. Marini, V. Olevano, A. Rubio, and L. Reining. Optical absorption and electron energy loss spectra of carbon and boron nitride nanotubes: a first-principles approach. *Applied Physics A*, 78(8):1157–1167, May 2004.

[221] R. Arenal, O. Stéphan, M. Kociak, D. Taverna, A. Loiseau, and C. Colliex. Electron energy loss spectroscopy measurement of the optical gaps on individual boron nitride single-walled and multiwalled nanotubes. *Phys. Rev. Lett.*, 95:127601, Sep 2005.

[222] A. Nojeh, B. Shan, K. Cho, and R. F. W. Pease. Ab initio. *Phys. Rev. Lett.*, 96:056802, Feb 2006.

[223] Jacques Dubochet. A reminiscence about early times of vitreous water in electron cryomicroscopy. *Biophys J*, 110(4):756–757, 2016.

[224] J. Ph. Perez, J. Sevely, and B. Jouffrey. Straggling of fast electrons in aluminum foils observed in high-voltage electron microscopy (0.3-1.2 mv). *Phys. Rev. A*, 16:1061–1069, Sep 1977.

[225] R. D. Leapman, C. E. Fiori, and C. R. Swyt. Mass thickness determination by electron energy loss for quantitative x-ray microanalysis in biology. *Journal of Microscopy*, 133(3):239–253, 1984.

[226] T. Malis, S. C. Cheng, and R. F. Egerton. Eels log-ratio technique for specimen-thickness measurement in the tem. *Journal of Electron Microscopy Technique*, 8(2):193–200, 1988.

[227] Shima Kadkhodazadeh, Jakob Rosenkrantz de Lasson, Marco Beleggia, Harald Kneipp, Jakob Birkedal Wagner, and Katrin Kneipp. Scaling of the surface plasmon resonance in gold and silver dimers probed by eels. *The Journal of Physical Chemistry C*, 118(10):5478–5485, 2014.

[228] A. Politano, V. Formoso, and G. Chiarello. Dispersion and damping of gold surface plasmon. *Plasmonics*, 3(4):165, Oct 2008.

[229] Jonathan A. Scholl, Aitzol García-Etxarri, Ai Leen Koh, and Jennifer A. Dionne. Observation of quantum tunneling between two plasmonic nanoparticles. *Nano Letters*, 13(2):564–569, 2013. PMID: 23245286.

[230] Eric C. Le Ru and Pablo G. Etchegoin. Single-molecule surface-enhanced raman spectroscopy. *Annual Review of Physical Chemistry*, 63(1):65–87, 2012. PMID: 22224704.

[231] Katrin Kneipp, Yang Wang, Ramachandra R. Dasari, and Michael S. Feld. Approach to single molecule detection using surface-enhanced resonance raman scattering (serrs): A study using rhodamine 6g on colloidal silver. *Appl. Spectrosc.*, 49(6):780–784, Jun 1995.

[232] Raza Soren, Stenger Nicolas, Kadkhodazadeh Shima, Fischer Soren V., Kostesha Natalie, Jauho Antti-Pekka, Burrows Andrew, Wubs Martijn, and Mortensen N. Asger. Blueshift of the surface plasmon resonance in silver nanoparticles studied with eels. *Nanophotonics*, 2:131–138, 2013.

[233] Jonathan A. Scholl, Ai Leen Koh, and Jennifer A. Dionne. Quantum plasmon resonances of individual metallic nanoparticles. *Nature*, 483(7390):421, March 2012.

[234] Ai Leen Koh, Kui Bao, Imran Khan, W. Ewen Smith, Gerald Kothleitner, Peter Nordlander, Stefan A. Maier, and David W. McComb. Electron energy-loss spectroscopy (eels) of surface plasmons in single silver nanoparticles and dimers: Influence of beam damage and mapping of dark modes. *ACS Nano*, 3(10):3015–3022, 2009. PMID: 19772292.

[235] K. Yabana and G. F. Bertsch. Optical response of small silver clusters. *Phys. Rev. A*, 60:3809–3814, Nov 1999.

[236] Ming-Wen Chu, Viktor Myroshnychenko, Cheng Hsuan Chen, Jing-Pei Deng, Chung-Yuan Mou, and F. Javier García de Abajo. Probing bright and dark surface-plasmon modes in individual and coupled noble metal nanoparticles using an electron beam. *Nano Letters*, 9(1):399–404, 2009. PMID: 19063614.

[237] F. Ouyang, P. E. Batson, and M. Isaacson. Quantum size effects in the surface-plasmon excitation of small metallic particles by electron-energy-loss spectroscopy. *Phys. Rev. B*, 46:15421–15425, Dec 1992.

[238] Jaysen Nelayah, Mathieu Kociak, Odile Stephan, F. Javier García de Abajo, Marcel Tence, Luc Henrard, Dario Taverna, Isabel Pastoriza-Santos, Luis M. Liz-Marzan, and Christian Colliex. Mapping surface plasmons on a single metallic nanoparticle. *Nat. Phys.*, 3:348–353, 2007.

[239] Charles Kittel. *Quantum Theory of Solids*. John wiley edition, 1963.

[240] Neil W. Ashcroft and N. David Mermin. *Solid State Physics*. Holt, Rinehart and Winston, 1976.

[241] P.M. Echenique, F. Flores, and R.H. Ritchie. Dynamic screening of ions in condensed matter. volume 43 of *Solid State Physics*, pages 229 – 308. Academic Press, 1990.

[242] F. J. García de Abajo and A. Howie. Relativistic electron energy loss and electron-induced photon emission in inhomogeneous dielectrics. *Phys. Rev. Lett.*, 80:5180–5183, Jun 1998.

[243] Natalia E. Koval, Daniel Sánchez-Portal, Andrey G. Borisov, and Ricardo Díez Muiño. Dynamic screening of a localized hole during photoemission from a metal cluster. *Nanoscale Research Letters*, 7(1):447, Aug 2012.

[244] Iurii Timrov, Nathalie Vast, Ralph Gebauer, and Stefano Baroni. turboeels-a code for the simulation of the electron energy loss and inelastic x-ray scattering spectra using the liouville-lanczos approach to time-dependent density-functional perturbation theory. *Computer Physics Communications*, 196(Supplement C):460 – 469, 2015.

[245] V.J. Keast. Ab initio calculations of plasmons and interband transitions in the low-loss electron energy-loss spectrum. *Journal of Electron Spectroscopy and Related Phenomena*, 143(2):97 – 104, 2005. Electron Energy Loss Spectroscopy in the Electron Microscope.

[246] Gael Donval, Philippe Moreau, Julien Danet, Severine Jouanneau-Si Larbi, Pascale Bayle-Guillemaud, and Florent Boucher. A hybrid method using the widely-used wien2k and vasp codes to calculate the complete set of xas/eels edges in a hundred-atoms system. *Phys. Chem. Chem. Phys.*, 19:1320–1327, 2017.

[247] J Enkovaara, C Rostgaard, J J Mortensen, J Chen, M Dulak, L Ferrighi, J Gavnholt, C Glinsvad, V Haikola, H A Hansen, H H Kristoffersen, M Kuisma, A H Larsen, L Lehtovaara, M Ljungberg, O Lopez-Acevedo, P G Moses, J Ojanen, T Olsen, V Petzold, N A Romero, J Stausholm-Moller, M Strange, G A Tritsaris, M Vanin, M Walter, B Hammer, H Häkkinen, G K H Madsen, R M Nieminen, J K Norskov, M Puska, T T Rantala, J Schiøtz, K S Thygesen, and K W Jacobsen. Electronic structure calculations with gpaw: a real-space implementation of the projector augmented-wave method. *Journal of Physics: Condensed Matter*, 22(25):253202, 2010.

[248] T.P. Mehay, R. Warmbier, and A. Quandt. Investigation of density fluctuations in graphene using the fluctuation-dissipation relations. *Computational Condensed Matter*, 13:1 – 5, 2017.

[249] J. M. Pruneda, D. Sánchez-Portal, A. Arnau, J. I. Juaristi, and Emilio Artacho. Electronic stopping power in lif from first principles. *Phys. Rev. Lett.*, 99:235501, Dec 2007.

[250] A. G. Borisov, J. I. Juaristi, R. Díez Muiño, D. Sánchez-Portal, and P. M. Echenique. Quantum-size effects in the energy loss of charged particles interacting with a confined two-dimensional electron gas. *Phys. Rev. A*, 73:012901, Jan 2006.

[251] Keisuke Tsubonoya, Chunping Hu, and Kazuyuki Watanabe. Time-dependent density-functional theory simulation of electron wave-packet scattering with nanoflakes. *Phys. Rev. B*, 90:035416, Jul 2014.

[252] M. Kuisma, A. Sakko, T. P. Rossi, A. H. Larsen, J. Enkovaara, L. Lehtovaara, and T. T. Rantala. Localized surface plasmon resonance in silver nanoparticles: Atomistic first-principles time-dependent density-functional theory calculations. *Phys. Rev. B*, 91:115431, Mar 2015.

[253] M.S. Dresselhaus R. Saito, G. Dresselhaus. *Physical Properties of Carbon*. Imperial College Press, London, 1998.

[254] Philip Ewels, Thierry Sikora, Virginie Serin, Chris P. Ewels, and Luc Lajaunie. A complete overhaul of the electron energy-loss spectroscopy and x-ray absorption spectroscopy database: eelsdb.eu. *Microscopy and Microanalysis*, FirstView:1–8, 2 2016.

[255] Denis Jacquemin, Ivan Duchemin, and Xavier Blase. 0-0 energies using hybrid schemes: Benchmarks of td-dft, cis(d), adc(2), cc2, and bse/gw formalisms for 80 real-life compounds. *Journal of Chemical Theory and Computation*, 11(11):5340–5359, 2015. PMID: 26574326.

[256] Murilo L. Tiago and James R. Chelikowsky. First-principles gw-bse excitations in organic molecules. *Solid State Communications*, 136(6):333 – 337, 2005.

[257] Angel Rubio, Jennifer L. Corkill, and Marvin L. Cohen. Theory of graphitic boron nitride nanotubes. *Phys. Rev. B*, 49:5081–5084, Feb 1994.

[258] X. Blase, A. Rubio, S. G. Louie, and M. L. Cohen. Stability and band gap constancy of boron nitride nanotubes. *EPL (Europhysics Letters)*, 28(5):335, 1994.

[259] R. S. Lee, J. Gavillet, M. Lamy de la Chapelle, A. Loiseau, J.-L. Cochon, D. Pigache, J. Thibault, and F. Willaime. Catalyst-free synthesis of boron nitride single-wall nanotubes with a preferred zig-zag configuration. *Phys. Rev. B*, 64:121405, Sep 2001.

[260] X. Blase, A. De Vita, J.-C. Charlier, and R. Car. Frustration effects and microscopic growth mechanisms for bn nanotubes. *Phys. Rev. Lett.*, 80:1666–1669, Feb 1998.

[261] Lin gun Liu and William A. Bassett. Compression of ag and phase transformation of nacl. *Journal of Applied Physics*, 44(4):1475–1479, 1973.

[262] Hellmut Haberland. Looking from both sides. *Nature*, 494(7435):E1–E2, Feb 2013.

[263] S. A. Maier. Plasmonics: The promise of highly integrated optical devices. *IEEE Journal of Selected Topics in Quantum Electronics*, 12(6):1671–1677, Nov 2006.

[264] M. Barbry, N. E. Koval, J. Aizpurua, D. Sánchez-Portal, and P. Koval. Size dispersion of the plasmon frequency in metal clusters: ab-initio atomistic description. *in preparation*, 2018.

[265] Niels Verellen, Pol Van Dorpe, Dries Vercruysse, Guy A. E. Vandenbosch, and Victor V. Moshchalkov. Dark and bright localized surface plasmons in nanocrosses. *Opt. Express*, 19(12):11034–11051, Jun 2011.

[266] Federico Marchesin, Peter Koval, Marc Barbry, Javier Aizpurua, and Daniel Sanchez-Portal. Optical response of metallic nanojunctions driven by single atom motion. *ACS Photonics*, 3(2):269–277, sep 2016.

[267] Bruno Pettinger, Philip Schambach, Carlos J. Villagómez, and Nicola Scott. Tip-enhanced raman spectroscopy: Near-fields acting on a few molecules. *Annual Review of Physical Chemistry*, 63(1):379–399, 2012. PMID: 22263910.

[268] Schluecker S. *Surface Enhanced Raman Spectroscopy*. Wiley-VCH Verlag, 2011.

[269] P. G. Etchegoin and E. C. Le Ru. A perspective on single molecule sers: current status and future challenges. *Phys. Chem. Chem. Phys.*, 10:6079–6089, 2008.

[270] D. Steele. *Theory of Vibrational Spectroscopy*. Saunders, Philadelphia, 1971.

[271] E. B. Wilson J. C. Decius and P. C. Cross. *Molecular Vibrations*. McGraw-Hill, New York, 1955.

[272] John R. Ferraro. *Introductory Raman spectroscopy*. Elsever Science, 2003.

[273] Dirk Porezag and Mark R. Pederson. Infrared intensities and raman-scattering activities within density-functional theory. *Phys. Rev. B*, 54:7830–7836, Sep 1996.

[274] M. Cardona. *Light Scattering in Solids*. Springer-Verlag, Berlin, 1982.

[275] C. R. Bailey. The raman and infra-red spectra of carbon dioxide. *Nature*, 123:410, 1929.

[276] J. E. Cahill and G. E. Leroi. Raman spectra of solid co2, n2o, n2, and co. *The Journal of Chemical Physics*, 51(4):1324–1332, 1969.

[277] Yukio Yamaguchi, Michael Frisch, Jeffrey Gaw, Henry F. Schaefer III, and J. Stephen Binkley. Analytic evaluation and basis set dependence of intensities of infrared spectra. *The Journal of Chemical Physics*, 84(4):2262–2278, 1986.

[278] Paolo Giannozzi et al. Quantum espresso: a modular and open-source software project for quantum simulations of materials. *Journal of Physics: Condensed Matter*, 21(39):395502, 2009.

[279] Alan Campion and Patanjali Kambhampati. Surface-enhanced raman scattering. *Chem. Soc. Rev.*, 27:241–250, 1998.

[280] Zhenglong Zhang, Shaoxiang Sheng, Rongming Wang, and Mengtao Sun. Tip-enhanced raman spectroscopy. *Analytical Chemistry*, 88(19):9328–9346, 2016. PMID: 27571253.

[281] R. Dronskowski and R. Hoffmann. *Computational Chemistry of Solid State Materials: A Guide for Materials Scientists, Chemists, Physicists and others*. Wiley, 2008.

[282] J.D. Wilson and C.A. Hernández-Hall. *Physics Laboratory Experiments*. Cengage Learning, 2014.

[283] L. Jensen, J. Autschbach, and G. C. Schatz. Finite lifetime effects on the polarizability within time-dependent density-functional theory. *The Journal of Chemical Physics*, 122(22):224115, 2005.

[284] Achim Hartschuh, Erik Sánchez, X. Xie, and Lukas Novotny. High-resolution near-field raman microscopy of single-walled carbon nanotubes. *Phys. Rev. Lett.*, 90:095503, 2003.

[285] Jordan M. Gerton, Lawrence A. Wade, Guillaume A. Lessard, Z. Ma, and Stephen R. Quake. Tip-enhanced fluorescence microscopy at 10 nanometer resolution. *Phys. Rev. Lett.*, 93:180801, Oct 2004.

[286] Federico Marchesin. Ab-initio theoretical study of electronic excitations and optical properties in nanostructures, 2017. Universidad del Pais Vasco.

[287] Otto F. Sankey and David J. Niklewski. Ab initio. *Phys. Rev. B*, 40:3979–3995, Aug 1989.

[288] SIESTA repository: A first-principles materials simulation code using DFT, 2016.

[289] Emilio Artacho José María Cela Julian D. Gale Alberto García Javier Junquera Richard M. Martin Pablo Ordejón Daniel Sánchez-Portal José M. Soler. User's guide siesta 4.1. 2017.

[290] http://mbpt-domiprod.wikidot.com/list-of-parameters. Mbpt-lcao website.

[291] http://mbpt-domiprod.wikidot.com/local–files/silver-clusters-series/Ag-clusters.tar.gz. Mbpt-lcao: silver clusters input files.

[292] Jeanette F. *Intel Math Kernel Library. Reference Manual*. Intel Corporation, 2016.

[293] C. L. Lawson, R. J. Hanson, D. R. Kincaid, and F. T. Krogh. Basic linear algebra subprograms for fortran usage. *ACM Trans. Math. Softw.*, 5(3):308–323, September 1979.

[294] Volodymyr Kindratenko. Scientific computing with gpus. *Computing in Science and Engineering*, 14:8–9, 2012.

[295] PG 02829 001 v8.0. *CUDA C PROGRAMMING GUIDE*. NVIDIA, 2017.